NPS 68-89-009

NAVAL POSTGRADUATE SCHOOL
Monterey, California

THESIS

F4983

DEVELOPMENT OF A LARGE-SCALE COUPLED
SEA-ICE MODEL FOR INTERANNUAL SIMULATIONS
OF ICE COVER IN THE ARCTIC

by

Gordon H. Fleming

September 1989

Thesis Advisor: Albert J. Semtner

Approved for public release; distribution is unlimited.

PREPARED FOR:

NATIONAL SCIENCE FOUNDATION
1800 G STREET
WASHINGTON, DC 20550

T247248

NAVAL POSTGRADUATE SCHOOL
Monterey, CA. 93943

Rear Admiral Ralph W. West, Jr.
Superintendent

Harrison Shull
Provost

This project was funded by the National Science Foundation, 1800 G Street, N.W., Washington, DC 20550.

Reproduction of this report is authorized.

Released By:

REPORT DOCUMENTATION PAGE

REPORT SECURITY CLASSIFICATION UNCLASSIFIED	1b RESTRICTIVE MARKINGS
SECURITY CLASSIFICATION AUTHORITY	3 DISTRIBUTION/AVAILABILITY OF REPORT APPROVED FOR PUBLIC RELEASE; DISTRIBUTION IS UNLIMITED.
DECLASSIFICATION/DOWNGRADING SCHEDULE	
PERFORMING ORGANIZATION REPORT NUMBER(S) IPS 68-89-009	5 MONITORING ORGANIZATION REPORT NUMBER(S)

NAME OF PERFORMING ORGANIZATION NAVAL POSTGRADUATE SCHOOL	6b OFFICE SYMBOL (If applicable) 68	7a NAME OF MONITORING ORGANIZATION NAVAL POSTGRADUATE SCHOOL	
ADDRESS (City, State, and ZIP Code) MONTEREY, CA 93943-5000		7b. ADDRESS (City, State, and ZIP Code) MONTEREY, CA 93943-5000	
NAME OF FUNDING/SPONSORING ORGANIZATION NATIONAL SCIENCE FOUNDATION	8b. OFFICE SYMBOL (If applicable)	9. PROCUREMENT INSTRUMENT IDENTIFICATION NUMBER	
ADDRESS (City, State, and ZIP Code) 1800 G STREET, N.W. WASHINGTON, DC 20550		10. SOURCE OF FUNDING NUMBERS	
		PROGRAM ELEMENT NO.	PROJECT NO. / TASK NO / WORK UNIT ACCESSION NO.

TITLE (Include Security Classification)
DEVELOPMENT OF A LARGE-SCALE COUPLED SEA-ICE MODEL FOR INTERANNUAL SIMULATIONS OF ICE COVER IN THE ARCTIC

PERSONAL AUTHOR(S)
FLEMING, GORDON H.

TYPE OF REPORT	13b. TIME COVERED	14. DATE OF REPORT (Year, Month, Day)	15 PAGE COUNT
PhD Dissertation	FROM _____ TO _____	1989, SEPTEMBER	245

SUPPLEMENTARY NOTATION THE VIEWS EXPRESSED IN THIS DISSERTATION ARE THOSE OF THE AUTHOR AND DO NOT REFLECT THE OFFICIAL POLICY OR POSITION OF THE DEPARTMENT OF DEFENSE OR THE U.S. GOVERNMETN.

COSATI CODES			18. SUBJECT TERMS (Continue on reverse if necessary and identify by block number)
FIELD	GROUP	SUB-GROUP	SEA-ICE, NUMBERICAL MODELING, ARCTIC, ICE FORECASTING, POLAR

ABSTRACT (Continue on reverse if necessary and identify by block number)

A COUPLED ICE-OCEAN NUMERICAL MODEL IS DEVELOPED WHICH IMPROVES THE SIMULATION OF THE ANNUAL CYCLE AND INTERANNUAL VARIATIONS IN ICE COVER IN THE ARCTIC. THE MODEL IS A FURTHER DEVELOPMENT OF THE WORK BY SEMTNER (1987). ALTHOUGH THE ACCURACY OF THE SIMULATED ICE CONCENTRATION IS INCREASED, THE ANNUAL CYCLE OF ICE COVERAGE IS STILL EXAGGERATED. SEVERAL EXPERIMENTS ARE CONDUCTED TO DETERMINE THE IMPORTANCE OF INCORPORATING A FULLY INTERACTIVE OCEAN, TO SELECT AN OPTIMUM STRENGTH PARAMETER FOR USE IN THE ICE RHEOLOGY, TO INVESTIGATE THE MODEL'S SENSITIVITY TO CHANGES IN THE ALBEDO OF THE FROZEN SURFACE AND TO DETERMINE THE RELATIVE IMPORTANCE OF THE

DISTRIBUTION/AVAILABILITY OF ABSTRACT ☒ UNCLASSIFIED/UNLIMITED ☐ SAME AS RPT. ☐ DTIC USERS	21. ABSTRACT SECURITY CLASSIFICATION UNCLASSIFIED
NAME OF RESPONSIBLE INDIVIDUAL ALBERT J. SEMTNER	22b TELEPHONE (Include Area Code) (408) 646-3267 / 22c OFFICE SYMBOL 68Se

DD FORM 1473, 84 MAR 83 APR edition may be used until exhausted
All other editions are obsolete

SECURITY CLASSIFICATION OF THIS PAGE

☆ U.S. Government Printing Office: 1986—606-243

LINE #19 (CONT.)

VARIOUS DYNAMIC AND THERMODYNAMIC FORCING MECHANISMS. THE REGIONAL DEPENDENCE OF THESE MECHANISMS AND AN ASSESSMENT OF TWO STATISTICAL ANALYSIS TECHNIQUES USED TO MEASURE MODEL IMPROVEMENT ARE ALSO EXAMINED.

INCLUSION OF A FULLY PROGNOSTIC OCEAN COMPONENT VICE A TEN-YEAR MEAN OCEAN CYCLE IN THE MODEL IMPROVES THE CORRELATION OF SIMULATED ICE CONCENTRATION FIELDS WITH OBSERVED DATA. THIS IS THE CASE FOR ALL REGIONS IN THE ARCTIC; FOR BOTH THE ANNUAL CYCLE AND INTERANNUAL VARIATIONS OF THE ICE COVER. A REDUCED STRENGTH PARAMETER VALUE, $P^{*}=HX10^{4}$, IS FOUND TO IMPROVE THE SIMULATION OF THE ICE THICKNESS DISTRIBUTION WITH INCREASED OVERALL THICKNESS AND BETTER COMPRESSION NORTH OF THE CANADIAN ARCHIPELAGO AND GREENLAND. IN CONTRAST TO RESULTS USING ICE MODELS WITHOUT A FULLY PROGNOSTIC OCEAN COMPONENT, THIS MODEL IS QUITE INSENSITIVE TO CHANGES IN THE FROZEN SURFACE ALBEDO. EXCEPTIONS ARE EVIDENT WHERE THE OCEAN HEAT FLUX INTO THE MIXED LAYER IS SMALL AND THE ICE IS THIN.

AT THE SPATIAL (110 KM) AND TEMPORAL (MONTHLY) SCALES USED HERE, THE HEAT PROVIDED BY THE OCEAN APPEARS TO BE THE DOMINANT MECHANISM CONTROLLING THE POSITION OF THE ICE EDGE AND THE EXTENT OF THE ICE PACK. WITHIN THE PACK, IT IS THE DYNAMIC FORCING AND, IN PARTICULAR, THE WIND FORCING WHICH CONTROLS THE ICE THICKNESS AND THICKNESS DISTRIBUTION. THE OCEAN CIRCULATION BELOW THE MIXED LAYER APPEARS TO POSITION THE HEAT UNDERNEATH THE MIZ. THE MIZ IS ALSO THE REGION WHERE THE ICE THICKNESS TENDS TO DECREASE THROUGH DIVERGENCE. THE LINKAGE BETWEEN THE SUBSURFACE HEAT AND THE THINNED ICE COVER IS APPARENTLY CONTROLLED BY CONDITIONS AT THE SURFACE AND THE RESULTING RESPONSE OF THE MIXED LAYER.

Approved for public release; distribution is unlimited.

DEVELOPMENT OF A LARGE-SCALE COUPLED SEA-ICE MODEL FOR INTERANNUAL SIMULATIONS OF ICE COVER IN THE ARCTIC

by

Gordon H. Fleming
Lieutenant Commander, Canadian Navy
B.Sc., Royal Roads Military College, 1978
M.Sc., Naval Postgraduate School, 1987

Submitted in partial fulfillment of the
requirements for the degree of

DOCTOR OF PHILOSOPHY IN PHYSICAL OCEANOGRAPHY

from the

NAVAL POSTGRADUATE SCHOOL
September 1989

C.1

ABSTRACT

A coupled ice-ocean numerical model is developed which improves the simulation of the annual cycle and interannual variations in ice cover in the Arctic. The model is a further development of the work by Semtner (1987). Although the accuracy of the simulated ice concentration is increased, the annual cycle of ice coverage is still exaggerated. Several experiments are conducted to determine the importance of incorporating a fully interactive ocean, to select an optimum strength parameter for use in the ice rheology, to investigate the model's sensitivity to changes in the albedo of the frozen surface and to determine the relative importance of the various dynamic and thermodynamic forcing mechanisms. The regional dependence of these mechanisms and an assessment of two statistical analysis techniques used to measure model improvement are also examined.

Inclusion of a fully prognostic ocean component vice a ten-year mean ocean cycle in the model improves the correlation of simulated ice concentration fields with observed data. This is the case for all regions in the Arctic; for both the annual cycle and interannual variations of the ice cover. A reduced strength parameter value, $P^{*}=hx10^{4}$, is found to improve the simulation of the ice thickness distribution with increased overall thickness and

better compression north of the Canadian Archipelago and Greenland. In contrast to results using ice models without a fully prognostic ocean component, this model is quite insensitive to changes in the frozen surface albedo. Exceptions are evident where the ocean heat flux into the mixed layer is small and the ice is thin.

At the spatial (110 km) and temporal (monthly) scales used here, the heat provided by the ocean appears to be the dominant mechanism controlling the position of the ice edge and the extent of the ice pack. Within the pack, it is the dynamic forcing and, in particular, the wind forcing which controls the ice thickness and thickness distribution. The ocean circulation below the mixed layer appears to position the heat underneath the MIZ. The MIZ is also the region where the ice thickness tends to decrease through divergence. The linkage between the subsurface heat and the thinned ice cover is apparently controlled by conditions at the surface and the resulting response of the mixed layer.

TABLE OF CONTENTS

I. INTRODUCTION 1

A. NUMERICAL MODELLING PERSPECTIVE 2

B. PREVIOUS ARCTIC MODELLING 7

C. OBJECTIVES 14

D. METHODOLOGY 15

II. ARCTIC CLIMATOLOGY 20

A. ATMOSPHERE 21

B. WATER MASSES 27

C. CURRENTS 32

D. ICE 38

III. COUPLED NUMERICAL MODEL 42

A. OCEAN MODEL 42

B. ICE MODEL 48

C. GRID 55

D. BOUNDARY AND INITIAL CONDITIONS 56

E. FORCING FIELDS 61

F. SOLUTION 64

G. ICE-OCEAN MODEL COUPLING 67

IV. INTERACTIVE OCEAN EXPERIMENT 71

A. EXPERIMENTAL SETUP 71

B. RESULTS 73

C. DISCUSSION 123

D. CONCLUSIONS 125

V. ICE STRENGTH EXPERIMENT 127
A. EXPERIMENTAL SETUP 128
B. RESULTS 129
C. DISCUSSION 137
D. CONCLUSION 141
VI. ALBEDO EXPERIMENT 143
A. EXPERIMENTAL SETUP 144
B. RESULTS 148
C. DISCUSSION 158
D. CONCLUSIONS 162
VII. DOMINANT MECHANISM EXPERIMENT 164
A. EXPERIMENTAL SETUP 164
B. RESULTS 165
C. DISCUSSION 182
D. CONCLUSIONS 186
VIII. STATISTICAL CONSIDERATIONS 189
A. METHOD 190
B. RESULTS 193
C. DISCUSSION 199
D. CONCLUSIONS 200
IX. SUMMARY 202
A. MAIN CONCLUSIONS 202
B. MODEL LIMITATIONS 208
C. PROPOSED FUTURE WORK 210
D. FINAL GEM 212

BIBLIOGRAPHY 213

INITIAL DISTRIBUTION LIST 219

LIST OF TABLES

1 VERTICAL LAYER THICKNESSES AND CORRESPONDING DEPTHS .. 59

2 CONSTANTS 70

3 DIFFERENCE BETWEEN THE ABSOLUTE SUM OF SIMULATED AND OBSERVED ICE AREA 105

4 DIFFERENCE BETWEEN ABSOLUTE SUM OF SIMULATED AND OBSERVED ICE AREA ANOMALY (MEAN ANNUAL CYCLE REMOVED) 114

5 CORRELATIONS OF ICE AREA BETWEEN SIMULATION B AND OBSERVED (CORR B) AND SIMULATION C AND OBSERVED (CORR C) 114

6 CORRELATIONS OF ICE AREA BETWEEN SIMULATION B AND OBSERVED (CORR B) AND SIMULATION D AND OBSERVED (CORR D) 138

7 CORRELATIONS OF ICE AREA BETWEEN SIMULATION B AND OBSERVED (CORR B) AND SIMULATION D AND OBSERVED (CORR D) 146

8 MEANS, STD DEVIATIONS AND CONFIDENCE INTERVALS OF THE CORRELATIONS OF 10, 1-YEAR SUBSETS. RESULTS FOR EXPERIMENT B (FIRST LINE) AND C (SECOND LINE) IN ALL FOUR REGIONS 194

9 CORRELATION DIFFERENCES BETWEEN B AND C FOR THE TOTAL TIME SERIES AND FOR THE 10 PSEUDO SUBSETS (ONE YEAR REMOVED) 196

10 PSEUDO VALUES FOR THE ICE AREA TIME SERIES MEANS, STD DEVIATIONS AND 95% CONFIDENCE INTERVALS OF THE PSEUDO VALUES 197

11 PSEUDO VALUES FOR THE ICE AREA ANOMALY TIME SERIES MEANS, STD DEVIATIONS AND 95% CONFIDENCE INTERVALS OF THE PSEUDO VALUES 198

LIST OF FIGURES

1.1 Geography of the Arctic Ocean as represented in the model. The small boxes indicate the centers of land gridpoints. Latitude circles every two degrees are shown over the ocean gridpoints. The arrows point to the mouths of the indicated rivers and the numbers indicate the regions (from Semtner, 1987). 18

2.1 Composite maximum and minimum ice extents at the end of August and February. The hatched region is the difference between extreme positions of the 0.5 ice concentration lines based on 25 August grids and 25 February grids (1953-1977). The dots represent the grid points used in digitization of monthly ice concentration data (from Walsh and Johnson, 1979). .. 22

2.2 The radiation balance showing the short-wave incident radiation, Q, the absorbed short-wave radiation, Q_a, the effective back radiation, Q_b, and the net radiation, Q_n (from Huyer and Barber, 1970). 24

2.3 Vertical profiles of temperature and salinity for various northern high-latitude basins (from Coachman and Aagaard, 1974). 29

2.4 Vertical sections of observed temperature and salinity along the prime meridian, from Coachman and Aagaard (1974) (upper panels); and vertical sections of simulated temperature and salinity across the model domain at approximately 20 degrees E (lower panels). The lower panels have a stretched vertical scale. (from Semtner, 1984b) 32

2.5 Schematic of the large-scale horizontal circulation patterns in the surface waters of the Arctic region (from Parkinson et al., 1987). 35

2.6 Comparison of the simulated circulation in the Atlantic layer (565 m) (upper diagram)(from Semtner, 1987) with the reassessed subsurface circulation presented by Aagaard (lower diagram) (from Aagaard, 1988). 36

3.1 Schematic of fluxes and ice processes incorporated in the thermodynamic portion of the ice model. The total heat flux provided by the ocean circulation below the mixed layer is shown as Q_{ocean} and Q_{cond} is the amount of heat conducted through the ice from the surface. The heat reservoir can only receive heat when the ice is snow free; however, it can provide heat whenever the net heat balance at the surface becomes negative. 53

3.2 The distribution of levels and grid points. Labels to the right and left of the grid points refer to ocean and sea-ice variables, respectively. 57

3.3 Arctic bathymetry plotted with a 500 m contour interval. (from Semtner, 1987). 58

4.1 Observed ice concentration (A) in tenths for month 76 (April, 1977). Contour line labelled -1.5 is coastline. 74

4.2 Simulated ice concentration using prognostic ocean model (B) for month 76 (April, 1977). Contour line labelled -1.6 is coastline. Contours are in tenths. 75

4.3 Simulated ice concentration using 10-year mean ocean data (C) for month 76 (April, 1977). Contour line labelled -1.6 is coastline. Contours are in tenths. 76

4.4 Observed ice concentration (A) in tenths for month 93 (September, 1979). 77

4.5 Simulated ice concentration using prognostic ocean model (B) for month 93 (September, 1979). Contours are in tenths. 78

4.6 Simulated ice concentration using 10-year mean ocean (C) for month 93 (September, 1979). Contours are in tenths. 79

4.7 10-year mean, level two (40 m depth) ocean currents for April. Maximum vector 0.246 m/s. 80

4.8 Simulated level two (40 m depth) ocean currents for month 76 (April, 1977). Maximum vector 0.162 m/s. .. 81

4.9 10-year mean level two (40 m depth) ocean currents for September. Maximum vector 0.152 m/s. 82

4.10 Simulated level two (40 m depth) ocean currents for month 93 (September, 1979). Maximium vector 0.344 m/s. 83

4.11 10-year mean ocean heat flux through the 30 m mixed layer for April. Units are degrees C/sec/cm^2 scaled by 1 x 10^8. Conversion factor to W/m^2 is 1.25 x 10^8. L and H indicate relative lows and highs respectively. 84

4.12 Simulated ocean heat flux through the 30 m mixed layer for month 76. Units are degrees C/sec/cm^2 scaled by 1 x 10^8. Conversion factor to W/m^2 is 1.25 x 10^8. L and H indicate relative lows and highs respectively. 85

4.13 10-year mean ocean heat flux through the 30 m mixed layer for Sep. Units are degrees C/sec/cm^2 scaled by 1 x 10^8. Conversion factor to W/m^2 is 1.25 x 10^8. L and H indicate relative lows and highs respectively. 86

4.14 Simulated ocean heat flux through the 30 m mixed layer for month 93. Units are degrees C/sec/cm^2 scaled by 1 x 10^8. Conversion factor to W/m^2 is 1.25 x 10^8. L and H indicate relative lows and highs respectively. 87

4.15 Simulated thickness contours using prognostic ocean (B) for month 76. Contours are cm of ice thickness. 89

4.16 Simulated thickness contours using 10-year mean ocean (C) for month 76. Contours are cm of ice thickness. 90

4.17 Simulated thickness contours using prognostic ocean (B) for month 93. Contours are cm of ice thickness. 91

4.18 Simulated thickness contours using 10-year mean ocean (C) for month 93. Contours are cm of ice thickness. 92

4.19 Time series of total ice area in region 1. Observed (A) is the solid line, prognostic ocean model (B) is the dashed line and 10-year mean ocean model (C) is the dash-dot line. X axis is months from Jan 1971 to Dec 1980. Y axis is 10's of km^2. 93

4.20 Time series of total ice area in region 2. Observed (A) is the solid line, prognostic ocean model (B) is the dashed line and 10-year mean ocean model (C) is the dash-dot line. X axis is months from Jan 1971 to Dec 1980. Y axis is 10's of km^2. 94

4.21 Time series of total ice area in region 3. Observed (A) is the solid line, prognostic ocean model (B) is the dashed line and 10-year mean ocean model (C) is the dash-dot line. X axis is months from Jan 1971 to Dec 1980. Y axis is 10's of km^2. 95

4.22 Time series of total ice area in region 4. Observed (A) is the solid line, prognostic ocean model (B) is the dashed line and 10-year mean ocean model (C) is the dash-dot line. X axis is months from Jan 1971 to Dec 1980. Y axis is 10's of km^2. 96

4.23 Time series of simulated minus observed total area in region 1. B-A is the solid line, C-A is the dashed line. X axis is months from Jan 1971 to Dec 1980. Y axis is 10's of km^2. 97

4.24 Time series of simulated minus observed total area in region 2. B-A is the solid line, C-A is the dashed line. X axis is months from Jan 1971 to Dec 1980. Y axis is 10's of km^2. 98

4.25 Time series of simulated minus observed total area in region 3. B-A is the solid line, C-A is the dashed line. X axis is months from Jan 1971 to Dec 1980. Y axis is 10's of km^2. 99

4.26 Time series of simulated minus observed total area in region 4. B-A is the solid line, C-A is the dashed line. X axis is months from Jan 1971 to Dec 1980. Y axis is 10's of km^2. 100

4.27 10-year mean annual cycle of total ice area in region 1. Observed (A) is the solid line, simulated (B) is the dashed line and simulated (C) is the dash-dot line. X axis is months and Y axis is 10's of km^2. 101

4.28 10-year mean annual cycle of total ice area in region 2. Observed (A) is the solid line, simulated (B) is the dashed line and simulated (C) is the dash-dot line. X axis is months and Y axis is 10's of km^2. 102

4.29 10-year mean annual cycle of total ice area in region 3. Observed (A) is the solid line, simulated (B) is the dashed line and simulated (C) is the dash-dot line. X axis is months and Y axis is 10's of km^2. 103

4.30 10-year mean annual cycle of total ice area in region 4. Observed (A) is the solid line, simulated (B) is the dashed line and simulated (C) is the dash-dot line. X axis is months and Y axis is 10's of km^2. 104

4.31 Difference from mean annual cycle or anomaly time series of total ice area for region 1. Observed anomaly is the solid line, simulated (B) anomaly is the dashed line. X axis is months, Y axis is 10's of km^2. 106

4.32 Difference from mean annual cycle or anomaly time series of total ice area for region 1. Observed anomaly is the solid line, simulated (C) anomaly is the dashed line. X axis is months, Y axis is 10's of km^2. 107

4.33 Difference from mean annual cycle or anomaly time series of total ice area for region 2. Observed anomaly is the solid line, simulated (B) anomaly is the dashed line. X axis is months, Y axis is 10's of km^2. 108

4.34 Difference from mean annual cycle or anomaly time series of total ice area for region 2. Observed anomaly is the solid line, simulated (C) anomaly is the dashed line. X axis is months, Y axis is 10's of km^2. 109

4.35 Difference from mean annual cycle or anomaly time series of total ice area for region 3. Observed anomaly is the solid line, simulated (B) anomaly is the dashed line. X axis is months, Y axis is 10's of km^2. 110

4.36 Difference from mean annual cycle or anomaly time series of total ice area for region 3. Observed anomaly is the solid line, simulated (C) anomaly is the dashed line. X axis is months, Y axis is 10's of km^2. 111

4.37 Difference from mean annual cycle or anomaly time series of total ice area for region 4. Observed anomaly is the solid line, simulated (B) anomaly is the dashed line. X axis is months, Y axis is 10's of km^2. 112

4.38 Difference from mean annual cycle or anomaly time series of total ice area for region 4. Observed anomaly is the solid line, simulated (C) anomaly is the dashed line. X axis is months, Y axis is 10's of km^2. 113

4.39 Mean ice draft (m) in winter derived from submarine upward looking echo sounder data. Draft is averaged over three months, centered on the first of March (from Bourke and Garret, 1987). 117

4.40 Mean ice draft (m) in spring derived from submarine upward looking echo sounder data. Draft is averaged over three months, centered on the first of June (from Bourke and Garret, 1987). 118

4.41 Mean ice draft (m) in summer derived from submarine upward looking echo sounder data. Draft is averaged over three months, centered on the first of September (from Bourke and Garret, 1987). 119

4.42 Mean ice draft (m) in fall derived from submarine upward looking echo sounder data. Draft is averaged over three months, centered on the first of December (from Bourke and Garret, 1987). 120

4.43 10-year mean ocean heat flux through the 30 m mixed layer for July. Units are degrees $C/sec/cm^2$ scaled by 1×10^9. Conversion factor to W/m^2 is $.125 \times 10^9$. L and H indicate relative lows and highs respectively. 121

5.1 Simulated ice thickness contours (cm) for August, 1974. $P^* = h \times 1 \times 10^5$. 131

5.2 Simulated ice thickness contours (cm) for August, 1974. $P^* = h \times 5 \times 10^4$. 132

5.3 Simulated ice thickness contours (cm) for August, 1974. $P^* = h \times 3 \times 10^4$. 133

5.4 Simulated ice thickness contours (cm) for August, 1974. $P^* = h \times 1 \times 10^4$. 134

5.5 Simulated ice thickness contours (cm) for August, 1974. $P^* = h \times 5 \times 10^3$. 135

5.6 Simulated ice thickness contours (cm) for August, 1974. $P^* = h \times 1 \times 10^3$. 136

6.1 Simulated ice thickness contours (cm) for September, 1977. High albedo case (run A6). 149

6.2 Simulated ice thickness contours (cm) for September, 1977. Low albedo case (run A7). 150

6.3 Simulated ice thickness contours (cm) for July, 1977. High albedo case (run D6). 152

6.4 Simulated ice thickness contours (cm) for July, 1977. Low albedo case (run D6). 153

6.5 Simulated ice thickness contours (cm) for July, 1977. High albedo case (run D7). 154

6.6 Simulated ice thickness contours (cm) for July, 1977. Low albedo case (run D7). 155

6.7 Simulated ice thickness contours (cm) for July, 1977. High albedo case (run D8). 156

6.8 Simulated ice thickness contours (cm) for July, 1977. Low albedo case (run D8). 157

7.1 Simulated ice thickness contours (cm) for April, 1977. Base model (run D1). 166

7.2 Simulated ice thickness contours (cm) for August, 1977. Base model (run D1). 167

7.3 Simulated ice thickness contours (cm) for April, 1977. Constant ocean heat flux = 25 W/m^2 (run D2). 168

7.4 Simulated ice thickness contours (cm) for August, 1977. Constant ocean heat flux = 25 W/m^2 (run D2). 169

7.5 Simulated ice thickness contours (cm) for April, 1977. Ocean heat flux = 0.0 W/m^2 (run D3). 171

7.6 Simulated ice thickness contours (cm) for August, 1977. Ocean heat flux = 0.0 W/m^2 (run D3). 172

7.7 Simulated ice thickness contours (cm) for April, 1977. Level two current velocities = 0.0 m/s (run D4). 173

7.8 Simulated ice thickness contours (cm) for August, 1977. Level two current velocities = 0.0 m/s (run D4). 174

7.9 Simulated ice thickness contours (cm) for April, 1977. Ocean heat flux and level two velocities = 0.0. (run D5). 176

7.10 Simulated ice thickness contours (cm) for April, 1977. Wind stress = 0.0. (run D6). 177

7.11 Simulated ice thickness contours (cm) for August, 1977. Wind stress = 0.0. (run D6). 178

7.12 Simulated ice thickness contours (cm) for April, 1977. Wind and ocean current stress = 0.0. (run D7). 180

7.13 Simulated ice thickness contours (cm) for August, 1977. Wind and ocean current stress = 0.0. (run D7). 181

7.14 Simulated ice thickness contours (cm) for April, 1977. Wind and ocean current stress and ocean heat flux = 0.0. (run D8). 183

7.15 Simulated ice thickness contours (cm) for August, 1977. Wind and ocean current stress and ocean heat flux = 0.0. (run D8). 184

ACKNOWLEDGEMENTS

I would like to acknowledge my sincere appreciation to Dr. Albert Semtner, my thesis advisor, for his assistance and support in all aspects of this work. He suggested the topic, provided the basic numerical code and also made available the substantial amount of computer time required to run it. He permitted me the freedom to pursue those areas of particular interest to me yet also supplied sufficient direction to ensure that the work was properly focused. His objective critiques and advice smoothed many of the difficulties encountered and made this work a most challenging, rewarding and enjoyable experience.

The remainder of my Doctoral Committee consisting of Dr. Robert Bourke, Dr. David Smith IV, Dr. Mary Batteen, Dr. Robert Haney and Dr. Laura Johnson provided many valuable ideas and constructive comments, especially within their respective areas of expertise. Their cooperation and responsiveness to my requests were very much appreciated. Dr. John Walsh of the University of Illinois, in addition to providing most of the forcing and observed field data, has also been a continual source of encouragement and useful discussion.

The computing for this work was conducted at the National Center for Atmospheric Research, which is funded by the National Science Foundation.

I. INTRODUCTION

Interest in the complex geophysical processes occurring in, above and around the Arctic Ocean continues to increase as the economic, strategic and political values of this region become more important. In the case of economic concerns, vast oil reserves are being exploited in this area and the search for more reserves continues. Much of Western Europe, northern Canada and the USSR are supplied via shipping routes which are dependent on weather and ice conditions in the Arctic regions. Arctic waters also contain some of the most valuable fishing grounds in the world; however our ability to use them is again dependent on the state of ice, water and weather.

The Arctic Ocean spans the shortest distance between North America and the USSR and is therefore of obvious strategic importance. However the extreme environmental conditions encountered there make military operations very difficult and expensive. Naval vessels used in northern waters must be properly designed if they are to function with any effectiveness and their performance will normally be significantly degraded. The requirement for an ice breaking capability is obvious. In addition, the highly variable temperatures, surfaces, and material compositions of water, ice and snow have a dramatic effect on both the air and water boundary layers. This in turn affects electro-magnetic,

electro-optical, and acoustic transmission and reception. Sea-ice is a strong source of ambient acoustic noise and radar scatter. Detection of surface or low level air targets by radar or submarines by passive or active acoustic means becomes very difficult.

Several countries border the Arctic mediterranean and have strong political motives for establishing or extending their sovereignty and/or economic control as far offshore as possible. The presence of several "chokepoints" within the region provides the opportunity to influence operations in the entire Arctic Basin by controlling only limited areas.

Obviously, a comprehensive knowledge of the Arctic environment, including the ocean, atmosphere and sea-ice, and a capability to predict this environment with some accuracy would be of great value. The expense of establishing a complete observational network is prohibitive. An important role must be played by numerical modelling which has the potential to provide both a full analysis of the current conditions based on limited data, and a prediction capability for future conditions.

A. NUMERICAL MODELLING PERSPECTIVE

It is recognized that the atmosphere, ice and ocean interact in a highly complex nonlinear fashion. Consideration of one of these three components cannot be realistically done in total isolation of the other two. However a complete

understanding of all the physics involved in describing each parameter and its interaction with the others is lacking. Therefore our ability to mathematically describe the physics involved is also lacking. Furthermore, when significant theoretical advances have been made in the past, memory and speed limitations in computing facilities have been an obstacle. Even with today's supercomputers, compromises must be made to balance computing requirements (memory, expense and time) against the accuracy desired. In order to minimize these compromises, the three component problem has generally been broken up into its three individual components of atmosphere, ocean and ice. The two components which are not being specifically examined in a model are then parameterized in some fashion or they are represented by prescribed empirical data.

Numerical modelling was first applied to the atmosphere. Impetus was provided by public as well as military interests. Great strides have been made by meteorologists in predicting the weather by numerical models. Numerous atmospheric numerical models of varying complexity have been developed and are currently in use by the various National Weather Centers. However, despite a great deal of effort and expense, deterministic prediction of daily weather fluctuations is presently limited to five to ten days. Theoretical arguments suggest that the ultimate practical range of such predictions is about two weeks.

Numerical modelling of the global oceans requires a thousandfold increase in computer power. Compared to numerical modelling of the global atmosphere, the horizontal resolution of the global oceans must be ten times as great, and the numerical time step therefore ten times as small, to accommodate the smaller radius of deformations and faster gravity wave speeds. Ocean modelling is further complicated by irregular borders, islands, widely varying density structures, internal and boundary mixing processes, complex and varied boundary layers and a marked paucity of observations. Nevertheless with the major contributions of Bryan (1969) and numerous others such as Takano (1974), Semtner (1974), Cox (1984) and Semtner and Chervin (1988), viable three-dimensional, baroclinic numerical models have been developed which simulate the state of the world's oceans quite well. These models are currently in wide use in circulation studies, tracer distribution analysis, etc.

Numerical modelling of the ice has also progressed significantly over the past twenty years. The physics of this problem are now considered to be fairly well understood. Prediction of the ice both in areal extent and thickness distribution, is known to be a function of dynamic forcing (both internal and external) and thermodynamic forcing. The work of Hibler (1979, 1980) has provided details of the important dynamic processes. Maykut and Untersteiner (1969, 1971) have constructed a detailed one-dimensional

thermodynamic model which provided a comprehensive view of the thermodynamic aspects. In the short term (days), wind stress appears to be the dominant factor in ice prediction. On this time scale the thermodynamic effects of freezing and melting and the dynamic effects of weak ocean currents are small. As a result, predictions of sea-ice on this time scale can be reasonably accurate with only minimal consideration (simple parameterizations) of the ocean's influence. However, attempts to predict ice on a seasonal basis using either a thermodynamic or a dynamic model, or some combination of the two, without adequate consideration of the ocean's influence, have met with only limited success. The ice and ocean are closely linked over the long time scale and the interactions which occur between them must be accounted for.

The U.S. Navy's current operational ice forecasting model run at the Fleet Numerical Oceanography Center (FNOC) is called the NORDA/FNOC Polar Ice Prediction System (PIPS). One of the limitations of this model is its use of the monthly average ocean currents and ocean heat fluxes produced from the Hibler and Bryan (1987) ice-ocean model. This model was forced for several years of integration by repeatedly using a single year of observed atmospheric forcing data (December 1978 to November 1979). This year was chosen because it was the "FGGE" year in which a large number of drifting buoys were in the Arctic Basin which could provide a check for the model currents. The time period was not chosen for its similarity

to an average condition and, as noted by Hibler and Bryan (1987), it was in fact substantially different from the long term average. Additionally, the ocean below the mixed layer was constrained, with a three year damping time, to the observed circulation. Therefore, the ocean fluxes and currents calculated from the output of this model may very well be limiting the accuracy of the PIPS model predictions. This problem has yet to be resolved.

The present work is aimed at improving our understanding and capability to numerically predict the location and thickness of Arctic ice on a seasonal time scale. This will be done through the further development of a linked ice-ocean numerical model using observed atmospheric forcing and a fully prognostic ocean model formulation. Several sensitivity studies will also be conducted to gain a better appreciation of the relative importance of the various mechanisms controlling the ice cover and to improve their representation in the model. The remainder of this chapter briefly describes previous efforts in ice-ocean modelling which have provided the background for this work. The specific goals and objectives of this research are also listed. Chapter II provides the geophysical context in which the model operates and Chapter III is a description of the model itself including the assumptions, boundary conditions and forcing fields under which it is run. Chapter IV examines the importance of including a fully interactive ocean model in studies of

interannual ice cover variations and Chapter V examines the effect of ice strength on those same variations and the ice thickness distribution. Chapter VI investigates the sensitivity of the model to frozen surface albedo changes and Chapter VII is a comprehensive examination of the various dynamic and thermodynamic processes included in the model and their relative importance to the evolution of the ice cover. Chapter VIII addresses the value of comparing the model simulations statistically and Chapter IX is a final summary which includes the conclusions from this work.

B. PREVIOUS ARCTIC MODELLING

Coupled ice-ocean models of the Arctic on seasonal time scales were developed only recently. Construction of such models was initiated primarily in response to the lack of quantified success of previous large scale ice modelling efforts by numerous investigators. General seasonal trends and basin-wide distributions similar to observed fields were achieved in these earlier efforts. However, the accuracy of regional ice distributions and/or the phase of the annual cycle were often poor.

Manabe and Stouffer (1980) developed a coupled ice-ocean-atmosphere model which used a one-dimensional mixed layer ocean and a motionless slab with no leads for the ice. The atmospheric model provided daily variable forcing. This produced a wintertime ice cover about double that normally

observed in the Arctic. Washington et al. (1976, 1980) used a simple thermodynamic ice model but did not include any ice dynamics. Their model produced an excess of ice in the North Atlantic in all but the summer months and ice thicknesses in the central Arctic were less than half those interpreted from submarine surveys (LeSchack et al., 1971; LeSchack, 1980).

Once the emphasis shifted to prediction of the ice, the atmospheric portion of the coupled models was generally dropped in favor of prescribed atmospheric forcing and more elaborate ocean and ice models. The detailed thermodynamic ice model of Maykut and Untersteiner (1969, 1971) included the effects of ice salinity, brine pockets, shortwave radiation heating, vertical density variations, conductivity and specific heat of ice and water. However, this model required a great deal of computation to reach an equilibrium state. This made it impractical for application to a large scale three-dimensional coupled model. Semtner (1976a) simplified this complex model by parameterizing several of the processes. With the use of a three-layer version he was able to closely reproduce the results of Maykut and Untersteiner (1969,1971) in a wide variety of simulations, yet this simplified model had fewer computational requirements than one layer of ocean in a multi-level ocean model. This made it ideal for inclusion into a large three-dimensional gridded coupled model.

The Parkinson and Washington (1979) ice model used a further simplified "zero-layer" thermodynamic ice model (also proposed and tested successfully by Semtner (1976a)), in conjunction with a dynamic forcing model. The dynamics were based on stresses from wind, water, Coriolis force, internal ice resistance and ocean surface tilt. The atmosphere was represented by monthly climatological fields of temperature and pressure and the ocean was represented by a simple 30 m deep ocean mixed layer with a constant vertical heat flux. This model produced a reasonable yearly cycle of sea ice extent; however, the ice thickness distribution did not compare well with observational evidence. The combined thermodynamic-dynamic ice model concept was further improved by Hibler (1979, 1980). He also used the "zero-layer" thermodynamic approach of Semtner (1976a) but combined it with a more complex dynamic model and used daily observed atmospheric forcing data. The ocean was again represented by a simple fixed-depth mixed layer with a constant vertical heat flux applied beneath it. The essential difference in the Hibler approach was to link the dynamics of ice motion to the ice thickness by allowing the ice interaction to become stronger as the ice grew in thickness and/or concentration. In order to do this consistently, a viscous-plastic ice rheology was used. Arctic simulations with this model showed that the spatial distribution of ice thickness was strongly influenced by the ice dynamics. The results compared

favorably with the ice distribution observations of LeSchack (1980) and were a significant improvement over previous efforts. The improved ice dynamics as well as daily atmospheric forcing permitted a much better representation of lead formation. The proper representation of leads was considered important because heat and salt fluxes, as well as ice formation rates are nominally an order of magnitude larger in open leads than under the pack ice.

Further analysis of the Semtner (1976a) thermodynamic ice model was conducted by Semtner (1984a). He concluded that an oversimplification of the thermodynamics tends to exaggerate the seasonal sea-ice cycle. The "three-layer" version of the thermodynamic model involves twice as much computation as the "zero-layer" version but does provide a much better representation of the ice. The computational requirements remain negligible compared to that of the ocean model. Therefore the "three-layer" model was recommended for use in large coupled models where accurate representation of the regional and temporal changes in the ice field are important.

Several experiments have been conducted to determine the importance of atmospheric forcing. Three years of interannually variable forcing was applied by Hibler and Walsh (1982) to the Hibler (1979) ice model, but omitting interactive ocean circulation effects. Their results again demonstrated the importance of ice dynamics for achieving accurate ice forecasts. Quantitative agreement with observed

interannually varying ice volume and transport was achieved; however, a noticeable seasonal bias was evident. The ice extent and thickness in winter and spring for all years was excessive while the extent and thickness of summer ice was too small with too much melting and excessive open water. They concluded that accurate parameterization of oceanic effects and a better treatment of the snow cover would probably be necessary in order for Arctic ice to be accurately modeled. Walsh et al. (1984, 1985) increased the interannually varying atmospheric forcing period to 30 years and used a more elaborate thermodynamic model with the Hibler (1979) ice dynamics. The seasonal bias in ice concentration was again evident in this model and it also showed considerable sensitivity to the number of vertical layers in the thermodynamic portion.

An Arctic ocean circulation model was developed by Semtner (1976b) as an extension to the numerical ocean model of Bryan and Cox (Bryan, 1969). Many of the observed features of the Arctic Ocean and Greenland Sea circulation were reproduced by this Arctic model despite the simplifications of mean annual wind forcing and a non-interactive ice cover. In order to develop an ice model suitable for seasonal ice predictions and daily variable atmospheric forcing, Hibler and Bryan (1984, 1986) coupled the Semtner (1976b) Arctic ocean model with a somewhat simplified Hibler (1979) thermodynamic-dynamic ice model. This resulted in the first seasonal,

coupled, ice-ocean numerical model. A linear term was included in the ocean model which damped the ocean's temperature and salinity values below the mixed layer to climatology. This "robust-diagnostic" forcing was chosen to have a three year relaxation time. Multi-year drift from climatology was prevented; yet shorter term variations, particularly in the mixed layer, could still be prognostically simulated. The inclusion of the oceanic component greatly improved the simulated ice edge, removing much of the seasonal biases evident in the earlier work by Hibler and Walsh (1982) and Walsh et al. (1984, 1985). Hibler and Bryan (1987) showed that many of the features of ice growth and decay, in various regions of the Arctic, result from a combination of numerous influences, often with opposing effects. For example, the East Greenland ice edge is forced southward by the East Greenland Current and by winter freezing. However, due to a strong vertical heat flux from the ocean, the amount of ice melted actually exceeds the amount frozen in this region. The southward extension of the ice zone is thus significantly inhibited.

The Hibler and Bryan (1984, 1986) model simulated the seasonal variations in ice cover more accurately than any of the previous modelling efforts. However, Semtner (1987) noted that the three year diagnostic constraint may have dominated the forcing for the ocean model and thereby controlled the ice simulation. The constraint also prevented ocean circulation

and ice phenomena occurring on multi-year time scales (bottom water formation, carbon dioxide effects, etc.) from being forecast. Additionally, the climatological ocean was unrealistic in the variable-current, shallow-water regions of the Barents and East Siberian Seas. A fully prognostic, coupled, ice-ocean model would have no such limitations and was therefore developed (Semtner, 1987). This model, hereafter referred to as SM, is the basis of the current work. SM incorporated the best features of the previous modelling efforts. The Semtner (1976b) ocean model, optimized for high speed computers, was combined with the "three-layer" thermodynamic ice model (Semtner, 1976a) and a modified Hibler (1979) dynamic model. The daily forcing ice dynamics formulation of Hibler (1979) required more computation than a complete ocean model. This was not considered an equitable distribution of computation load. The Hibler dynamics were modified to use monthly averaged forcing instead of daily forcing, yet still retain the first-order dynamic effects (Hibler, 1988). This also permitted a much longer time step and longer integrations. A simple 30 year mean seasonal cycle was computed from the forcing data used in Walsh et al. (1985) for atmospheric forcing. Monthly values of water inflow at the appropriate salinity, temperature and volume from rivers and the southern ocean boundaries were specified. These water mass fluxes were invariate in time. The model produced realistic representations of the average seasonal ice cycle

in distribution and concentration. The ocean circulation, including the major surface currents, water masses, and possible water transformation regions were also well simulated to the limits of the resolution. Results from SM emphasized the high degree of thermodynamic and dynamic interaction between the ice and ocean.

C. OBJECTIVES

The objectives of this work were to gain further understanding of the relative importance of mechanisms controlling the ice cover in the Arctic Basin and to develop a numerical model capable of accurately simulating the operationally and climatologically important interannual variations of ice cover in this region. In particular, the following points unique to this work were to be investigated:

- Determine the importance of including a fully prognostic and interactive ocean component in a linked ice-ocean model. The importance was to be assessed relative to the accuracy of simulations of interannual variability in the Arctic ice cover.

- Determine the sensitivity of the model to changes in the ice rheology strength parameter and subsequently select an optimum value of this parameter for incorporation into the model.

- Determine the sensitivity of the model to changes of snow and ice albedo and if appropriate incorporate a more sophisticated albedo representation into the model.

- Determine the relative importance of the various dynamic and thermodynamic ice cover forcing mechanisms included in the model, particularly the two features inherent in the ocean model (vertical ocean heat flux and ocean current stress).

- Assess the regional dependency of the above ice cover control mechanisms.
- Assess the statistical significance of the differences between the various model run results.

D. METHODOLOGY

This research was accomplished through the utilization and further development of the coupled numerical model of Semtner (1987). The Semtner (1987) model is the most freely prognostic, physically representative and computationally efficient of the large-scale, linked, ice-ocean numerical models previously developed for the Arctic. Considerable skill has been demonstrated with the model in reproducing the annual cycle of ice extent with climatological forcing. Most importantly, the inclusion of an interactive ocean reduced the pronounced tendency of previous ice-only simulations to exaggerate the annual ice cycle.

Numerous model integrations were conducted. In each experiment the model was modified to examine some particular mechanism which was expected to influence the interannual variability of the ice cover. In the majority of cases the model was integrated for ten years. However, some of the sensitivity testing required a large number of repeated runs and in those cases the model runs were limited to one integration year. Additionally, in the sensitivity runs where inclusion of an interactive ocean was of limited concern, the model was run with a prescribed ten-year average ocean

condition vice a prognostic ocean component. The ice cover simulations were evaluated from January 1971 to December 1980 inclusive. These years were chosen because the observed ice concentration data set, to which the modelled ice concentrations were compared, was most accurate in this period. This was especially true after 1972 due to the assimilation of microwave remotely sensed data. Parkinson et al. (1987) was also an excellent source of comparison data for the years 1973-1976.

The observed ice concentration fields were provided by Walsh, and were the same as those used in Fleming (1987) but converted through bi-linear interpolation to the grid used here. The observed ice concentration fields were regarded as the "true" monthly ice concentrations. However, they were in fact the average of data received from several sources, each with its own source of error (Walsh and Johnson, 1979). Nevertheless, these fields were still the most comprehensive and accurate representations of real data available and covered a long enough time period to permit viable statistical analysis. All 120 months of observed ice concentration were contoured to gain a qualitative appreciation of the annual cycle, its variability and absolute extent. This also provided the baseline view for visual comparison with the simulated ice concentration data.

The seasonal average ice draft contours from Bourke and Garrett (1987) were the primary source of comparison data for

the simulated ice thicknesses and thickness distributions. Although these contours represent "observed" data from submarine transits, the data were heavily averaged in time and space to produce the contours. Nevertheless, the general thickness and distribution patterns did provide an indication of the true seasonal ice thickness distribution.

The monthly varying atmospheric forcing fields were also provided by Walsh. These fields were produced from the same data used by Walsh et al. (1985) and were also the source of the 30-year mean forcing using in Semtner (1987).

It was shown by Fleming (1987) and Garcia (1988) that correlations between ice concentration and thermodynamic forcing variables (sea surface temperature (SST) and air temperature) and dynamic forcing variables (winds and previous ice condition) vary significantly between regions which experience different dynamic ocean conditions. To gain some appreciation for these regional differences but still maintain the amount of data manipulation within reasonable limits, the complete grid space was divided into four regions (see Figure 1.1). The divisions were selected based on the general ocean current regime. The four regimes represented were:

- Region 1 X=1,18 Beaufort Gyre.
- Region 2 X=19,27 Transpolar Drift, Ellesmere Is. and Greenland ice convergence zone.

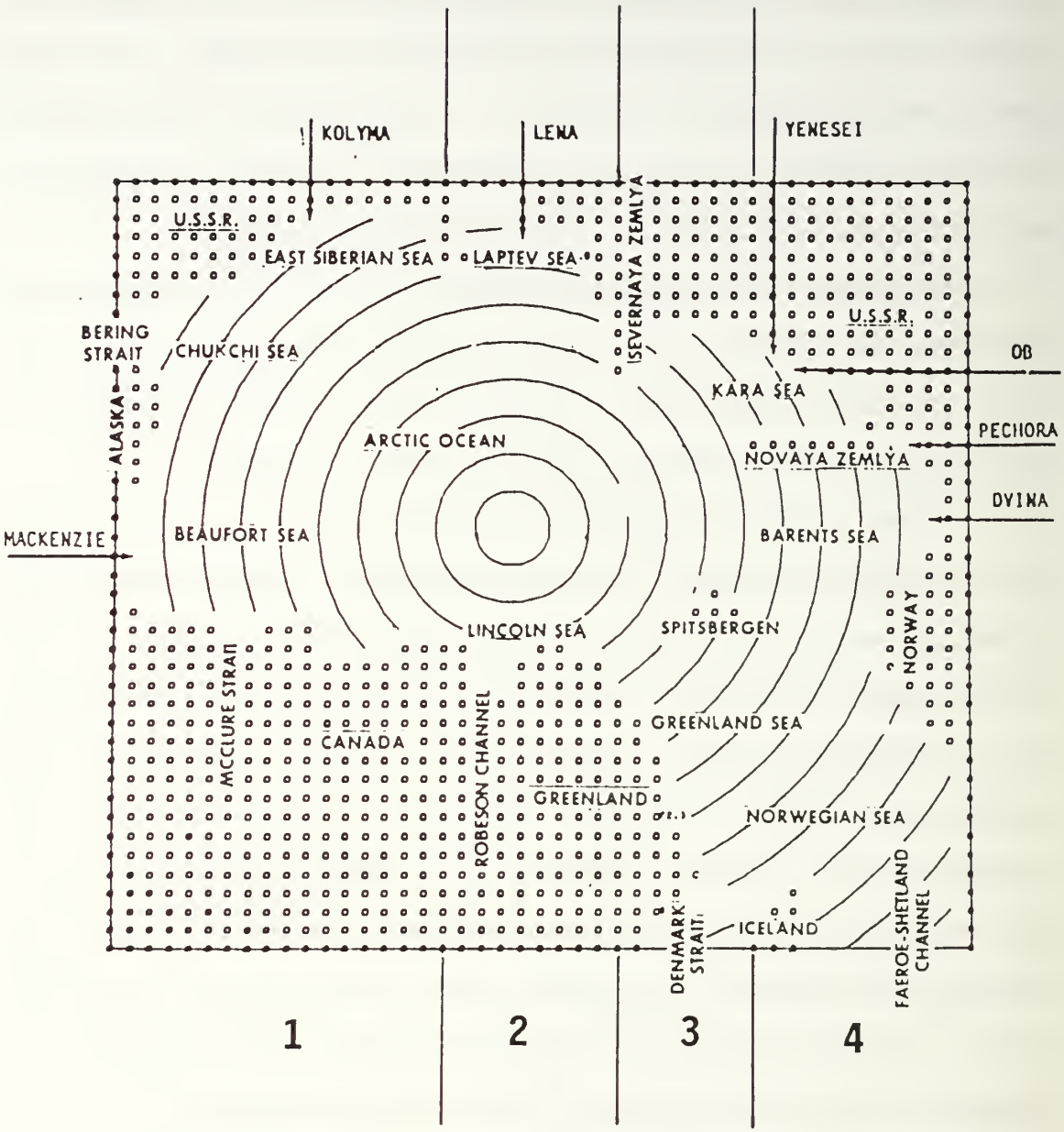

Figure 1.1 Geography of the Arctic Ocean as represented in the model. The small boxes indicate the centers of land gridpoints. Latitude circles every two degrees are shown over the ocean gridpoints. The arrows point to the mouths of the indicated rivers and the numbers indicate the regions (from Semtner, 1987).

- Region 3 X=28,34 Transpolar Drift (TPD), East Greeenland Current (EGC).

- Region 4 X=35,45 Norwegian Current.

where X defines the location of the region on the X axis of the grid. Each region extends from 1 to 42 on the Y axis of the grid. In those cases where the modified model simulations produced ice fields more representative of the observed ice fields than before the modifications were made, the appropriate changes were incorporated into the model.

II. ARCTIC CLIMATOLOGY

This chapter presents the geophysical characteristics of the Arctic region emphasizing those features which are most relevant to numerical modelling of the ice cover and ocean.

The primary dynamic driving forces for sea ice growth and movement are the air stress resulting from wind-induced surface drag and the water stress resulting from ocean currents. Variations in wind forcing are determined by the passage of synoptic scale weather systems having spatial scales of 100 to 1000 km and durations of several days. The response of the sea ice to mesoscale features of the atmosphere and ocean is to produce eddies and other fluctuations with length scales of approximately 10 km and time scales of hours to days. Inertial oscillations of drifting sea ice have similar periods. Longer term fluctuations, with time scales of weeks to seasons, represent responses to atmospheric and ocean forcing integrated over equivalent time scales. No firm evidence exists to suggest that small time and spatial forcing is unimportant to the seasonal evolution of the ice cover. However numerical modelling of the Arctic ice has not developed sufficiently at present to resolve such forcing for long periods over the entire Arctic basin. Therefore, the emphasis in this work will be on the monthly time and larger spatial scale features.

When examining fluctuations varying on time scales of a season to several decades, the dominant signal in sea ice variability is clearly the annual cycle (Parkinson et al., 1987). Figure 2.1 shows the 25-year (1953-1977) envelopes of the positions of the Arctic ice edge at the end of August and February. At most longitudes the seasonal change from the summer to the winter ice edge positions is considerably greater than the 25-year range of extremes for a particular month. The overall annual freeze-melt cycle is primarily a response to the seasonally varying insolation, albeit with a large amount of feedback and interaction with the ocean.

A. ATMOSPHERE

The climate in the Arctic region is largely determined by four aspects (Sater et al., 1971):

- A distinctive cycle of prolonged periods of daylight with net positive surface heat balance followed by prolonged periods of darkness with a net negative surface heat balance.
- A very persistent, cold-cored, circumpolar, upper level vortex which steers the mesoscale surface-level weather systems.
- A surface cover of snow or ice for periods of the year, which causes significant changes in surface albedo and therefore surface heat absorption.
- A strong temperature inversion above snow or ice surfaces which acts to decouple the surface from higher level atmospheric activity.

Many factors are involved in determining the net surface heat balance for any particular region of the Arctic. These will not all be examined here. Suffice it to say that the

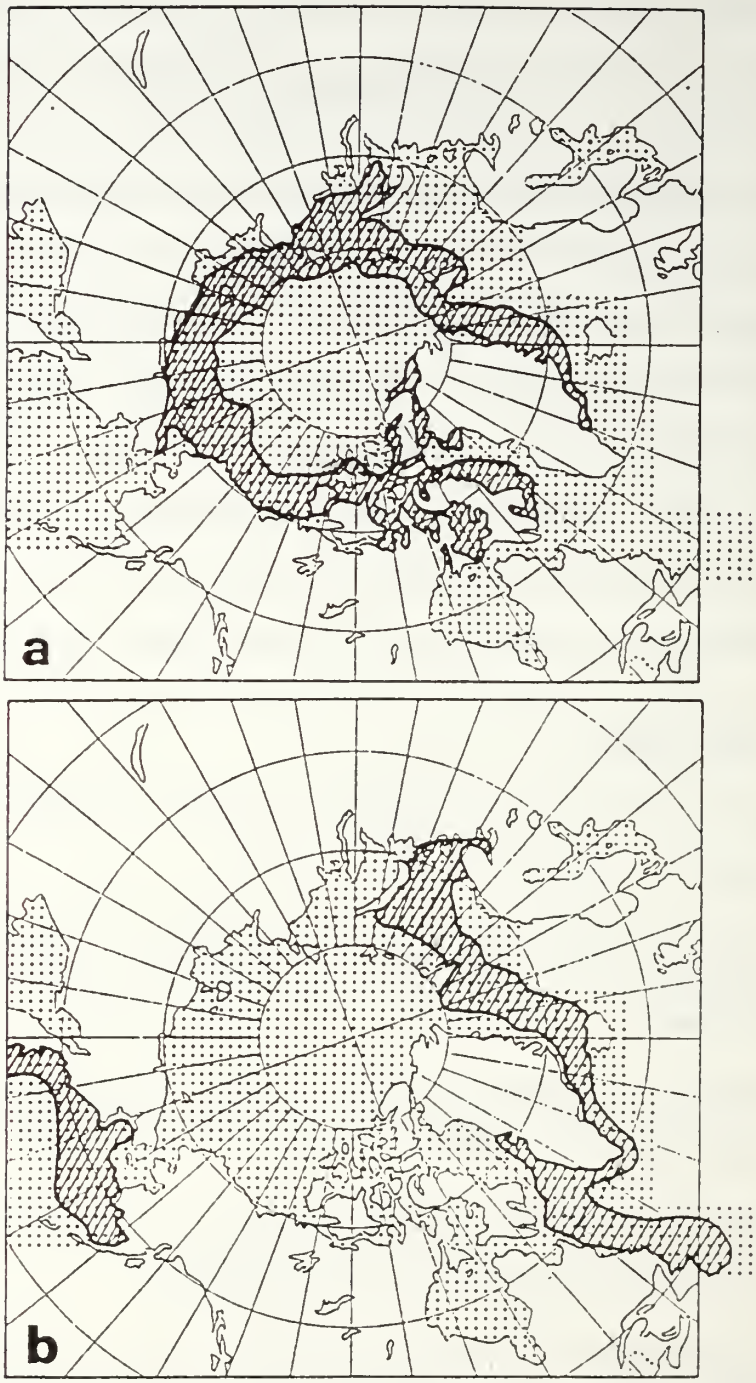

Figure 2.1 Composite maximum and minimum ice extents at the end of August and February. The hatched region is the difference between extreme positions of the 0.5 ice concentration lines based on 25 August grids and 25 February grids (1953-1977). The dots represent the grid points used in digitization of monthly ice concentration data (from Walsh and Johnson, 1979).

main factor is believed to be the insolation rate. Figure 2.2 summarizes the effects in a radiation balance diagram determined for the Barrow Strait region. The diagram shows long periods of net heat loss which correspond to the polar winter and periods of large ice production. The long heat loss periods are followed by short intense periods of net heat gain corresponding to the long daylight hours and the ice melting of summer. This figure is reasonably representative of the heat balance in the Arctic in general. However, a term which is missing and which is regionally and spatially quite variable is the advective heat flux, Q_v. This term represents the heat supplied to the surface from vertical and horizontal advection in the ocean. Mixing processes could also be included. Huyer and Barber (1970) suggested that this term was negligible in the Barrow Strait. However, in other regions of the Arctic, large differences in latitudinal extent of the ice exist as can be seen in Figure 2.1. This suggests that Q_v may be very significant to the surface heat balance in other regions in the Arctic.

Surface weather systems, especially cyclones, are primarily generated in regions of strong differential heating. Significant differences in surface temperatures occur at land-sea, ice-sea, and warm-cold current boundaries. Several such boundaries are found in the Arctic in fairly constant positions. Weather systems are therefore more prevalent in

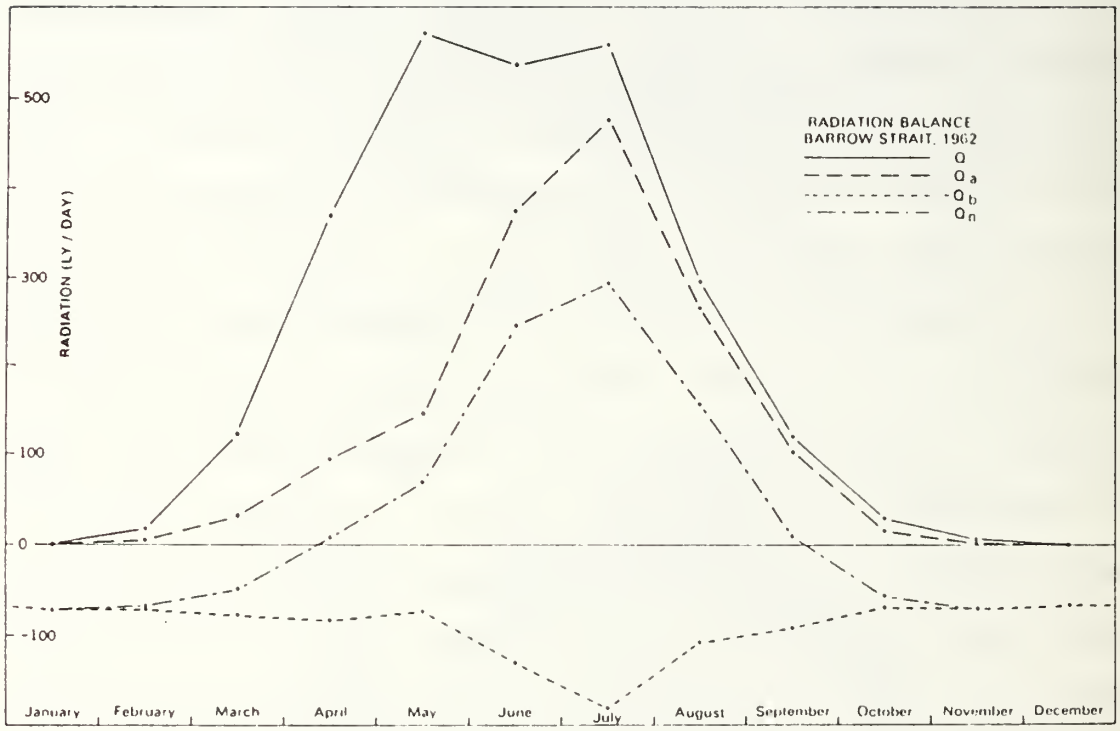

Figure 2.2 The radiation balance showing the short-wave incident radiation, Q, the absorbed short-wave radiation, Q_a, the effective back radiation, Q_b, and the net radiation, Q_n (from Huyer and Barber, 1970).

these regions, but their subsequent influence on other areas is dependent on the upper level steering and the conditions of the surface over which they pass. The cyclones will tend to increase in intensity if they remain over relatively warm open water, which provides heat and moisture. However, they will tend to weaken and occlude if they travel over cold and dry (ice or land) surfaces. These factors imply that considerable variability exists in the dynamic atmospheric forcing between different regions and in different seasons in the Arctic. Climatological averages or even monthly averages of atmospheric forcing will undoubtedly mask some of this variability.

Variations in surface albedo cause the percentage of solar radiation absorbed to differ by as much as 70% between different types of snow, ice and open water. Robinson et al., (1986) have used comprehensive sets of satellite-derived data and ground confirmation data to identify four ice surface albedo classes in the Arctic. Albedos range from 0.80 for a surface with fresh snow covering 95% of the ice to 0.29 for a heavily ponded surface with less that 10% bare snow or ice. Kukla and Robinson (1980) determined that 0.10 was a reasonable albedo for open water in the high latitudes. These differences cause the melting and freezing processes to accelerate rapidly once started. Changes in the ice cover can be very dramatic over short periods of time. The Arctic stratus deck, common to the region in summer, also influences

surface albedo significantly, but this effect is very difficult to quantify. Considerable variability exists in the literature as to the correct albedo to use in large scale modeling. Numerous authors have shown that numerical thermodynamic ice models can be very sensitive to this variable (e.g., Shine and Henderson-Sellers, 1985; Ross and Walsh, 1987; Semtner, 1976a). Inclusion of a realistic albedo representation is therefore difficult but probably important in an accurate numerical sea-ice model.

Open leads probably account for less than 10% of the surface area encompassed by the Arctic ice; however the heat and moisture exchanges which occur above them can be an order of magnitude higher due to the large differences in temperature and radiation characteristics between seawater and the pack ice surface. This results in localized areas of high static instability, cloud formation and large heat and moisture fluxes. Leads are generally too small to resolve using current large-scale numerical ice models; however, they are important enough to require that their effects be parameterized.

The strong temperature inversion common to much of the Arctic is the result of the very cold ice and land surfaces. In winter the inversion layer can deepen to the 850 mb level, becoming most intense under calm, clear anti-cyclonic conditions (Sater et al., 1971). The inversion is a very persistent feature which will quickly reform after periods of

strong winds, cloud cover or storm precipitation as long as surface temperatures remain relatively low. In summer this feature is confined to the polar ice cap as surface temperatures over the ice-free water at more southern latitudes become too high. The inversion acts to insulate or decouple the surface from upper level winds and also tends to put a cap on any moisture which may be absorbed in the boundary layer. The result is relatively calm (average less than 5 m/s) surface wind conditions and a predominance of stratus clouds, especially when the melt season commences. Care must be taken to ensure that surface winds calculated from higher level pressure charts, if used as forcing fields, take this feature into account to ensure realistic wind forcing on the ice.

B. WATER MASSES

The waters of the Arctic Seas are often described on the basis of temperature and salinity. As such, they are comprised of three main water masses: Arctic Surface Water, Intermediate or Atlantic Water, and Deep or Bottom Water (Coachman and Aagaard, 1974). Arctic surface water is generally limited in depth to about 200 m. It has the most variable characteristics and can be modified by the weather, the season, and/or the physical environment. Temperatures in this layer vary from -1°C to over 2°C. The salinity may be uniform to approximately 50 m, below which a sharp halocline

increases the salinity to about 34.5 ppt at the bottom of the layer. The variety of conditions in the surface water is evident in Figure 2.3, where vertical profiles of temperature and salinity from a variety of Arctic basins are plotted. Coachman and Aagaard (1974, p. 9) state that:

> The most important processes conditioning and modifying the surface layer are:
>
> - Addition of mass (fresh water) from the land, primarily from the large Siberian rivers;
> - Addition of fresh water locally through melting of ice;
> - Heat gain through absorption of solar radiation in non-ice-covered areas during summer;
> - Concentration of salt and hence increase of density of surface water, through freezing of ice;
> - Heat loss to the atmosphere through any open water surface, including leads in the central Arctic pack ice; and
> - Inflow and subsequent mixing of Atlantic and Pacific waters.

Processes 1, 2, and 3 normally occur only from June to September and lead to a decrease in water density. These buoyant waters form a surface cap which absorbs radiation and warms. Therefore, in summer, ice free regions tend to have warmer and less saline surface layers. In areas where the ice does not recede, surface temperatures remain near freezing as incoming energy is used to melt the ice, but surface layer salinities are reduced due to ice melting.

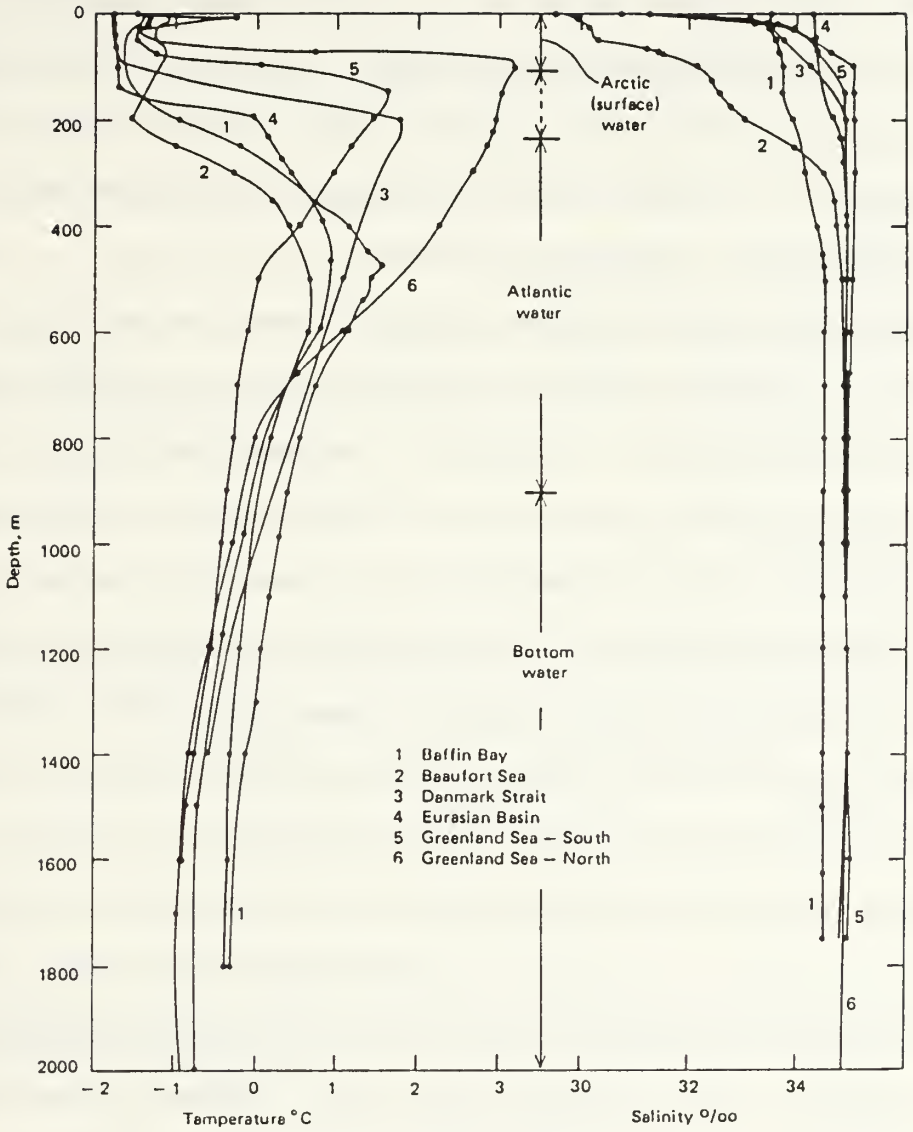

Figure 2.3 Vertical profiles of temperature and salinity for various northern high-latitude basins (from Coachman and Aagaard, 1974).

Processes 4 and 5 have the greatest impact in winter. In some areas, such as the shelf waters, conditions are such that the water becomes dense enough to penetrate into the intermediate Atlantic layer or in extreme cases even form bottom water (Aagaard et al., 1985). However, in general, the strong pycnocline at the base of the surface layer prevents mixing due to surface density changes from penetrating below 200 m (Coachman and Aagaard, 1974).

As a consequence of the halocline-derived mixing barrier, process 6 does not exert a great influence on the surface water variability. However, regions of high surface salinities (33 to 34.5 ppt) are found in the Greenland and Labrador Seas and east Baffin Bay. These high salinities are due to the advection of North Atlantic surface water into the Arctic via warm surface currents from the south. One further consequence of the halocline barrier is that the ice cover is often insulated from the relatively warm Atlantic layer. However, in some locations like the continental slopes, the Atlantic layer is forced to shallower-than-normal depths. Vigorous surface mixing can then break through the halocline and vertical heat fluxes can occur (Coachman and Aagaard, 1974). This results in the ice melting from the bottom or not forming at all, increasing the area of open water.

Many mixing events are small in scale but complicated and intense. In a large scale ice model these effects should be included, but as was the case for leads, they need to be

parameterized in some manner due to the scale limitations of the model.

The second water mass is called the Atlantic layer. This warm and salty (35.0 to 35.1 ppt) water originates as North Atlantic water flowing into the Arctic basin through the Fram Strait and the Barents Sea (Weigel, 1987). It extends from 200 m to 900 m with temperatures above 0°C. A temperature maximum of approximately 0.45°C, observed throughout the central and western Arctic Basin, occurs between 300 m and 500 m depth, dependent on location. The salinity gradually decreases to approximately 34.9 ppt in the Arctic Ocean and Greenland Sea and approximately 34.6 ppt in Baffin Bay. The intermediate layer is a source of heat which can be tapped by vertical circulation. As a result it may play an important role in the net heat balance of the surface mixed layer. The net heat balance in the mixed layer ultimately determines whether or not ice will form. The ocean model used here has been shown to simulate this warm intermediate layer quite well (Semtner, 1984, see Figure 2.4).

The third water mass, the deep and bottom waters, have temperatures below 0°C. The salinity is nearly constant from the bottom of the Atlantic layer to the ocean floor. The intermediate Atlantic water and deep water are advected into and out of the Arctic seas from adjacent areas, principally through Fram Strait in the North Atlantic. Both water masses

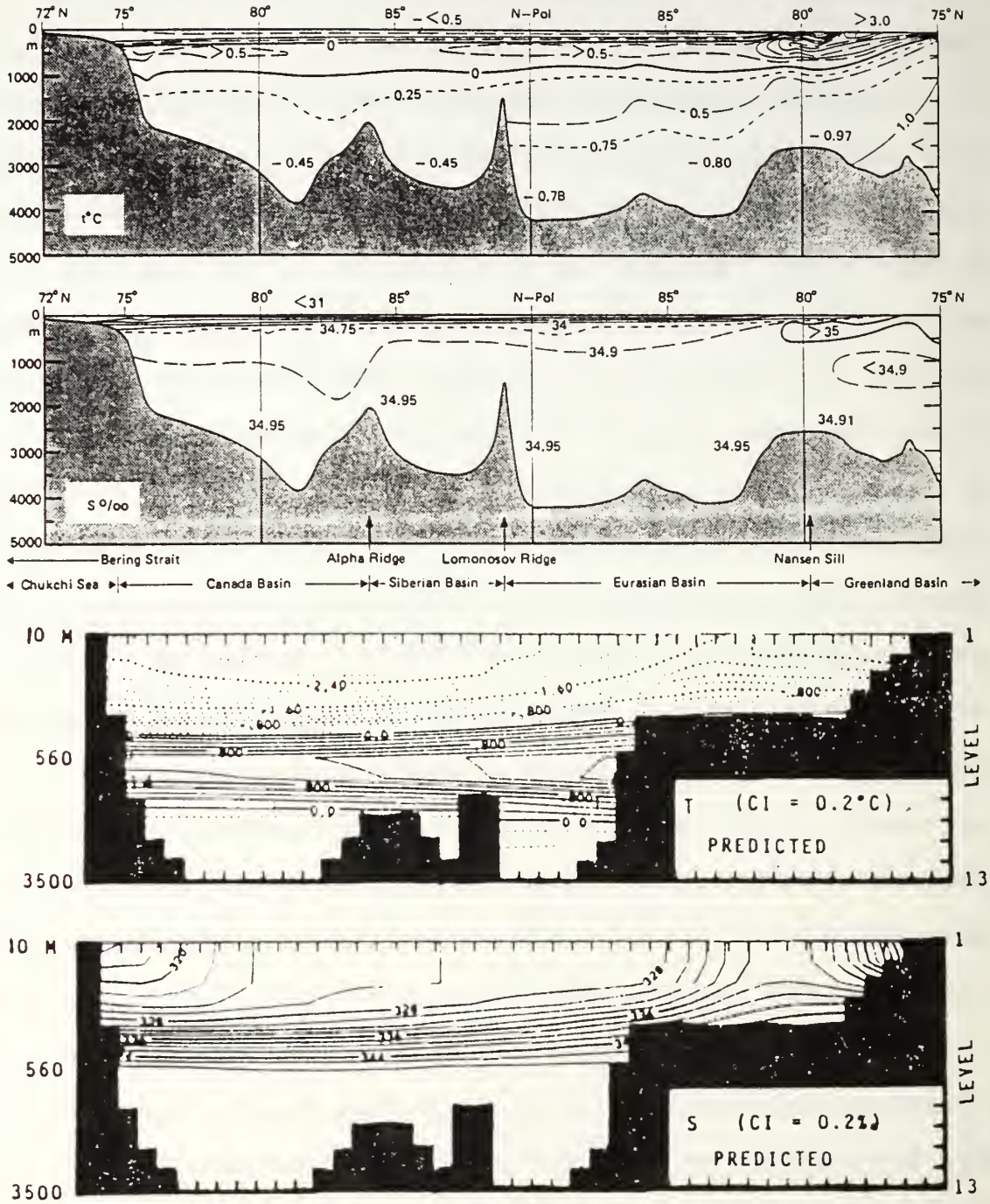

Figure 2.4 Vertical sections of observed temperature and salinity along the prime meridian, from Coachman and Aagaard (1974) (upper panels); and vertical sections of simulated temperature and salinity across the model domain at approximately 20 degrees E (lower panels). The lower panels have a stretched vertical scale. (from Semtner, 1984b)

are nearly isohaline and therefore of nearly uniform potential density.

A temperature difference exists between the deep and bottom waters of the Canadian and Eurasian Basins. The deep Canadian Basin averages approximately -0.45°C while the Eurasian basin temperature is approximately -0.79°C (Aagaard et al., 1985). The deep and bottom waters of the two basins are kept separated by the Lomonosov Ridge which acts as a sill between them.

Observations of the vertical structure at various stations have been taken over long time periods and in many different locations. A remarkable similarity in the profiles has led to the conclusion that the Arctic basins are in a long-term dynamic steady-state condition (Coachman and Barnes, 1961). It was further noted that observed distributions of Arctic water properties are a result of continuing processes within the basins. Therefore, surface water temperature-salinity (T-S) profiles reflect the local modifying processes, while T-S profiles for depths below 200 m reflect the common origin of the water.

The net heat balance ultimately determines how much ice is produced or melted. The heat flux provided by the ocean is an important parameter in determining the net heat balance at each grid point as noted in Chapter I. The ocean component of a linked ice-ocean model should therefore have sufficient resolution to reasonably define the boundaries of the various

water masses in three dimensions. It must also be able to simulate the water motion which advects oceanic heat to the ice and convects the cold saline water to the bottom.

C. CURRENTS

The surface circulation of the Arctic Basin has been derived from satellite observations, the trajectory of ice islands, buoys and floe stations, and the analysis of ship's tracks. The circulation of the Arctic waters is due both to water density differences and wind forcing. Large anomalies in the flow (compared to the long-term mean currents) are often observed; however, the long-term mean surface currents have been reasonably well documented in the northern Atlantic and Arctic Seas (Krauss, 1986). Figure 2.5 covers the area of interest in this study and indicates the major ocean currents. Recent moored current measurements have allowed a reassessment of the boundary and interior circulation in the Arctic Basin (Aagaard, 1988). Aagaard emphasizes the important role of mesoscale eddies in the Canadian Basin and proposes a separate cyclonic flow for the Eurasian Basin. This newest assessment is very similar to the simulated Atlantic layer circulation in Semtner (1987) and is a significant change from the previous basin-wide cyclonic circulation proposed by Coachman and Aagaard (1974). Figure 2.6 shows this comparison.

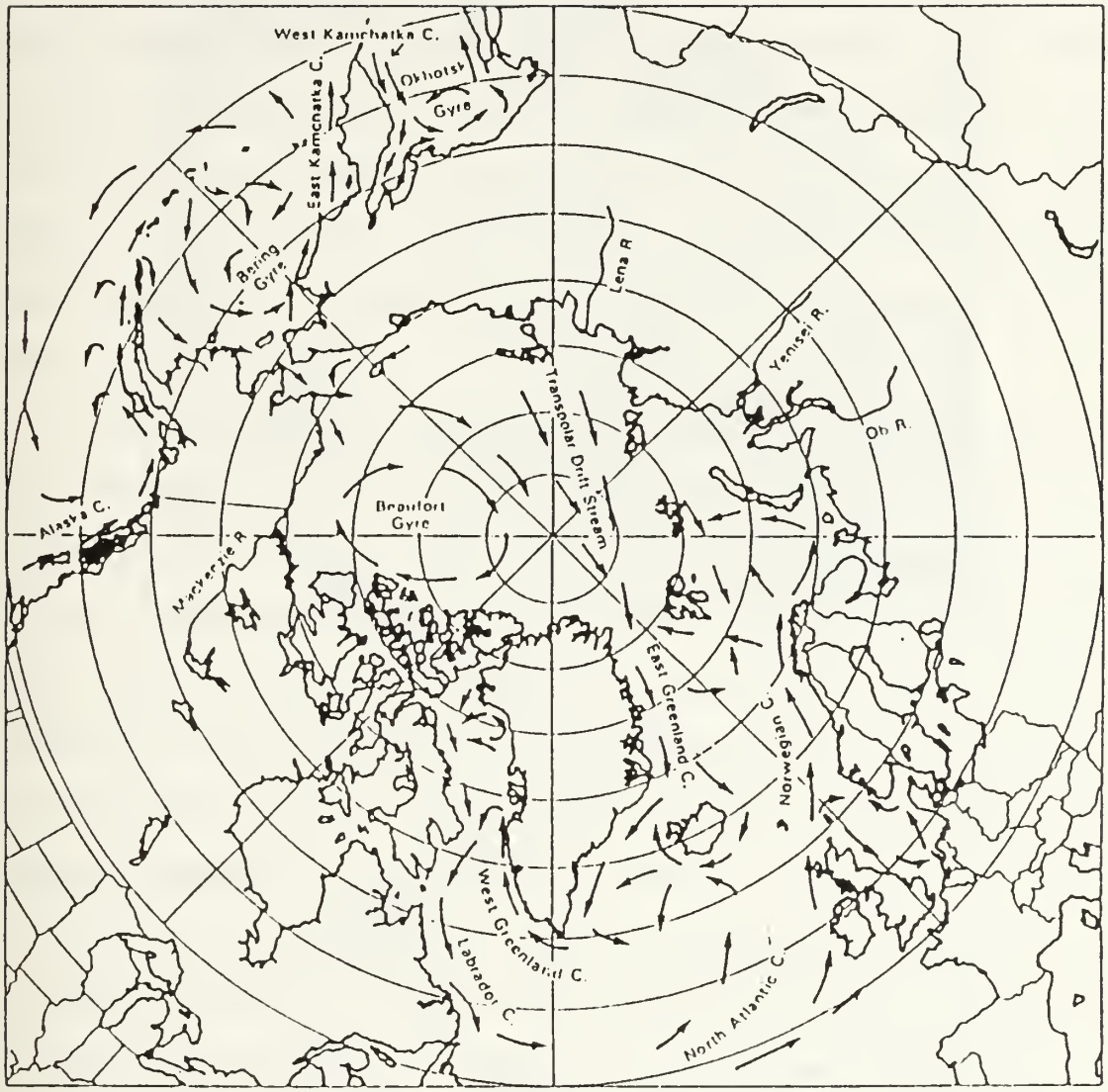

Figure 2.5 Schematic of the large-scale horizontal circulation patterns in the surface waters of the Arctic region (from Parkinson et al., 1987).

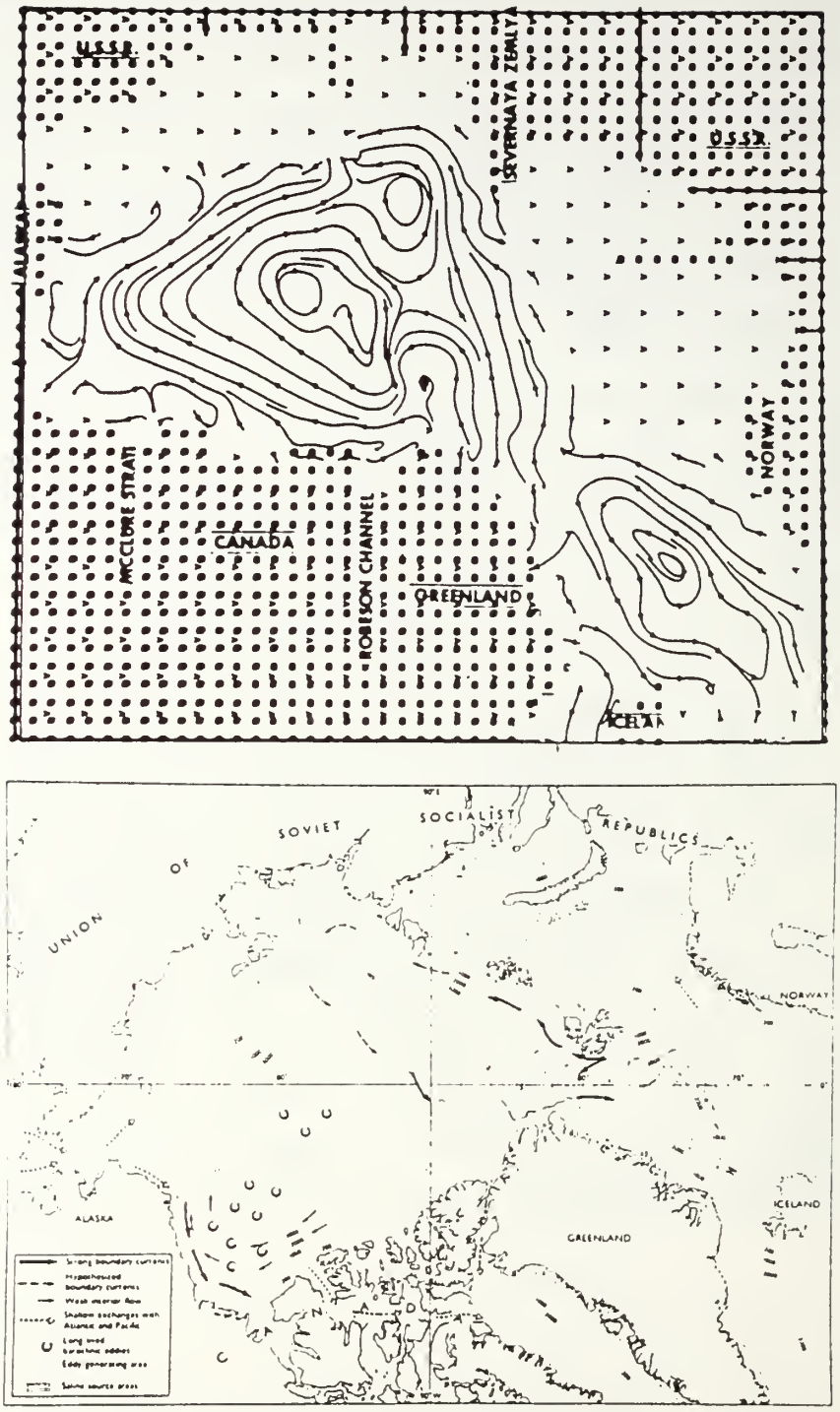

Figure 2.6 Comparison of the simulated circulation in the Atlantic layer (565 m) (upper diagram)(from Semtner, 1987) with the reassessed subsurface circulation presented by Aagaard (lower diagram) (from Aagaard, 1988).

The Arctic Ocean contains two main surface flow patterns. In the Canadian Basin, the Beaufort Sea gyre rotates clockwise. It is driven primarily by the mean wind. Across the Lomonosov Ridge, the Transpolar Drift Stream (TPD) flows directly across the Eurasian Basin, from the Laptev Shelf to the Fram Strait where it exits as the East Greenland Current (EGC). Several small, weak gyres split off the Transpolar Drift Stream as it passes close to the various islands off the coast of the USSR.

Circulation and ice movement patterns in the peripheral Atlantic seas of the Arctic Ocean are dominated by two major currents systems, one warm, the other cold (Krauss, 1986). The cold currents support ice growth and enhance the spatial extent of sea ice, while the warm currents advect heat and melt the ice or preclude its formation. The southerly extent of the ice edge between regions of dissimilar temperatures can vary as much as 30 degrees of latitude.

Sea ice off the east coast of Greenland is found to originate primarily in the Arctic basin and as a result can be quite thick. The EGC continually carries a wide belt of Arctic pack ice southward through Fram Strait. As the ice season develops, the ice edge extends further south down the east Greenland coast. In extreme years the ice edge will extend as far south as Kap Farvel or as far north as 70 degrees N (Sater et al., 1971).

Strong contrasts in ice coverage are also observed within the Baffin Bay-Davis Strait region. The warm West Greenland Current (WGC) follows the bathymetric contours of the southern and western Greenland continental shelf, keeping the southwest coast of Greenland ice free during most winters. However, the cold Labrador Current contributes to the large concentrations of ice found along Canada's east coast, well south of Baffin Island. This current also carries the majority of icebergs southward through the Grand Banks fishing zones, the Hibernia oil fields and into the North Atlantic sea lanes (CIA, 1978).

A reasonably accurate representation of the ocean currents is obviously important if sea ice is to be accurately simulated. The currents provide a direct influence through dynamic forcing as well as a thermodynamic influence via heat advection.

D. ICE

Sea ice is a feature which contributes to the uniqueness of the oceanography in the Arctic region. Coachman and Aagaard (1974) state:

> The general oceanographic consequences of a perennial or seasonal ice cover are:
>
> - The water temperature of the near-surface layer in the presence of ice is always maintained close to the freezing point for its salinity by the change of phase process.
>
> - Salt is excluded from the ice to a varying extent, but the water under the ice is always enriched in salt by any ice growth. The dependence of water density on temperature and salinity is such that close to the freezing point, density is almost solely a function

of salinity. Therefore, ice formation can increase the density locally and some vertical convection may result.

- In the transfer of momentum from the atmosphere to the ocean, the wind must act on the sea through the intermediary of the ice.

The Arctic Ocean ice pack is confined by a nearly continuous boundary of land. The associated constraint on equatorward transport is a major reason why Arctic ice survives longer and develops into more complex forms than ice found in southern polar regions. An annual net heat loss and stratification of the underlying water also contribute to the longevity of Arctic ice.

Ice formation in open water starts in autumn. As days grow shorter and nights longer, the amount of solar insolation decreases. Since long-wave radiation from the Arctic remains approximately constant during the year, the energy budget changes from a net gain in summer through equilibrium to a net loss in the fall (Figure 2.2). The relatively warm mixed ocean surface layer of summer is cooled until it reaches its freezing point and ice crystal formation commences. Ice initially forms around the boundaries of the polar ice pack and over the shallow protected waters of high-latitude coastlines. The ice-covered areas continue to expand until they merge, forming an ice-locked Arctic Ocean from October to June. The ice cover starts from a summer minimum of approximately 5.2×10^6 km^2 then more than doubles in areal

extent to a maximum of 11.7 x 10^6 km^2 by the end of the ice season (CIA, 1978, p. 12).

The ice cover grows continuously until spring. Once the days start to lengthen, the amount of solar radiation increases until the surface energy budget is again positive. As noted earlier, snow cover will reflect approximately 80 percent of the sun's incident radiation, which slows the initial heating stages. However, once the air temperature reaches the snow's melting point, the albedo rapidly drops to 50 percent and lower. This results in a period of rapid snow melt. Continued heating initiates melting of the underlying ice, causing cracks and flaws to develop. The surface melt water drains through the cracks, further eroding them until the ice breaks up into floes. Eventually, the ocean surface layer heats up, the floes gradually dissolve, and the cycle is complete (Langleben, 1972).

Extremes of ice cover in summer and winter for the period 1953-1977 were shown in Figure 2.1. Obviously, the sea ice cover experiences a large degree of variability both seasonally and interannually. Ice cover is something of a misnomer as the sea surface is rarely covered by an unbroken expanse of ice. Even in the very thick ice regions of the winter polar pack, infrared measurements indicate that up to ten percent of the area of the Arctic ocean consists of open water or thin ice from recently refrozen leads (Sater et al., 1971, p. 41).

Multi-year ice (ice which has survived a summer's melting) comprises the majority of the polar pack, which averages 3 m in depth (Bourke and Garret, 1987). First-year ice rarely grows to a thickness greater than 2 m. However, the depth of the ice in any location is largely dependent on the external forces of wind and currents. These cause the ice to converge and diverge. When a region of ice converges, it buckles, folds, and overlaps, forming a rugged terrain and areas of considerably thick ice. For example, the Beaufort Gyre's anticyclonic flow causes ice to converge along the north coast of Ellesmere Island and Greenland. The number of ridges in this region is well above the average for the Arctic pack (Weeks et al., 1971). The mean ice thickness here is of the order of 6 m to 8 m (Bourke and Garrett, 1987). In contrast, the ice pack east of Spitsbergen (Svalbard) is not confined by land and is free to diverge. Here, the average ice thickness is significantly less, averaging approximately 2 m.

The thickness, distribution and concentration of sea-ice are influenced by both dynamic and thermodynamic factors. The ice portion of an accurate ice-ocean linked model needs to include as much of the physics of these mechanisms as possible.

III. COUPLED NUMERICAL MODEL

The coupled model used in this study contains an ice model with both dynamic and thermodynamic forcing linked to a fully prognostic primitive equation ocean model. The grid domain includes the Norwegian and Greenland Seas, and the entire Arctic basin. The geography is smoothed due to the limitations of the resolution leaving only Spitsbergen and Iceland as true islands. Bottom topography is included. The model is forced by wind stress and energy balances at the sea surface and water mass balance at open boundaries. The ocean model is coupled with the ice model by momentum, heat, and salt exchanges through a common ocean mixed layer. Much of this chapter follows the very clear descriptions of Van Ypersele (1986) who applied a similar model to the Antarctic.

A. OCEAN MODEL

The physical state of the ocean is characterized by seven quantities: pressure, potential temperature, salinity, density, and the three components of velocity. A three-dimensional ocean model must be able to predict the evolution of those seven quantities from an initial state when adequate boundary conditions are specified.

Seven equations are required to relate the seven variables and close the system. These equations are derived from basic

principles including the conservation of momentum, energy and mass as well as Newton's law of gravitation. An equation of state is used to calculate density from temperature, salinity, and depth. The equations must be simplified yet still retain the most important terms in order to solve them numerically and produce reasonable results. Following Semtner (1974, 1986b) the necessary simplification was provided by making the following approximations and assumptions about the system of equations:

- The ocean is incompressible. This eliminates acoustic waves from the possible solutions and leads to a simpler continuity equation without density terms. It is a reasonable assumption because the volume changes due to pressure are small. For example, the change of pressure corresponding to a change of depth of 1000 m would alter the volume of a typical sample of seawater by less than 0.5%. (Pond and Pickard, 1983).

- The ocean behaves as a horizontally isotropic fluid with constant kinematic eddy-viscosity coefficients in the vertical and horizontal directions. This means that an error is introduced in the mixing of momentum if the isopycnals are not horizontal.

- Exchanges of heat and salt which occur at sub-grid scale can be represented by similar eddy-diffusivity coefficients in the vertical and horizontal directions. On the molecular scale, salt diffusion in water is on the order of 100 times slower than heat diffusion. However, turbulent processes tend to dominate which permits use of the same eddy-diffusivity coefficients for both salt and heat.

- The thin-shell approximation is made. This allows certain terms in the horizontal momentum equations to be neglected because the depth of the ocean is negligible compared to the radius of the earth.

- The hydrostatic assumption is made. The differential of pressure with respect to depth is considered only a function of the product of density and the acceleration of gravity. This approximation is a result of scale

analysis of the vertical momentum equation which reduces to the form:

$$\frac{\partial p}{\partial z} = -\rho g \tag{3.1}$$

- The Boussinesq approximation is made. This is basically the neglect of small density variation effects on the fluid momentum and therefore on the acceleration for a given force, while maintaining these same effects on weight in the earth's gravity field (buoyancy). Consequently, average density over the domain can be used in the horizontal momentum equations. However, the actual density values are required to derive pressure from Equation 3.1.

- The Coriolis terms and the viscous terms involving the vertical speed, w, in the horizontal momentum equations are neglected on the basis of scale analysis.

- The rigid lid approximation is made. This is achieved by specifying that the vertical velocity, w, be zero at the upper surface. This process filters out high-speed surface gravity waves in order to permit use of a longer timestep.

The three momentum equations are derived from Newton's second law of motion. The resultant equations in vector form are often called the Navier-Stokes equations. They provide a relation between the velocity, the pressure gradient force, the viscous stresses, and the body forces such as gravity and Coriolis (e.g., Tritton, 1977).

After the simplifications are made, as allowed by the assumptions and approximations described above, the momentum equations in spherical coordinates become:

$$\frac{\partial u}{\partial t} + L(u) - \frac{uv\tan\phi}{r_e} - fv = -\frac{1}{\rho_0 r_e \cos\phi}\frac{\partial p}{\partial \lambda} + A_z\frac{\partial^2 u}{\partial z^2}$$

$$+ A_h\left\{\nabla^2 u + \frac{(1-\tan^2\phi)u}{r_e^2} - \frac{2\sin\phi}{r_e^2\cos^2\phi}\frac{\partial v}{\partial \lambda}\right\} \tag{3.2}$$

$$\frac{\partial v}{\partial t} + L(v) + \frac{u^2 \tan\phi}{r_e} + fu = -\frac{1}{\rho_0 r_e}\frac{\partial p}{\partial \phi} + A_z\frac{\partial^2 v}{\partial z^2}$$

$$+ A_h\left\{\nabla^2 v + \frac{(1-\tan^2\phi)v}{r_e^2} - \frac{2\sin\phi}{r_e^2\cos^2\phi}\frac{\partial u}{\partial \lambda}\right\} \qquad (3.3)$$

$$\frac{\partial p}{\partial z} = -\rho g \qquad (3.4)$$

where f is the Coriolis parameter ($f = 2\Omega\sin\phi[s^{-1}]$), Ω is the angular speed of rotation of the earth, ($\Omega = 7.272 \times 10^{-5}$ rad/s). A_z and A_h are the vertical and horizontal eddy viscosity coefficients, respectively (0.3×10^{-4} m^2/s and 12×10^4 m^2/s). r_e is the earth's radius (6.37×10^8 m). $L(\alpha)$ is the advection operator which in spherical coordinates becomes:

$$L(\alpha) = \frac{1}{r_e\cos\phi}\frac{\partial}{\partial\lambda}(u\alpha) + \frac{1}{r_e\cos\phi}\frac{\partial}{\partial\phi}(v\alpha\cos\phi) + \frac{\partial}{\partial z}(w\alpha) \qquad (3.5)$$

The horizontal Laplacian operator becomes:

$$\nabla^2(\alpha) = \frac{1}{r_e^2\cos^2\phi}\frac{\partial^2\alpha}{\partial\lambda^2} + \frac{1}{r_e^2\cos\phi}\frac{\partial}{\partial\phi}\left[\cos\phi\frac{\partial\alpha}{\partial\phi}\right] \qquad (3.6)$$

where α is an arbitrary quantity.

Equation 3.4 is the hydrostatic equation governing the depth related variation of pressure in the ocean. It assumes that a perfect balance of forces exists in the vertical (i.e.,

vertical accelerations are negligible). This is valid for large scale motions, but it is not adequate to describe small-scale convection, where horizontal and vertical scales of motion tend to be similar. Therefore, the model must be supplemented by an implicit treatment of convection, which will prevent the unrealistic condition of unstable stratification. The convective adjustment scheme adopted here is such that if the condition

$$\rho(\theta,S,p)_k > \rho(\theta,S,p)_{k+1} \tag{3.7}$$

is verified, then the new values of temperature and salinity are recomputed from

$$\theta_k = \theta_{k+1} = \overline{\theta} \qquad \text{and} \qquad S_k = S_{k+1} = \overline{S} \tag{3.8}$$

Level k + 1 is taken to be the common reference level, and ($\bar{}$) indicates a weighted average over layers k and k + 1.

The conservation of mass, together with the assumption of incompressibility, gives the continuity equation:

$$\nabla \cdot V = 0 \tag{3.9}$$

In spherical coordinates this becomes:

$$\frac{1}{r_e \cos\phi}\frac{\partial u}{\partial \lambda} + \frac{1}{r_e \cos\phi}\frac{\partial}{\partial \phi}(v\cos\phi) + \frac{\partial w}{\partial z} = 0 \tag{3.10}$$

The theory of thermal transfer in a fluid of constant heat capacity, together with an eddy-diffusivity closure hypothesis, gives a conservation equation relating the evolution of temperature to the motion field and the first and second spatial derivatives of the potential temperature:

$$\frac{\partial \Theta}{\partial t} + L(\theta) = K_z \frac{\partial^2 \theta}{\partial z^2} + K_h \nabla_h^2 \theta \qquad (3.11)$$

K_z and K_h are the vertical and horizontal eddy diffusivity coefficients, respectively (0.3×10^{-4} m^2/s and 2×10^3 m^2/s). A similar equation is derived for salinity:

$$\frac{\partial S}{\partial t} + L(S) = K_z \frac{\partial^2 S}{\partial z^2} + K_h \nabla_h^2 S \qquad (3.12)$$

An equation of state is used to express the density as a function of potential temperature, salinity, and pressure:

$$\rho = \rho(\theta, S, p) \qquad (3.13)$$

For the purposes of numerical modelling, the equation of state is expressed as a polynomial approximation to the results of laboratory experiments. The approximation of Eckart (1958), utilized by Semtner (1974) will also be used for this study.

B. ICE MODEL

The sea-ice portion of the coupled model contains both thermodynamics and dynamics. The thermodynamic portion is based on the three-layer thermodynamic ice model proposed in Semtner (1976a), which is a simplification of the comprehensive ice model of Maykut and Untersteiner (1971). It is forced from above by the atmospheric fluxes computed from atmospheric data, and from below by oceanic heat fluxes prescribed by the ocean model. The dynamic portion is a simplification of the "viscous-plastic" rheology approach used by Hibler (1979). The simplification reduces the computational load significantly and permits use of the same monthly averaged atmospheric data for forcing as used by the ocean model.

For the three-layer thermodynamic model, sea-ice is assumed to be a horizontally uniform slab of ice, represented by two layers of equal thickness. A covering layer of snow is possible. When ice is present, the temperature in the oceanic mixed layer below the ice cover is assumed to be at the freezing point of seawater (-1.9°C). The temperature profile through the ice and snow is governed by the one-dimensional heat equation:

$$\rho C \frac{\partial T}{\partial t} = k \frac{\partial^2 T}{\partial z^2} \qquad (3.14)$$

where ρ is the density [900 and 330 kg m^{-3} for ice and snow, respectively], C is the specific heat capacity [2.09 kJ kg^{-1} K^{-1} for both ice and snow], T is the temperature [K], and k is the thermal conductivity [4.068 and 0.31 W $m^{-1}K^{-1}$ for ice and snow, respectively].

At the top and bottom surfaces of the cover (ice or snow as applicable), a balance of fluxes is forced to exist such that any heat excess or deficit that occurs at either boundary is used to melt or freeze, respectively. Melting can occur at either surface; however freezing can only occur at the ice bottom. Therefore when a negative flux imbalance occurs at the surface, the heat equation is applied to the ice to ascertain the effect at the ice bottom before the amount of freezing is determined. The melting point for snow is set at 0°C and for ice -0.1°C. The heat of fusion for snow is set at 110 MJ/m^3 and for ice at 301 MJ/m^3. Diffusive fluxes must be equal at the internal snow-ice interface.

By late summer, the ice will have completely melted in certain regions. A heat budget equation is then applied to the vertically isothermal surface mixed layer and its temperature is allowed to increase. Horizontal mixing and advection of the warmed oceanic surface layer can then spread the heat under adjacent ice covered areas to speed the melting process there. Once the freezing season commences, the heat budget cools the mixed layer to its freezing point, ice starts

to form and the heat equation for ice/snow must again be applied.

In order to determine the final temperature of the upper surface when ice is present, several conditions are imposed to control the way the various fluxes are applied. If the initial temperature at the upper surface, $T_{surf} < T_{melt}$, the upper surface flux balance equation is given by:

$$Q_{SW}(1-I_0)\,(1-a_{surf}) + Q_{LW}^{\downarrow} - Q_{LW}^{\uparrow} + Q_H + Q_{LE} + Q_{cond} = 0 \qquad (3.15a)$$

where a_{surf} is the surface albedo and I_0 is the fraction of solar radiation absorbed in the ice cover. I_0 is set equal to 0 for snow and to 0.17 for bare ice. The remainder of the terms are:

- Q_{LW} longwave heat flux, the arrow indicates downward (+ve) or upward (-ve).
- Q_H sensible heat flux (+ve downward).
- Q_{LE} latent heat flux.
- Q_{SW} short wave solar flux.
- Q_{cond} flux conducted downward from the surface to the bottom of the ice.

These are described in more detail in section E (Forcing Fields).

If $T_{surf} = T_{melt}$, the upper surface flux balance equation is given by:

$$Q_{SW}(1-I_0)\,(1-a_{surf}) + Q^{\downarrow}_{LW} - Q^{\uparrow}_{LW} + Q_H + Q_{LE} + Q_{cond} =$$

$$-L_M\left[\rho_i\frac{\partial h_i}{\partial t} + \rho_s\frac{\partial h_s}{\partial t}\right]_{z=0} \qquad (3.15b)$$

where h_i and h_s are the thicknesses of the ice and snow, respectively, and L_M is the latent heat of fusion.

At the bottom of the ice, the flux balance equation is:

$$Q_{cond} - Q_{ocean} = L_M\rho_i\frac{\partial h_i}{\partial t}\bigg|_{z=h_i} \qquad (3.16)$$

where Q_{ocean} is the oceanic heat flux [W m^{-2}].

The outgoing longwave radiation Q_{LW} follows the Stefan-Boltzmann law:

$$Q^{\uparrow}_{LW} = \epsilon\sigma T^4_{surf} \qquad (3.17)$$

where ϵ is the surface emissivity (non-dimensional, and assumed equal to 1), and σ is the Stefan-Boltzmann constant [= 5.67 x 10^{-8} W m^{-2} K^{-4}].

The final temperature at the upper surface, T_{surf}, is obtained by linearizing the blackbody emission term 3.17.

The conductive flux Q_{cond} inside the snow and ice is computed by assuming a linear vertical temperature profile between grid points, so that at the bottom of the ice:

$$Q_{cond} = k_i \frac{(T_{wfreez} - T_2)}{(h_i/4)} \qquad (3.18)$$

where k_i is the ice thermal conductivity, T_{wfreez} is the freezing point of seawater [=271.3 K], T_2 is the temperature of the second layer of ice, and h_i is the ice thickness.

The storage of latent heat in brine pockets is modeled by an internal heat reservoir as in Semtner (1976a). The reservoir accumulates a fraction of the solar radiation that penetrates the snow-free ice $[Q(1-I_0)(1-a_{ice})]$. Total heat in the reservoir is limited to 50% of the heat needed to melt all the ice at that position. This stored heat adds inertia to the simulated melting process. The effects of rapid changes in thermodynamic forcing are smoothed and the onset of the melting season is delayed. A schematic of the fluxes and processes incorporated in the thermodynamic portion of the ice model is shown in Figure 3.1. The numerical scheme used to compute the ice and snow thickness and the temperature at the different levels is contained in Semtner (1976a) and will not be repeated here.

The ice dynamics portion of the model uses a simplified Hibler (1979) rheology called "bulk viscous" (Washington and Parkinson, 1986; Hibler, 1988). This approach was developed for use on seasonal time scale ice models with slowly varying forcing. Semtner (1987) used this rheology and was able to produce annual ice cycles very similar to the Hibler and Bryan

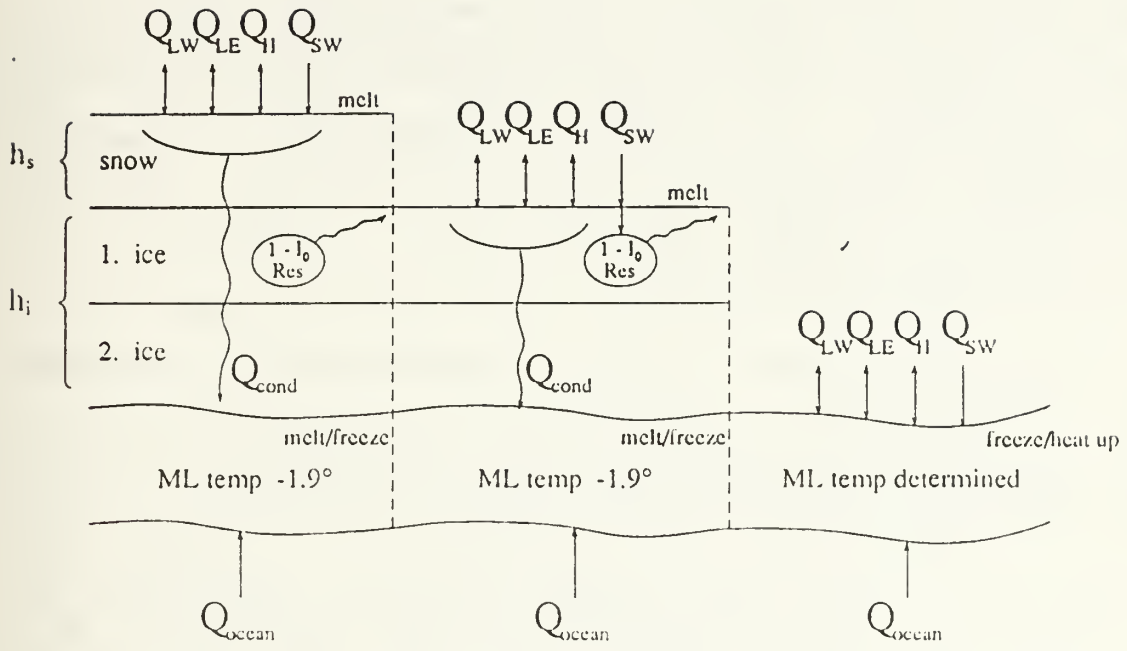

Figure 3.1 Schematic of fluxes and ice processes incorporated in the thermodynamic portion of the ice model. The total heat flux provided by the ocean circulation below the mixed layer is shown as Q_{ocean} and Q_{cond} is the amount of heat conducted through the ice from the surface. The heat reservoir can only receive heat when the ice is snow free; however, it can provide heat whenever the net heat balance at the surface becomes negative.

(1986) model which, as noted earlier, used the complete daily variable forcing dynamic approach of Hibler (1979). The smoothed forcing permits an explicit timestepping technique to be used vice an iterative approach and the stress tensor formulation is much simpler. These two factors reduce the computational requirements by approximately 66%. The dynamics portion of the ice model predicts changes to the ice thickness and concentration from advection, diffusion (a numerical requirement) and compression effects. The sea-ice velocity, V_i, is predicted as follows:

$$DV_i/Dt = 1/m(-mfV_i + \tau_a + \tau_w - mg\ \nabla h + F) \qquad (3.18a)$$

where D/Dt is the substantial time derivative, f is the Coriolis parameter and F is the internal ice stress. τ_a and τ_w are the wind and ocean current stresses, respectively and ∇h is the sea surface slope. m is the mass and g is the acceleration of gravity.

The bulk viscous rheology causes the ice to resist compression in a plastic fashion but allows unimpeded divergence. In the Hibler (1979) notation the stress tensor is reduced to:

$$\sigma_{ij} = \zeta\ \epsilon_{ij}\ \delta_{ij} \qquad (3.18b)$$

where the strain rate tensor ϵ_{ij} is:

$$\epsilon_{ij} = \frac{1}{2}\left[\frac{\partial u_j}{\partial x_j} + \frac{\partial u_j}{\partial x_i}\right] \qquad (3.18c)$$

The bulk viscosity ζ is set to zero for divergence ($\epsilon_{ij} \geq 0$). For convergence, $\zeta = P^*/2\epsilon_{ij}$, where $P^* = h_i \times 10^4$ [N/m^2]. The bulk viscosity is not allowed to exceed $2.5 \times 10^8 \times P^*$ [sec].

C. GRID

The ocean model uses a spherical coordinate system with the equator of the system passing through the geographic North Pole and the prime meridian situated at 40 degrees East longitude. Shifting the poles of the spherical coordinate system 90 degrees to the geographic equator, removes the singularities of the system and provides more uniform horizontal resolution within the Arctic region. The resulting horizontal grid interval is approximately 110 kilometers. The position of a grid point is defined by latitude, longitude and ocean depth.

The ice portion of the linked model is run on a cartesian grid with 110 km spacing. The two grids coincide exactly at the pole but are slightly offset at the southern boundaries. This introduces a small error in the ice mass balance and salt fluxes into the ocean in these areas. Hibler and Bryan (1987) determined that the maximum errors introduced into their model using a similar scheme were only 10%. A 10% error at the southern fringes of the grid was not considered critical to the results of this work.

The gridded domain used in this study was shown in Figure 1.1. The grid points are staggered on a lattice of type B

(Mesinger and Arakawa, 1976), where the temperature, salinity, and stream function points are located at the center of a grid box. The horizontal components u and v of the velocity are at the middle of the vertical edges. The vertical component w is computed at the center of the horizontal faces for the determination of heat and salt vertical advection, and at the box corners for the calculation of u and v (Figure 3.2).

A total of 13 levels are used in the vertical in order to resolve the bathymetric variations shown in Figure 3.3. The uppermost level is treated as an isentropic mixed layer of 30 m. The levels are thinnest near the surface to allow five of these levels above the continental shelf, which is at approximately 250 m depth. Three more levels are defined down to approximately 1100 m depth for representation of the Atlantic layer. Table 1 lists the 13 layer thicknesses and the depth at the bottom of each layer.

D. BOUNDARY AND INITIAL CONDITIONS

The rigid lid approximation requires that w=0 at the upper boundary (z=0). The wind stress τ[Pa] is specified at the surface by

$$\tau(\lambda,\phi) = \rho_0 A_z \frac{\partial}{\partial z}(u,v) \quad \text{at } z = 0 \tag{3.19}$$

The small amount of water mass which is transferred at the ocean surface is neglected. This includes precipitation minus evaporation, ice melt and minor river runoff. However,

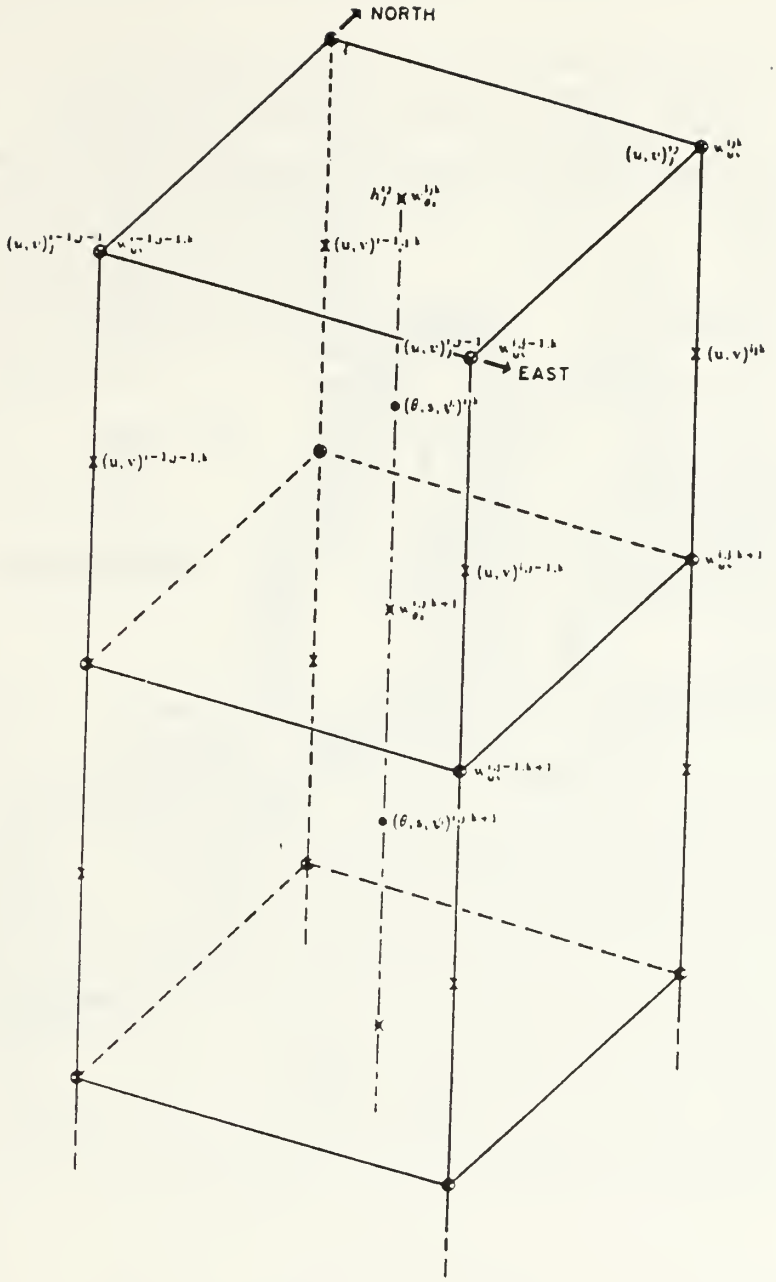

Figure 3.2 The distribution of levels and grid points. Labels to the right and left of the grid points refer to ocean and sea-ice variables, respectively.

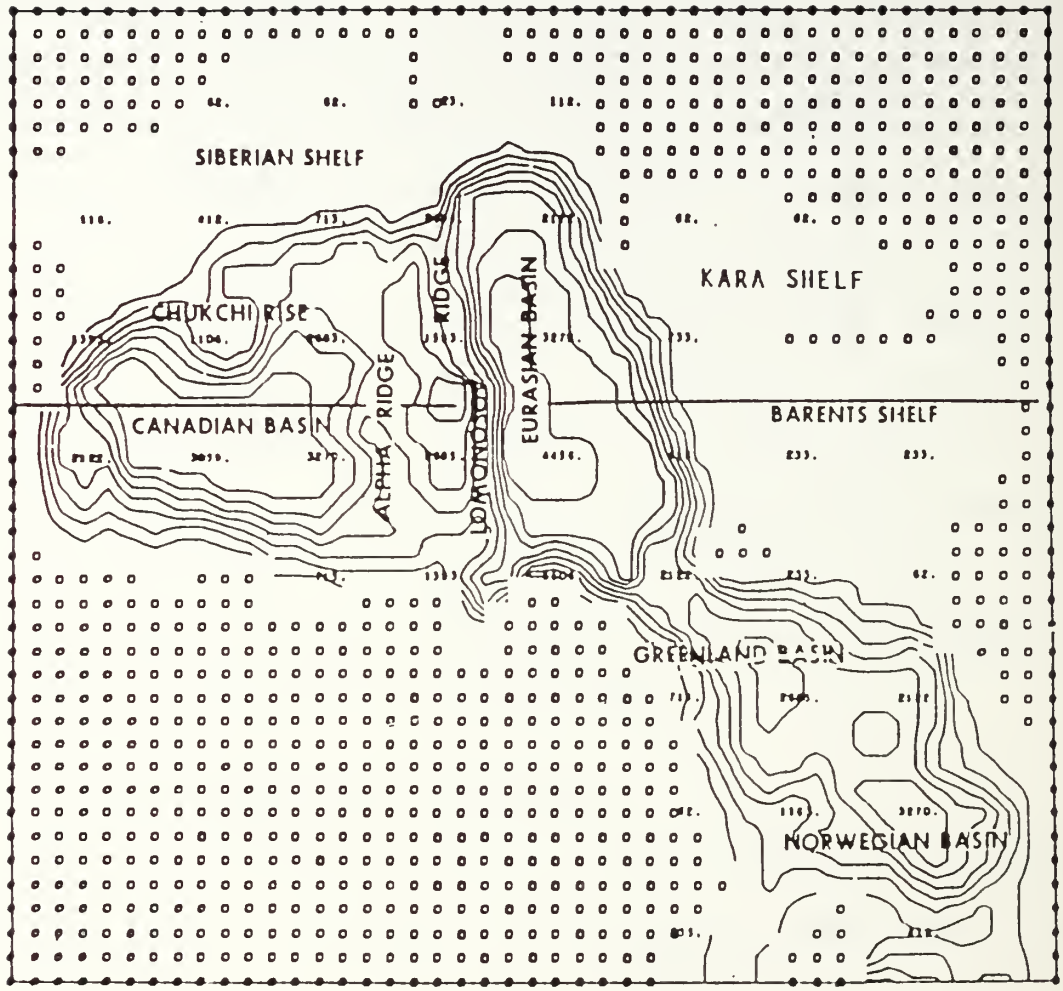

Figure 3.3 Arctic bathymetry plotted with a 500 m contour interval. (from Semtner, 1987).

TABLE 1

VERTICAL LAYER THICKNESSES AND CORRESPONDING DEPTHS

LAYER	THICKNESS (M)	DEPTH (M)
1	30	30
2	20	50
3	40	90
4	60	150
5	100	250
6	183	433
7	299	732
8	391	1123
9	487	1610
10	529	2139
11	563	2702
12	585	3287
13	589	3876

the resultant changes in salinity from these processes are accounted for by applying prescribed negative salt fluxes at the surface. The prescribed salt fluxes, as well as the salt flux introduced during simulated freezing, are accounted for by the salt flux density $Q_s[K_g\ m^{-2}\ s^{-1}]$:

$$Q_S = \rho_w K_z \frac{\partial S}{\partial z} = -\rho_w SSW \tag{3.20}$$

where SSW [m/s] is the sum of all fluxes of fresh water at the surface.

A heat flux density $Q_T[Wm^{-2}]$ specified at the surface (z=0) affects the temperature field in the same way:

$$Q_T = K_z \frac{\partial T}{\partial z} = SSH \tag{3.21}$$

where SSH [W/m^2] is the net energy flux density at the surface.

Vertical motion is forced at the ocean bottom as the currents respond to the vertical contours of the bottom slope. Bottom friction is determined using a quadratic drag law in the same manner as Weatherly (1972). Vertical advective fluxes of heat, salt and momentum at the bottom are taken to be zero. The vertical diffusive fluxes of heat and salt at the bottom are also zero.

$$\rho_0 K_z \frac{\partial}{\partial z}(T,S) = 0 \qquad \text{at } z = -H(\lambda,\phi) \tag{3.22}$$

The horizontal boundaries coincide (to the limits of the resolution) with the geographic coastlines and islands of the Arctic Ocean and adjacent seas. A no-slip condition, i.e., (u,v)=0, is imposed at lateral walls, with no heat or salt fluxes across them.

Each model run simulates the ocean and ice cover for one year, producing output fields for the end of each month. The decade from 1971-1980 was simulated by conducting ten successive runs using the final (end December) ocean and ice condition from the previous year's simulation, as the start condition for the current simulation. Since the analysis begins with 1971, December 1970 would be used as the very first start condition. However, because the model requires some time to achieve a steady state after each modification, a three year run-up was used. That is, the runs were started

at 1968, giving the model a chance to stabilize before the data from 1971-1980 were produced and subsequently extracted for analysis.

E. FORCING FIELDS

This section describes the various forcing fields and data used to drive the coupled model. Several formulas are presented which contain empirical constants. While the values used for these constants represent current estimates, their true values remain uncertain.

Monthly averages of observed atmospheric surface pressure, specific humidity, long and short wave radiation and air temperature were provided by Dr. J. Walsh. The pressure fields were obtained from the NCAR daily analysis of surface pressure. This analysis is based on daily reports from stations on the periphery of the Arctic Basin and several ice stations. Recent comparisons of these analyses with Arctic Buoy data show that the average error is limited to 1-2 mb (Walsh, private communication). Temperature fields were also obtained from periphery meteorological stations and ice stations however they were compiled as monthly averages. The temperatures were assumed to be 10 m values. Specific humidity at 10 m, q_{10}, was calculated using the prescribed temperature fields and an assumed relative humidity of 90%. Specific humidity at the surface, q_s, was calculated using the surface temperature produced by the model and assuming

saturation. The long and shortwave radiation fields were determined in a similar manner to Parkinson and Washington (1979). Radiation was calculated for each hour as a function of prescribed zenith angle and cloud cover. The cloud cover varied monthly over an annual cycle but was constant across the domain.

Since the prescribed cloud cover was probably the weakest of the assumptions made, Walsh has noted (private communication) that the long and shortwave radiation fields probably contain the most error of all the atmospheric forcing data. The specific humidities are limited by the 10 m height and 90% relative humidity assumptions, but are still considered reasonable. The pressure and temperature fields appear quite accurate as confirmed by monitoring stations.

These were the same forcing data used in Walsh et al., (1985). That work, as well as that of Hibler and Walsh (1982), showed that inclusion of the dynamic influences from interannually varying atmospheric forcing provided improved simulations of the interannual variations in the sea-ice cover. Time interpolation on a daily basis was conducted using a cubic spline method similar to Maykut and Untersteiner (1971). The smoothed daily forcing, as opposed to the observed daily forcing, was used in order to employ a simplified Hibler ice dynamics parameterization as used in Semtner (1987). This reduced the computational load of the ice portion of the model considerably.

Wind stress on the ice and open ocean was computed by conventional aerodynamic bulk formula methods in the same manner as Semtner (1987):

$$\tau_a = C_d \rho_a \| V_g \| V_g [B] \qquad (3.23)$$

where C_d is the drag coefficient (1.75×10^{-3}). This value is larger than the value used by Hibler and Bryan (1987) to compensate for the use of time-averaged wind. B is a rotation matrix which shifts the forcing vector 25 degrees to the left of the surface geostrophic wind when the stress acts on the ice. When the wind stress is applied to the open ocean, B was set to one (no deflection). The wind stress on the ice-covered ocean was not computed explicitly but was computed interactively through the ice (See Section G. Ice-Ocean Model Coupling.)

Mass inflow through the Faroe-Shetland Channel and the Bering Strait and matched outflow through the Denmark Strait and the Canadian Archipelago were prescribed. These values are the same as in Semtner (1987). The mass and T,S values of the inflow, and the mass of the outflow are invariant in time, but the T,S properties of the outflow are dependent on the simulated fields produced by the model. The inflow of fresh water from major rivers around the margins of the Arctic Basin is specified on the basis of monthly values tabulated by Cattle (1985). Cubic splines are used to interpolate to daily values.

The flux of sensible heat, Q_H (positive downward), is computed by the standard aerodynamic bulk formula method (e.g., Gill, 1982).

$$Q_H = \rho_a C_p C_H \|V_g\|(T_a - T_w) \tag{3.24}$$

where C_p is the specific heat of air (1004 J/kg/K) for dry air (Huschke, 1959), C_H is a dimensionless transfer coefficient for sensible heat called the Stanton Number (1.75 x 10^{-3} (Maykut, 1978), and T_w is the water surface temperature.

The flux of latent heat, Q_{LE}, is computed in a similar fashion:

$$Q_{LE} = \rho_a L_E C_E \|V_g\|(q_{10} - q_{surf}) \tag{3.25}$$

where L_E is the latent heat of vaporization or sublimation (2.58 x 10^6 J/kg). C_E is a dimensionless transfer coefficient called the Dalton Number (1.75 x 10^{-3} (Maykut, 1978)), and q_{10} and q_{surf} are the specific humidities at 10 m and at the surface, respectively.

F. SOLUTION

A comprehensive description of the solution methods for the ocean model is contained in Semtner (1986b). The following brief summary provides a general overview of the procedures.

The numerical solution of Equations 3.2, 3.3, 3.4, 3.7, 3.8, 3.9, 3.11, 3.12 and 3.13 is conducted in several steps.

The horizontal velocity is decomposed into a baroclinic (effect of vertical shear) and a barotropic (vertically averaged) component:

$$(u,v) = (u',v') + (\bar{u},\bar{v}) \tag{3.26}$$

The vertically averaged velocity components (u,v) are written in terms of a stream function ψ. The vertically integrated flow is non-divergent which guarantees the existence of ψ. The stream function represents the integrated mass transport:

$$\begin{aligned}\bar{u} &= \frac{1}{h}\int_{-h}^{0} u\,dz = -\frac{1}{hr_e}\frac{\partial\psi}{\partial\phi} \\ \bar{v} &= \frac{1}{h}\int_{-h}^{0} v\,dz = \frac{1}{hr_e\cos\phi}\frac{\partial\psi}{\partial\lambda}\end{aligned} \tag{3.27}$$

A prediction equation for the stream function, independent of the surface pressure is then derived; first by vertically averaging and then by taking the curl of the horizontal momentum Equations 3.2 and 3.3:

$$\begin{aligned}&\left[\frac{\partial}{\partial\lambda}\left[\frac{1}{h\cos\phi}\frac{\partial^2\psi}{\partial\lambda\partial t}\right] + \frac{\partial}{\partial\phi}\left[\frac{\cos\phi}{h}\frac{\partial^2\psi}{\partial\phi\partial t}\right]\right] - \left[\frac{\partial}{\partial\lambda}\left[\frac{f}{h}\frac{\partial\psi}{\partial\phi}\right] - \frac{\partial}{\partial\phi}\left[\frac{f}{h}\frac{\partial\psi}{\partial\lambda}\right]\right] \\ &= -\left[\frac{\partial}{\partial\lambda}\left[\frac{g}{\rho_0 h}\int_{-h}^{0}\int_{z}^{0}\frac{\partial\rho}{\partial\phi}dz'dz\right]\right. \\ &= -\left.\frac{\partial}{\partial\phi}\left[\frac{g}{\rho_0 h}\int_{-h}^{0}\int_{z}^{0}\frac{\partial\rho}{\partial\lambda}dz'dz\right]\right] \\ &\quad + \left[\frac{\partial}{\partial\lambda}\left[\frac{r_e}{h}\int_{-h}^{0} G^{\phi}dz\right] - \frac{\partial}{\partial\phi}\left[\frac{r_e\cos\phi}{h}\int_{-h}^{0} G^{\lambda}dz\right]\right]\end{aligned} \tag{3.28}$$

where G^{ϕ} and G^{λ} represent all the nonlinear and viscous terms in Equations 3.2 and 3.3.

Equation 3.28 essentially relates the time derivative of the Laplacian of the stream function to the curl of the vertically averaged sum of all the forcing terms in the Navier-Stokes equations. The solution requires inversion of a second-order differential operator in a closed or multiply connected domain. The stream function ψ must be a constant along coastlines to avoid mass transport across the boundaries. ψ is held constant in time along the continent boundaries. On the islands, ψ varies in response to the changing circulation in the same manner as Takano (1974), but with some modification to allow for variable bottom topography. Essentially this involves integrating the curl of the vertically averaged momentum equations around each island. The condition is then applied so that the line integral of the surface pressure gradient, ∇P_s , around each island is zero which produces an equation to predict the change of ψ on each island.

A prediction equation for the vertical shear of velocity is found by differentiating the equation of horizontal motion with respect to depth z, and applying the hydrostatic relation to eliminate the atmospheric pressure P_a. The baroclinic and barotropic components of the velocity are then added to obtain the total u and v.

The prediction equations for temperature and salinity (3.11) and (3.12) are much easier to solve. A "leapfrog" timestep is used for advection and a "forward" timestep is used for diffusion to maintain numerical stability. Additionally, a forward timestep is applied every 10 steps for the advection calculations. This was an efficient method to suppress the computational mode of the leapfrog timestepping technique.

Two different timesteps were used based on the different rates of change of temperature, salinity, and velocity in the ocean model. Temperature and salinity calculations employed 6-hour timesteps while the faster varying velocity field used a shorter timestep of 22.5 minutes. This reduced the total number of calculations required, thereby speeding up the numerical integration. The same technique was used successfully by Bryan (1984). Different timesteps were also used in the ice model. Thermodynamic timesteps were 15 minutes and dynamic timesteps were 15 seconds to maintain numerical stability as in Semtner (1987).

G. ICE-OCEAN MODEL COUPLING

The ocean and sea-ice portions of the linked model are coupled through momentum, heat and salt exchanges. The momentum transfer involved with the coupling occurs at the ice-ocean interface. The ice to water momentum transfer is modeled by a linear drag formula:

$$\tau_w = A_z \frac{\partial V_w}{\partial z} = C_{io}(V_i - V_w) \qquad (3.29)$$

where V_i is the ice velocity, V_w is the ocean velocity in the first (mixed) layer and the linear drag coefficient C_{io} is assigned a value of 27.5×10^{-3} following Semtner (1987). If both ice and open water are present in a grid space, the wind stress is applied to the open water with Equation 3.19 and the ice to ocean stress is computed by Equation 3.29. The average stress is then computed by weighting the two contributions appropriately by the ice concentration.

The oceanic heat flux into the mixed layer is provided by the ocean model. The computation of the mixed layer temperature at each time step and grid point is made in three parts:

- The first computation isolates the first layer thermodynamically and dynamically from the rest of the ocean. The temperature of the layer T_{ml}, is determined simply from the mixed layer/atmospheric heat balance. If T_{ml} reaches the freezing point of seawater, sea-ice is formed. The change in temperature from the preceding time step is equivalent to a heat flux density Q_{ml} (W/m^2) at the surface:

$$Q_{ml} = \rho_w C_w h_{ml} \frac{\partial T_{ml}}{\partial t} \qquad (3.30)$$

  where h_{ml} is the depth of the mixed layer (30 m).

- The second step uses the Q_{ml} calculated in Equation 3.30 as an upper surface thermodynamic forcing for the computation of vertical heat diffusion in the ocean. The ocean distributes this input of energy by horizontal diffusion, advection and convection. A new temperature $T_{dynamic}$ is then obtained for the mixed layer.

- The final step ensures that energy is conserved. If sea-ice is present at the grid point being worked with, and if $T_{dynamic}$ is higher than the freezing point of seawater, T_{wfreez}, then enough ice is melted to decrease $T_{dynamic}$ back to the freezing temperature. In the rare cases where $T_{dynamic}$ is actually lower than the freezing temperature, ice will accrete to the bottom of the existing ice until the latent heat of freezing provides enough heat to return the layer to the freezing temperature.

Salt exchanges are computed by prescribing the salt flux based on the amount of sea-ice melting and accretion, precipitation, evaporation and glacial melt. When no sea-ice is present, the mixed layer salinity is computed from Equation 3.12 and 3.20 by specifying the fresh-water flux at the surface, SSW.

When sea-ice is present, ice accretion and melting produce positive and negative salt fluxes, respectively. It is assumed that upon freezing, 70% of the initial salt content of the seawater is rejected (Semtner, 1987). Therefore the salt flux density Q_{salt} (kg $s^{-1}m^{-2}$) at the upper surface (z=0) is given by:

$$Q_{salt} = K_z \frac{\partial S}{\partial z}\left[\rho_s \frac{\partial(A_i h_s)}{\partial t}\sigma_{snow}^{melt} + 0.70\rho_i \frac{\partial(A_i h_i)}{\partial t}\right] - \rho_w[(P-E)(1-A_i)+R] \qquad (3.31)$$

where A_i is the area of the ice cover; σ_{snow}^{melt} = 1 if snow is melting and 0 otherwise. P is the precipitation rate, E is the evaporation rate and R is the amount of glacial melt.

Table 2 is a summary of the constants used in the model.

TABLE 2

CONSTANTS

Time steps	ocean T and S	6 hr
	ocean velocity	22.5 min
	ice T	15 min
	ice velocity	15 sec
Arakawa type B grid		
g , acceleration of gravity		9.8 m/s
Ω , earth's speed of rotation		7.272×10^{-5} rad/s
r_e, earth's radius		6.37×10^{8} m
A_z, vertical eddy viscosity (u,v)		0.3×10^{-4} m^2/s
A_h, horizontal eddy viscosity (u,v)		12×10^{4} m^2/s
K_z, vertical eddy diffusivity (T,S)		0.3×10^{-4} m^2/s
K_h, horizontal eddy diffusivity (T,S,ice)		2×10^{3} m^2/s
ρ_a, density of air		1.3 kg/m^3
ρ_s, density of snow		330 kg/m^3
ρ_i, density of ice		900 kg/m^3
C , specific heat capacity of ice and snow		2.09 kJ/(kg K)
C_p, specific heat capacity of air		1.004 kJ/(kg K)
C_H, Stanton Number		1.75×10^{-3}
C_E, Dalton Number		1.75×10^{-3}
k_i, thermal conductivity of ice		4.068 W/(m K)
k_s, thermal conductivity of snow		0.31 W/(m K)
L_{Hs}, latent heat of fusion for snow		110 MJ/m^3
L_{Hi}, latent heat of fusion for ice		301 MJ/m^3
L_t, latent heat of evap. (and sublim.)		2.58×10^{6} J/kg
melting point for snow		0 °C
melting point for snow		-0.1 °C
surface emissivity		1
Stefan-Boltzman constant		5.67×10^{-8} $W/(m^2 K^4)$
ζ_{max}, maximum limit for bulk viscosity		$P^* \times 2.5 \times 10^{8}$ sec
C_d, air/sea and air/ice drag coefficient		1.75×10^{-3}
C_{io}, ice/water linear drag coefficient		27.5×10^{-3}
albedo of ice		0.70
albedo of snow		0.80
albedo of melting snow		0.745
albedo of open ocean		0.07

IV. INTERACTIVE OCEAN EXPERIMENT

This experiment was conducted to determine the importance of incorporating a fully interactive prognostic ocean model into a linked ice-ocean numerical model. Many numerical models of sea ice have been developed which do not include a prognostic ocean component. This experiment was designed to test the validity of that omission. The importance of including a prognostic ocean was judged with respect to the accuracy of the simulation of the interannual and annual variations of sea-ice cover in the Arctic. Evaluation was based on comparisons between observed fields of ice concentration and simulated ice concentration fields produced by the model.

A. EXPERIMENTAL SETUP

The linked ice-ocean model was initially run for ten years with a fully interactive ocean and monthly varying atmospheric forcing. All oceanic variables were saved on a regular basis from this first run, in order to examine their variability and to calculate a ten-year average annual cycle. The second run used the same atmospheric forcing, integration period and ice portion as in the first run. However the interactive, prognostic ocean portion was replaced by prescribing the average annual cycle from the first run. The outputs from

both runs were analyzed to determine each model's skill in reproducing the observed annual cycle and interannual variations of ice concentration. Modifications to the Semtner (1987) model included:

- Run 1
    - Changing the atmospheric forcing from a 30-year mean annual cycle to an interannually varying cycle of observed monthly averages.
    - Defining the initial conditions for each modelled year as the end condition for the previous year vice averaged or constant fields. This permitted consecutive integration of as many years as desired.
    - Storing and then averaging simulated oceanic heat flux and layer 2 ocean velocities at every time step for ten years. The oceanic heat flux saved for each grid box was the summation of all the heat the ocean model provided to the mixed layer in that box. Layer 2 velocities (corresponding to a depth of 40 m) were used because they simulated the geostrophic currents quite well. The current velocities in the mixed layer were unrealistic because all the induced Ekman flow was confined within that layer. A new data file containing the 10-year average annual cycle of these variables was then created.
- Run 2
    - Incorporating the 10-year average annual cycle of oceanic heat flux and layer 2 velocities into the model's spline smoothing routine. This permitted the continued use of the modified Hibler (1979) ice dynamics.
    - Replacing the ocean model with a parameterization of the average oceanic forcing (thermodynamic and dynamic). This forcing was applied to the base of the mixed layer.

B. RESULTS

The average computing time for a single simulation year using the fully prognostic, interactive ocean in run 1 was 575 seconds on the CRAY XMP. The average time for a single year in run 2 with the prescribed ocean was 275 seconds. For labeling and descriptive purposes, the observed data were designated as A data, Run 1 output as B data and Run 2 output as C data.

The simulated ice concentration contours for all 120 months were produced for B and C in the same manner as for the observed fields. As representative examples, Figures 4.1 - 4.6 show the ice concentration contours for months 76 and 93 (Apr 77 and Sep 78) for all three data sets (A, B and C). These contours are typical for minimum and maximum ice extent periods.

Layer 2 velocities (Figures 4.7 - 4.10) and contours of oceanic heat flux into the mixed layer (Figures 4.11 - 4.14) for each month for B and the corresponding average fields for C are also shown. Heat units are degrees C per second, applied to the volume of the mixed layer within each grid box (3.63×10^{11} m^3).

Ice thickness was another useful predicted variable. The ice thickness distribution provided a good indication of how the ice dynamics in combination with the ice rheology modified the ice cover within the high ice concentration regions.

1.50
1.50
1.50

Figure 4.2 Simulated ice concentration using prognostic ocean model (B) for month 76 (April, 1977). Contour line labelled -1.6 is coastline. Contours are in tenths.

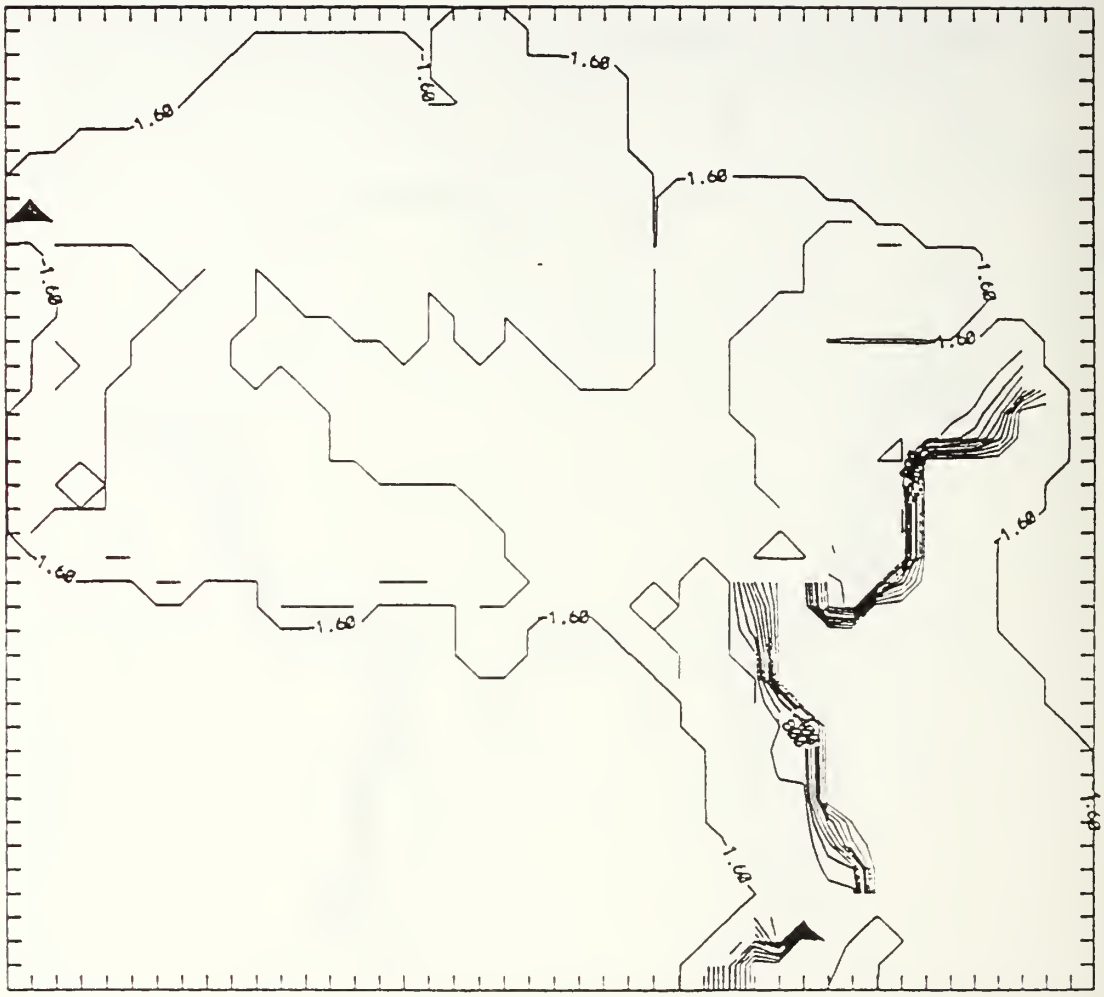

Figure 4.3 Simulated ice concentration using 10-year mean ocean data (C) for month 76 (April, 1977). Contour line labelled -1.6 is coastline. Contours are in tenths.

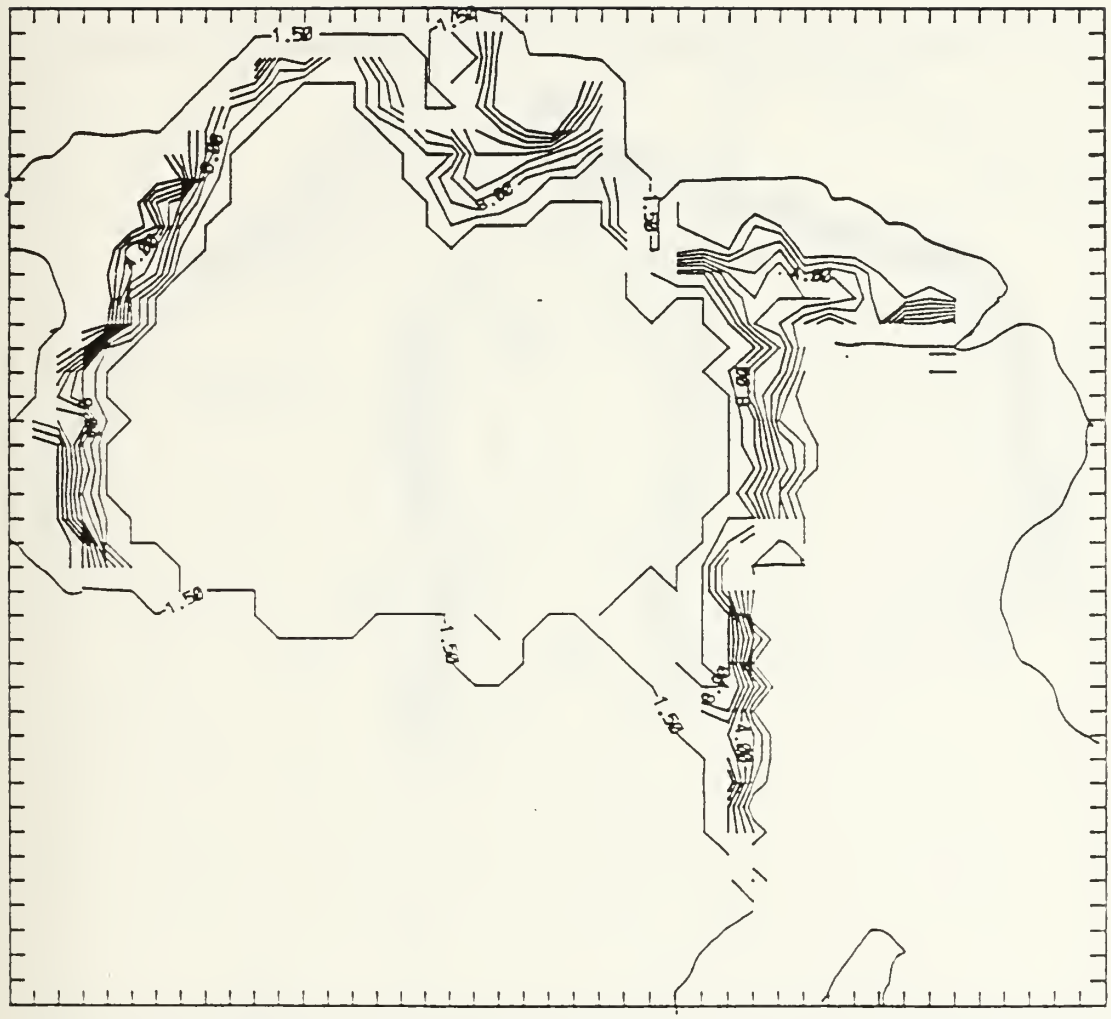

Figure 4.4 Observed ice concentration (A) in tenths for month 93 (September, 1979).

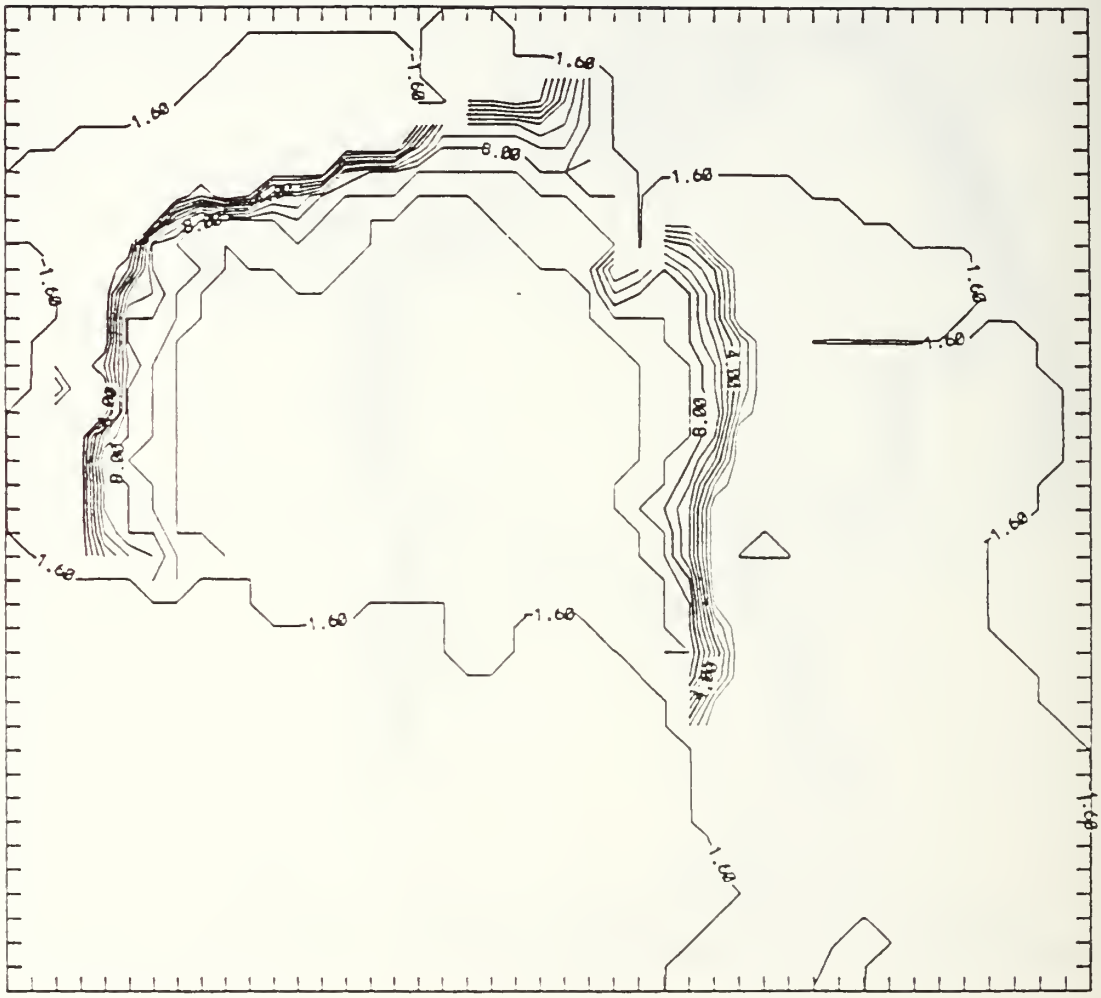

Figure 4.5 Simulated ice concentration using prognostic ocean model (B) for month 93 (September, 1979). Contours are in tenths.

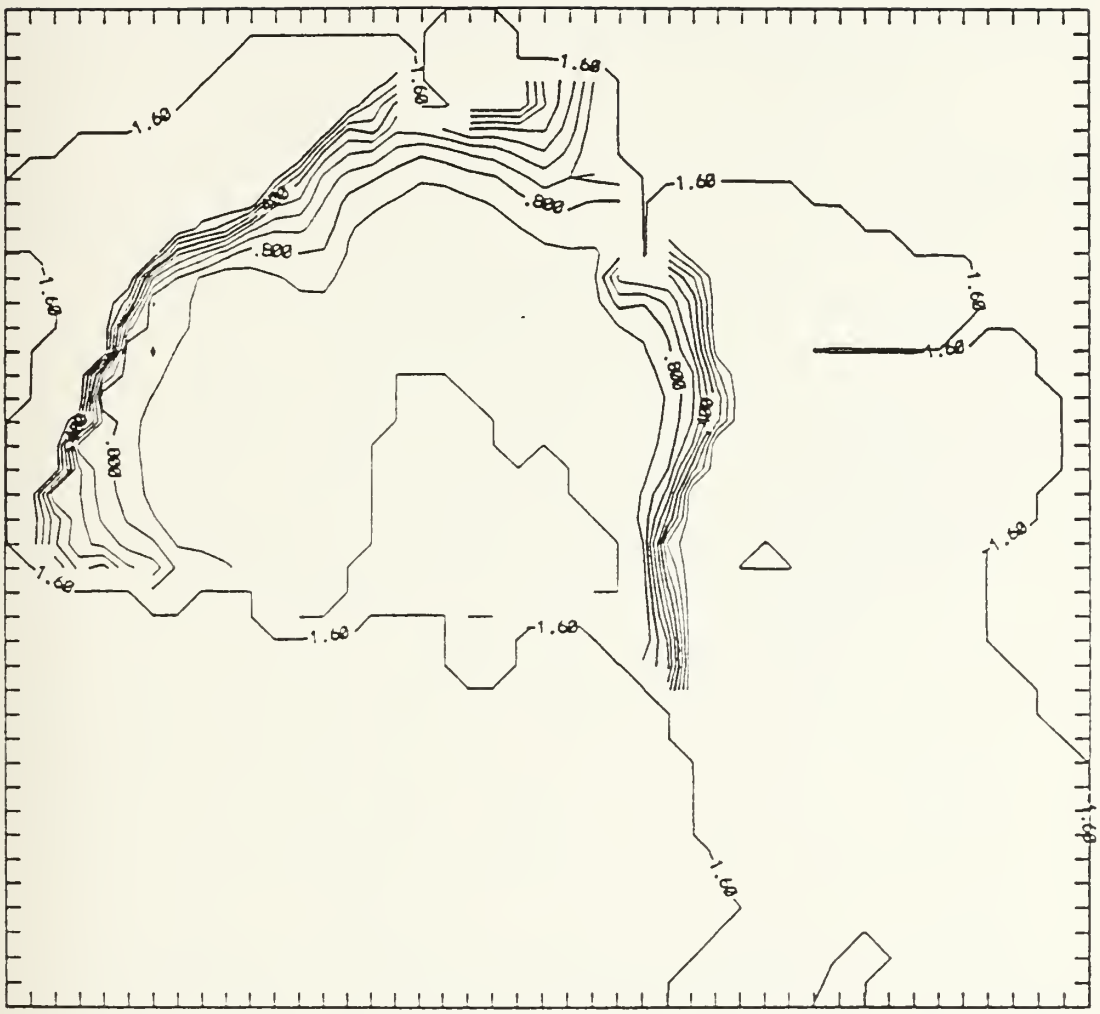

Figure 4.6 Simulated ice concentration using 10-year mean ocean (C) for month 93 (September, 1979). Contours are in tenths.

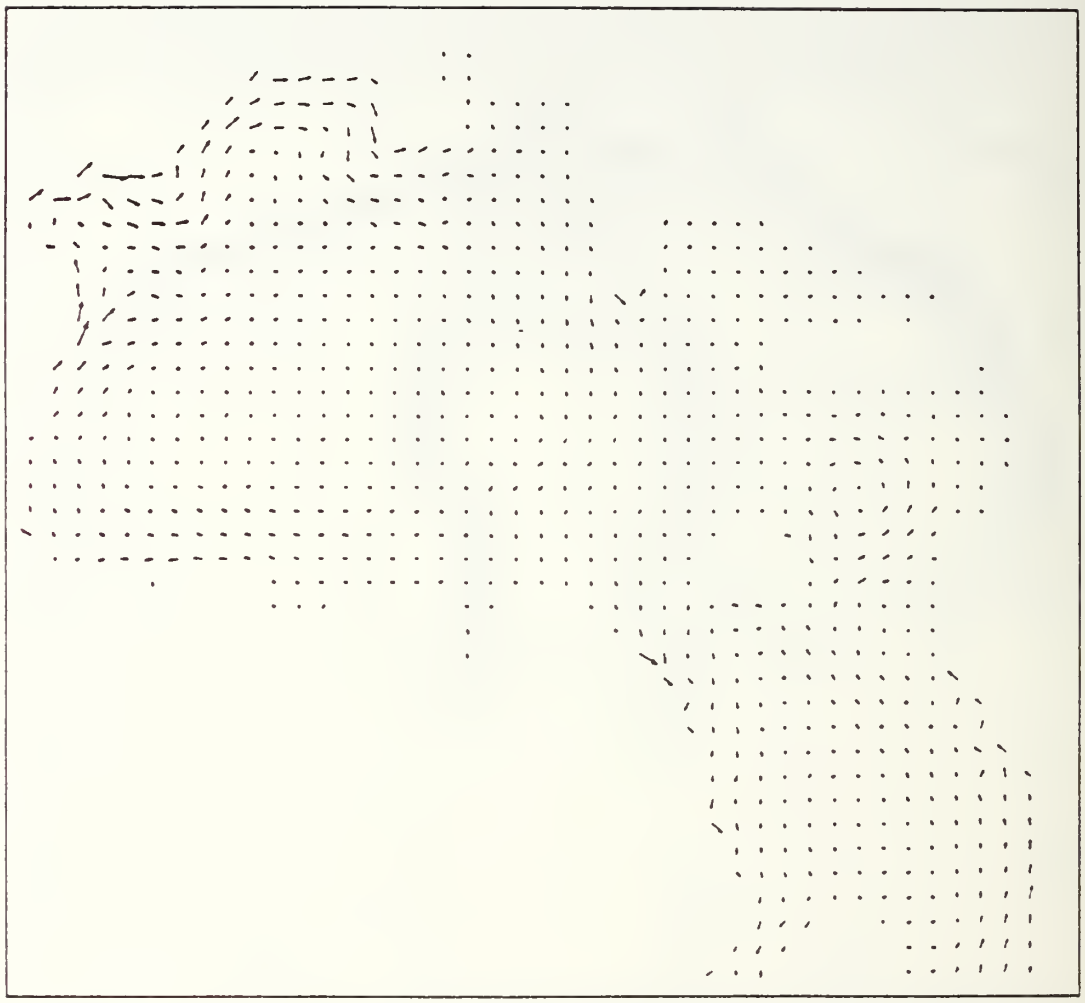

Figure 4.7 10-year mean, level two (40 m depth) ocean currents for April. Maximum vector 0.246 m/s.

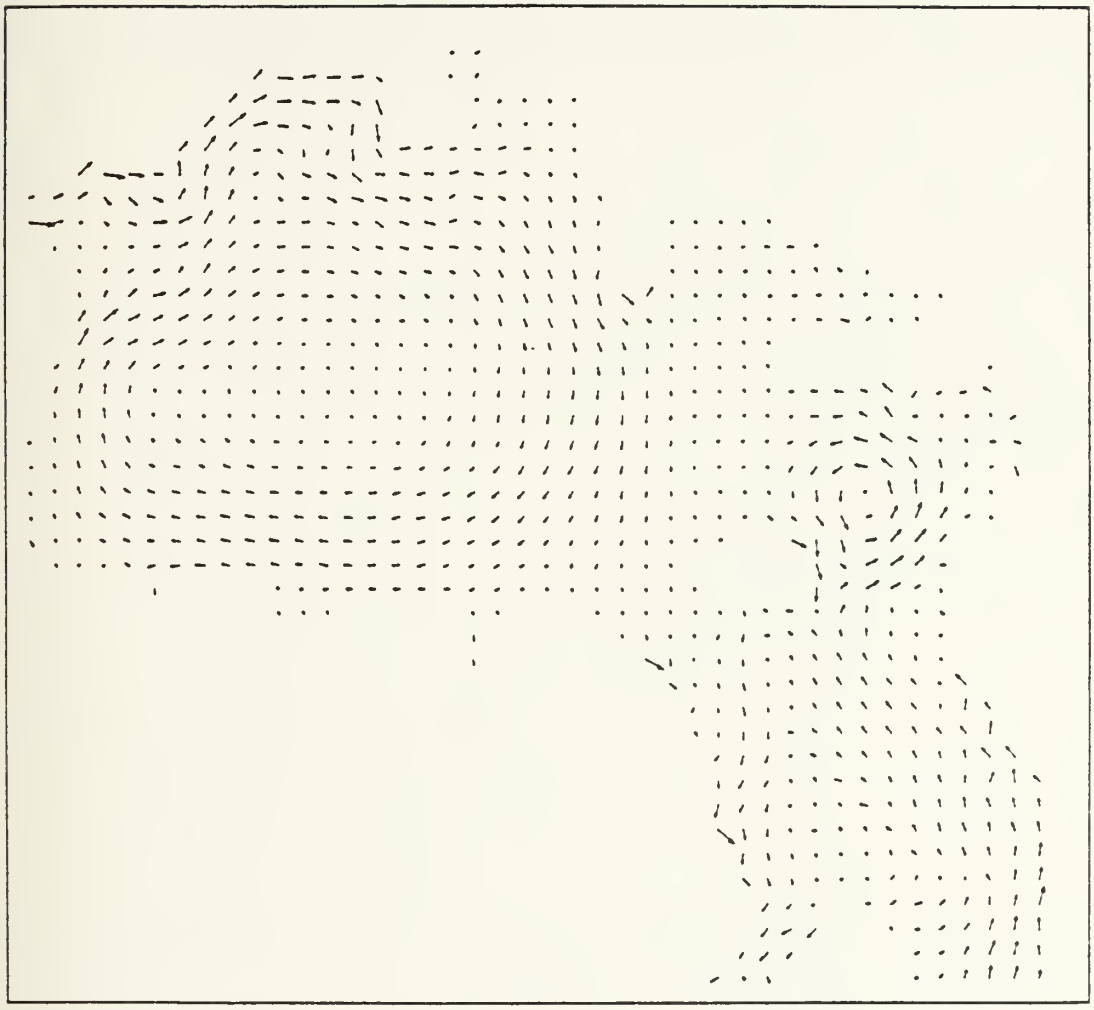

Figure 4.8 Simulated level two (40 m depth) ocean currents for month 76 (April, 1977). Maximum vector 0.162 m/s.

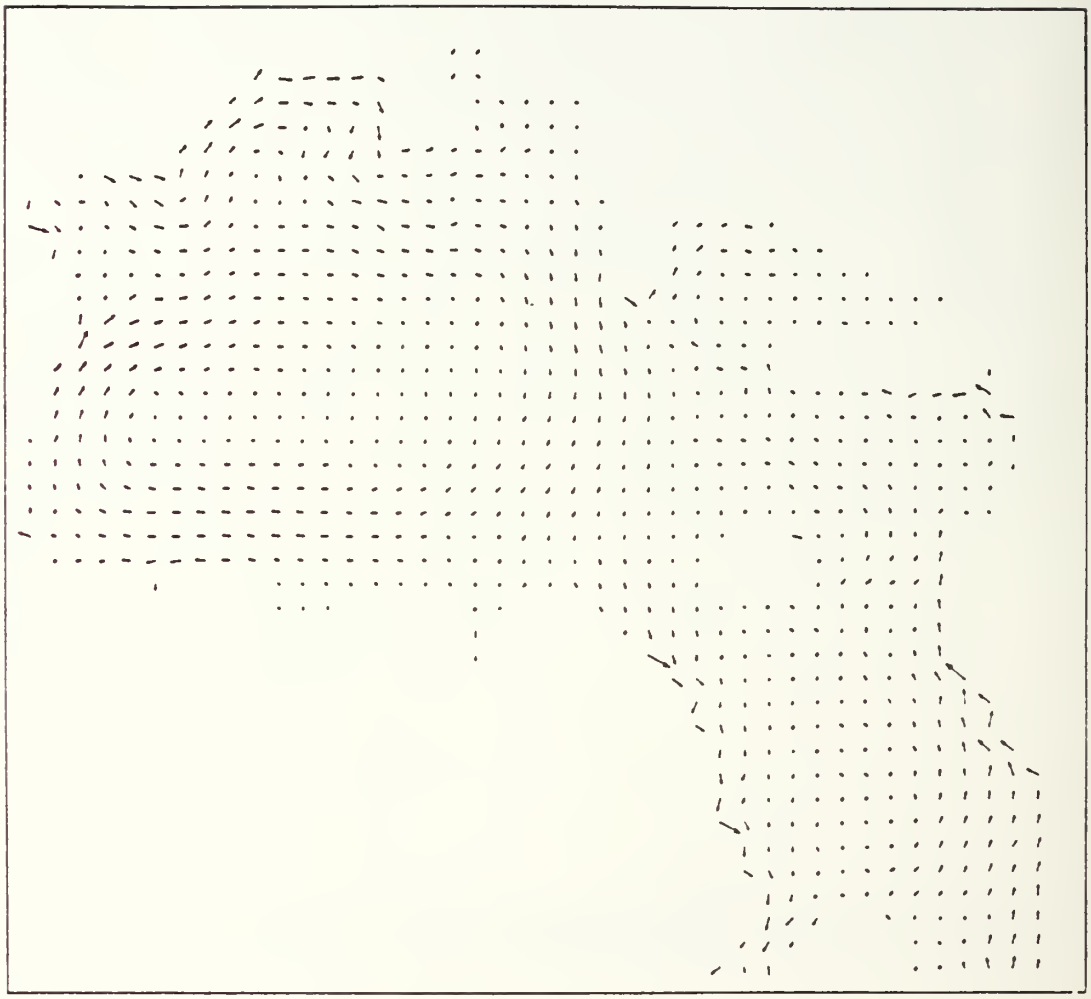

Figure 4.9 10-year mean level two (40 m depth) ocean currents for September. Maximum vector 0.152 m/s.

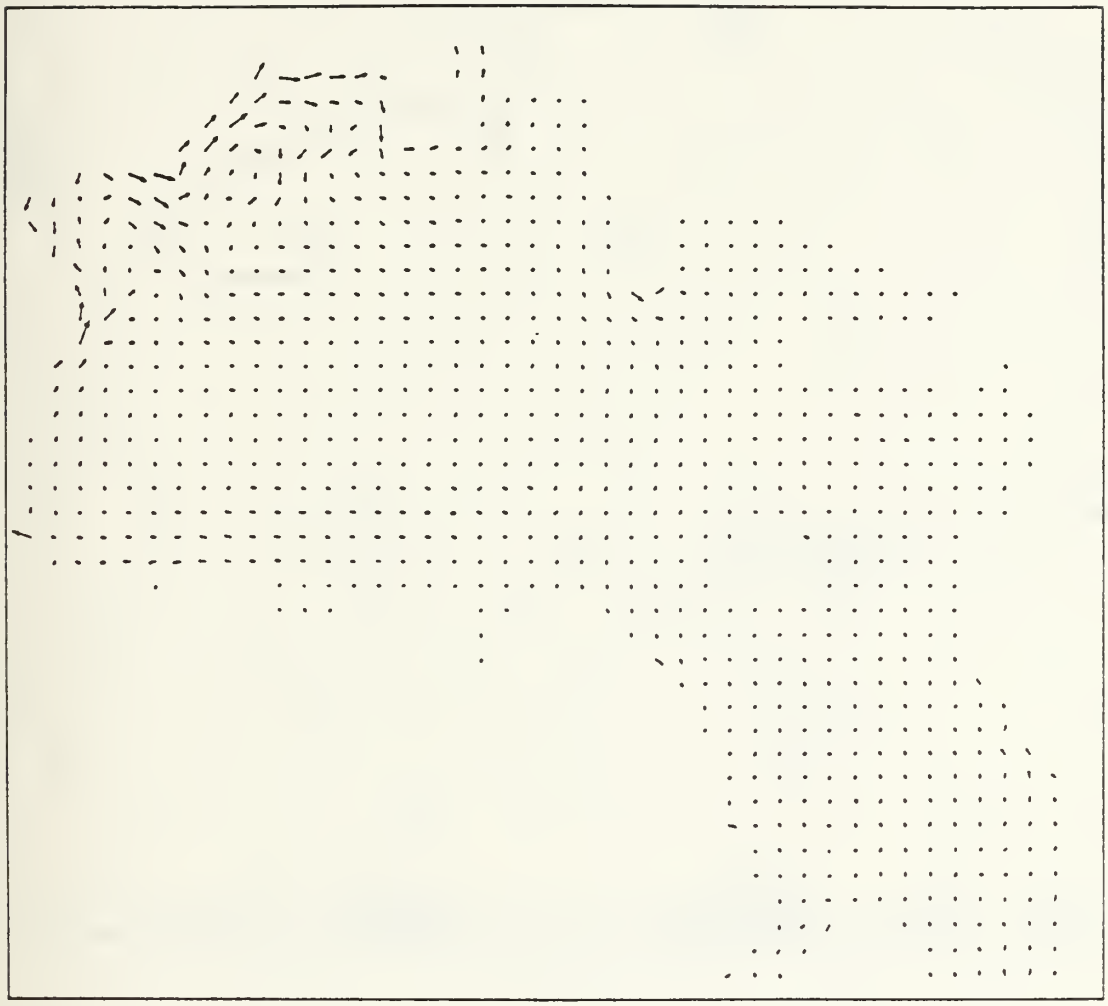

Figure 4.10 Simulated level two (40 m depth) ocean currents for month 93 (September, 1979). Maximium vector 0.344 m/s.

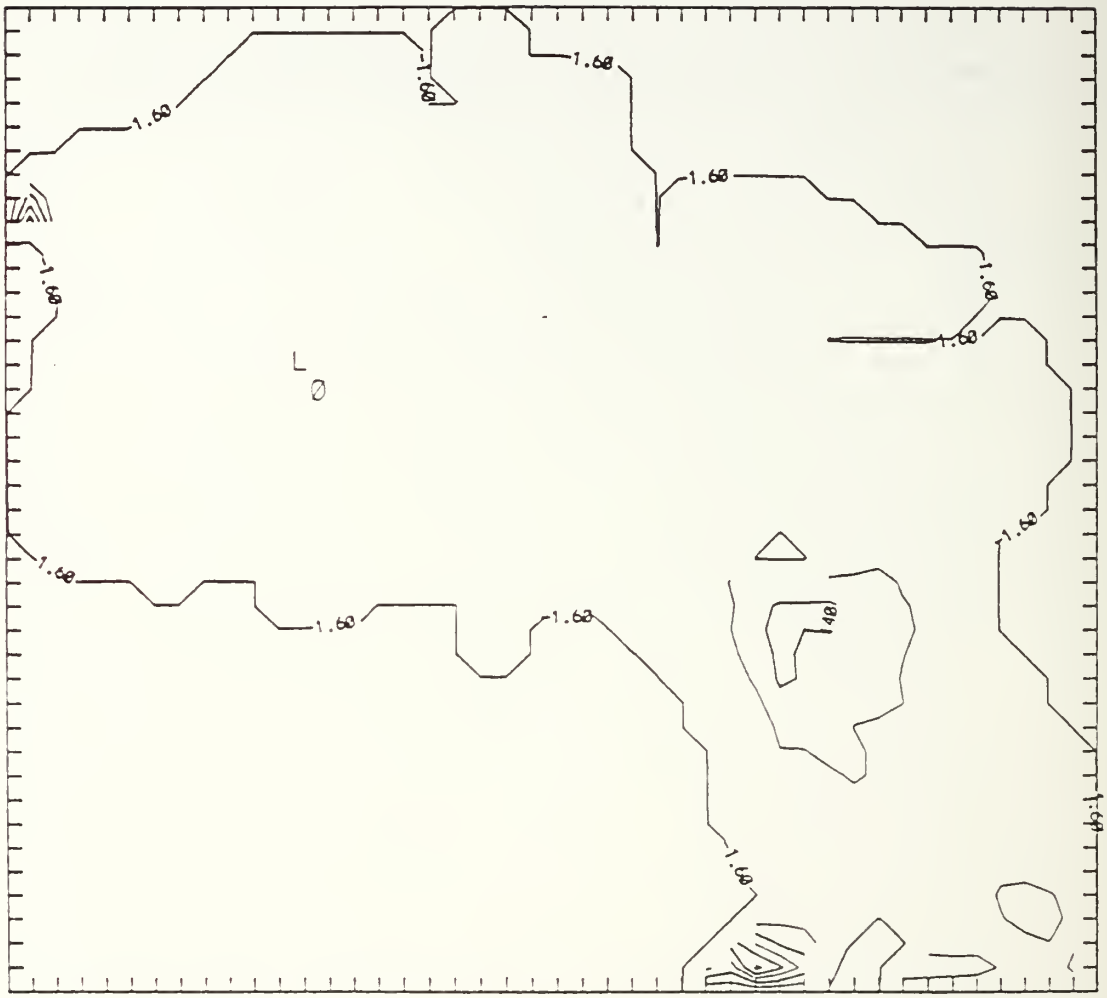
1.60
1.60
1.60

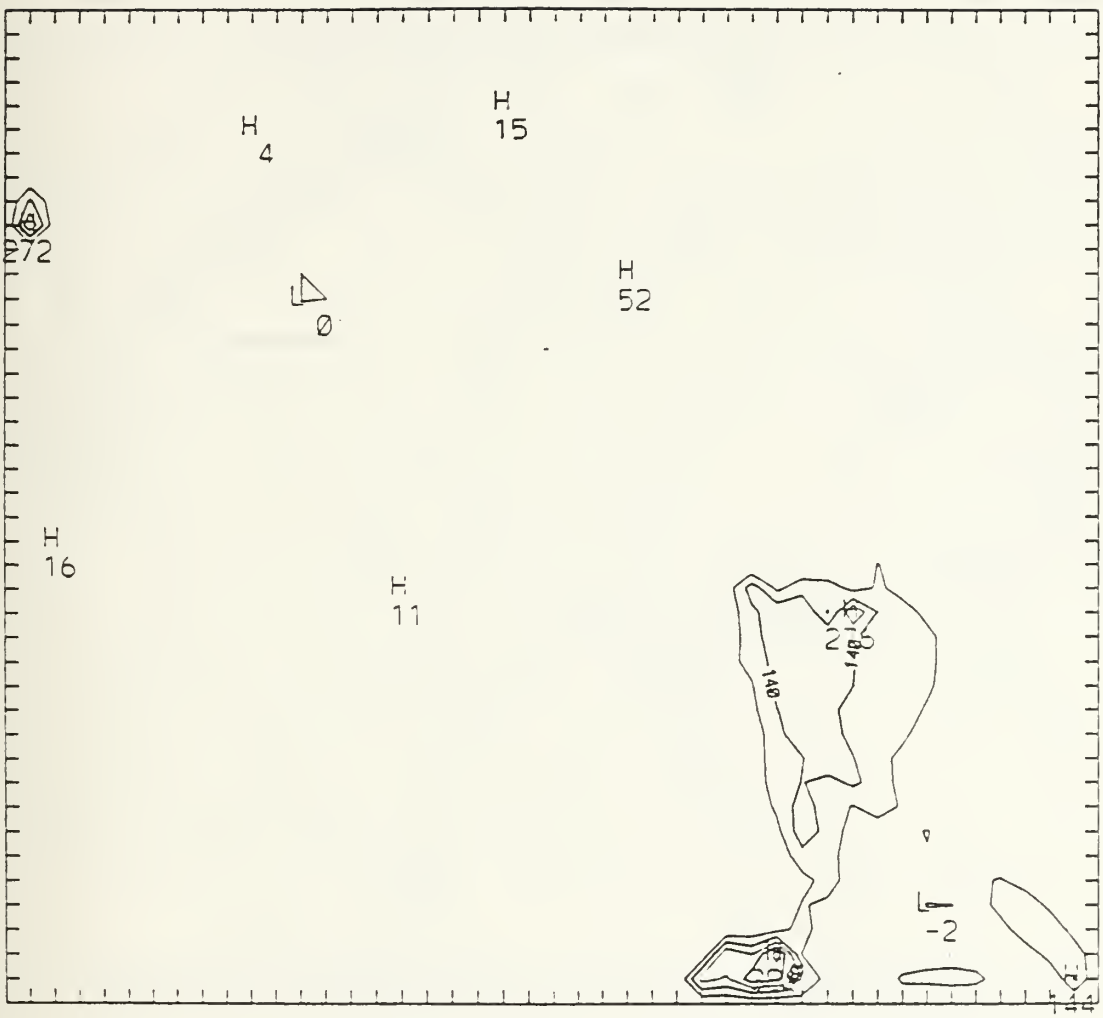

Figure 4.12 Simulated ocean heat flux through the 30 m mixed layer for month 76. Units are degrees C/sec/cm^2 scaled by 1 x 10^8. Conversion factor to W/m^2 is 1.25 x 10^8. L and H indicate relative lows and highs respectively.

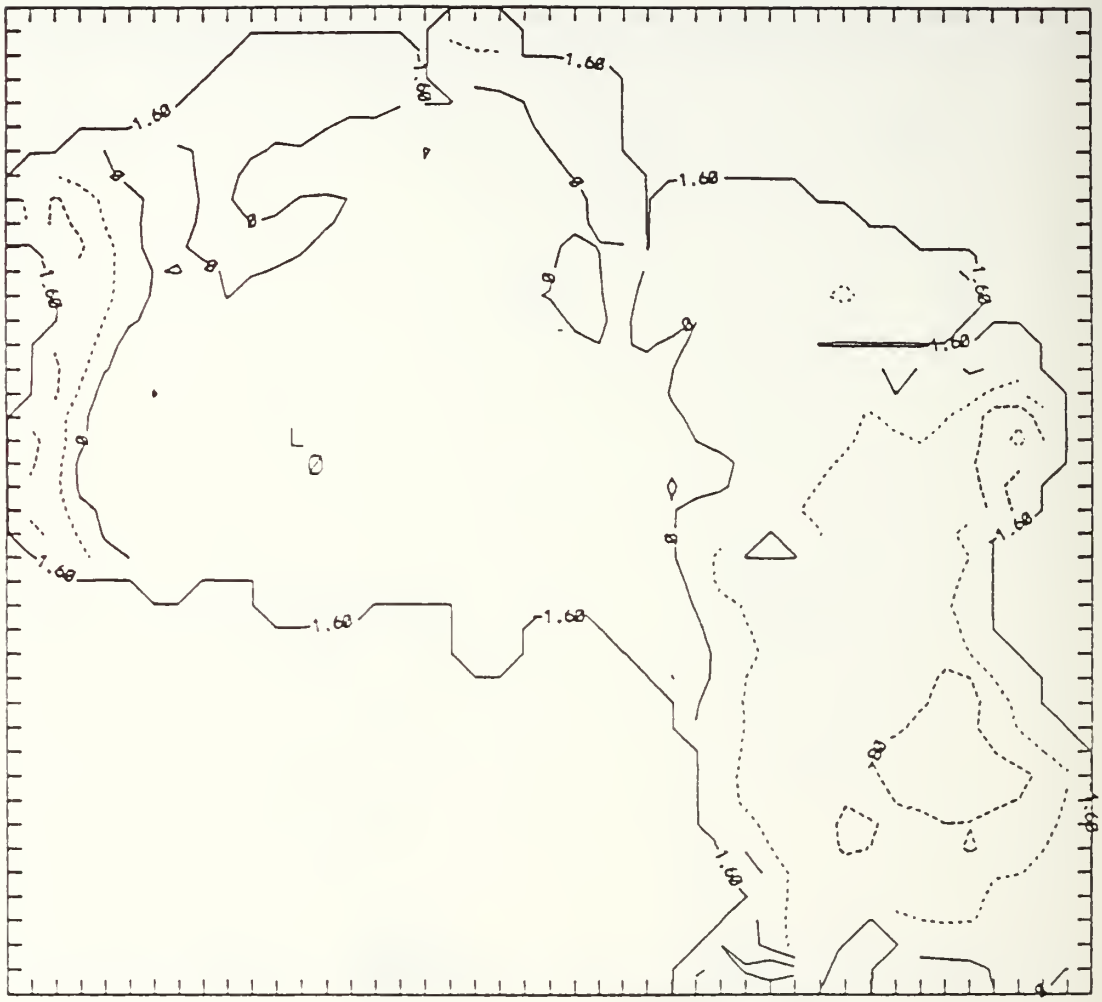

Figure 4.13 10-year mean ocean heat flux through the 30 m mixed layer for Sep. Units are degrees C/sec/cm^2 scaled by 1 x 10^8. Conversion factor to W/m^2 is 1.25 x 10^8. L and H indicate relative lows and highs respectively.

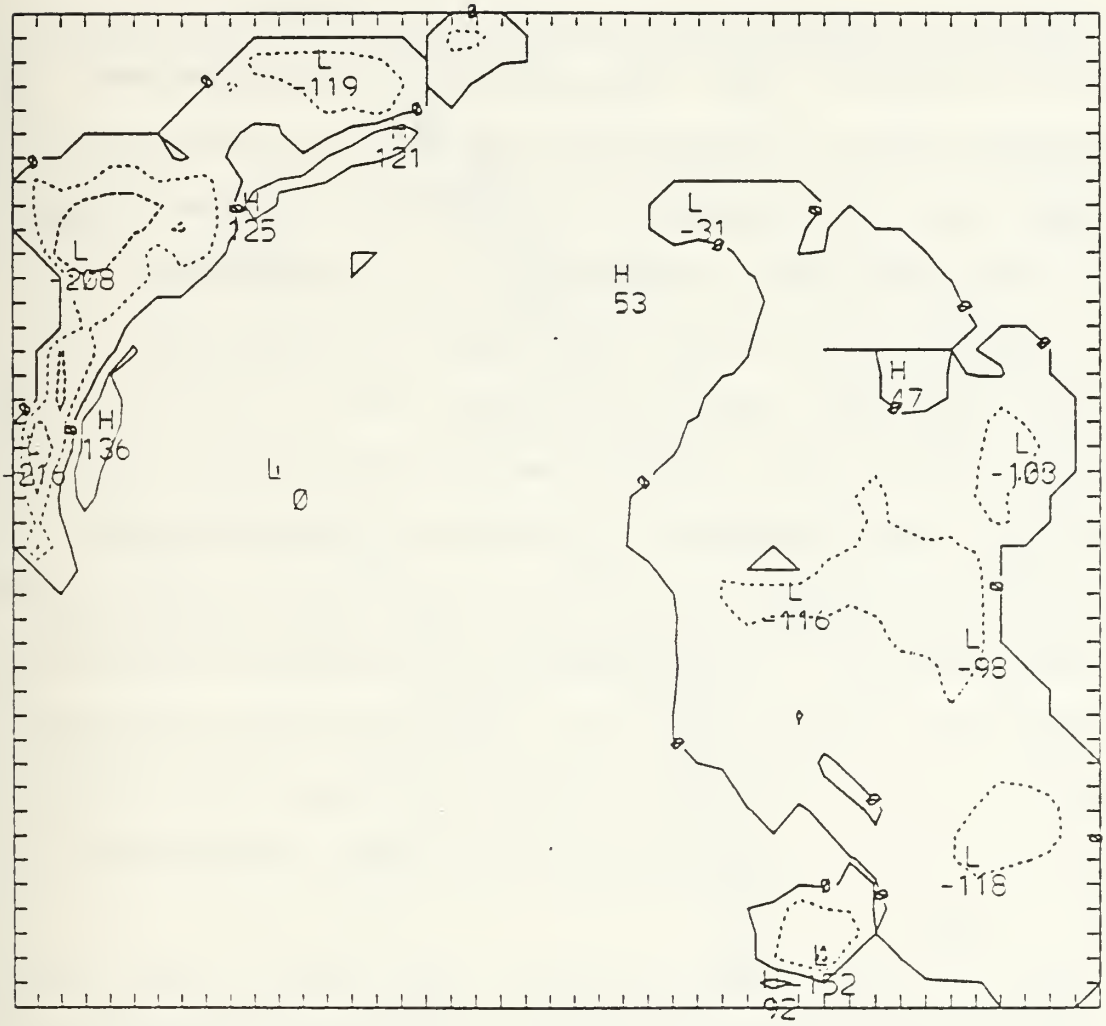

Figure 4.14 Simulated ocean heat flux through the 30 m mixed layer for month 93. Units are degrees C/sec/cm^2 scaled by 1 x 10^8. Conversion factor to W/m^2 is 1.25 x 10^8. L and H indicate relative lows and highs respectively.

Representative ice thickness contours for B and C in months 76 and 93 are shown in Figures 4.15 - 4.18.

In order to gain a more quantitative appreciation of the differences between the various outputs (A, B and C), a series of comparative graphs were produced. The total monthly ice area for each of the four regions was determined by multiplying the ice concentration at each grid point by the grid box area and summing over the region (Figures 4.19 - 4.22). The observed ice concentration (A) was subtracted from the B and C fields to show the amount each simulated field differed from the observed (Figures 4.23 - 4.26). The absolute sum of the areal differences for B and C in each region was then calculated. A measure of the improvement in simulating the annual cycle of total ice area in each region was then possible. The absolute sum of B-A was consistently less than the absolute sum of C-A indicating that the B data were closer to the observed data and on average more accurate than the C data. The results from these calculations are shown in Table 3.

Figures 4.19 - 4.22 indicated that both B and C had obvious biases in total ice area. In order to examine the interannual variations, these biases, as well as the mean annual cycle of ice cover, were removed. The ten-year average annual cycles of A,B and C were calculated (Figures 4.27 - 4.30) and subtracted from each of their respective data fields to produce anomaly (difference from annual cycle) fields of

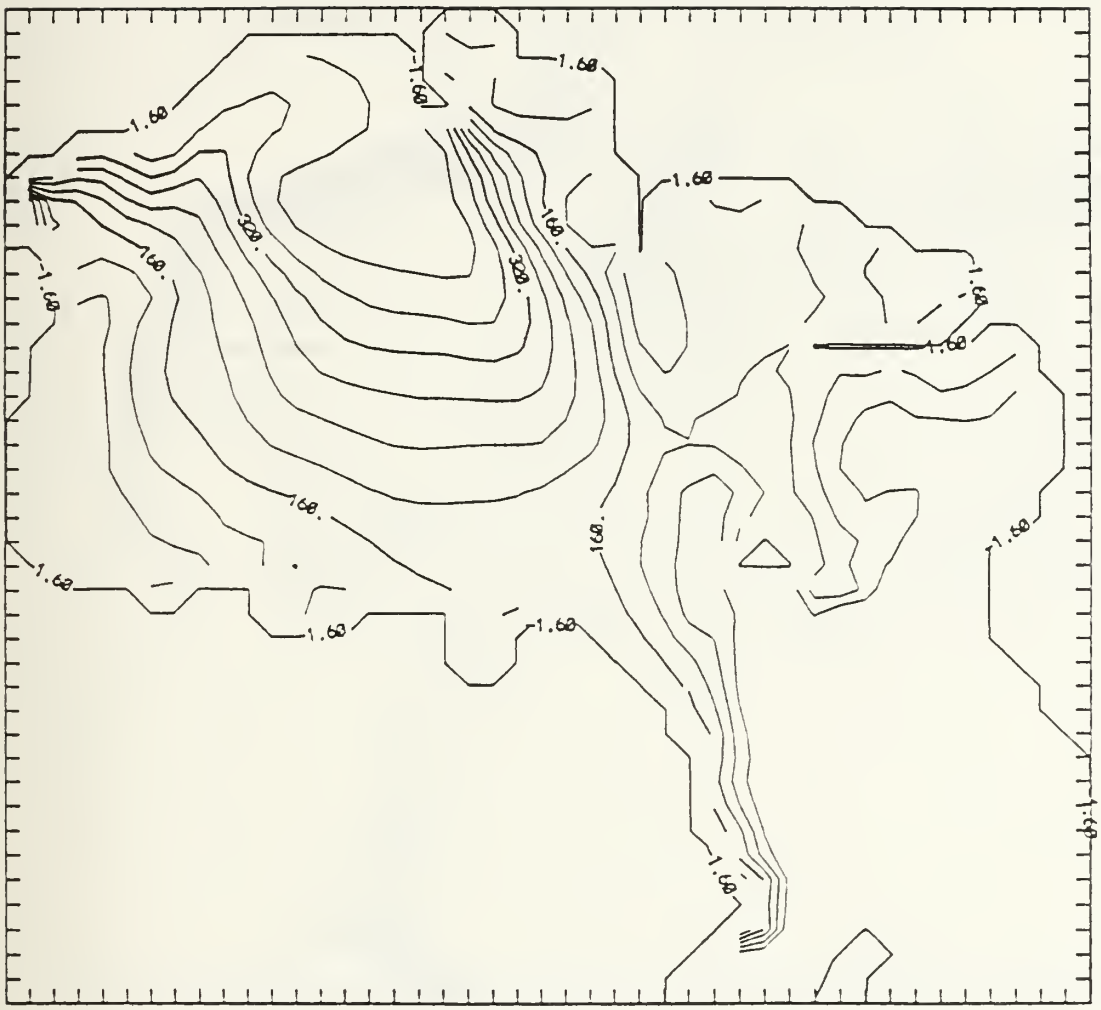
1.60
1.60
1.60

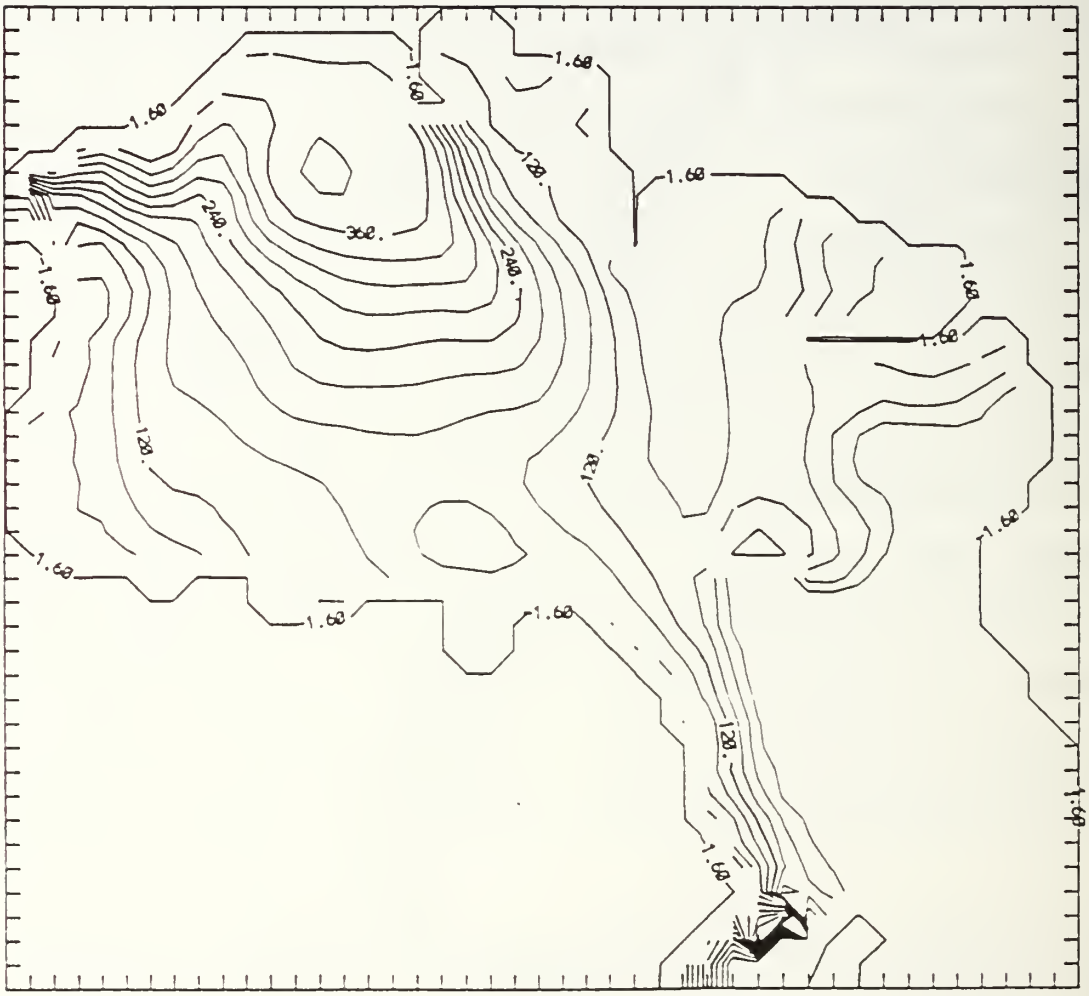

Figure 4.16 Simulated thickness contours using 10-year mean ocean (C) for month 76. Contours are cm of ice thickness.

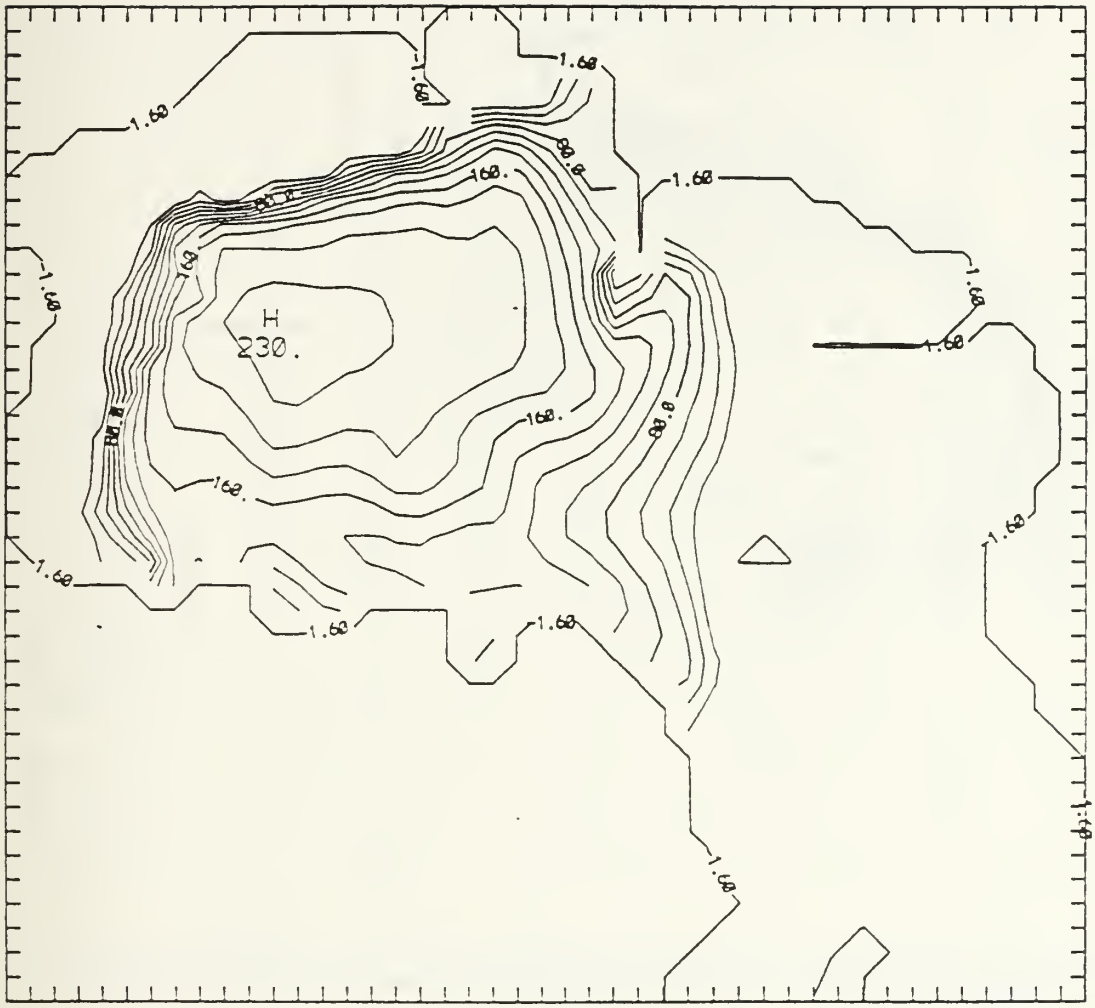

Figure 4.17 Simulated thickness contours using prognostic ocean (B) for month 93. Contours are cm of ice thickness.

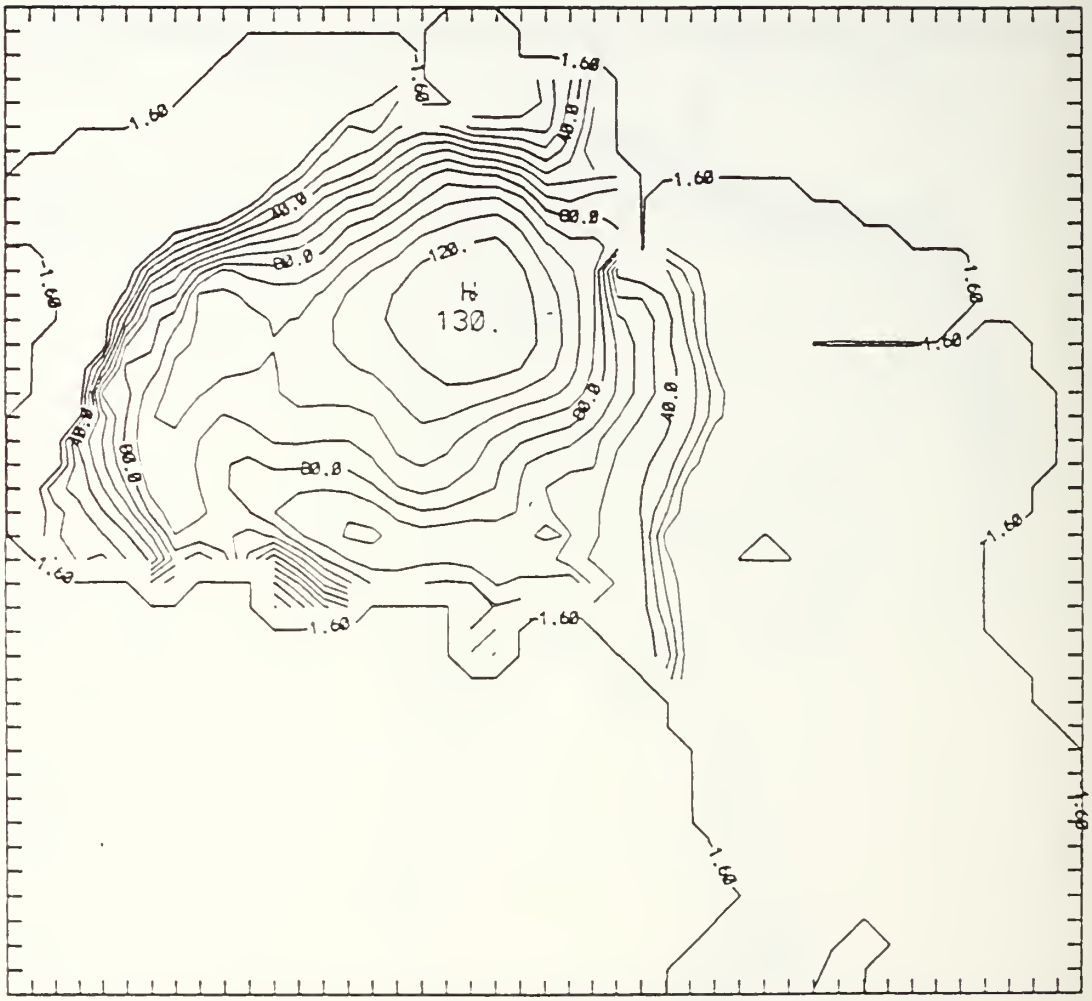
1.60
1.60
1.60

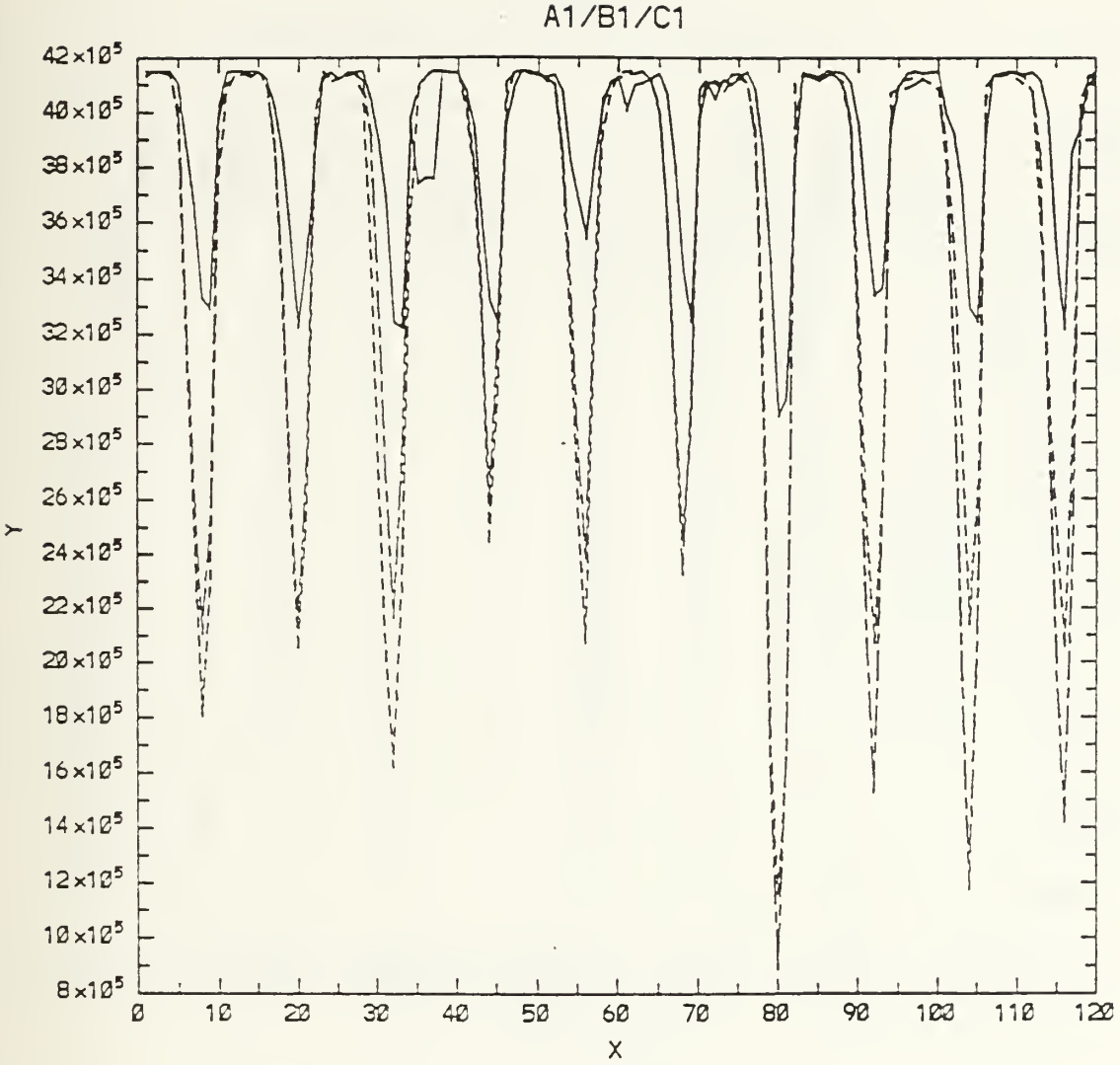

Figure 4.19 Time series of total ice area in region 1. Observed (A) is the solid line, prognostic ocean model (B) is the dashed line and 10-year mean ocean model (C) is the dash-dot line. X axis is months from Jan 1971 to Dec 1980. Y axis is 10's of km^2.

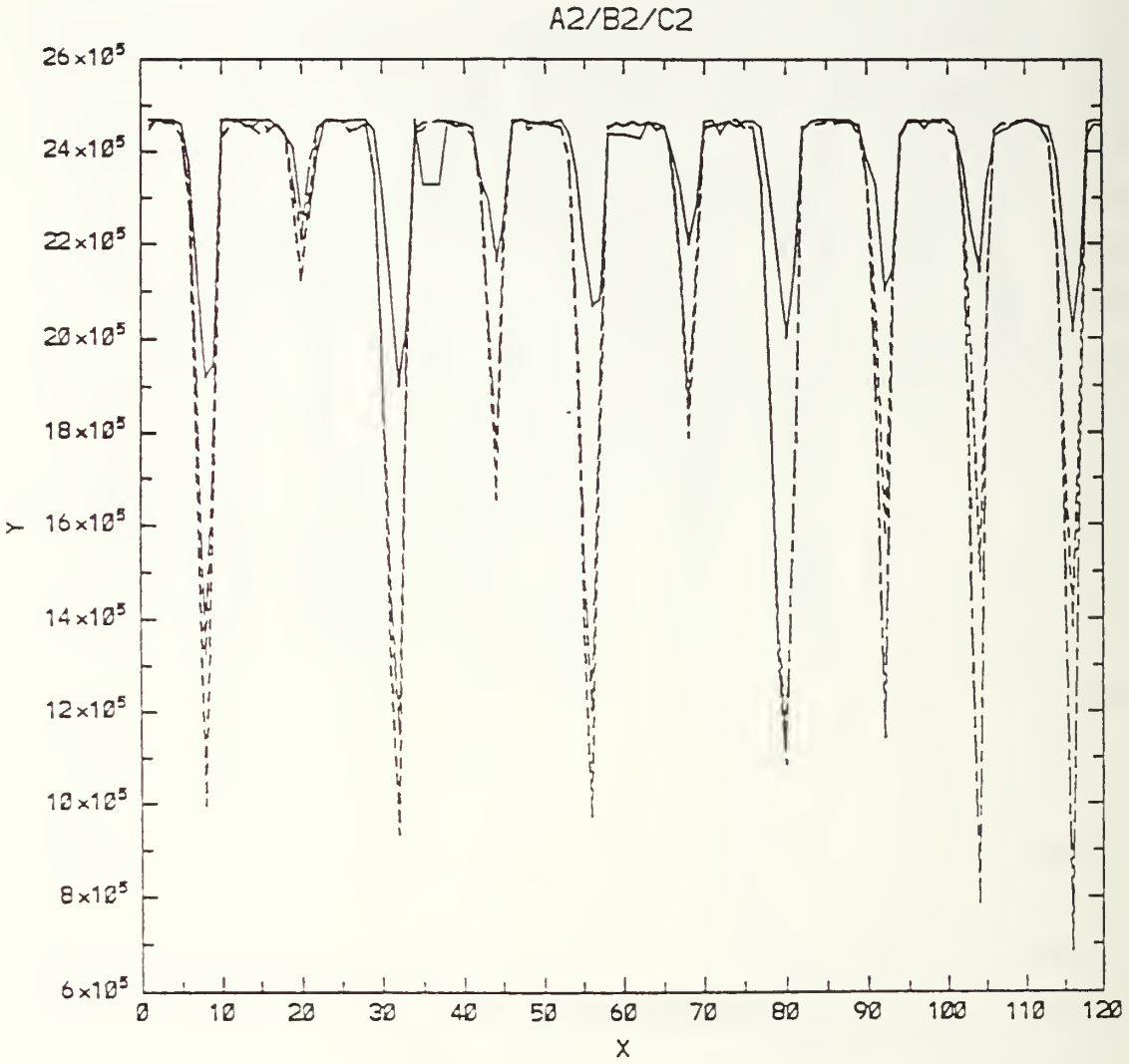

Figure 4.20 Time series of total ice area in region 2. Observed (A) is the solid line, prognostic ocean model (B) is the dashed line and 10-year mean ocean model (C) is the dash-dot line. X axis is months from Jan 1971 to Dec 1980. Y axis is 10's of km^2.

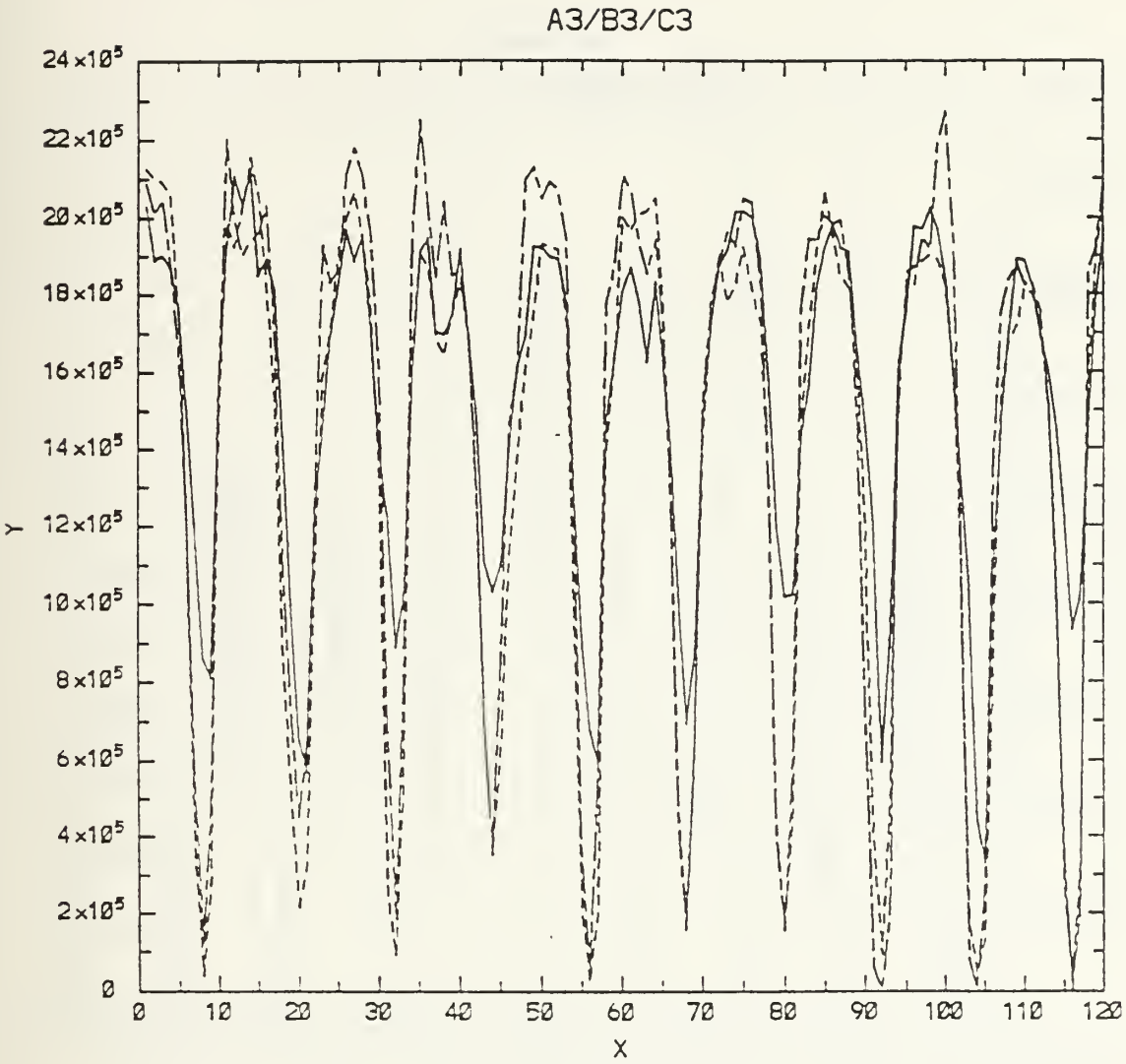

Figure 4.21 Time series of total ice area in region 3. Observed (A) is the solid line, prognostic ocean model (B) is the dashed line and 10-year mean ocean model (C) is the dash-dot line. X axis is months from Jan 1971 to Dec 1980. Y axis is 10's of km^2.

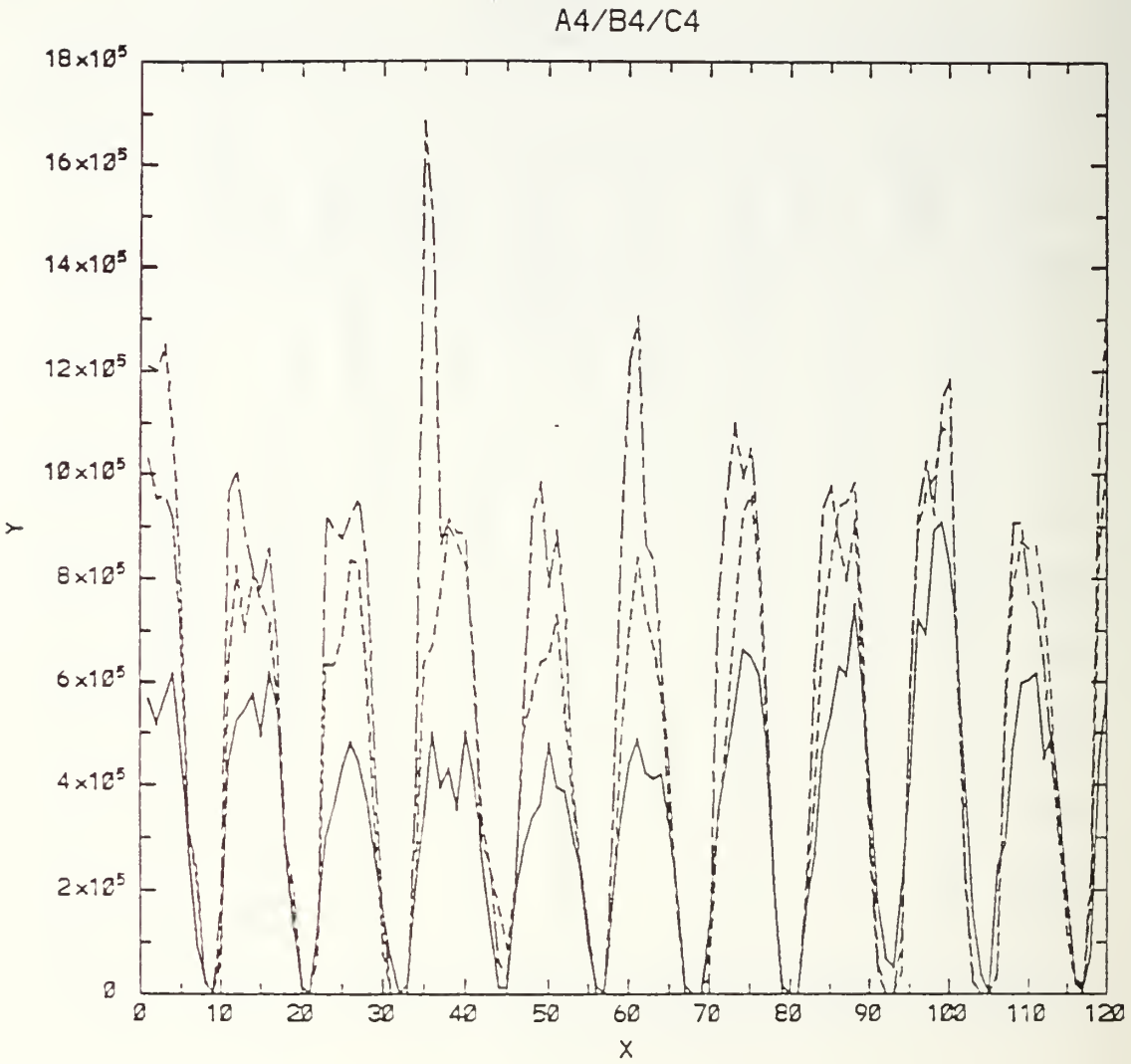

Figure 4.22 Time series of total ice area in region 4. Observed (A) is the solid line, prognostic ocean model (B) is the dashed line and 10-year mean ocean model (C) is the dash-dot line. X axis is months from Jan 1971 to Dec 1980. Y axis is 10's of km^2.

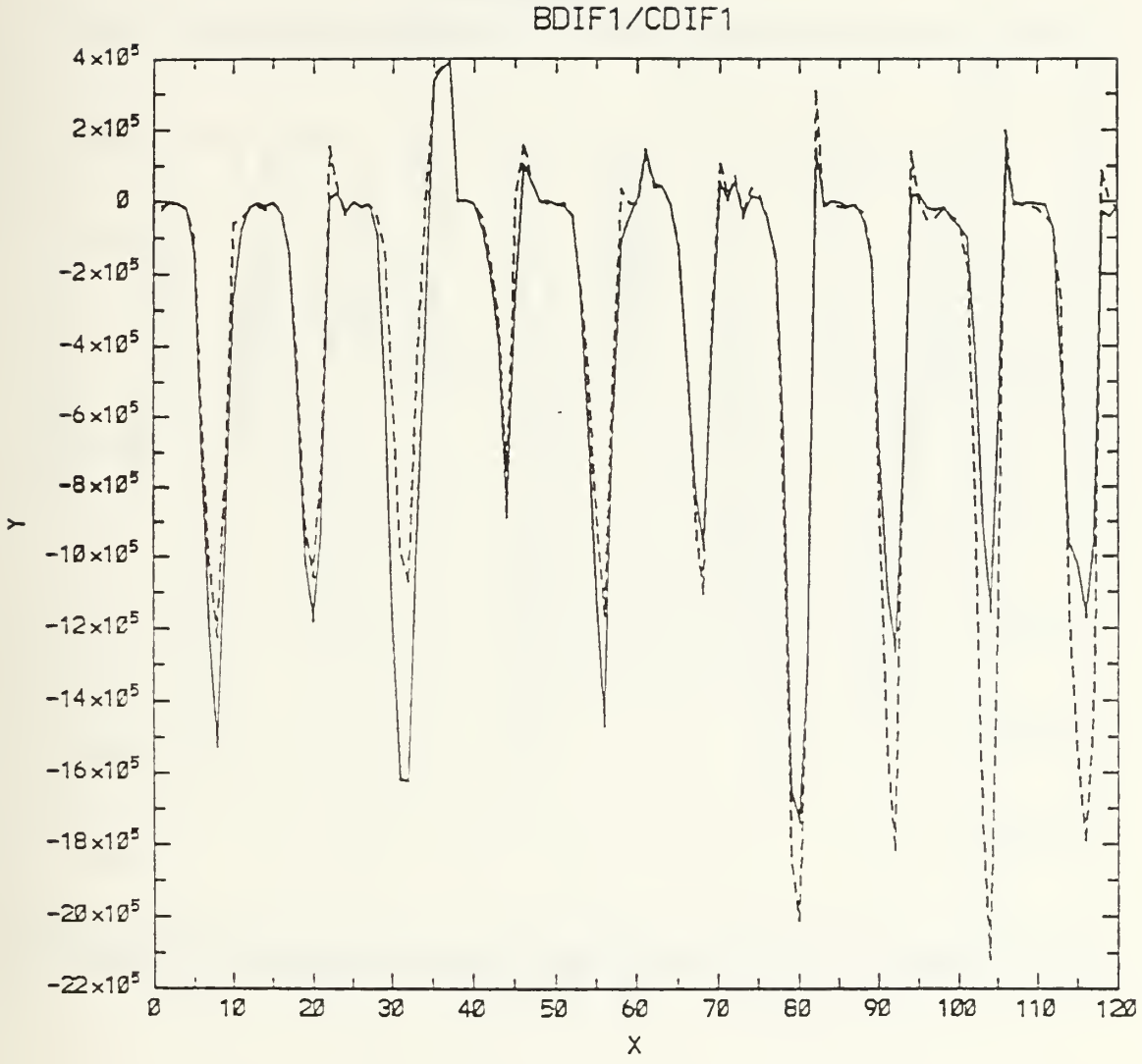

Figure 4.23 Time series of simulated minus observed total area in region 1. B-A is the solid line, C-A is the dashed line. X axis is months from Jan 1971 to Dec 1980. Y axis is 10's of km^2.

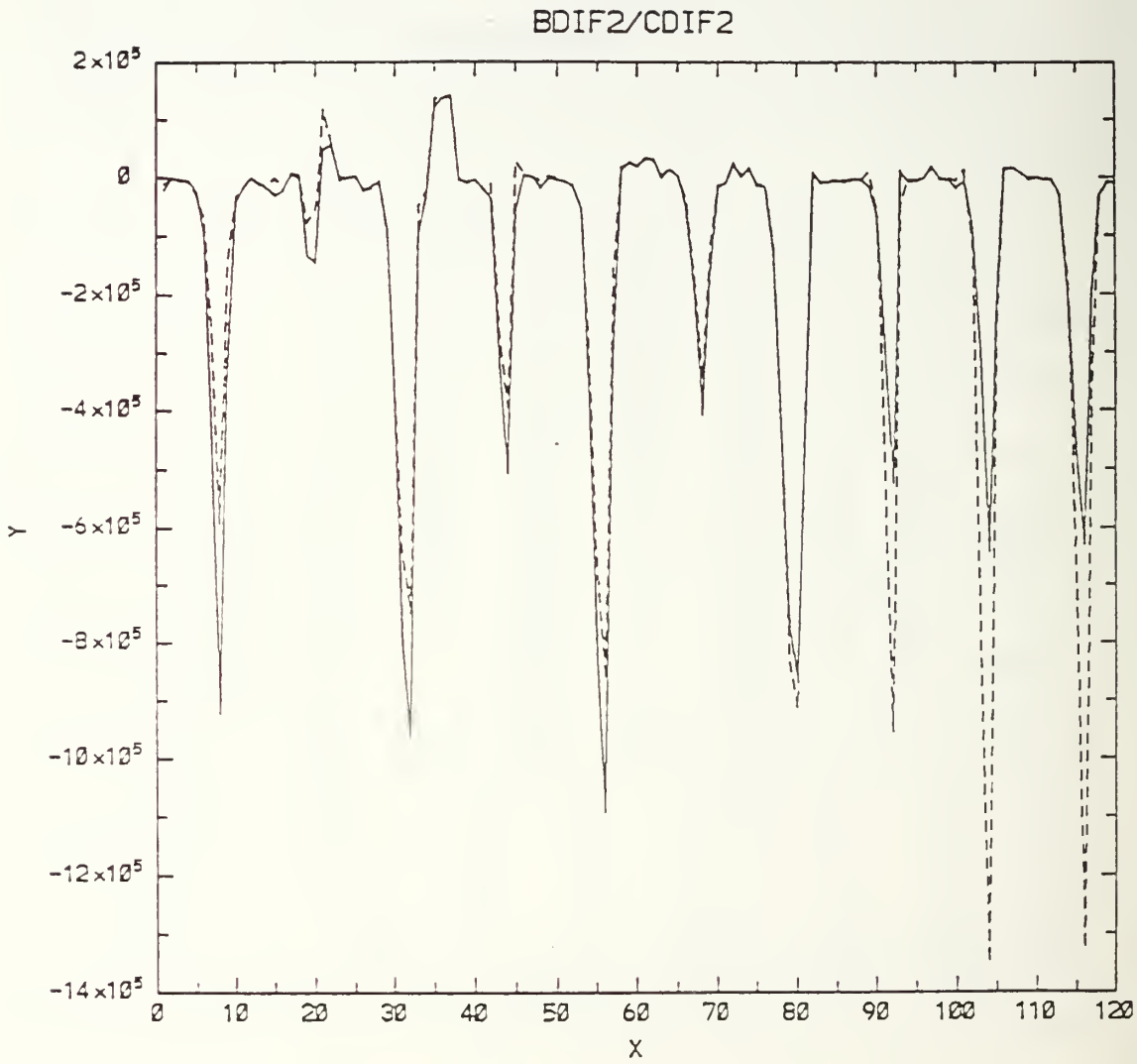

Figure 4.24 Time series of simulated minus observed total area in region 2. B-A is the solid line, C-A is the dashed line. X axis is months from Jan 1971 to Dec 1980. Y axis is 10's of km^2.

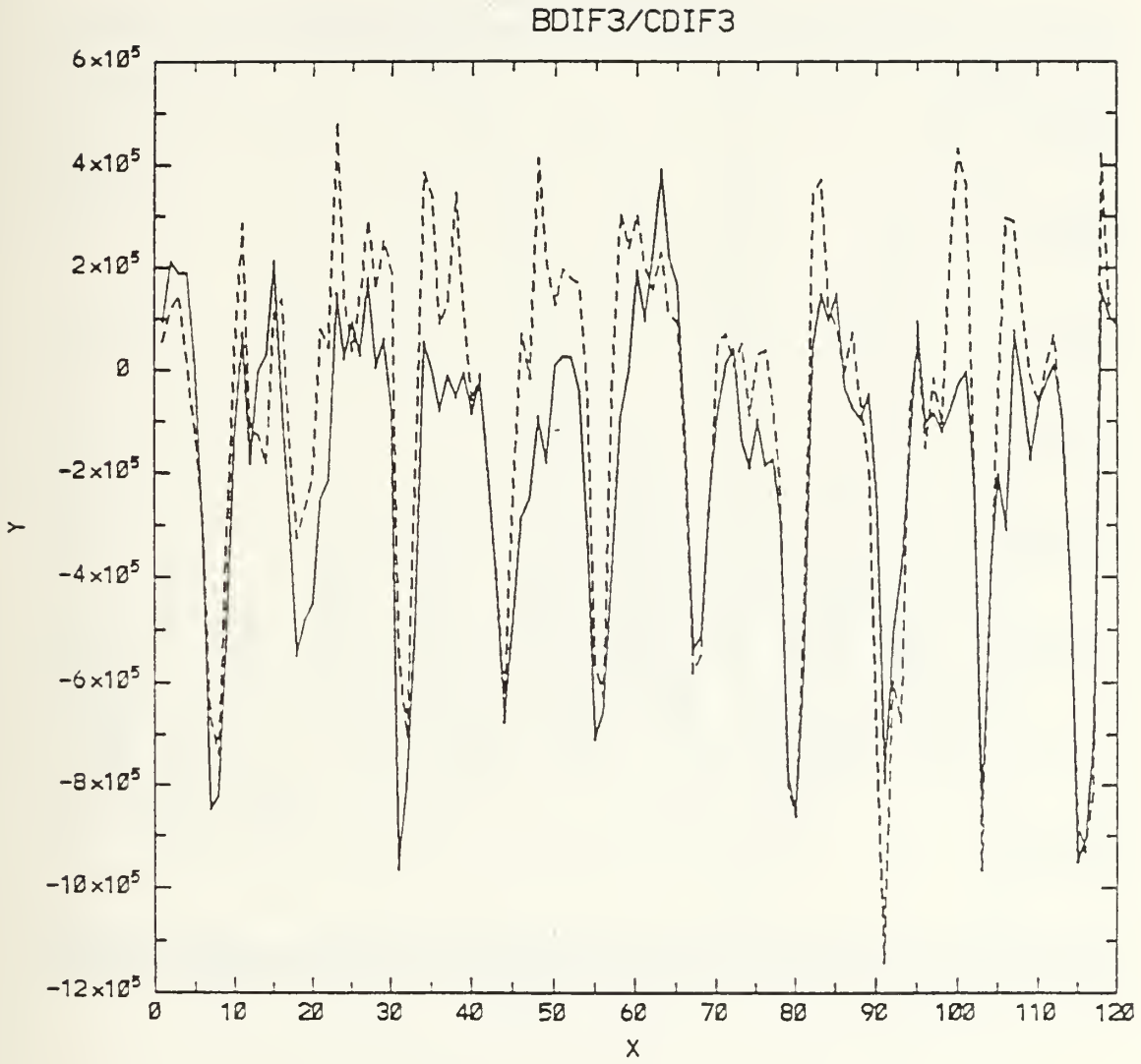

Figure 4.25 Time series of simulated minus observed total area in region 3. B-A is the solid line, C-A is the dashed line. X axis is months from Jan 1971 to Dec 1980. Y axis is 10's of km^2.

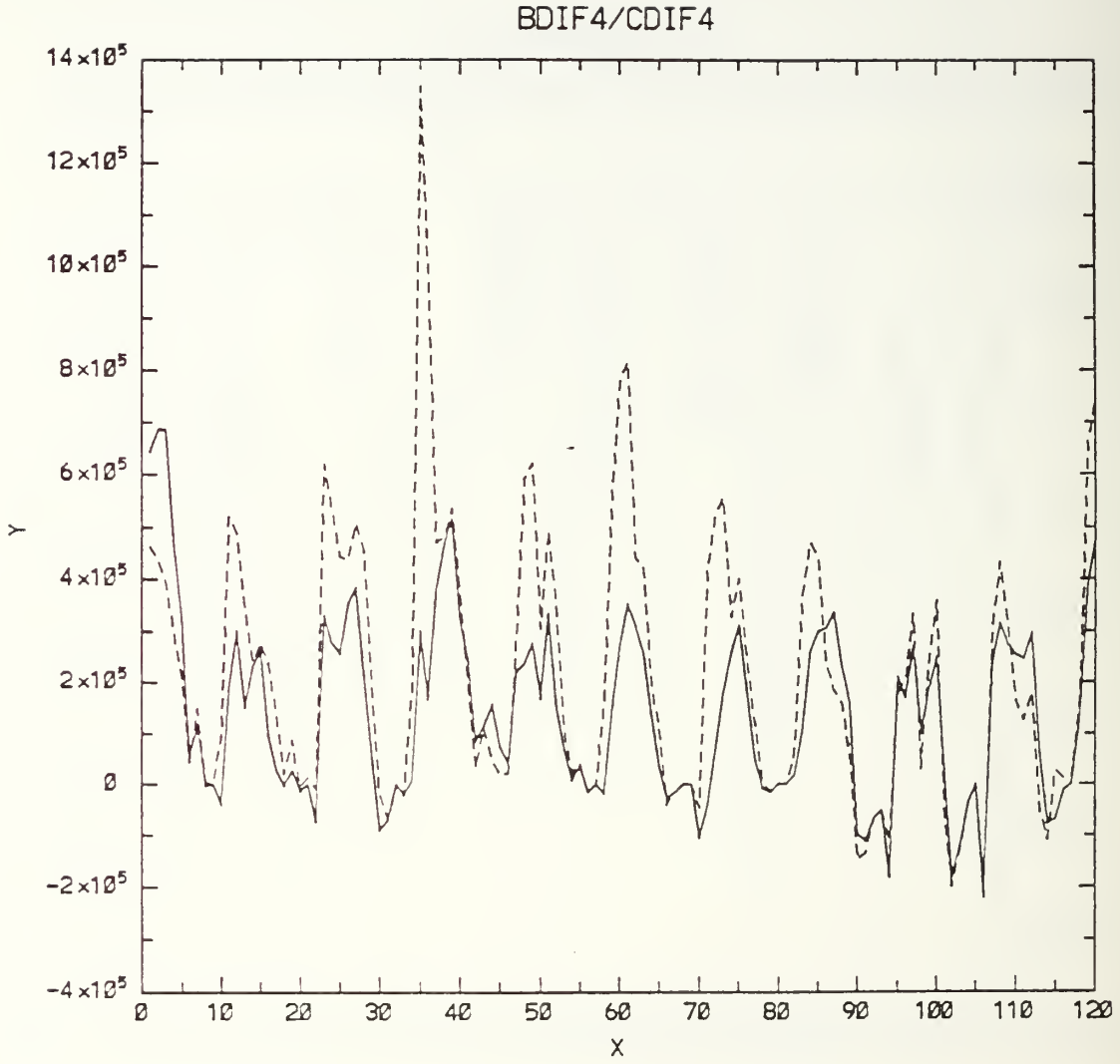

Figure 4.26 Time series of simulated minus observed total area in region 4. B-A is the solid line, C-A is the dashed line. X axis is months from Jan 1971 to Dec 1980. Y axis is 10's of km^2.

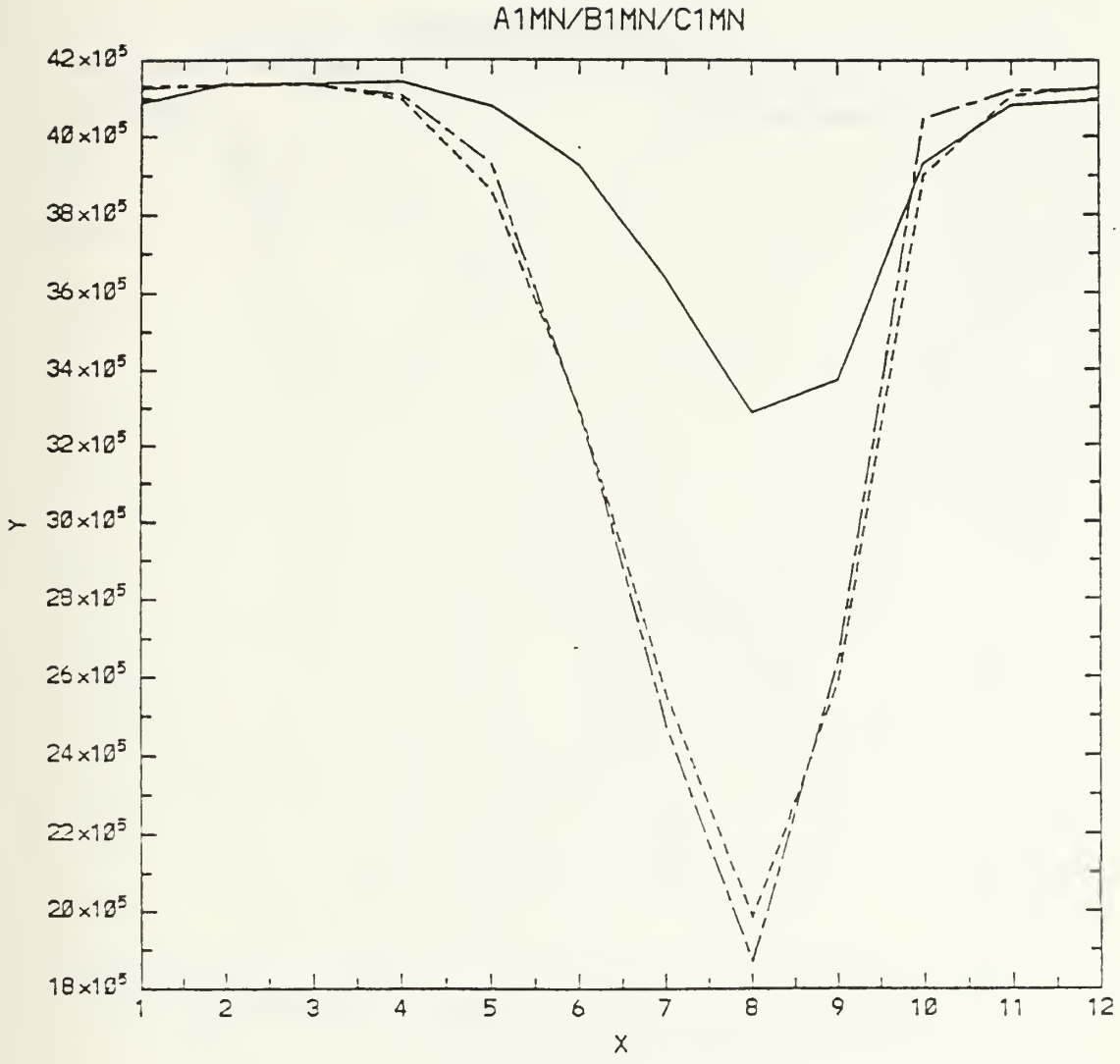

Figure 4.27 10-year mean annual cycle of total ice area in region 1. Observed (A) is the solid line, simulated (B) is the dashed line and simulated (C) is the dash-dot line. X axis is months and Y axis is 10's of km^2.

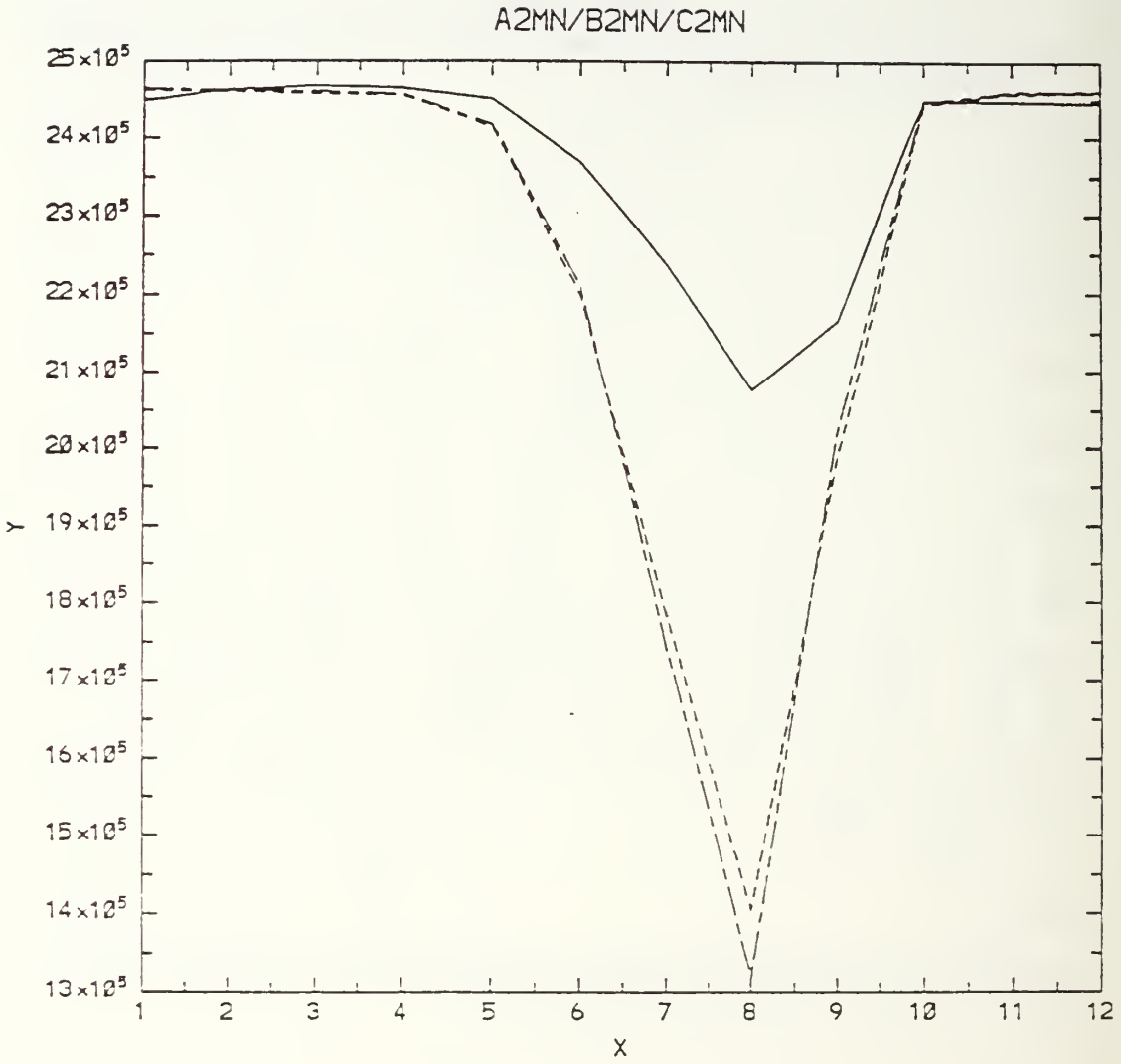

Figure 4.28 10-year mean annual cycle of total ice area in region 2. Observed (A) is the solid line, simulated (B) is the dashed line and simulated (C) is the dash-dot line. X axis is months and Y axis is 10's of km^2.

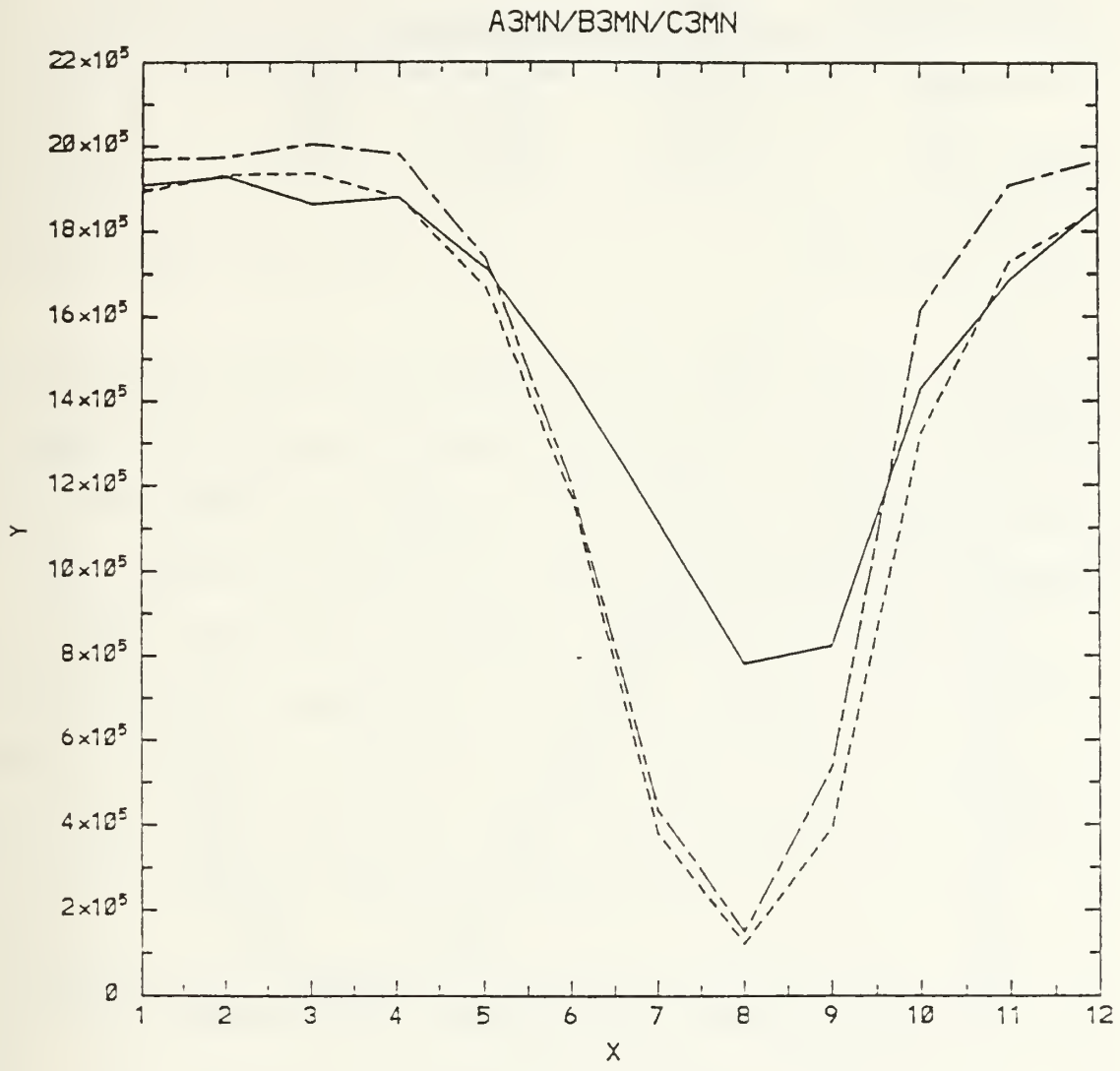

Figure 4.29 10-year mean annual cycle of total ice area in region 3. Observed (A) is the solid line, simulated (B) is the dashed line and simulated (C) is the dash-dot line. X axis is months and Y axis is 10's of km^2.

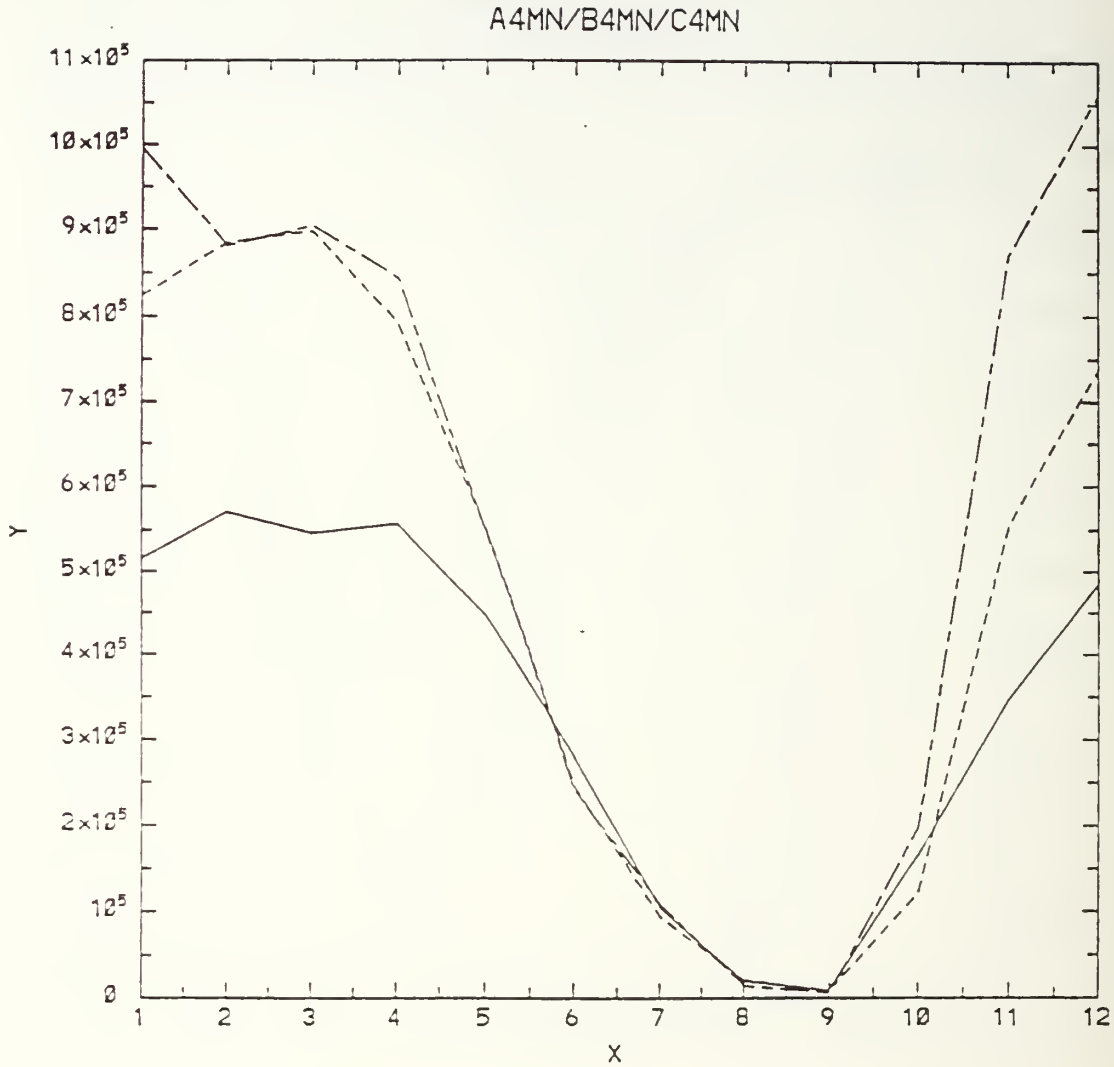

Figure 4.30 10-year mean annual cycle of total ice area in region 4. Observed (A) is the solid line, simulated (B) is the dashed line and simulated (C) is the dash-dot line. X axis is months and Y axis is 10's of km^2.

TABLE 3

DIFFERENCE BETWEEN THE ABSOLUTE SUM OF SIMULATED AND OBSERVED ICE AREA

REGION	B - A	C - A	CHANGE	% IMPROVEMENT
1	.4391	.4472	.0081	2%
2	.1645	.1729	.0084	5%
3	.2945	.3131	.0186	6%
4	.2043	.2935	.0892	43%

area in km^2 x 1 x 10^8

ice concentration for A,B and C in each region. The B and C anomaly time series are shown with the A anomaly time series for each region in Figures 4.31 - 4.38. The ability of the B and C anomaly series to follow the A series was a measure of their ability to model interannual variability. A quantitative appreciation of this ability was made in a similar manner as with the annual cycle. The A anomaly field was subtracted from both B and C and the absolute sum of each of the anomaly difference fields was then calculated. The results are shown in Table 4. Correlations were also calculated between the observed and modelled ice area fields for both the annual cycle and anomaly time series. The calculated correlation coefficients are shown in Table 5.

Several hundred contour plots and graphs were examined and compared including observed and simulated ice concentration and ice thickness, simulated ocean heat flux, simulated layer

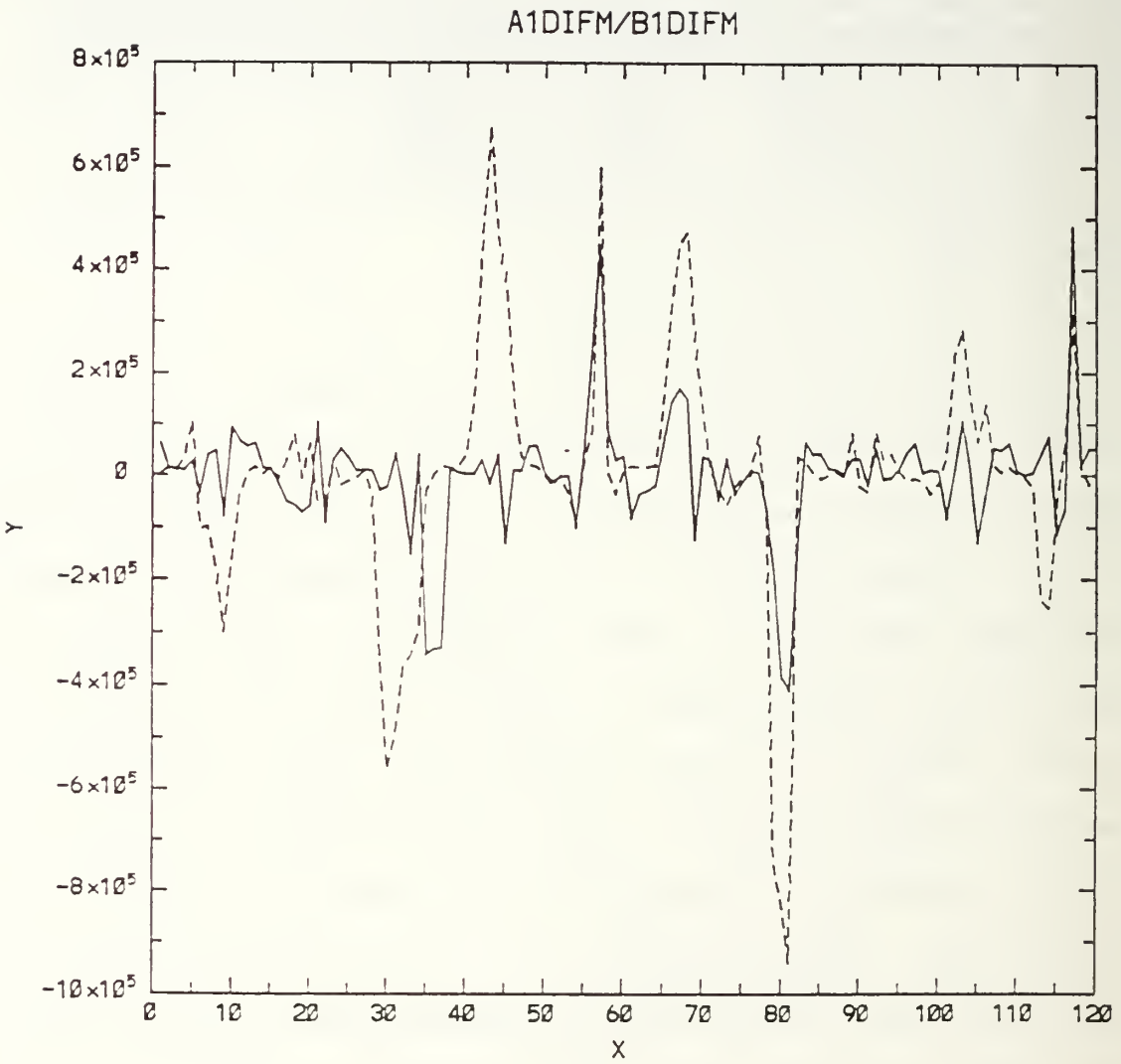

Figure 4.31 Difference from mean annual cycle or anomaly time series of total ice area for region 1. Observed anomaly is the solid line, simulated (B) anomaly is the dashed line. X axis is months, Y axis is 10's of km^2.

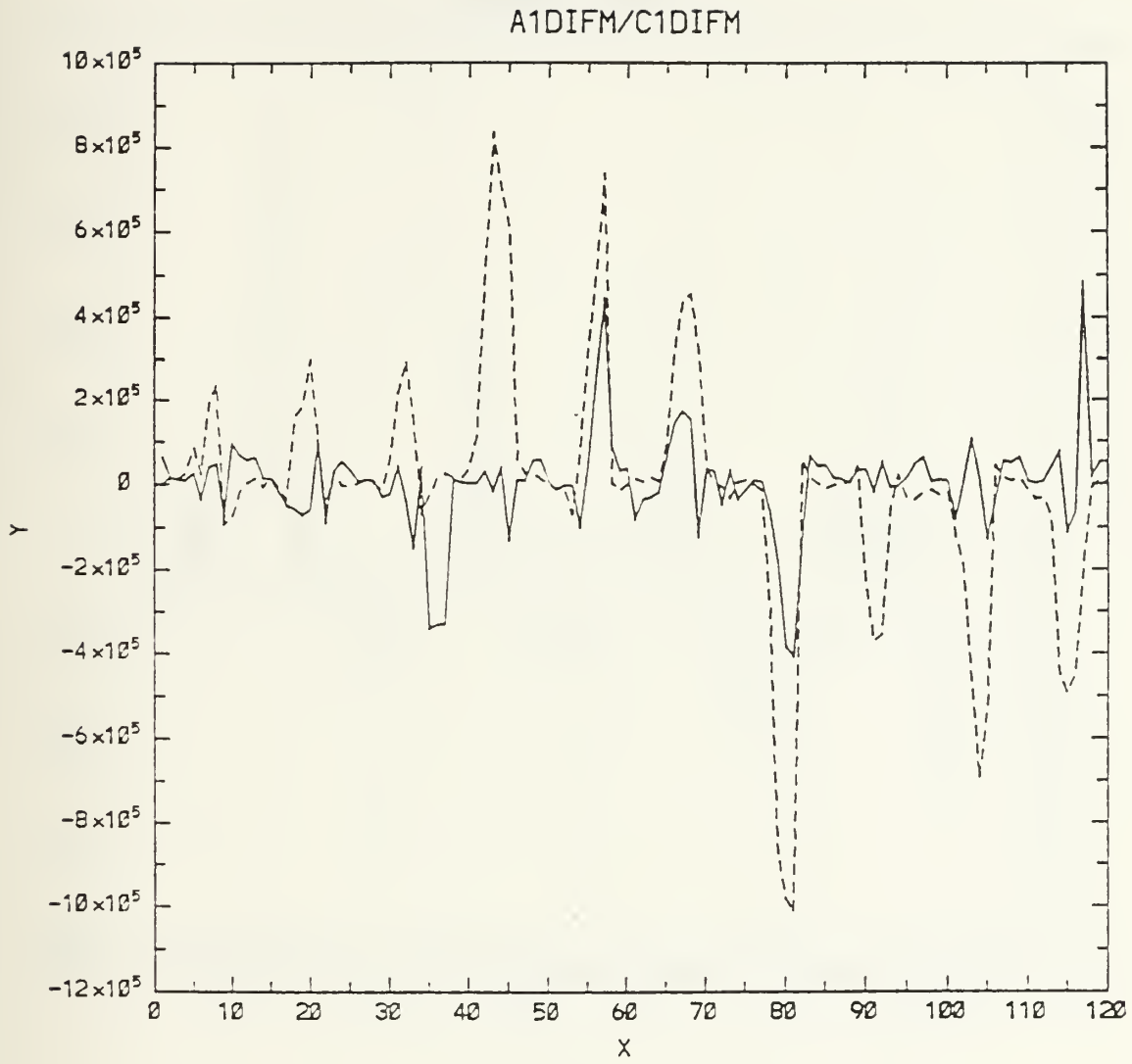

Figure 4.32 Difference from mean annual cycle or anomaly time series of total ice area for region 1. Observed anomaly is the solid line, simulated (C) anomaly is the dashed line. X axis is months, Y axis is 10's of km^2.

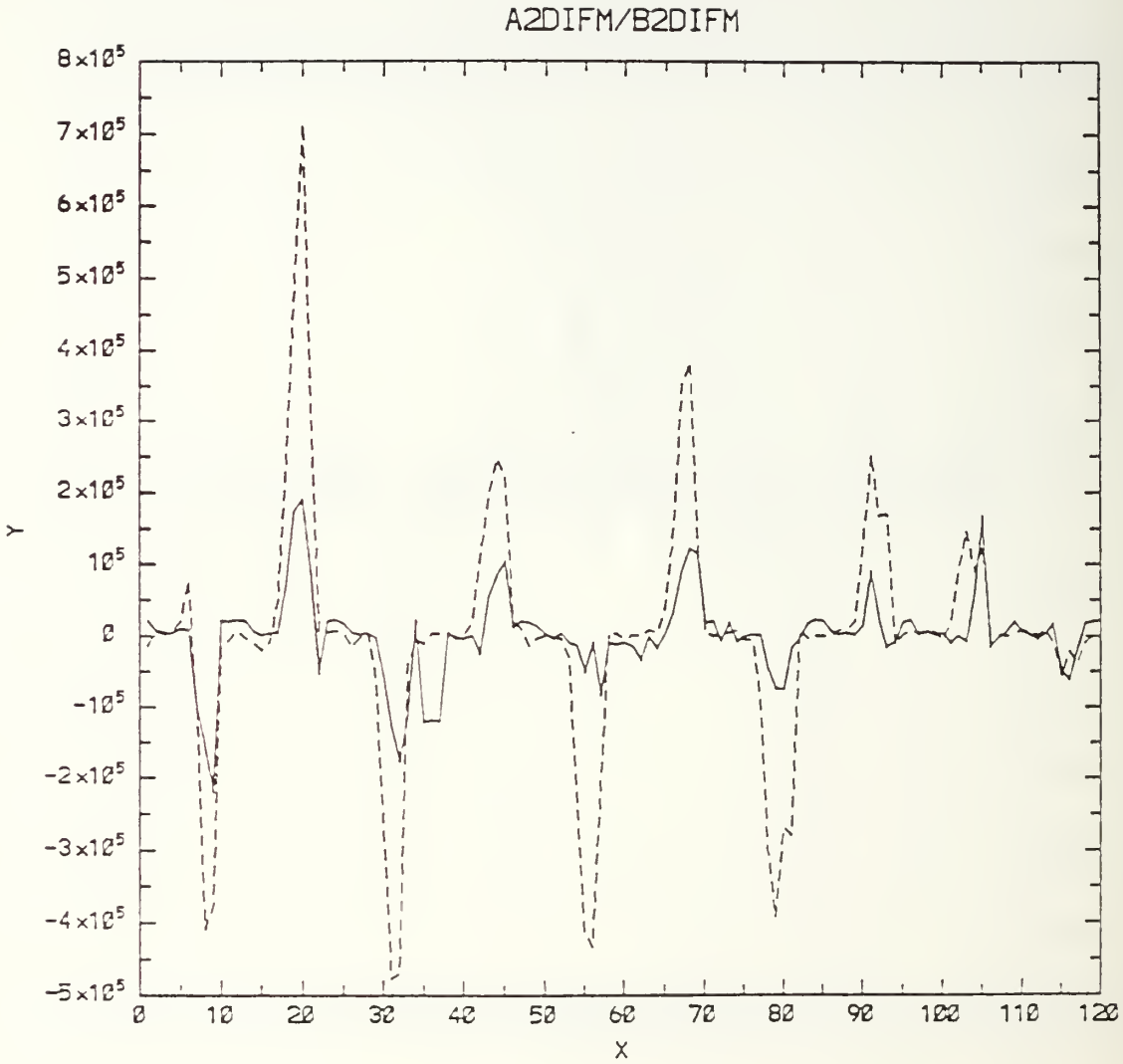

Figure 4.33 Difference from mean annual cycle or anomaly time series of total ice area for region 2. Observed anomaly is the solid line, simulated (B) anomaly is the dashed line. X axis is months, Y axis is 10's of km^2.

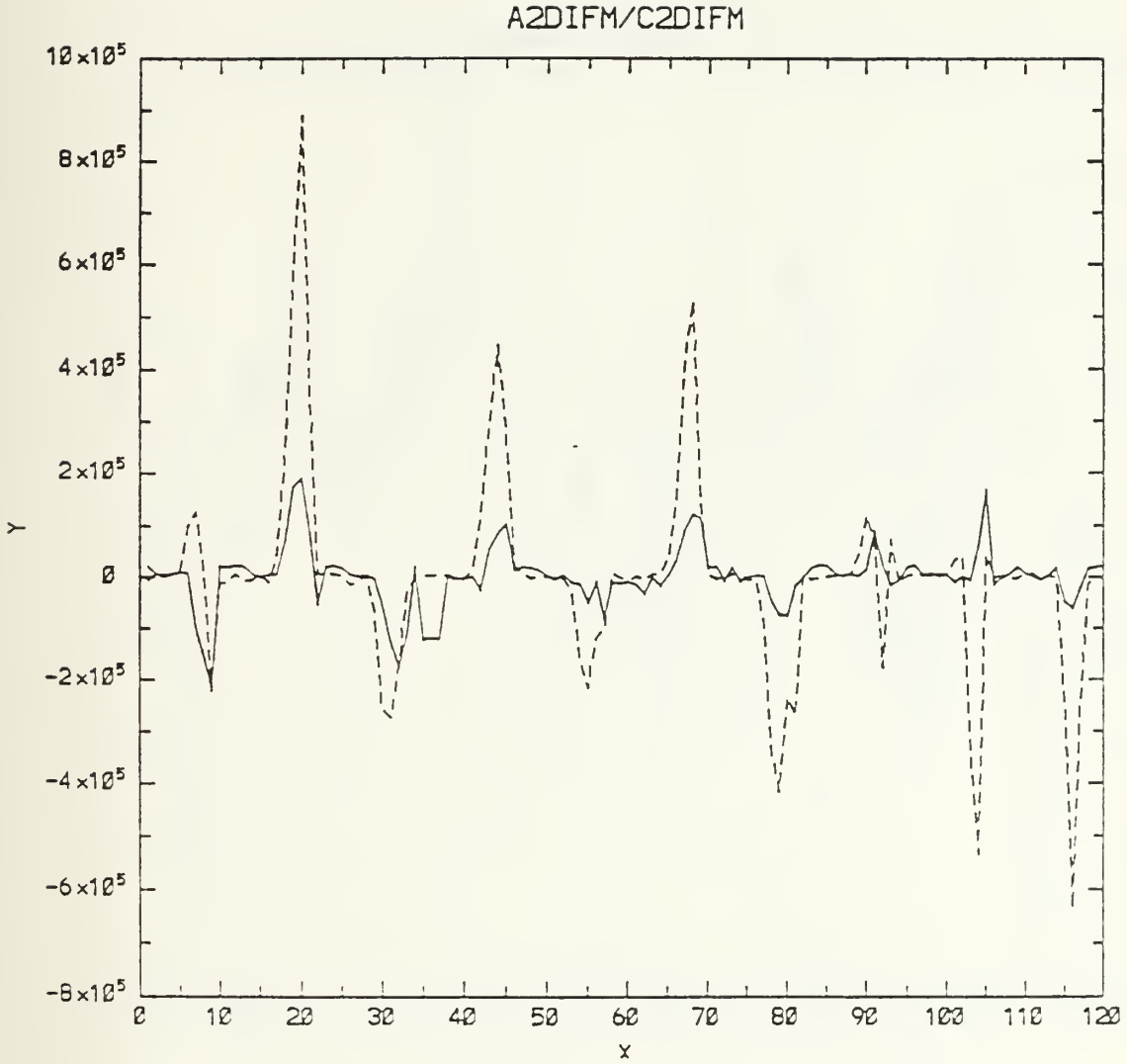

Figure 4.34 Difference from mean annual cycle or anomaly time series of total ice area for region 2. Observed anomaly is the solid line, simulated (C) anomaly is the dashed line. X axis is months, Y axis is 10's of km^2.

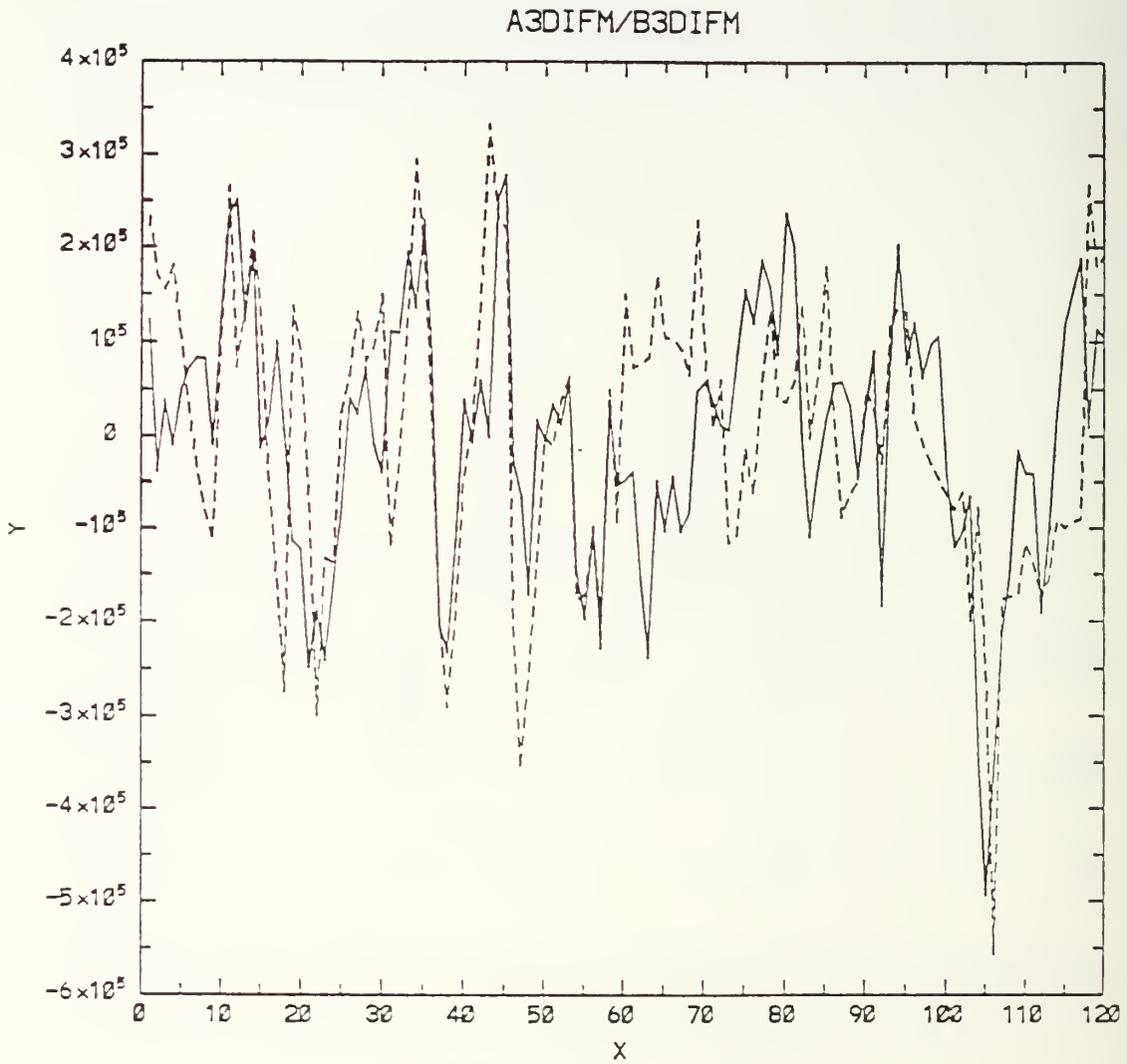

Figure 4.35 Difference from mean annual cycle or anomaly time series of total ice area for region 3. Observed anomaly is the solid line, simulated (B) anomaly is the dashed line. X axis is months, Y axis is 10's of km^2.

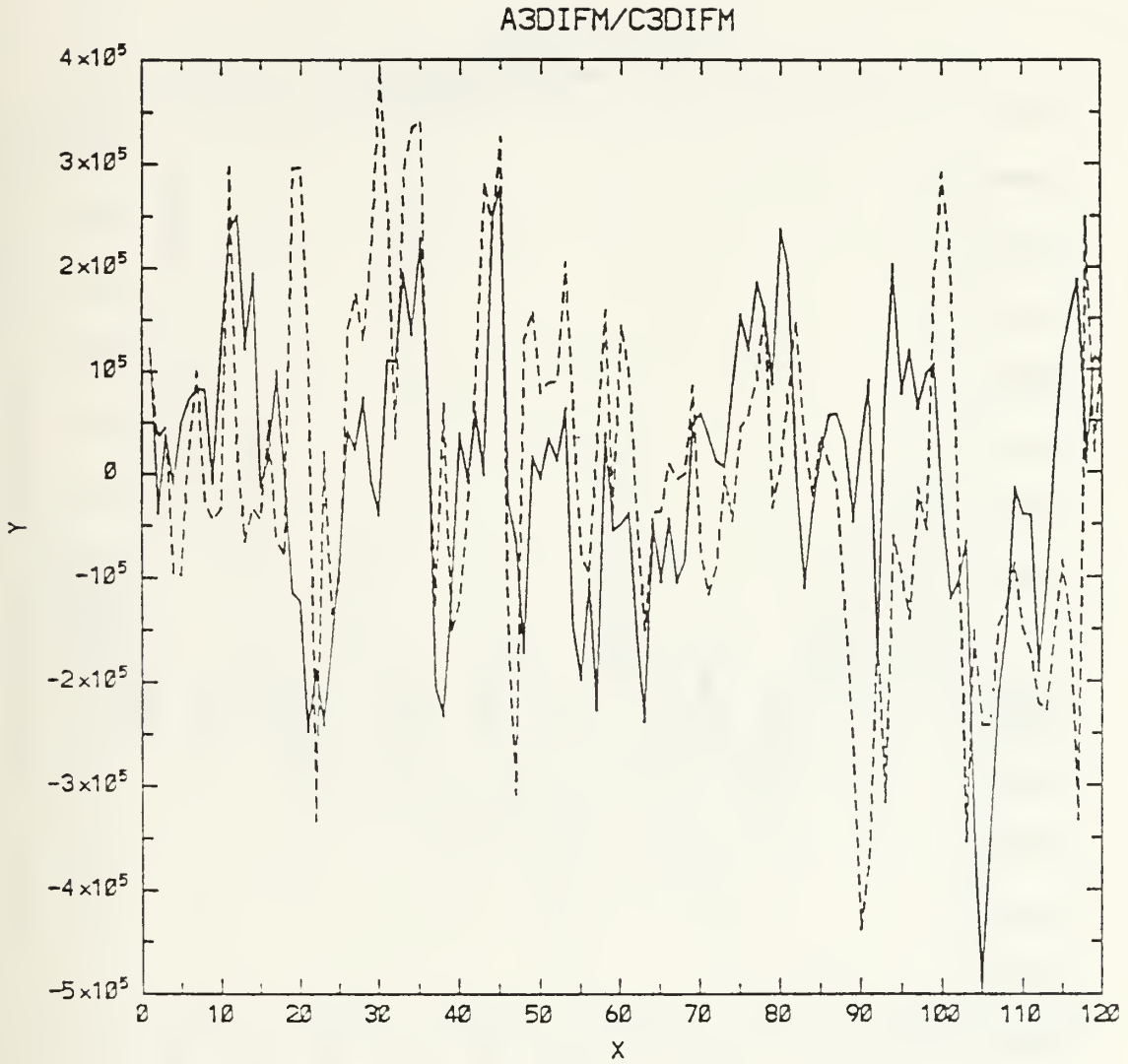

Figure 4.36 Difference from mean annual cycle or anomaly time series of total ice area for region 3. Observed anomaly is the solid line, simulated (C) anomaly is the dashed line. X axis is months, Y axis is 10's of km^2.

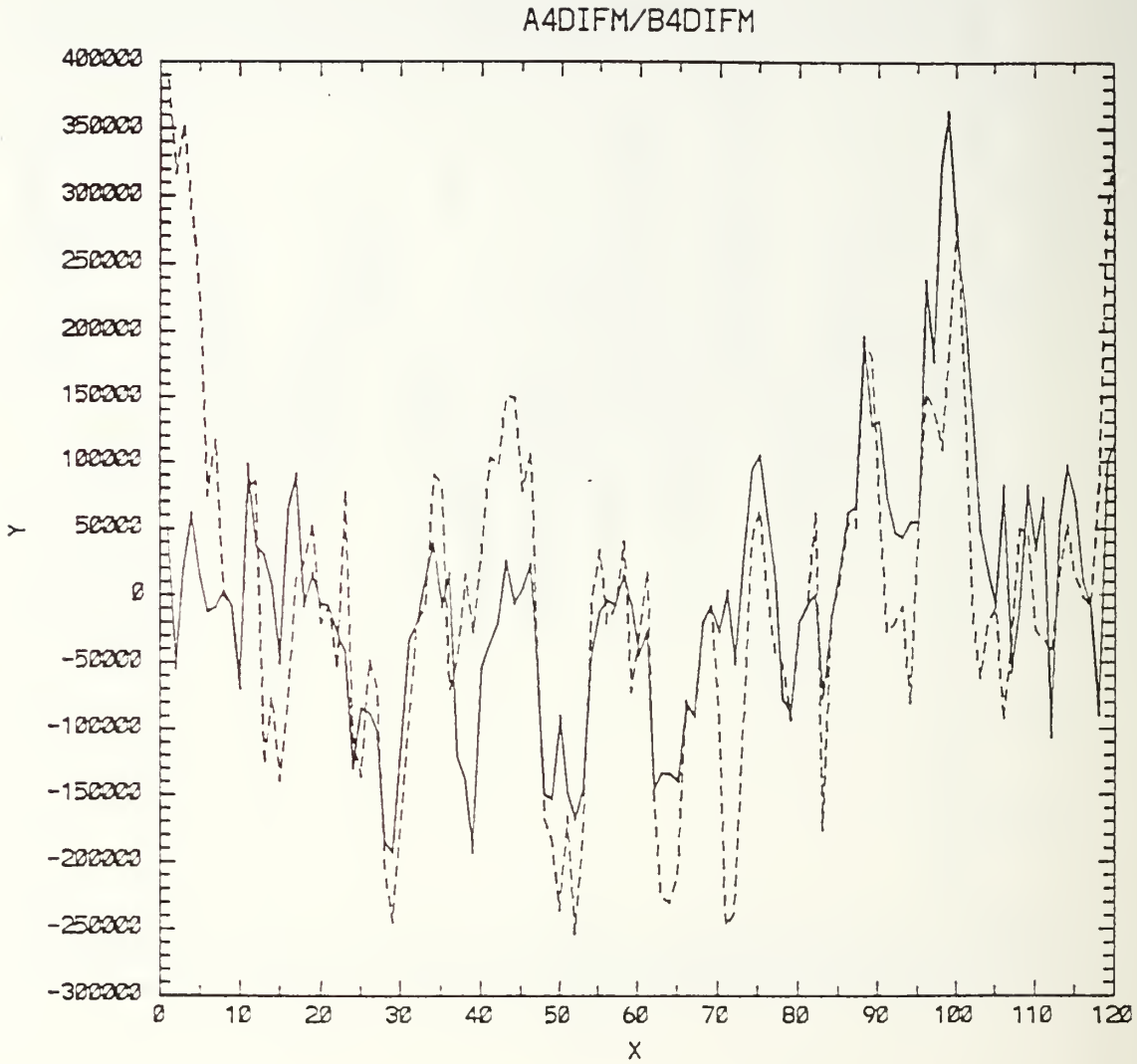

Figure 4.37 Difference from mean annual cycle or anomaly time series of total ice area for region 4. Observed anomaly is the solid line, simulated (B) anomaly is the dashed line. X axis is months, Y axis is 10's of km^2.

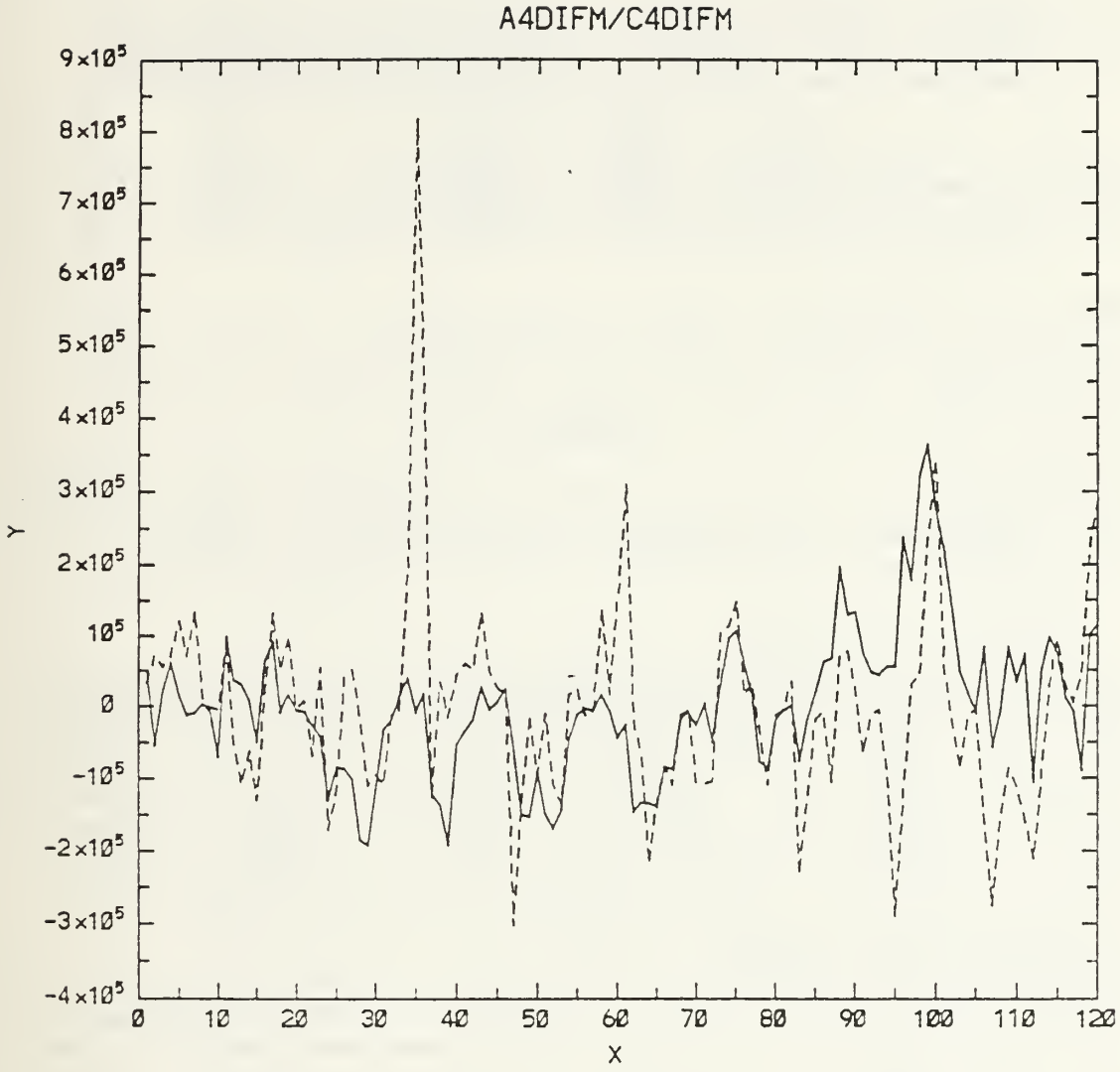

Figure 4.38 Difference from mean annual cycle or anomaly time series of total ice area for region 4. Observed anomaly is the solid line, simulated (C) anomaly is the dashed line. X axis is months, Y axis is 10's of km^2.

TABLE 4

DIFFERENCE BETWEEN ABSOLUTE SUM OF SIMULATED AND OBSERVED ICE AREA ANOMALY (MEAN ANNUAL CYCLE REMOVED)

REGION	B - A	C - A	CHANGE	% IMPROVEMENT
1	.1476	.1818	.0342	23%
2	.0864	.0985	.0121	14%
3	.1355	.1689	.0334	25%
4	.0888	.1157	.0268	30%

area in km^2 x 1 x 10^8

TABLE 5

CORRELATIONS OF ICE AREA BETWEEN SIMULATION B AND OBSERVED (CORR B) AND SIMULATION C AND OBSERVED (CORR C)

ICE AREA TIME SERIES

REG	STDEV OBS	STDEV B	STDEV C	CORR B	CORR C
1	.3169	.7776	.8246	.9126	.8852
2	.1434	.3729	.3996	.9271	.8807
3	.4283	.6755	.6910	.9461	.9106
4	.2292	.3667	.4220	.9186	.8332

ANOMALY TIME SERIES

REG	STDEV OBS	STDEV B	STDEV C	CORR B	CORR C
1	.1146	.2220	.2701	.4936	.3963
2	.0590	.1660	.1821	.7761	.5981
3	.1376	.1518	.1677	.5375	.3039
4	.0994	.1311	.1418	.6172	.3332

Standard deviation values x 1 x 10^6

B simulation was with fully interactive ocean model
C simulation was with 10-year mean cycle ocean

2 velocities and the time series' described above. On conclusion of this review, the following general observations were made:

- The region of transition from 10/10 to 0/10 ice concentration was narrower in both B and C than in A, i.e., the ice edge boundary was sharper, more well defined in B and C than in A.

- Both B and C overpredicted the ice coverage in winter, especially in the eastern Barents Sea (contained in region 4). B was usually closer to the observed coverage than C.

- Both B and C underpredicted the coverage in summer, especially in the Kara Sea to the east and the Beaufort, Chukchi and East Siberian Seas to the west. B was usually closer to the observed coverage than C in the eastern Arctic but the improvement in the central and western Arctic was minimal.

- The general shape of the ice edge was reasonably well simulated by both B and C. The Kara and Barents Seas were notable exceptions.

- The simulated surface (level 2) currents matched the observed annual mean currents (Figure 2.4) quite well. All the major currents were represented and their velocities appeared reasonable; however, some errors were evident in the secondary currents. The West Spitsbergen Current was not represented and the Irminger Current was flowing opposite to the observed mean direction. There were significant differences between the monthly varying fields and the 10-year average cycle fields of level 2 ocean velocities. The fields contained the same current features however these features differed in both strength and position.

- The ocean heat flux into the mixed layer was highly variable between regions and changed dramatically with the seasons. Winter values were highest in the Norwegian and Greenland Seas where it averaged approximately 180 W/m^2. Exceptional cases of heat flux in excess of 375 W/m^2 were observed occasionally in a localized area just south of Svalbard. Spring and summer heat fluxes in the Norwegian and Greenland Seas were generally weakly positive or negative. Isolated summer heat flux values less than -180 W/m^2 were observed just north of Iceland in some years. A similar positive to negative ocean heat flux cycle was observed in the western arctic although it

was generally confined to within 400 km of the Alaskan shoreline. The simulated ocean heat flux under the central pack in the Canadian and Eurasian Basins was negligible throughout the year. Similar to the velocities, there were significant differences between the monthly varying fields and the 10-year average cycle fields in both the strength and position of the main features.

- The simulated pack ice thicknesses in the central Arctic Basin were 1-2 m or 50-100% less than the average observed values, particularly in summer. B thicknesses tended to be larger than those for C. The simulated thickness data indicated that some ridging was occurring in the models poleward of Greenland and Ellesmere Island as expected, however the thickness values in this region were too low by a factor of three or more. The observed thickness fields used for comparison are shown in Figures 4.39 - 4.42.

- Region 1 and 2 had maximum ice areas limited by their boundaries. Region 4's minimum ice area was limited by zero (it becomes totally ice free). Region 3 came close to being ice free especially from 1978-1980. These minimum and maximum limits reduced the variability of the total ice area; however considerable yearly variability was still evident. Annual differences in ice areas in the observed data varied from approximately 15% of the mean in region 1 and 2, to 40% in region 3, to 100% in region 4. The simulated data had greater variance with interannual ice area differences ranging from approximately 40% of the mean in regions 1 and 3, to 60% in region 2, to 100% in region 4.

- The mean annual cycles of ice area for A,B and C showed that the melt/freeze cycle in the modelled cases was approximately in phase with the observed annual cycle but of higher amplitude. C generally displayed the largest amplitude.

- The time series' of ice area anomalies (difference from annual cycle) for both observed and simulated data varied significantly from region to region. Some similarities could be found in adjacent regions. However, if they were not adjacent, the correlations appeared to be very low.

- The degree of monthly variability or "noisiness" in the anomaly series increased markedly in regions 3 and 4 compared to regions 1 and 2.

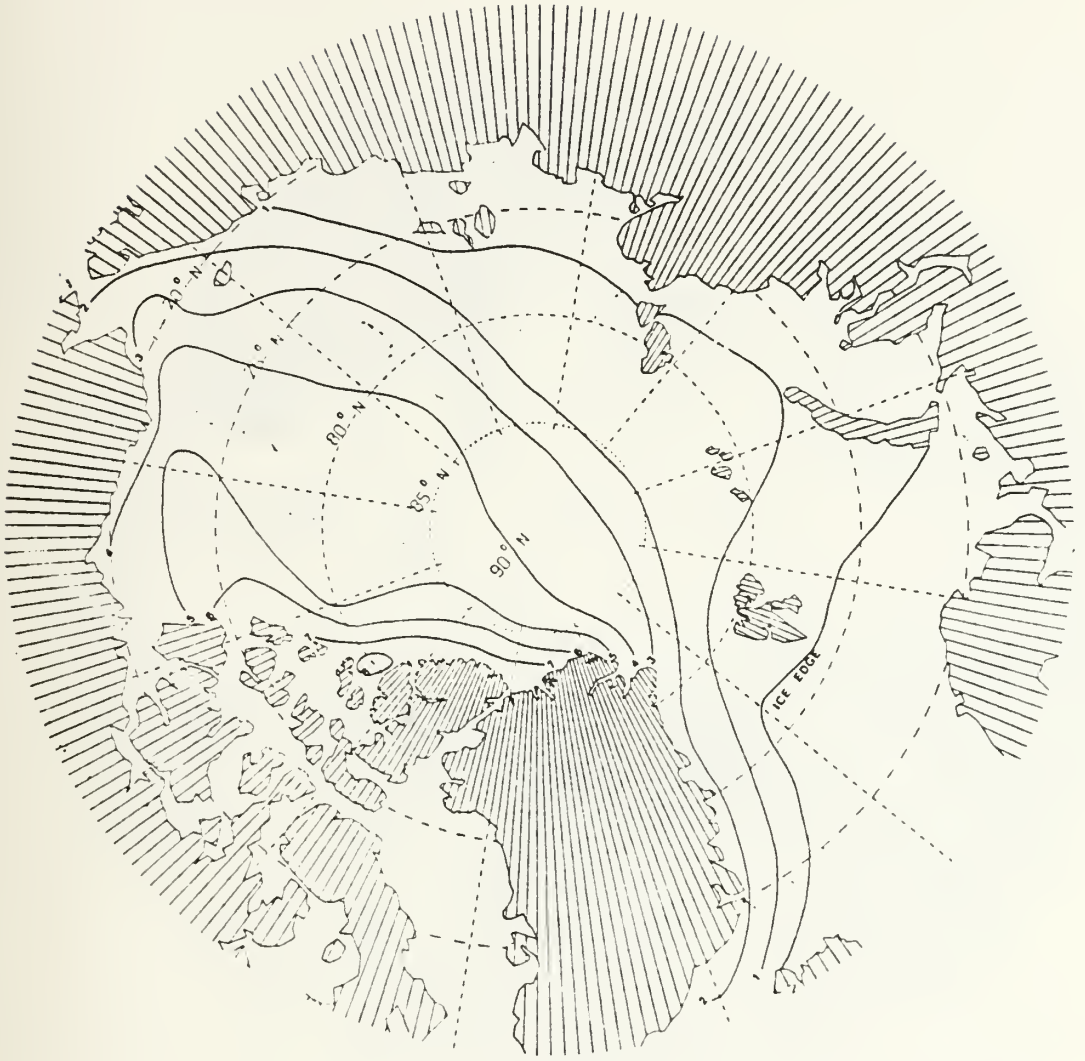

Figure 4.39 Mean ice draft (m) in winter derived from submarine upward looking echo sounder data. Draft is averaged over three months, centered on the first of March (from Bourke and Garret, 1987).

Figure 4.40 Mean ice draft (m) in spring derived from submarine upward looking echo sounder data. Draft is averaged over three months, centered on the first of June (from Bourke and Garret, 1987).

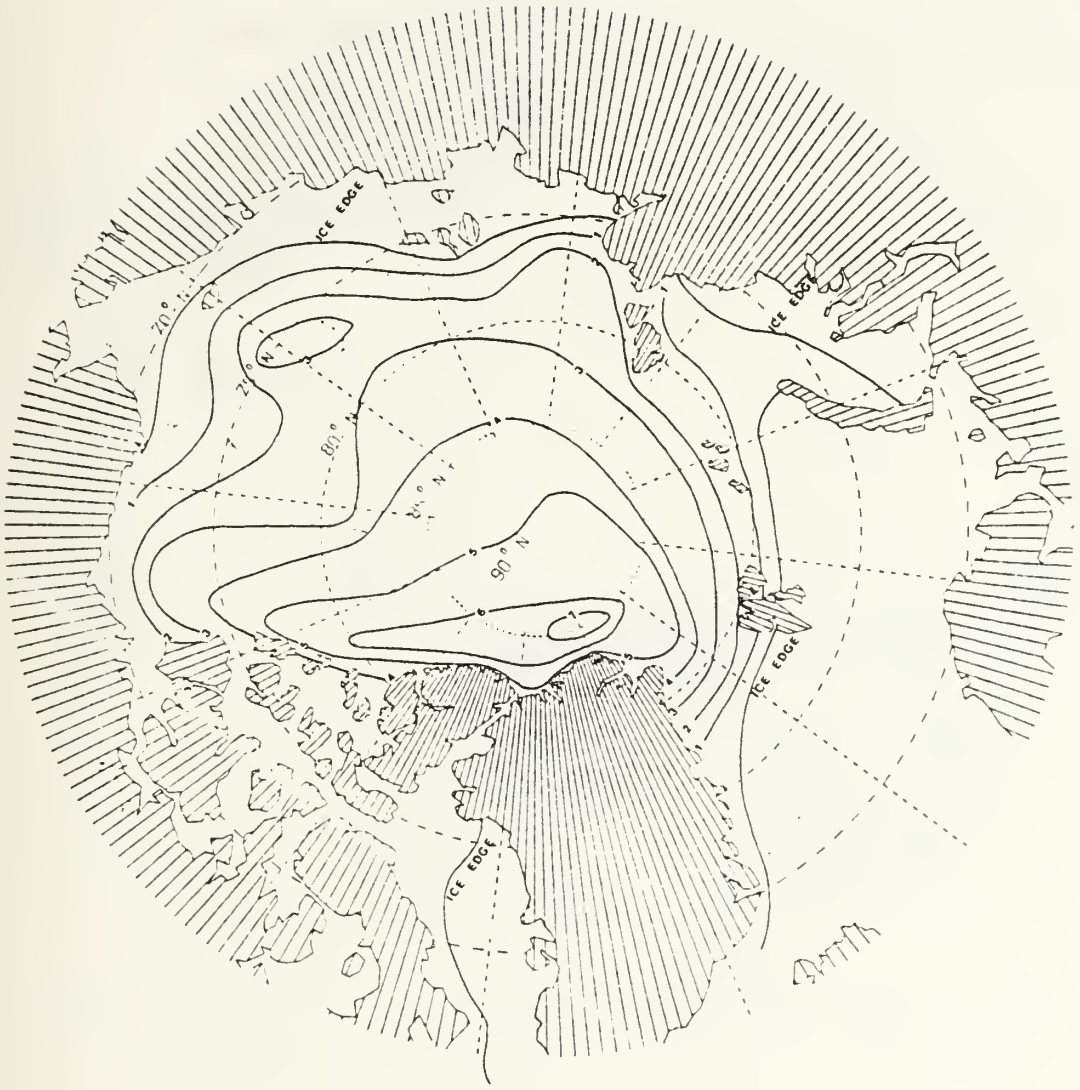

Figure 4.41 Mean ice draft (m) in summer derived from submarine upward looking echo sounder data. Draft is averaged over three months, centered on the first of September (from Bourke and Garret, 1987).

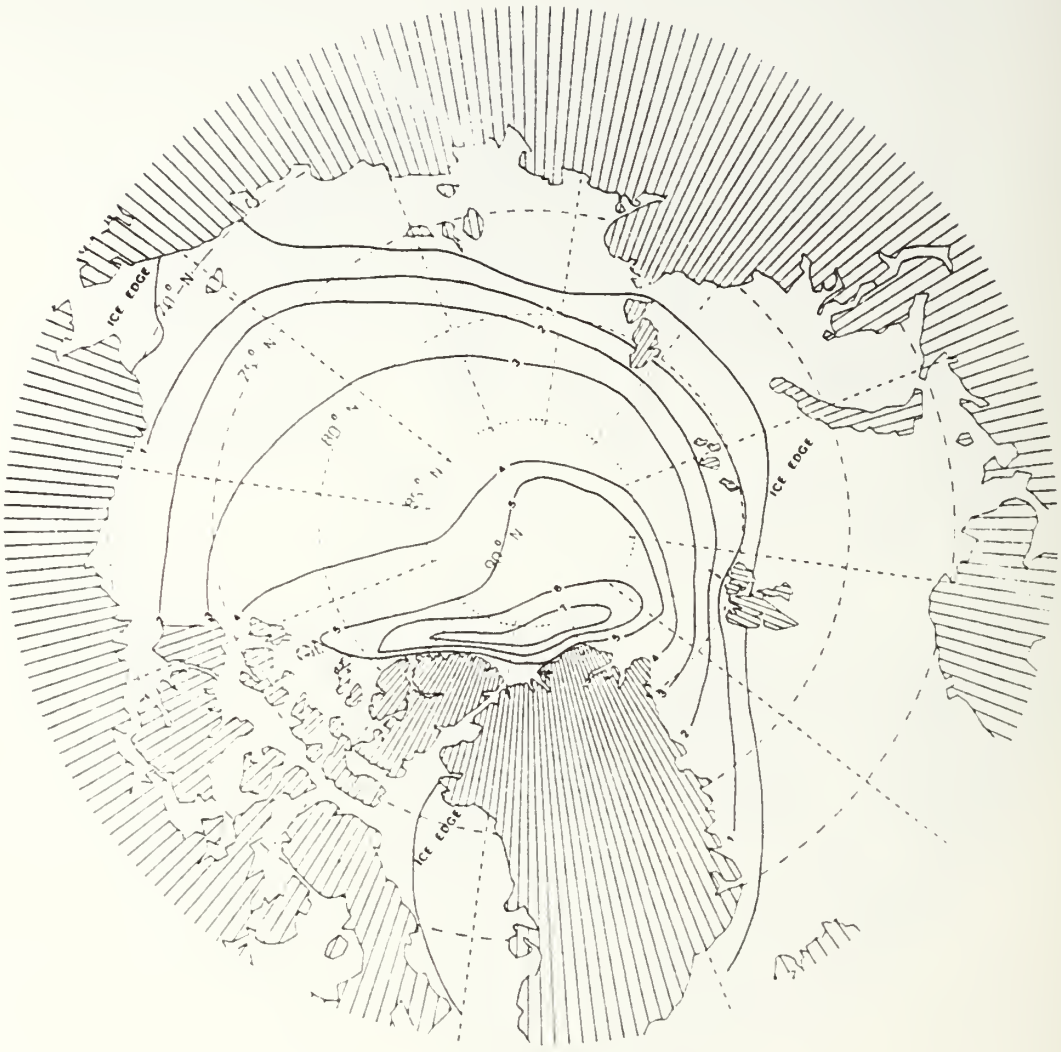

Figure 4.42 Mean ice draft (m) in fall derived from submarine upward looking echo sounder data. Draft is averaged over three months, centered on the first of December (from Bourke and Garret, 1987).

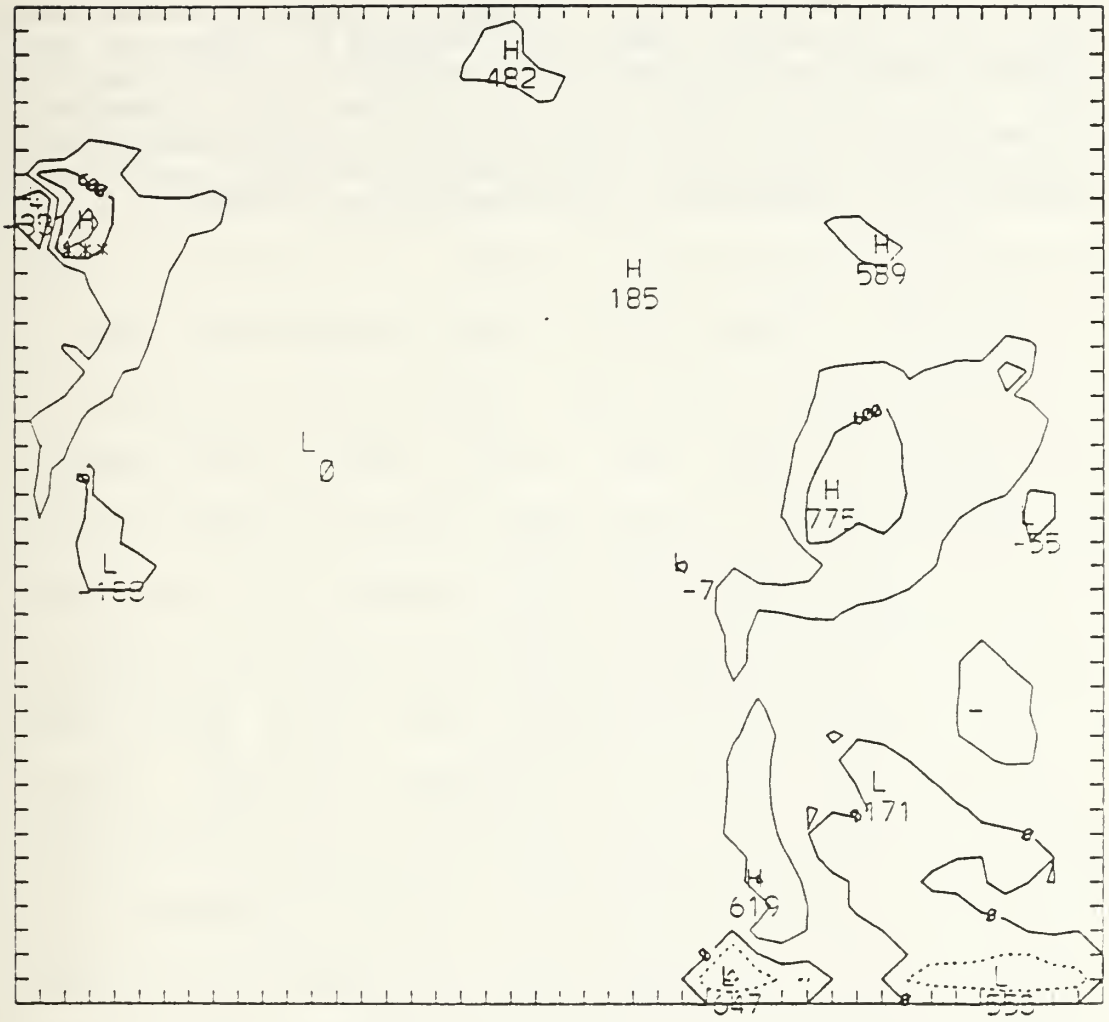

Figure 4.43 10-year mean ocean heat flux through the 30 m mixed layer for July. Units are degrees C/sec/cm^2 scaled by 1 x 10^9. Conversion factor to W/m^2 is .125 x 10^9. L and H indicate relative lows and highs respectively.

- The B anomaly time series was a better match to the observed (A) anomaly time series than C. There were time periods when both B and C were significantly different from A but with the same sign. There are also times when they both differed from the A anomalies but with opposite signs. No clear pattern was evident of a bias to either sign.

- Considering the entire 120 month time period, model runs using the interactive ocean (B) matched the observed data better than the average ocean case (C) in all regions. This was true for both total ice area and interannual variability. Both the absolute sums of total differential area and the correlation coefficients for each region were better for B than for C, particularly in region 4.

C. DISCUSSION

The excessive melting which occured in regions 1 and 2 was a common feature of both the prescribed ocean model and the prognostic ocean model. This suggests that an error or weakness common to both model formulations may be responsible. One possible weakness is the quite simple representation of the mixing processes within the surface layer and the rather large vertical resolution of the upper 500 m. Contours of ocean heat flux (e.g., Figure 4.43) show large positive values in summer when the melting rate is highest. The large amount of melting in this season would be expected to produce a surface cap of fresh water. The resultant stratification would insulate the mixed layer from the heat below and reduce this flux. It appears that this mechanism is not being represented properly as excessive heat continues to enter the mixed layer until late summer. Alternatively, the large lateral diffusion coefficients which are necessary for numerical stability may be mixing far too much heat throughout the intermediate layer. In this case, even if the vertical advection is reduced by stratification, there may still be enough heat available to cause the excessive summer ice retreat.

A second possibility becomes evident after sequentially viewing the ocean heat flux contours over several months. A close examination of those areas which appear most in error indicates several "hot" spots in winter and spring which

correspond to some of the locations of prescribed inflow. These same "hot" spots become "cold" spots during summer and fall. The constant prescribed inflow temperatures at the Bering Strait and Faeroe-Shetland Channel contrast with the simulated ocean temperatures produced by the model. The simulated temperatures vary monthly following the annual cycle of SST resulting in a cycle of anomalous temperatures at the inflow positions. Although the temperature of the river inflow is set to match the ocean temperature, similar "hot" spots occur at the river mouths too, particularly for the Mackenzie, Kolyma and Lena Rivers. The most probable causes for this appear to be geostrophic adjustment to the negative salt fluxes and/or bottom topography interaction. The heat from these hot spots is advected by the currents, spreading their effect and increasing the spring melting over a considerable area. The western boundary areas appear to be a good example of this.

The simulated winter ice cover, although not an exact match to the observed, is still a closer match than the summer condition. This would seem reasonable because the large freezing rates and surface cooling in the winter induce deep vertical mixing. This process can be better represented by the simple density mixing scheme used in this model than the shallow stratification process which occurs in summer. Realistic amounts of heat are brought to the surface and the simulated ice edge matches the observed quite well. The

improvement provided by the prognostic ocean in regions 3 and 4 is consistent because, if we consider that the winter vertical convection is reasonably well accounted for, an improvement in the interannually varying currents and ocean heat flux should have a direct improvement on the ice cover simulation.

D. CONCLUSIONS

Inclusion of the interactive ocean produced an improved accuracy of simulation of the annual cycle of total ice area, particularly in region 4. The model which included the interactive, prognostic ocean represented the variable ocean forcing (heat and momentum) much better than the average ocean model. This suggests that variable ocean forcing is important to the evolution of the ice cover in the eastern Arctic. By contrast, in regions 1 and 2, the interactive model did not improve the representation of the total ice area significantly. In these regions, it may be the atmospheric forcing, the ice rheology or as discussed above, mechanisms controlling mixing of heat in the upper ocean layers, that dominate the evolution of total ice area. These are parameters which were not changed between experiments. Alternatively, there could be errors in the ocean forcing which produces a bias in the ice field in both the variable ocean and the average ocean.

Inclusion of the interactive model produced significant improvements in simulating the interannually varying ice field in all regions of the Arctic. This indicates that the interannual changes in the ocean forcing are a major influence on the interannual variability of the ice field over the entire Arctic basin. The importance of including an interactive ocean in seasonal ice prediction models is therefore demonstrated.

Simulated ice thickness has not been improved substantially based on the data presented by Bourke and Garret (1987). Again, as for total ice area in the western Arctic, modifications to the way atmospheric forcing is handled (e.g., albedo, surface drag) or to the ice rheology may be required to improve this feature of the ice cover.

V. ICE STRENGTH EXPERIMENT

One of the most obvious inaccuracies in the simulated ice cover produced by the linked model was the ice thickness as discussed in Chapter IV. In the polar pack region, simulated thicknesses were approximately one half the observed values. Thicknesses in the ice convergence regions north of Greenland and the Canadian archipelago were too small by a factor of three or more.

Heavy ice buildup in the convergence regions is the result of the large amount of ridging and rafting which occurs there. The poor representation of this feature indicated that the ice rheology used was not portraying these mechanisms properly. Hibler (1979, 1980) was able to simulate reasonable ice thicknesses in the strong convergence areas along the north coast of Ellesmere Island, but noted that the simulated ice buildup in this region and overall spatial ice thickness variations were dependent on the ice strength value used. In the follow-on work by Hibler and Bryan (1987), a greater ice strength was used to provide more accurate ice velocities at the larger grid scale. However, the ice thickness in the convergence regions was considerably reduced, appearing quite similar to the initial results found in this work.

Examination of the ice strength value used in the model here indicated that the ice strength parameter, P^*, was

relatively large. This made the ice pack quite stiff, reducing the amount of ridging in areas of ice convergence. The ice rheology used in this model was the same as in the Semtner (1987) model. However, it should be noted that the strength parameter actually used by Semtner (1987) differed from the description contained in the Appendix to that reference. The P^* actually used was:

$$P^* = h \times 3 \times 10^5 \ (N/m^2)$$

where h is the ice thickness. This was 30 times larger than the value noted in the appendix. Semtner indicated (private communication) that this larger value was required to prevent the numerical instability which had occurred in earlier runs using a smaller P^* value.

This experiment investigated the effects of reducing P^*. The objective was to determine the best value for producing an accurate simulation of the ice thickness and thickness distribution.

A. EXPERIMENTAL SETUP

The fully prognostic ice-ocean model (B) was used for this experiment. Initial runs with varying P^* values indicated that changes to the simulated ice fields were dramatic. Indeed, changes were evident after only a single month of integration. Therefore, single year integrations were considered sufficient for the sensitivity study vice a ten

year integration period. The year 1974 was selected for the runs as it was a fairly average ice cover year.

Seven runs were conducted. P^* values were set as follows:

- $P^* = h \times 3 \times 10^5$
- $P^* = h \times 1 \times 10^5$
- $P^* = h \times 5 \times 10^4$
- $P^* = h \times 3 \times 10^4$
- $P^* = h \times 1 \times 10^4$
- $P^* = h \times 5 \times 10^3$
- $P^* = h \times 1 \times 10^3$

Once an optimum P^* was determined, the full ten year integration was conducted to produce ice concentration fields for comparison with the observed data.

B. RESULTS

Numerical instability occurred in this model at the reduced P^* values similar to Semtner's work (private communication). The instability originated at a grid point in the EGC, adjacent to where the grid representation of the Greenland coastline was very jagged. The jagged coastline was a result of the model's limited resolution. Ocean current velocities grew exponentially, producing artificially high ice velocities and excessive kinetic energy. The temperature and salinity values also became unreasonable. Reduction of the model's numerical time steps by a factor of two did not solve the problem. Numerical stability was eventually obtained by

imposing velocity, temperature and salinity limits. The limitations on these prognostic variables were as follows:

$$-75.0 < UICE,VICE < +75.0 \quad (cm/sec)$$

$$-2.0 < TSURF < 15.0 \quad (deg\ centigrade)$$

$$0 < SALINITY < 50 \quad (ppt).$$

Figures 5.1 - 5.6 show the simulated ice thickness contours for August 1974, using the P^* values from runs 2 through 7, respectively. In general, as P^* was reduced, the entire ice pack tended to shift toward the Fram Strait and thicknesses within the pack increased. The convergence along the north coast of Greenland became more intense eventually producing a reasonable simulation of the ridging and rafting processes. However the simulated region of maximum thicknesses was still thinner and was located further poleward than the average thickness fields in Bourke and Garrett (1987) (See Figures 4.39 - 4.42). The tendency for the model to produce too much meltback of the ice edge in summer was exacerbated, even with the increased ice thicknesses. This was especially evident in the Bering and East Siberian Seas.

The thickness gradients became increasingly stronger, irregular and spotty as the ice strength was set to the lower values. The two lowest P^* values produced thickness contours which appeared too "noisy" to be realistic.

A qualitative assessment of all the thickness contour plots and comparison with the Bourke and Garrett (1987) data indicated that $P^* = h \times 1 \times 10^4$ provided the most reasonable

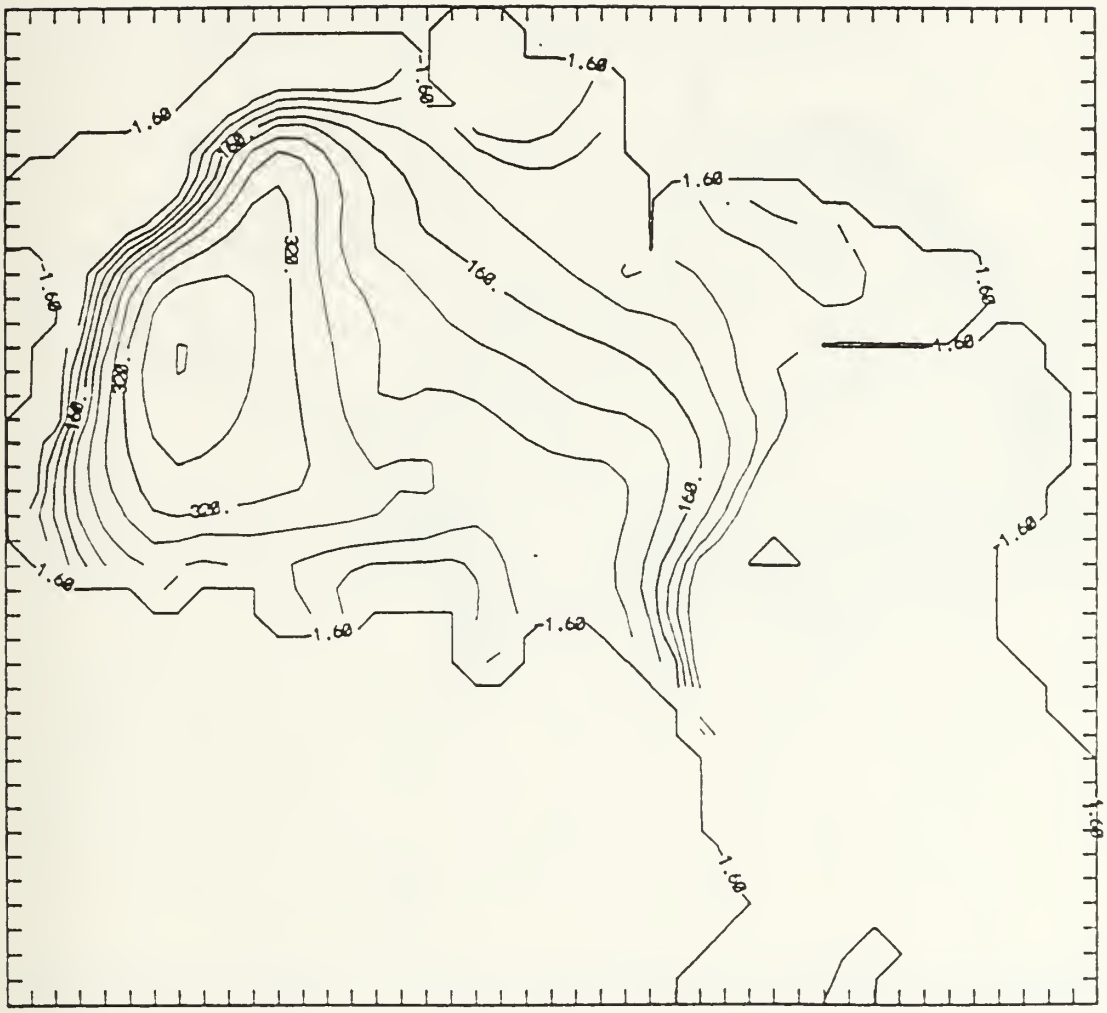
1.60
1.60
1.60

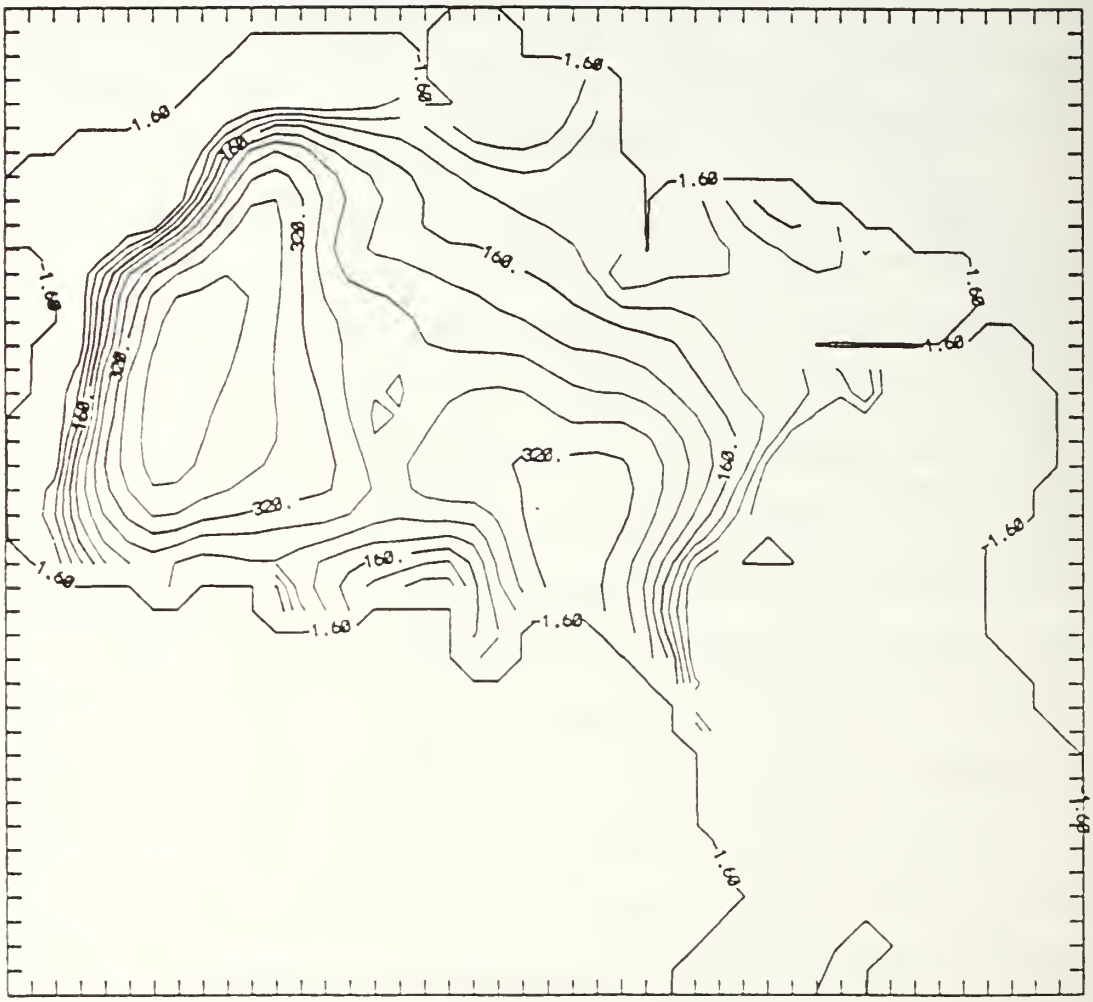
1.60
1.60
1.60

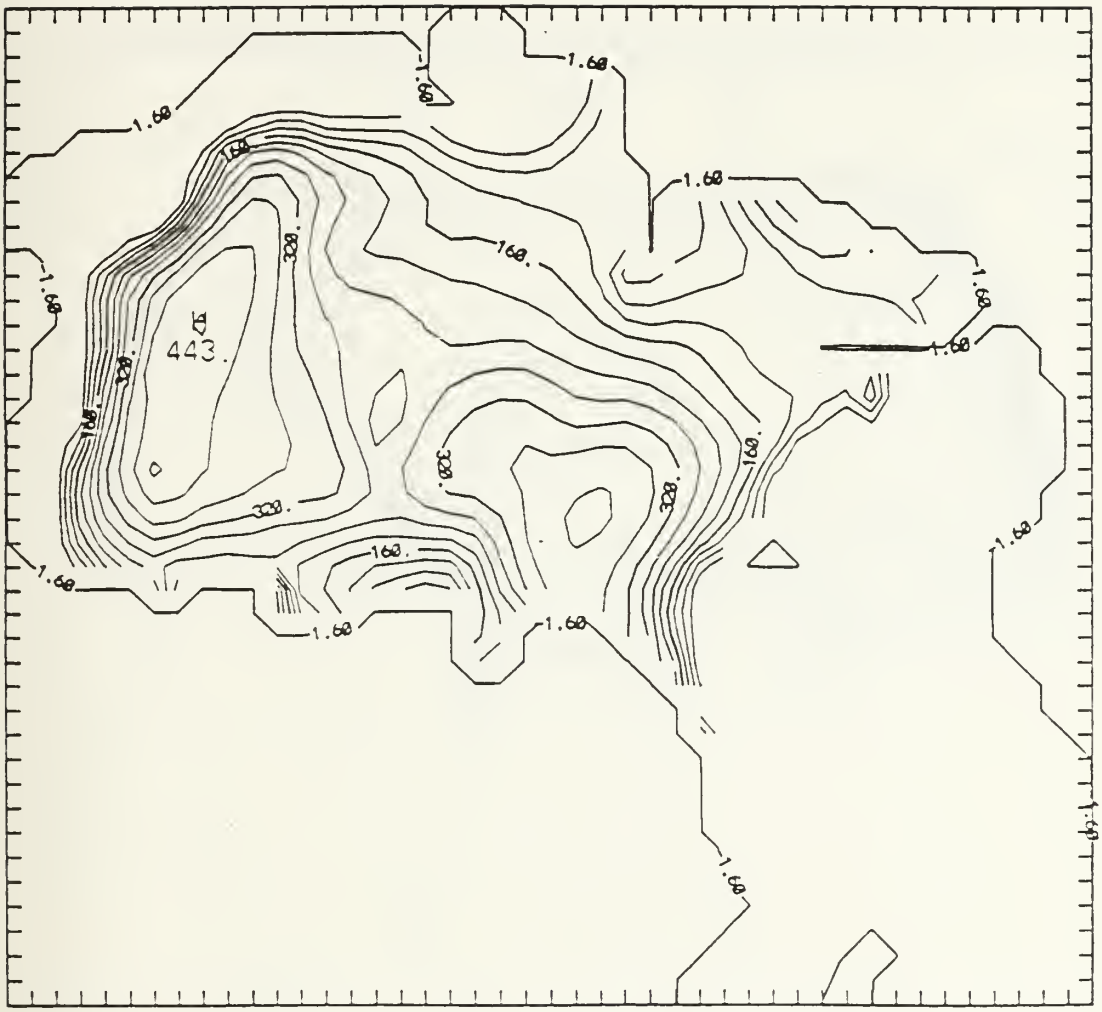
1.60
1.60
1.60

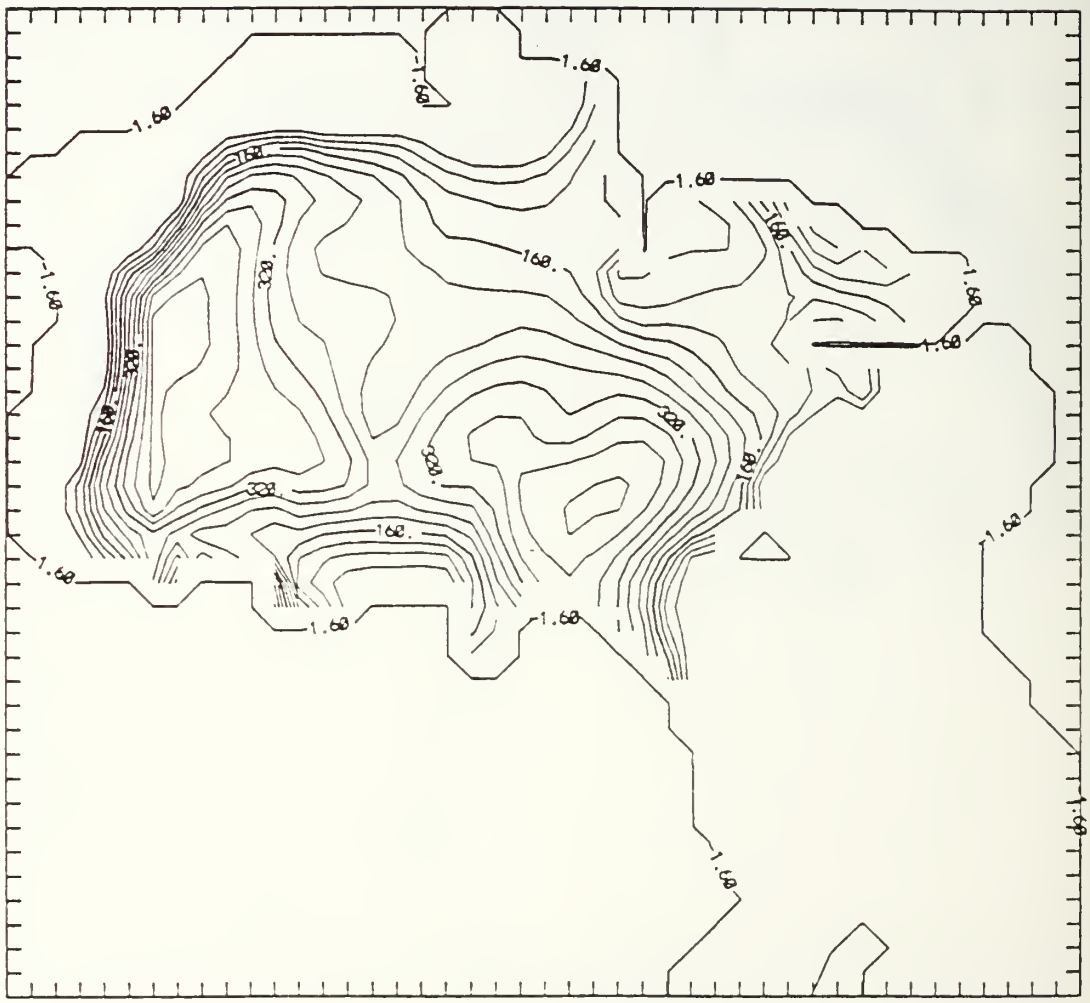
1.68
1.68
1.68

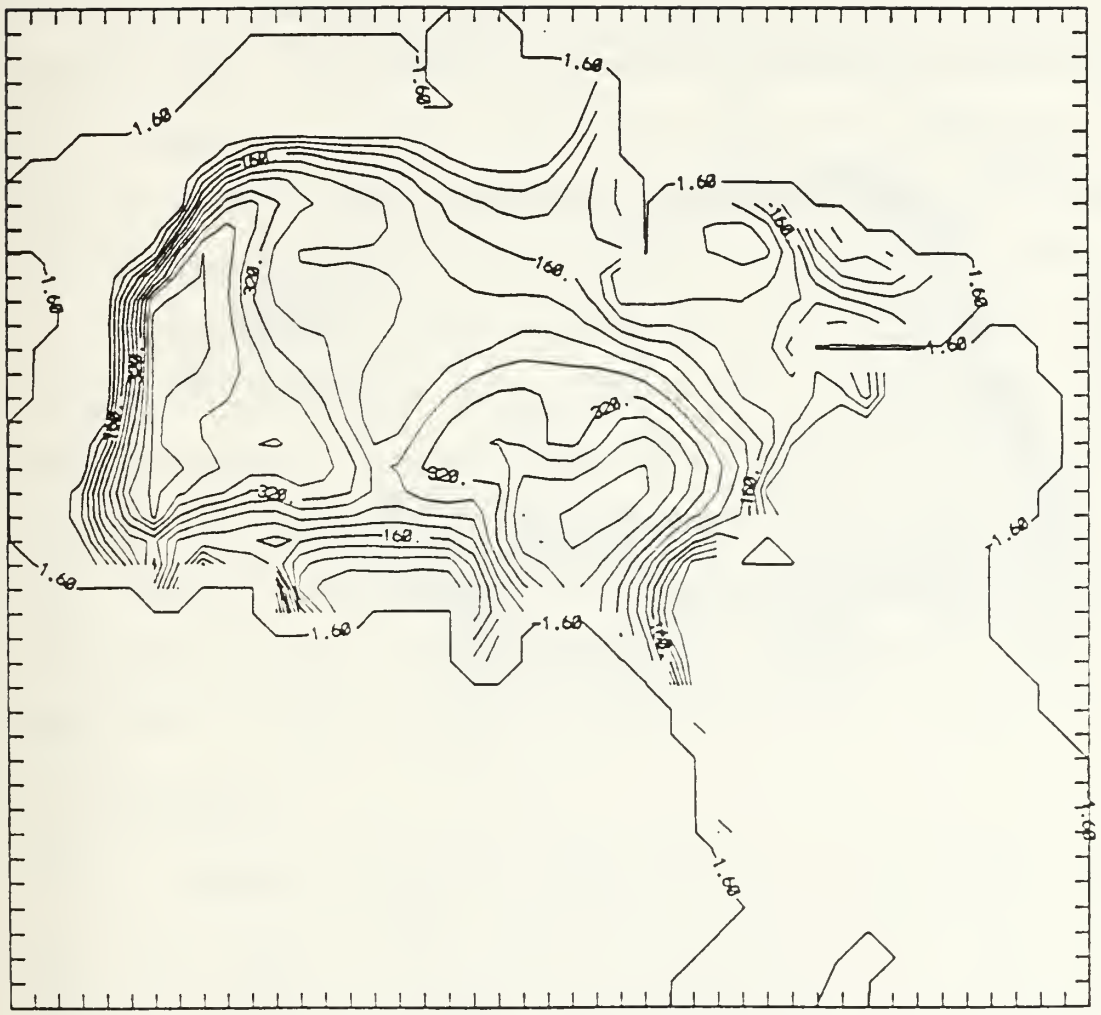
1.60
1.60
1.60

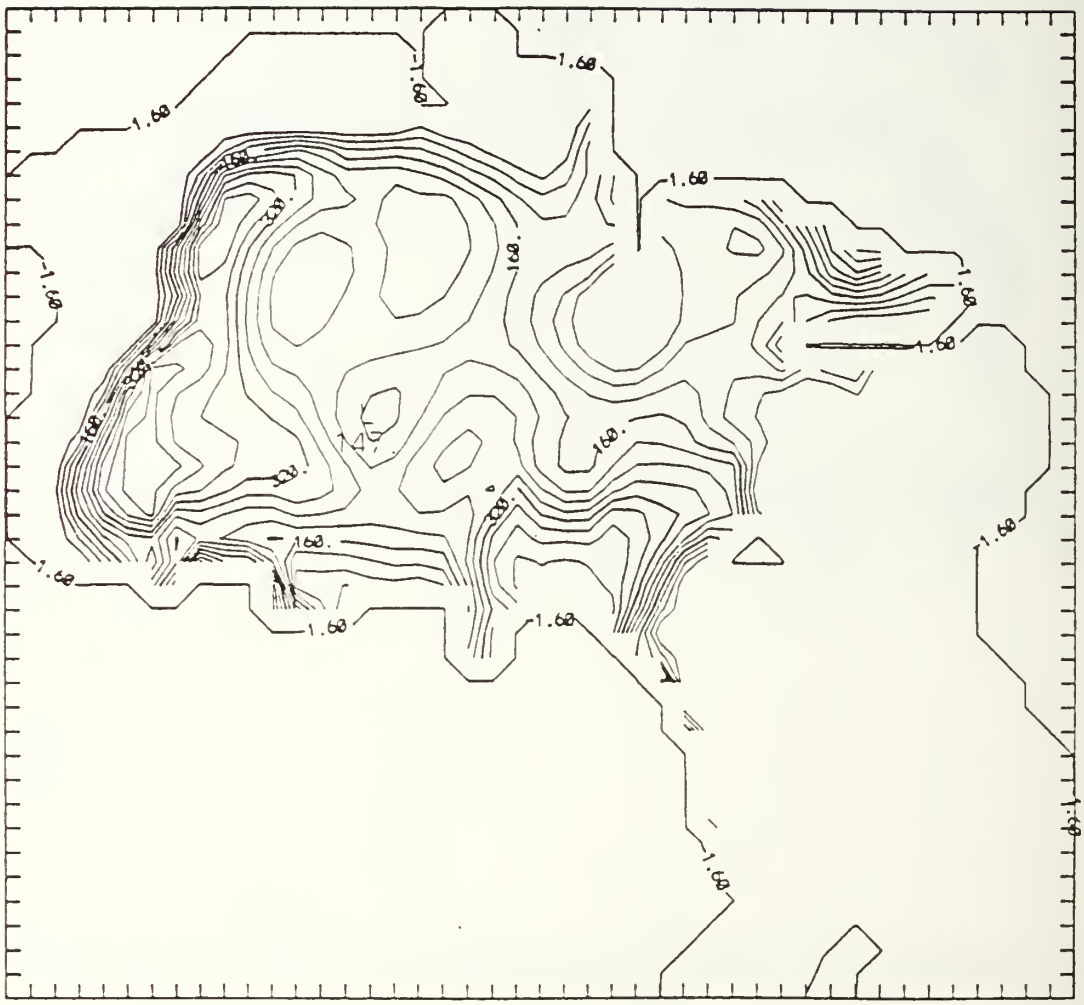

Figure 5.6 Simulated ice thickness contours (cm) for August, 1974. $P^* = h \times 1 \times 10^3$.

simulated overall ice thickness and thickness distributions. This value is somewhat larger than that used in Hibler (1979,1980) ($P^* = f(h) \times 5 \times 10^3$) and smaller than that used in Hibler and Bryan (1987) ($P^* = f(h) \times 2.75 \times 10^4$). Both of those were chosen by matching simulated drift rates with observed data. The reason for a different optimum value for P^* is probably due to the higher spatial resolution and monthly averaged daily atmospheric forcing used in this model vice the observed daily forcing used in the Hibler models.

The ten-year integration was run with the optimum P^* and a fully interactive ocean to produce ten years of simulated ice concentration fields. Correlations with the observed data for both the annual cycle and interannual variations for all four regions were calculated. The correlations using the reduced P^* model were considerably lower than when the experiment 1 model with a large P^* value was used (Table 6).

C. DISCUSSION

The linked ice-ocean model with a prognostic ocean displayed notable sensitivity to changes in the ice strength factor of the ice rheology. Reducing the P^* value by a factor of 30 improved the simulated ice thickness and distribution significantly. However, further reductions in ice strength appeared to introduce excessive "noise" in these fields. The contour lines became very rough and erratic with numerous "bullseyes" or spot irregularities. This was probably due to the diminished ability of the ice to sustain internal stress.

TABLE 6

CORRELATIONS OF ICE AREA BETWEEN SIMULATION B AND OBSERVED (CORR B) AND SIMULATION D AND OBSERVED (CORR D)

AREA TIME SERIES

REG	STDEV D	CORR B	CORR C	CORR D
1	.8160	.9126	.8852	.8610
2	.3882	.9271	.8807	.8866
3	.6709	.9461	.9106	.9322
4	.4394	.9186	.8332	.8623

ANOMALY TIME SERIES

REG	STDEV D	CORR B	CORR C	CORR D
1	.1697	.4936	.3963	.4294
2	.1499	.7761	.5981	.6292
3	.1748	.5375	.3039	.4536
4	.1788	.6172	.3332	.4354

Standard deviation values x 1 x 10^6

B simulation was with fully interactive ocean model
C simulation was with 10-year mean cycle ocean
D simulation was with the reduced P^*

As the ice strength was reduced, the ice approached a free drift condition with little resistance to either shearing or compressive forces. In this condition, the ice could respond rapidly and easily to any short term or small scale (a few hundred km) dynamic forcing resulting in the irregular appearance of the thickness contours at the lowest P^* values. Since the atmospheric forcing was smoothed, these shorter or small scale forcing events were probably from the ocean.

An explanation for the increased ice thicknesses when a moderate reduction in ice strength was introduced is that by reducing the ice strength, the long term dynamic influences of the Transpolar Drift Stream and atmosphere were able to push the ice further and faster to the southeast. The resultant ice divergence from the Bering and adjacent seas created large expanses of open water. Large heat losses to the atmosphere associated with this open water and cold air temperatures in fall and winter encouraged rapid ice production. The large volumes of new ice were then advected to the southeast where at the lower strength levels they were able to compress and undergo the appropriate ridging and rafting processes. This produced the large areas of thin ice on the Siberian shelves, increased the average ice pack thicknesses and resulted in the stronger thickness gradients evident in the simulated ice thickness fields.

The ice thickness and distribution fields from the reduced P^* model appeared to be so much improved, that the

correlations of ice concentration with the observed fields were expected to improve also. The subsequent determination that these correlations were actually degraded was surprising. Ice thickness and distribution appeared to improve substantially within the ice pack. However the amount of ocean area which experienced a total loss of ice actually increased, particularly in the Bering and East Siberian Seas. Since this exaggerated the already excessive ice edge retreat in summer, and no compensatory improvement in the ice edge position was produced in the other seasons, the correlations with the observed data decreased.

The increased ice edge retreat and areas of open water can be explained as follows. The large heat loss over the open water and the strong positive salt flux from the large freezing rate would promote increased convective overturning of the ocean in the Siberian shelf region. Strong convection would break through the halocline which serves to insulate the surface waters from the warmer waters below. Oceanic heat flux to the ocean surface would increase, slowing the freezing rate as winter progressed and keeping the ice cover relatively thin in those regions. Once the increased solar flux in spring produced a net positive heat flux at the ocean surface, the thin ice would rapidly melt and extensive areas of open water would form.

Hibler and Bryan (1987) describe the complex interactions and feedback mechanisms possible, particularly

in the marginal ice zone, when the effects of dynamics and an interactive ocean are included. They note that a fine balance of ice processes appears to exist. The initial freezing causes intense overturning. The resultant deeply mixed surface waters can withstand considerable amounts of melting at a later time without becoming stratified. This description is consistent with the process suggested here.

D. CONCLUSION

An appropriate function to use for ice strength in the ice rheology of this model appears to be:

$$P^* = h \times 1 \times 10^4$$

The ice thickness and distribution fields produced using this function were considerably more realistic in comparison with available observations than those produced using a greater ice strength. The simulated average pack thickness was doubled and strong ice buildup occurred in a manner and in areas consistent with observed data. A possible exception was the region immediately poleward of Greenland and the Canadian Archipelago. Ice thicknesses there were reduced, apparently due to advection because there did not appear to be significant ocean heat flux. Smaller ice strength values produced thickness fields which were considered too noisy.

Both the annual cycle and interannual variations of ice concentration produced using the reduced ice strength were

degraded, primarily because the total ocean area which became ice free in summer increased from the initial model runs. It is proposed that the reason for the increased area of open ocean in summer is an increase in the ocean heat flux. This occurs as a result of the strong convective penetration of the halocline resulting from greater heat losses to the atmosphere from regions where the ice has been thinned or removed and increased salt fluxes into the ocean caused by the larger freezing rates in the same regions.

These results indicate that the simulated heat flux provided by the ocean appears to be a dominant factor controlling the differences between simulated and observed ice edge position. Inclusion of the interactive ocean in the linked ice-ocean model provided a much more realistic representation of this flux. Consequently, simulated ice fields were much improved over the model which used only an average ocean condition. However, the inaccuracies that remain in the representation of ocean heat flux appear to be very important.

VI. ALBEDO EXPERIMENT

The excessive meltback of the ice edge in summer was a common feature of previous model runs in this work. Similar results have been reported by other ice modellers as well (e.g., Semtner, 1987; Hibler and Walsh, 1982). The ice strength experiment indicated that this may have been due to excessive simulated oceanic heat flux in the areas of severe melting. Alternatively, excessive atmospheric heat flux into the ice cover could also induce an exaggerated meltback of the ice edge. One of the most important elements determining the atmospheric heat flux into the ice is surface albedo.

Shine and Henderson-Sellers (1985) noted the differences in albedo representations used by several authors (e.g., Parkinson and Washington, 1979; Hibler and Walsh, 1982; Manabe and Stouffer, 1980). They showed that a thermodynamic ice model very similar to the one incorporated into this model was quite sensitive to changes in the surface albedo. Large differences between various model thickness predictions could be explained by these albedo differences.

The Shine and Henderson-Sellers (1985) study used a model which did not include ice dynamics nor an interactive ocean. As noted in Chapter V, inclusion of these in a linked model permits a much more realistic representation of the complex mixing and feedback processes which occur during freezing and

melting. The response of the more elaborate model used in this study to surface albedo changes was unknown and therefore was considered worthwhile for further investigation.

A. EXPERIMENTAL SETUP

The represention of surface albedo used in this model was described in Chapter III. Some allowance was made for the differences in albedo between ice and snow and for the changes which occur when melting commences (see Chapter III); however, the representation was very simple.

Ross and Walsh (1987) used a more elaborate surface albedo representation in conjunction with a dynamic-thermodynamic model to simulate surface albedo in the Arctic. The albedo representation was a linear function of air temperature which also accounted for the differences between ice and snow. The simulated albedos produced with that model matched the satellite-derived estimates by Robinson et al., (1986) very well. In view of the importance placed on an accurate representation of the surface albedo by Shine and Henderson-Sellers (1985), the albedo representation of Ross and Walsh (1987) was incorporated into the model used in this work as follows:

- $a_{snow} = 0.80$ $\quad T_{sfc} < -5.0$ deg C
- $a_{snow} = 0.65 - 0.03(T_{sfc})$ $\quad -5.0 < T_{sfc} < 0.0$ deg C
- $a_{snow} = 0.65$ $\quad T_{sfc} = 0.0$ deg C
- $a_{ice} = 0.65$ $\quad T_{sfc} < 0.0$ deg C

- $a_{ice} = 0.65 - 0.04(T_{air})$ $\quad 0.0 < T_{air} < 5.0$ deg C [1]

- $a_{ice} = 0.45$ $\quad T_{air} > 5.0$ deg C

- $a_{water} = 0.10$

where "a" is the albedo value, T_{sfc} is the surface temperature of the ice or snow and T_{air} is the air temperature above the ice or snow surface. The fraction of solar radiation absorbed internally by the ice was 0.35 as recommended by Ross and Walsh (1987).

A ten year integration was conducted using the new albedo model and radiation absorption constant. The resultant ice concentration fields were again correlated with the observed data as in the previous experiments. The ten-year correlations of simulated annual ice cycle and interannual variations are shown in Table 7. The correlation coefficients improved nominally in regions 2 and 4 and worsened nominally in regions 1 and 3.

Comparison of simulated ice concentration contours and ice thickness contours from model runs before and after the albedo changes showed only trivial differences. It appeared that the full model with ice dynamics and an interactive ocean was relatively insensitive to changes in albedo. This finding was a clear contrast to previous work using simpler ice models (e.g., Shine and Henderson-Sellers, 1985; Hibler, 1980).

---

[1] note that this is a correction to Ross and Walsh (1987) to make the albedo a linear function of temperature as described in the text.

TABLE 7

CORRELATIONS OF ICE AREA BETWEEN SIMULATION B AND OBSERVED (CORR B) AND SIMULATION D AND OBSERVED (CORR D)

ICE AREA TIME SERIES

REG	STDEV E	CORR B	CORR D	CORR E
1	.8066	.9126	.8610	.8606
2	.3778	.9271	.8866	.8870
3	.6647	.9461	.9322	.9321
4	.4387	.9186	.8623	.8648

ANOMALY TIME SERIES

REG	STDEV E	CORR B	CORR D	CORR E
1	.1715	.4936	.4294	.4277
2	.1491	.7761	.6292	.6328
3	.1767	.5375	.4536	.4522
4	.1798	.6172	.4354	.4556

Standard deviation values x 1 x 10^6.

B simulation was with fully interactive ocean model.
C simulation was with 10-year mean cycle ocean.
D simulation was with the reduced P^*.
E simulation was with the improved albedo representation.

Several sensitivity runs were made to further explore this observation. The range of the albedos was systematically increased until values well outside the normal range were prescribed. This was done to determine just how insensitive the model was to albedo modifications. These runs used a single year of integration (1977) in the same manner as for the ice strength sensitivity experiment. The surface albedo representations examined were as follows:

- A1. Albedo code as in Semtner (1987).
- A2. New albedo code as described above and used in Ross and Walsh (1987).
- A3. All ice and snow albedos in the new albedo code increased by 0.05.
- A4. All ice and snow albedos in the new albedo code increased by 0.1 and open water albedo increased to 0.15.
- A5. Ice albedo held constant at 0.65, snow albedo held constant at 0.80 and open water albedo at 0.15.
- A6. Ice albedo held constant at 0.85, snow albedo held constant at 0.90 and open water albedo at 0.15.
- A7. Ice albedo held constant at 0.35, snow albedo held constant at 0.40 and open water albedo at 0.10.

Several other runs were conducted using the high and low albedo representations of runs A6 and A7 but with different portions of the thermodynamic and dynamic forcing in the linked model removed. This was done to determine which of the features of the fully linked model reduced its sensitivity to albedo changes as compared to previous thermodynamic ice models. This work was done in conjunction with the objectives

of Chapter VII. For reference, a brief description of the various dynamic model variations are noted below. Further descriptions of the various runs D1 thru D8 and the rationale for their selection are contained in Chapter VII.

- D1. Base model using the 10-year average ocean. Start from Dec 1976 and use 1977 forcing over a single integration year.
- D2. Constant ocean heat flux into mixed layer (2.0×10^{-5} deg C/sec, equivalent to approximately 25 W m^{-2}).
- D3. No ocean heat flux.
- D4. No ocean current stress (level two (40 m) ocean velocities = 0.0 m/s).
- D5. Ocean heat flux = 2.0×10^{-5} and no ocean current stress.
- D6. No wind stress (surface drag coefficient = 0.0).
- D7. No wind or ocean current stress.
- D8. No wind stress, no ocean current stress and no ocean heat flux.

In cases D2 through D8, the description for each run indicates the changes from the Base Model (run D1).

B. RESULTS

The ice thickness distributions for September 1977 from runs A6 and A7 are shown in Figures 6.1 and 6.2. These two runs had the largest differences in albedos and September was the month which showed the greatest differences in ice thicknesses. The differences between runs A6 and A7 (and runs A1-A5 as well) were small. The ice cover did in general increase when the albedo was changed from a low to a high

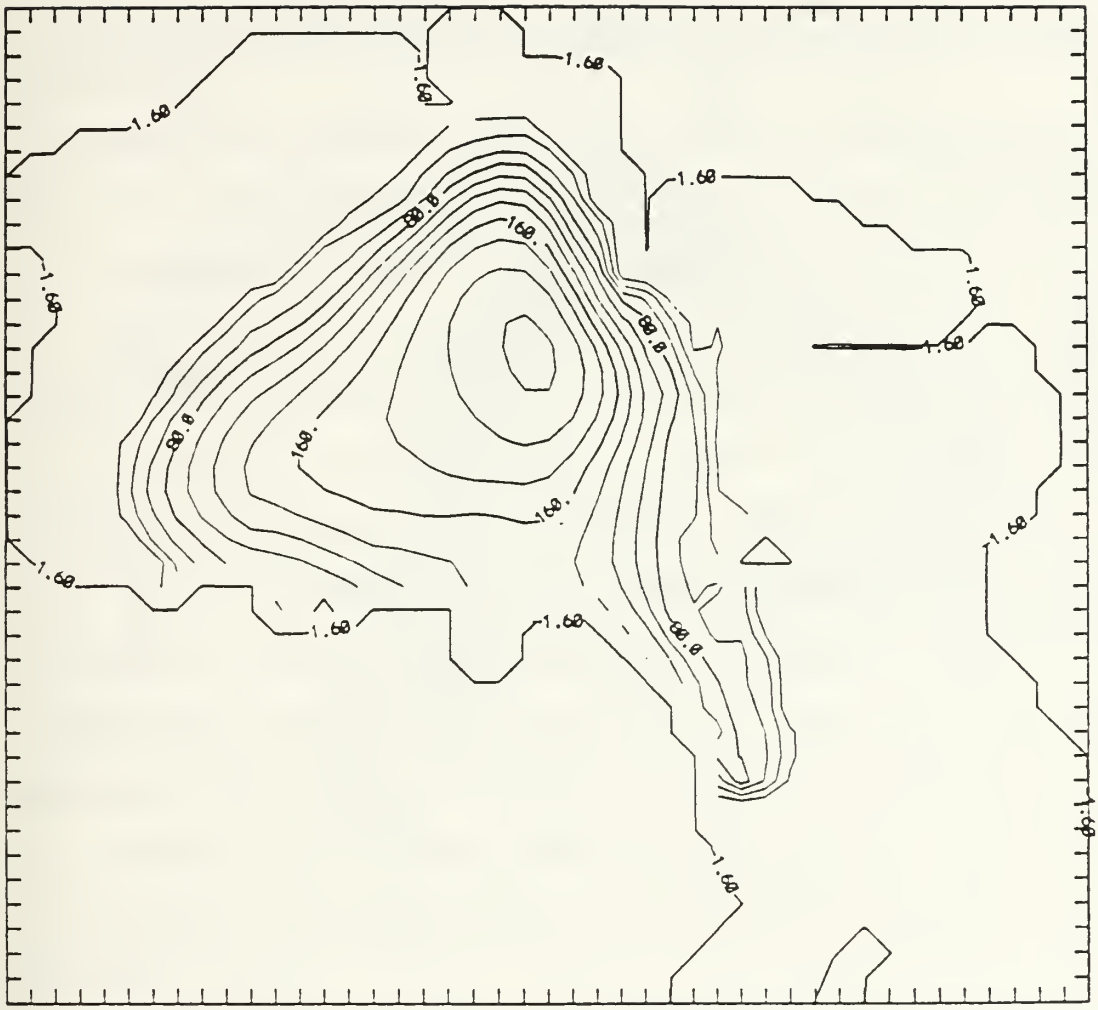
1.60
1.60
1.60

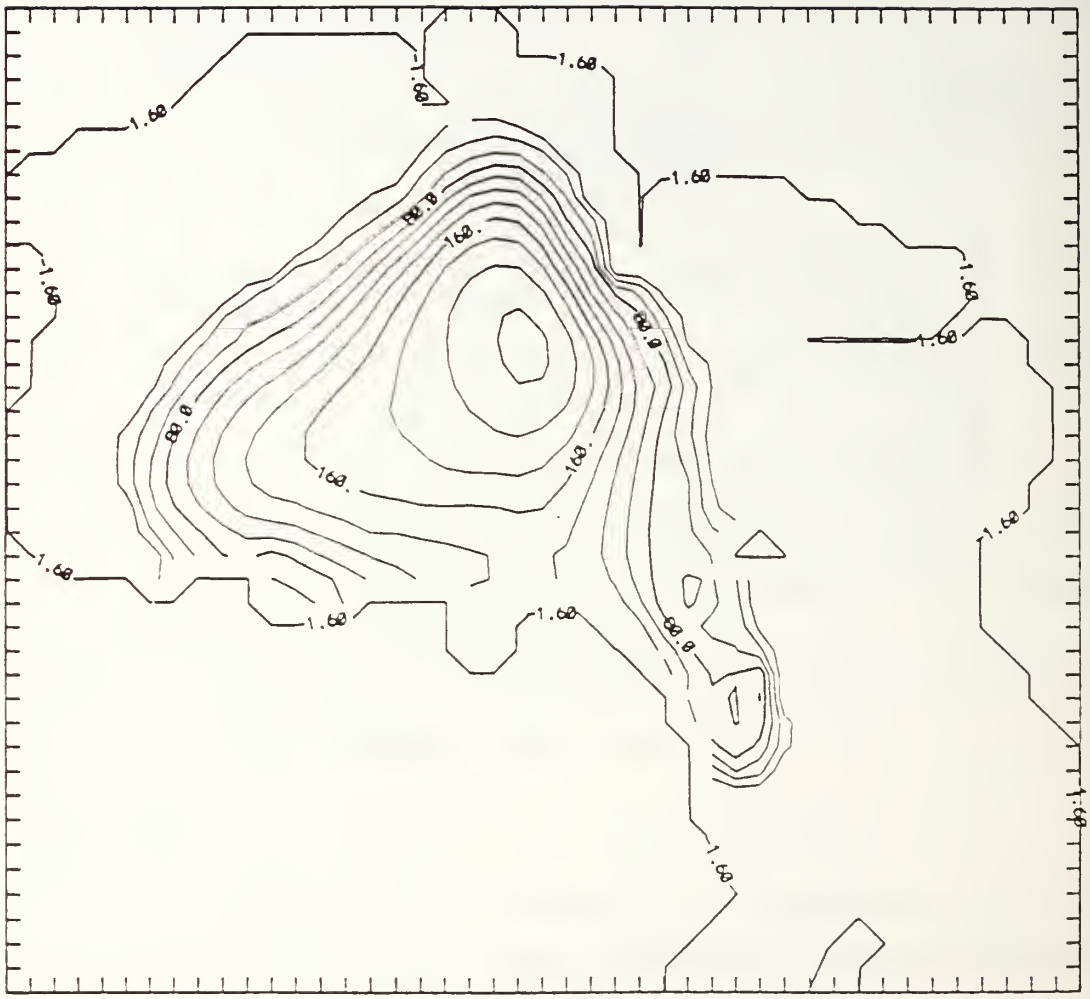
1.60
1.60
1.60

value; however, the ice edge advance rarely exceeded 50 km seaward. In fact, there were numerous examples in which the position of the ice edge and contours within the high thickness gradient regions were indistinguishable between the high and low albedo cases except for the smallest of irregularities.

Differences between simulations using modified albedos became more noticeable in runs D1-D8. The common differences were a southward extension of the marginal ice zone (MIZ) all around the Arctic Basin, a southward extension of the EGC, increased ice in the Kara Sea and in several cases an increase in ice poleward of Spitsbergen. Summer central ice pack thicknesses decreased very slightly (approximately 2%) in several of the high albedo runs presumably because the thicker ice around the margins reduced the amount of ice compression in the central pack. Differences between high and low albedo simulations were largest in the spring during periods of large scale melting. Once the melt was in full progress (and during the subsequent freezing period), the ice fields evolved almost identically.

Figures 6.3 - 6.8 show the ice thickness distributions in July 1977 for the high and low albedo conditions from runs D6, D7 and D8. These were the runs in which wind stress was reduced to zero. In these cases much more ice was evident in the eastern Arctic during summer and fall using the large albedo values. Increased southward extension of the MIZ was

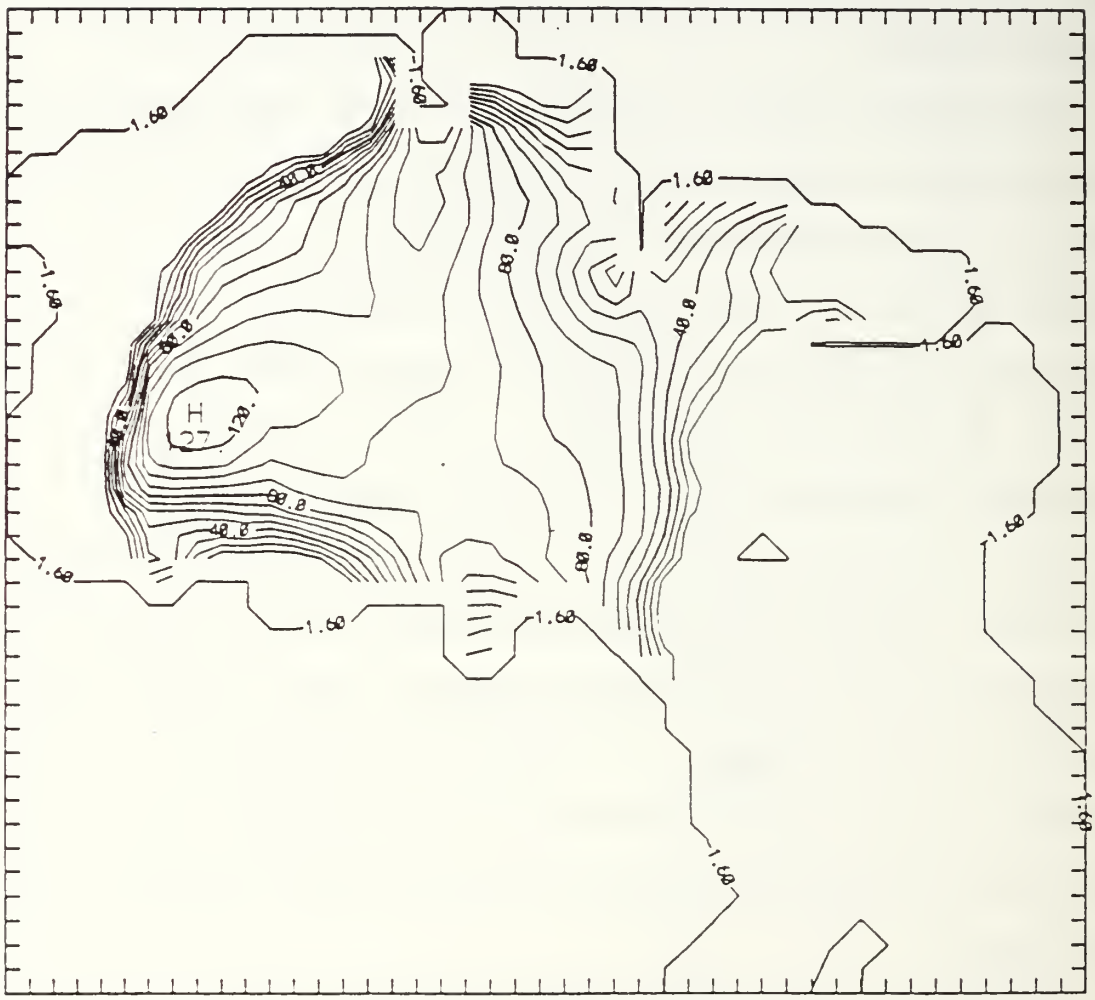

Figure 6.3 Simulated ice thickness contours (cm) for July, 1977. High albedo case (run D6).

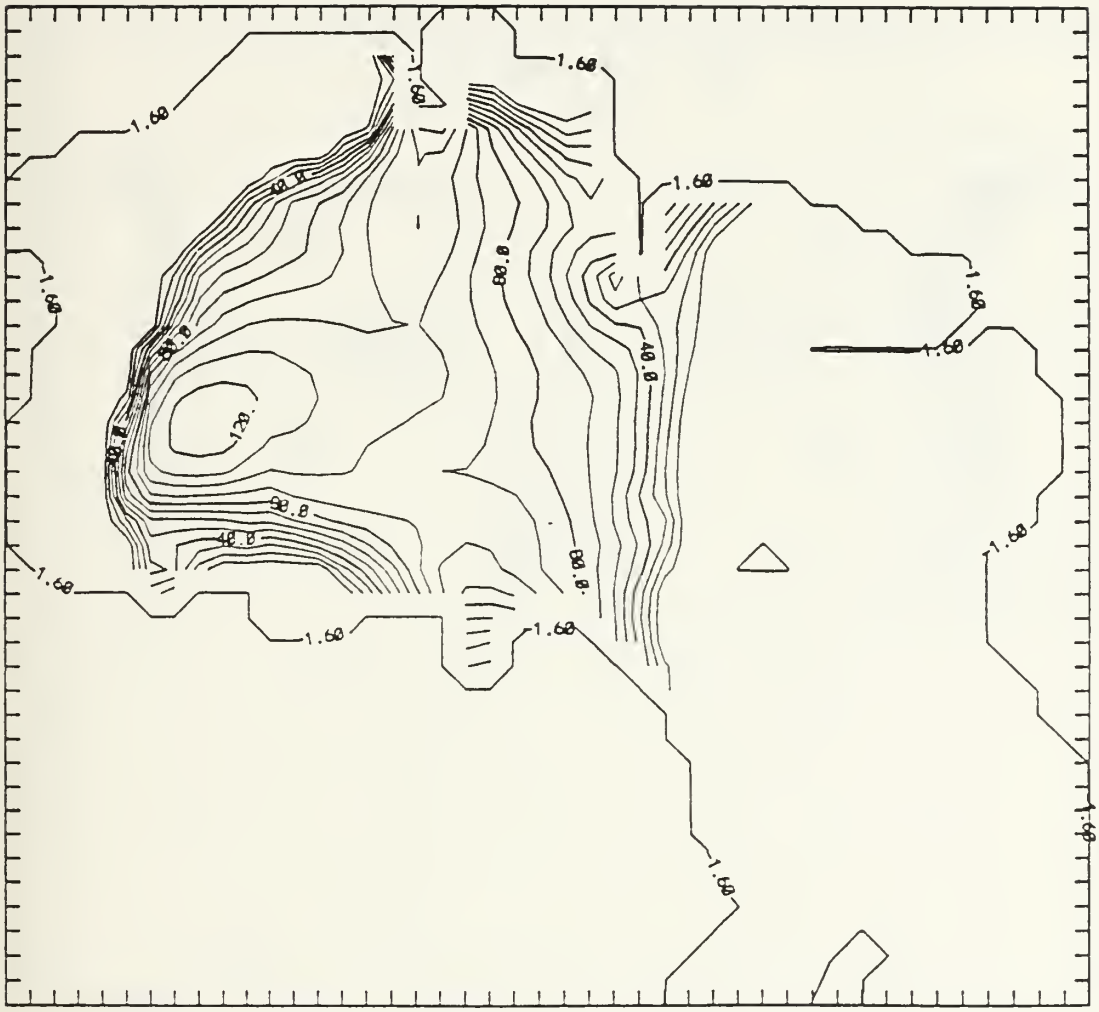
1.60
1.60
1.60

1.60
1.60
1.60

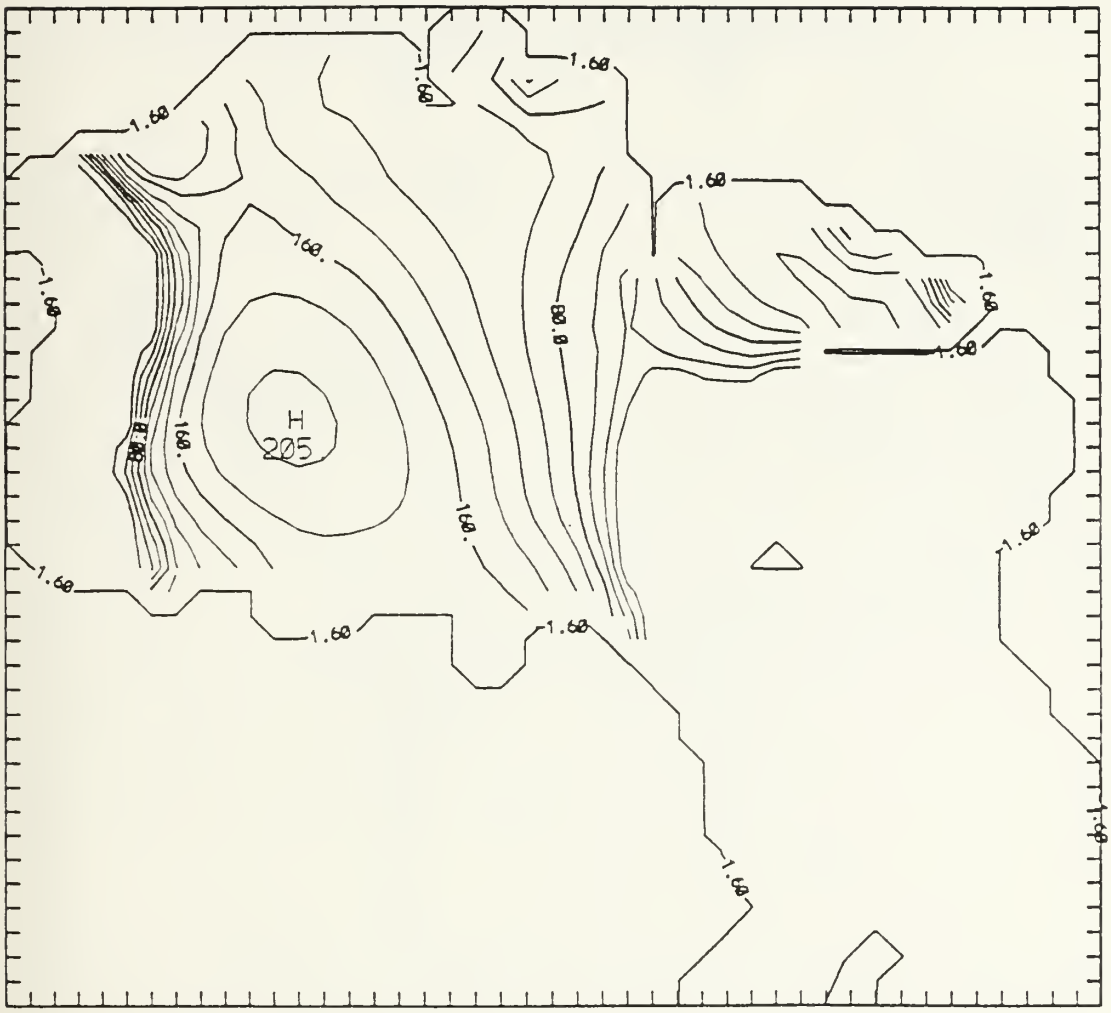

Figure 6.6 Simulated ice thickness contours (cm) for July, 1977. Low albedo case (run D7).

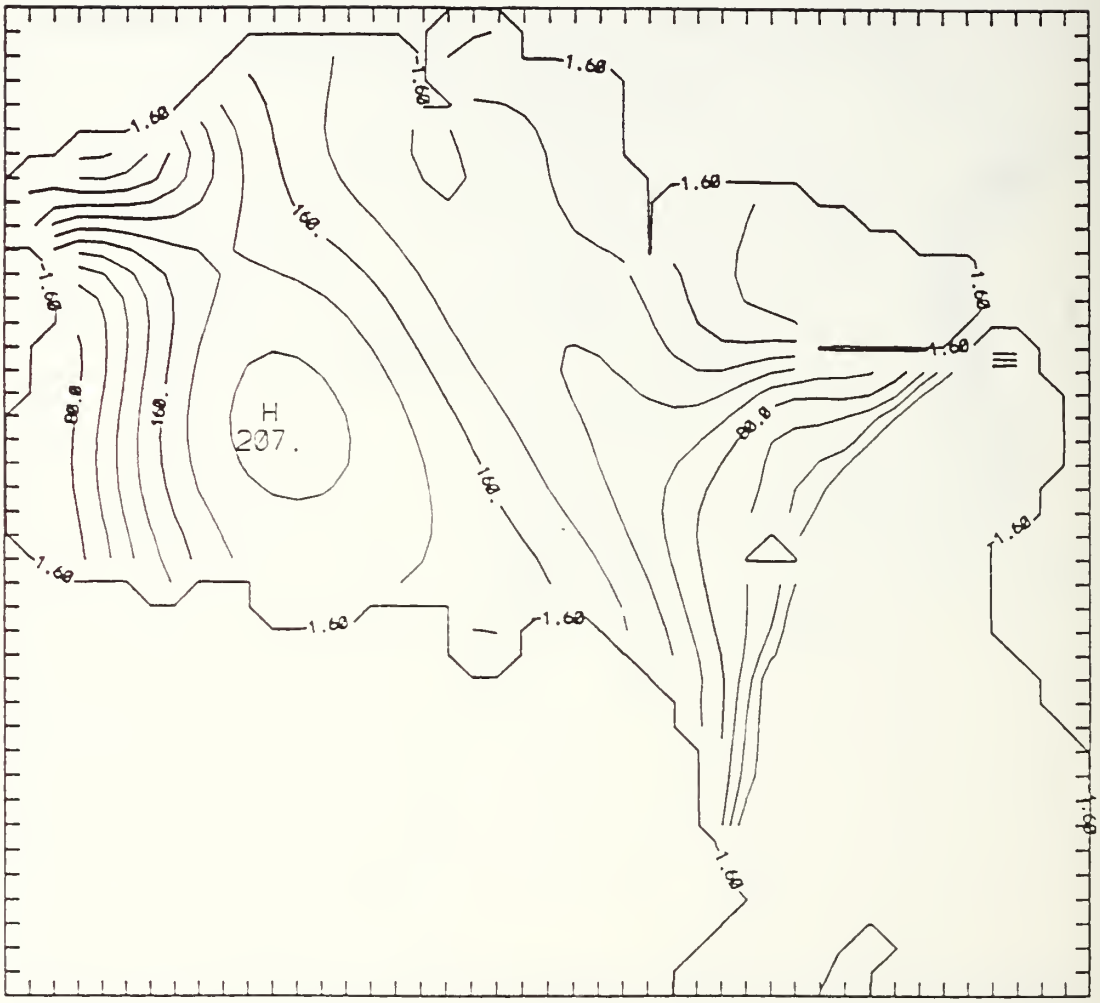
1.60
1.60
1.60

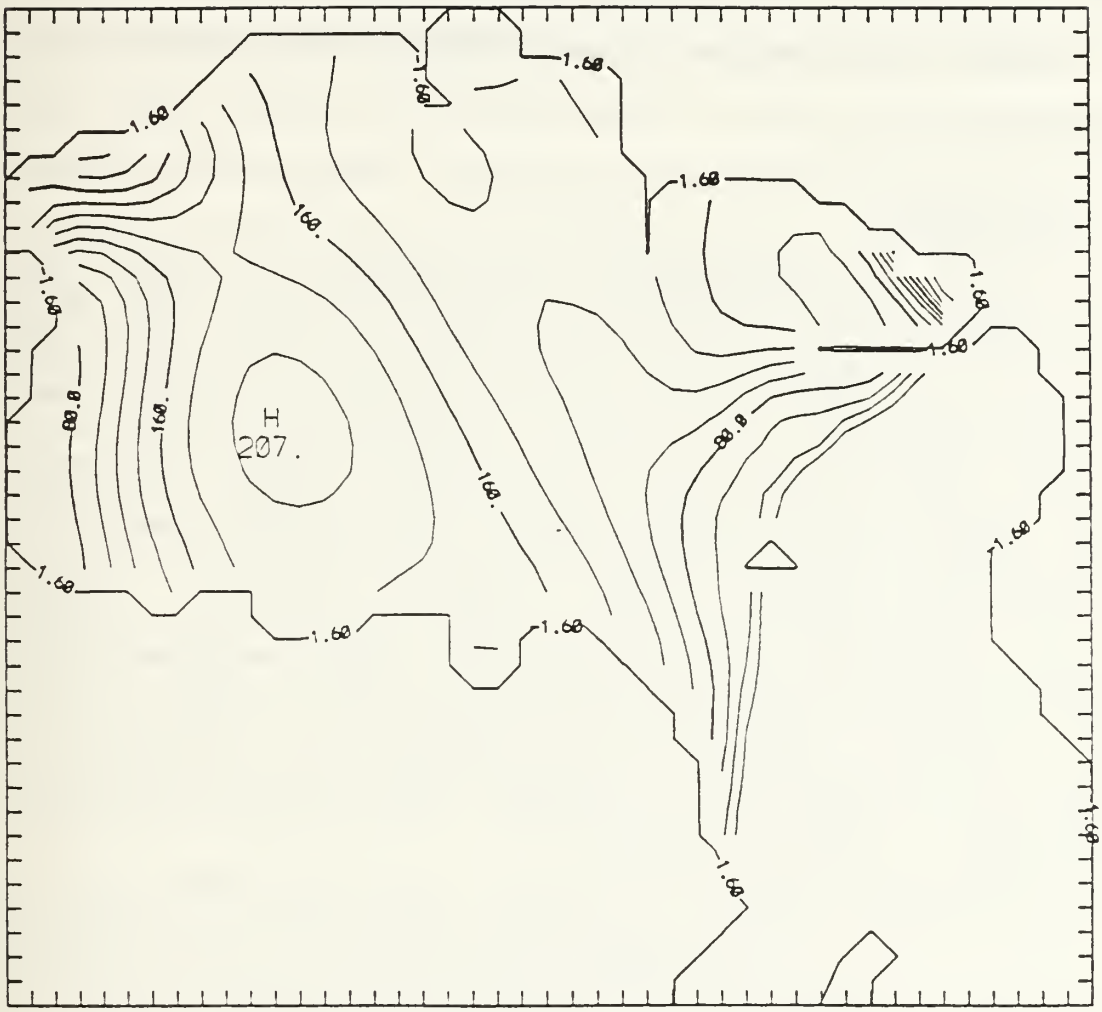
1.60
1.60
1.60

also observed in the western Arctic but relative to the eastern Arctic increase, this change was relatively small.

In contrast to the small differences in ice cover between simulations when the albedo was changed, the differences between simulations when the dynamic or thermodynamic forcing was changed were dramatic. These effects will be examined in Chapter VII.

C. DISCUSSION

Prior to this experiment, it was tempting to assume that the simple albedo representation used by Semtner (1987) and initially used here provided surface albedo values which were too low. For a model sensitive to albedo changes, this would cause earlier and increased melting and perhaps account for the excessive retreat of the ice edge in summer. A higher albedo, produced by a more "accurate" albedo representation, would reduce the excessive melting and enhance freezing. The resulting increased ice thicknesses would provide additional resistance to earlier meltoff.

The results of this experiment showed that this was not the case. Increasing the ice and snow albedo did result in nominally more ice area and thickness, especially near the edges of the pack ice, and less ice was produced at reduced albedos. However the differences were small even when the albedos were set well outside normal values.

One explanation could be that the upper ocean controls the extent of the ice cover directly. With a fixed albedo of 0.10, the surface water absorbs much more heat than the ice. Wherever open water and ice are adjacent during spring and summer, the warmed water is free to advect under and around the ice to promote melting regardless of the albedo of the ice. The reduced ice concentration in the MIZ would further promote this process. However, this mechanism would also be possible in the earlier thermodynamic-only ice models. Since those were the models which displayed considerable albedo sensitivity, this explanation can be rejected.

A second explanation is that the inclusion of the interactive ocean could permit a feedback mechanism which largely compensates for any changes to the frozen-surface albedo. For example, the greater ice production rate at higher albedos could initiate greater vertical mixing through salt extrusion and thereby bring more heat to the surface, slowing the ice growth. Similarly the reduced albedo would initiate more melting, create a stronger halocline and therefore less vertical heat advection.

A third explanation, and probably the most reasonable, is that the ocean heat flux, ocean currents and wind stress are much more dominant in controlling the ice edge than the atmospheric heat flux changes to the ice resulting from albedo modifications.

The primary difference between this ice model, which has been shown to be insensitive to ice surface albedo changes, and previous models which were sensitive to albedo changes was the inclusion of a fully prognostic ocean. Runs D2 - D8 were used to examine the impact of the dynamic features on the model's sensitivity to frozen-surface albedo changes. The greatest sensitivity was observed in the runs in which the wind stress was reduced to zero (D6-D8). This suggests that dynamic forcing, and, in particular the wind stress might act to remove, compensate or dominate most of the effect of changing the frozen-surface albedo. However the model used by Hibler (1980) accounted for the effects of wind stress in simulating the annual cycle of Arctic ice cover and still found that the model was sensitive to small changes in the ice albedo. The major difference remaining between the Hibler model and the model used here was that Hibler used a constant vertical ocean heat flux. One must therefore assume that it is this vertical heat flux from the ocean, which simulations from this work indicate varies dramatically in time and space, that reduces this model's sensitivity. It follows then that the vertical ocean heat flux is likely the most dominant factor in determining the thermodynamic balance near the ice edge.

The sensitivity of runs D6 and D7 to albedo changes, despite using a simulated variable ocean heat flux, indicated that another factor was also important to albedo sensitivity.

Ice thicknesses and areal coverage were severely reduced in run D6 compared to run D7, and run D6 also displayed more sensitivity to the albedo change. The areas of thin ice became ice free much more quickly and did not extend as far when the albedo was low. It would therefore appear that the model's albedo insensitivity was also dependent on the ice thickness.

Further support for this is evident by comparing runs D3 and D8. In both cases the ocean heat flux was reduced to zero; however D3 retained the dynamic forcing from wind and ocean currents. The lack of dynamic forcing in D8 reduced the simulated ice thicknesses in the central pack and the thickness gradients in the MIZ. The extended, thin ice MIZ in D8 was much more susceptible to the albedo change than the strong thickness gradient MIZ in D3.

There is an apparent contradiction in that D7 has thicker ice than D6 despite reduced dynamic forcing. However it appears that the water stress, which is accounted for in Run D6 but not in D7, advects the ice away from the thick compression areas to regions of high ocean heat flux where it is melted. This reduces the total ice volume and ice thicknesses, especially in the central pack and along the Canadian boundary of the Beaufort Gyre. This process may also explain the reduced ice thicknesses immediately adjacent to the Canadian Archipelago and northern Greenland evident in the ice strength experiment (Chapter V).

D. CONCLUSIONS

The use of only one integration year vice several years or decades of integration obviously limited the degree of ice cover modification possible between model runs with different surface albedo representations. However the objective here was not to determine what final end condition of ice cover could be produced but whether or not alteration of the albedos within reasonable limits could improve the simulation of interannually varying ice cover.

The largest error in the simulated ice fields was the excessive summer melt. A secondary, but still important error, was excessive winter ice coverage in the Barents Sea. This model appears quite insensitive to albedo changes of the snow/ice cover. Surface albedos had to be set well above reasonable levels to produce even a nominal decrease in the meltback in the western Arctic and the same albedo changes marginally worsened the simulation of the ice edge in the Barents Sea. Therefore, changing the albedo representation was not an effective method of improving the accuracy of the simulated ice cover. In fact, the insensitivity of this model to albedo modifications would suggest that even the very simple albedo representation initially used would be sufficient and would not degrade the model's accuracy.

The primary reason for this model's insensitivity to albedo changes in the frozen surface appears to be the dominance of the vertical ocean heat flux in the thermodynamic

balance near the ice edge. Albedo sensitivity in the model is only apparent in those few, small regions where both the vertical ocean heat flux is small and the ice is thin. Under these conditions, the changes to the thermodynamic balance induced by albedo changes in the ice cover are large enough to cause noticeable changes in the ice concentration and extent.

It should be reiterated here that this study deals with the ice cover on an average monthly basis at a fairly large scale. Albedo does have a major impact on the ice cover on shorter time scales as evidenced, for example, by the flash melt phenomenon. The entire ice surface in a region can melt in a few days when the reduced albedo of the melting surface accelerates the melting process. However, on the larger time and space scales used here, this type of effect is largely smoothed out leaving the consistent longer term ocean heat flux as the dominant controller of the ice cover.

The ocean currents, although not a major factor in albedo sensitivity, play a significant role in the evolution of ice thickness. They appear to advect the ice away from the thick compression regions to regions of high heat flux where the ice is usually melted. This has the effect of reducing the ice thickness in the compression regions, particularly along the northern limit of the Canadian Archipelago.

VII. DOMINANT MECHANISM EXPERIMENT

The albedo sensitivity experiment included several runs in which various dynamic and thermodynamic processes were removed from the base linked model to determine which processes were primarily responsible for the insensitivity of the model to albedo changes. Although the albedo changes continued to have relatively little impact on the simulated ice fields, the total ice field changed considerably from the base model output as the different processes were omitted.

This experiment was conducted to determine which elements of the thermodynamic and dynamic forcing were dominant in the linked ice-ocean model.

A. EXPERIMENTAL SETUP

The same base model as used in the albedo sensitivity study was used for this experiment. A single integration year was considered sufficient due to the high sensitivity of this model to dynamic changes. The year 1977 was again chosen as the integration year because the previous work had provided a large base of simulated 1977 ice field data for comparison. The following sensitivity runs were examined:

- D1. Base model. 10-year average ocean. Starting from Dec 1976 output fields. 1977 forcing. Single integration year.
- D2. Constant ocean heat flux into mixed layer (2.0×10^{-5} deg C/sec, equivalent to approximately 25 W/m^2).

- D3. No ocean heat flux.
- D4. No ocean current stress (level two (40 m) ocean velocities = 0.0 m/s).
- D5. Ocean heat flux = 2.0×10^{-5} and no ocean current stress.
- D6. No wind stress (surface drag coefficient = 0.0).
- D7. No wind or ocean current stress.
- D8. No wind stress, no ocean current stress and no ocean heat flux.

In cases D2 through D8, the description for each run indicates the changes from the Base Model (run D1).

B. RESULTS

The winter (April) and summer (August) ice thickness contours from run D1 are shown in Figures 7.1 - 7.2 for comparison with the contours from runs D2-D8.

The ocean heat flux value chosen for run D2 was the approximate median of the simulated average annual flux cycle over the Arctic region. Applying this constant value of 25 W/m^2 over the entire grid heavily exaggerated the basin-wide simulated ice cycle. The winter ice cover expanded much too far south into the Norwegian Sea and the summer ice cover was reduced to a small fraction of the observed cover (Figures 7.3 - 7.4). The central ice pack normally receives little or no ocean heat flux. The relatively large heat flux applied in this run rapidly reduced the pack ice thickness and areal coverage. By August, the central pack was almost completely melted off. The subsequent freezing in early winter produced

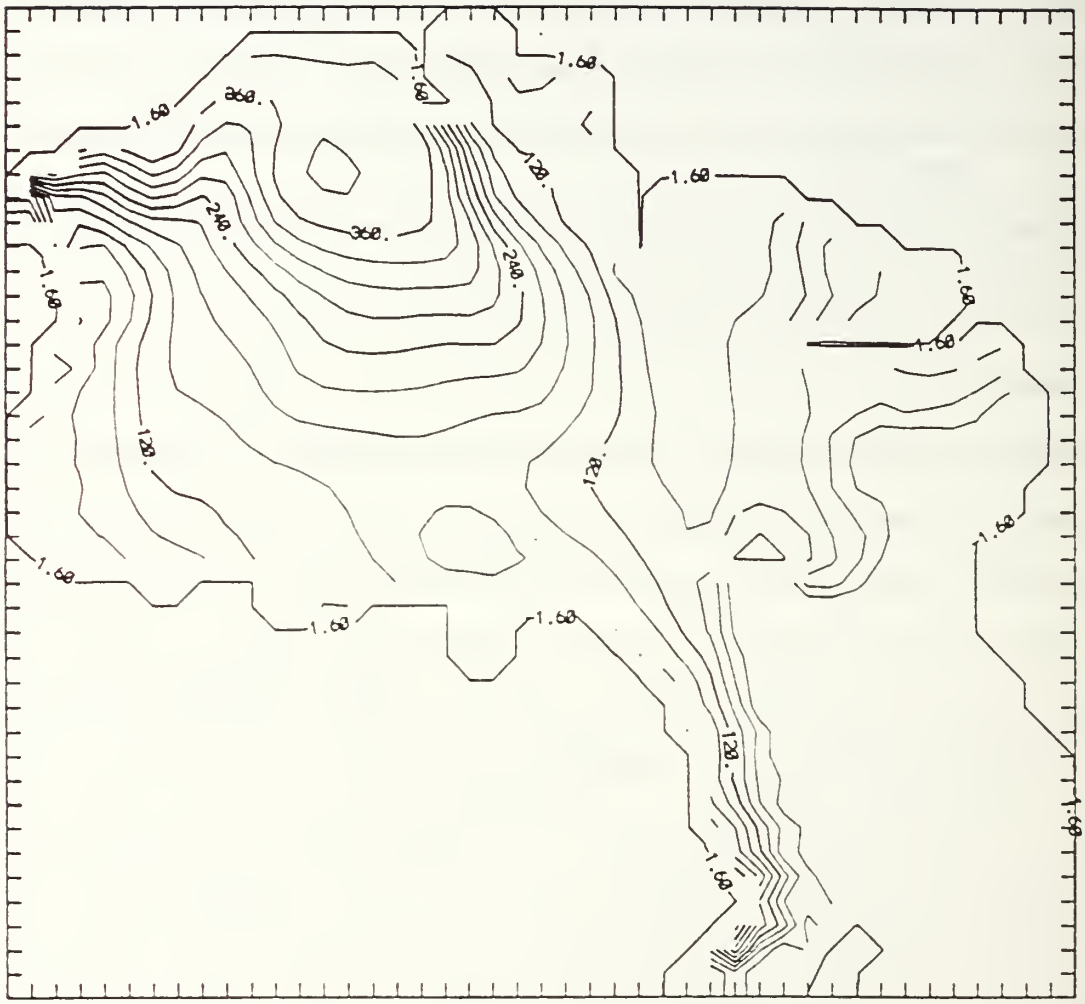

Figure 7.1 Simulated ice thickness contours (cm) for April, 1977. Base model (run D1).

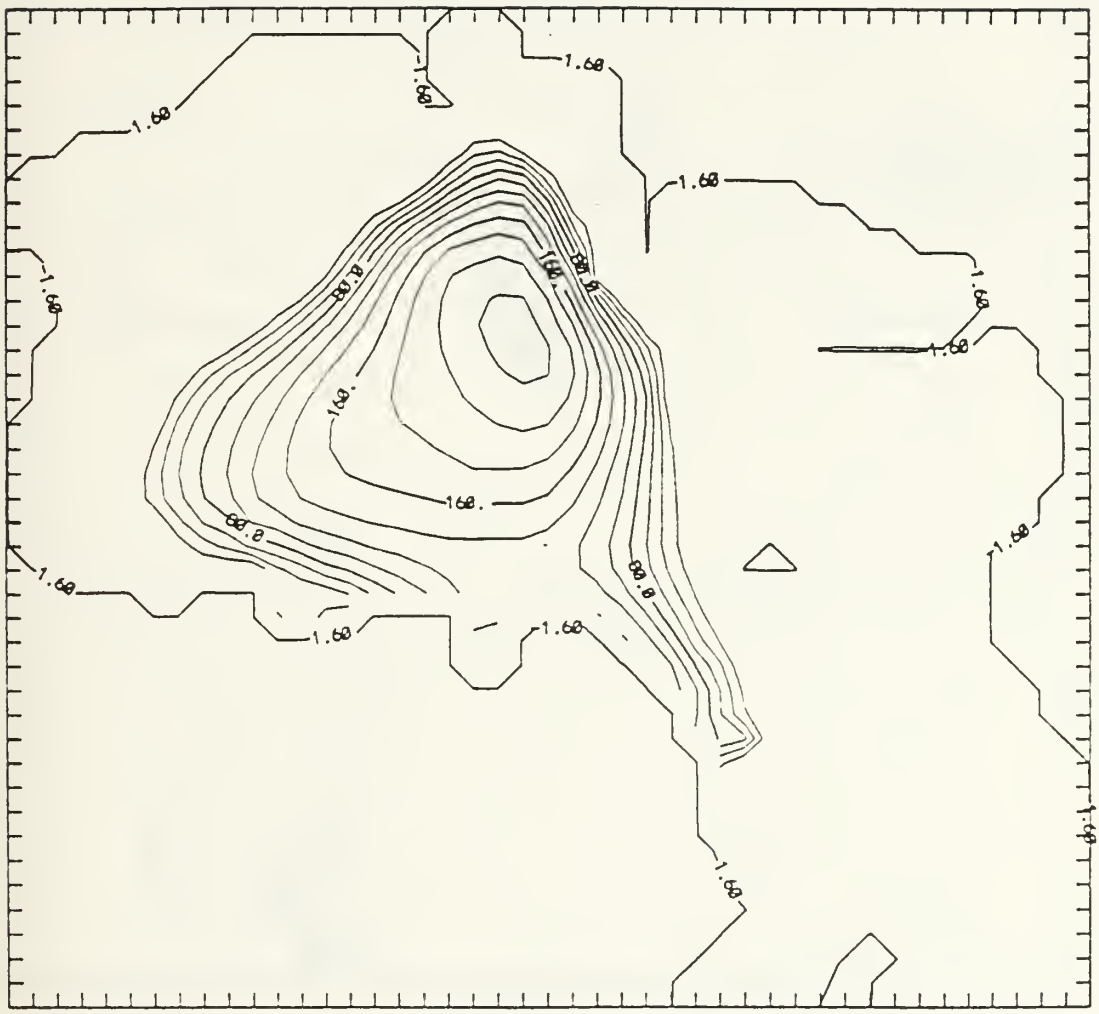
1.60
1.60
1.60

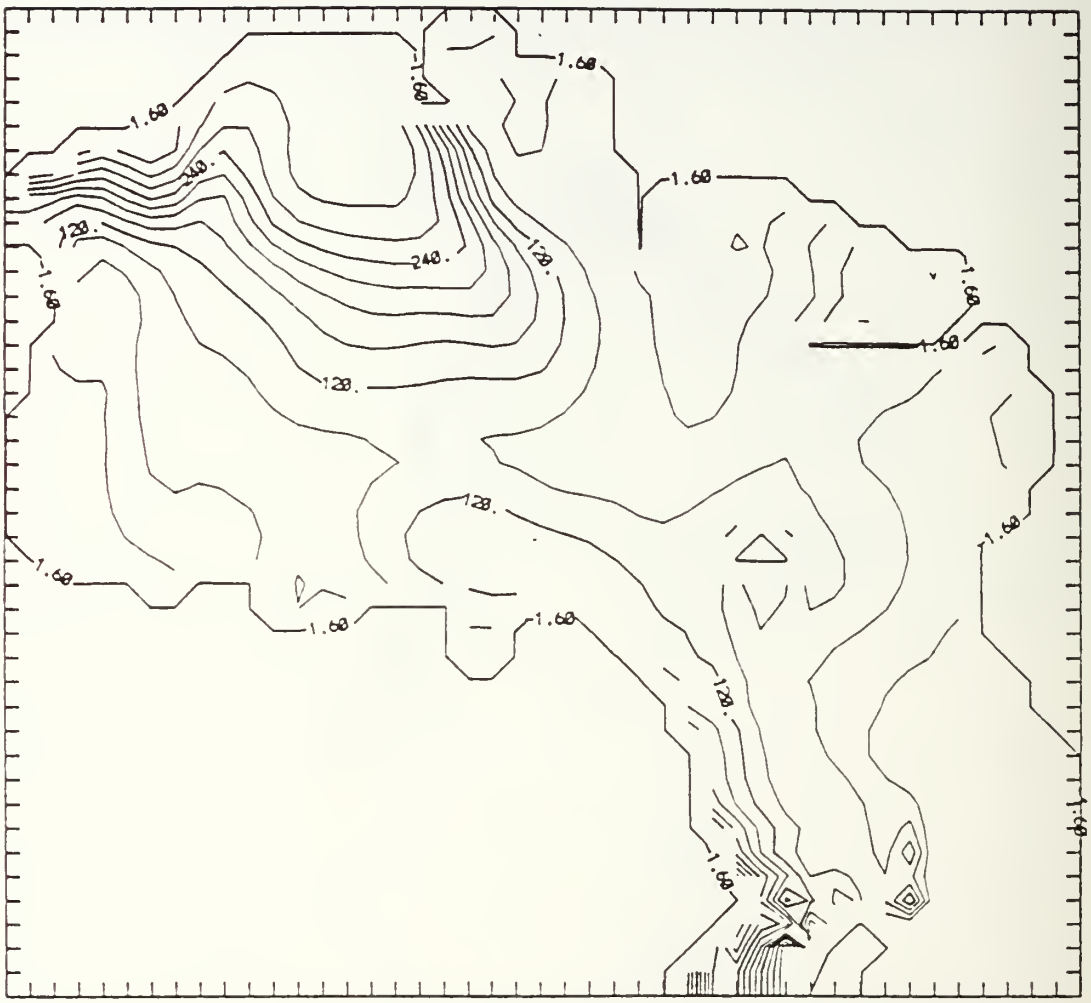

Figure 7.3 Simulated ice thickness contours (cm) for April, 1977. Constant ocean heat flux = 25 W/m^2 (run D2).

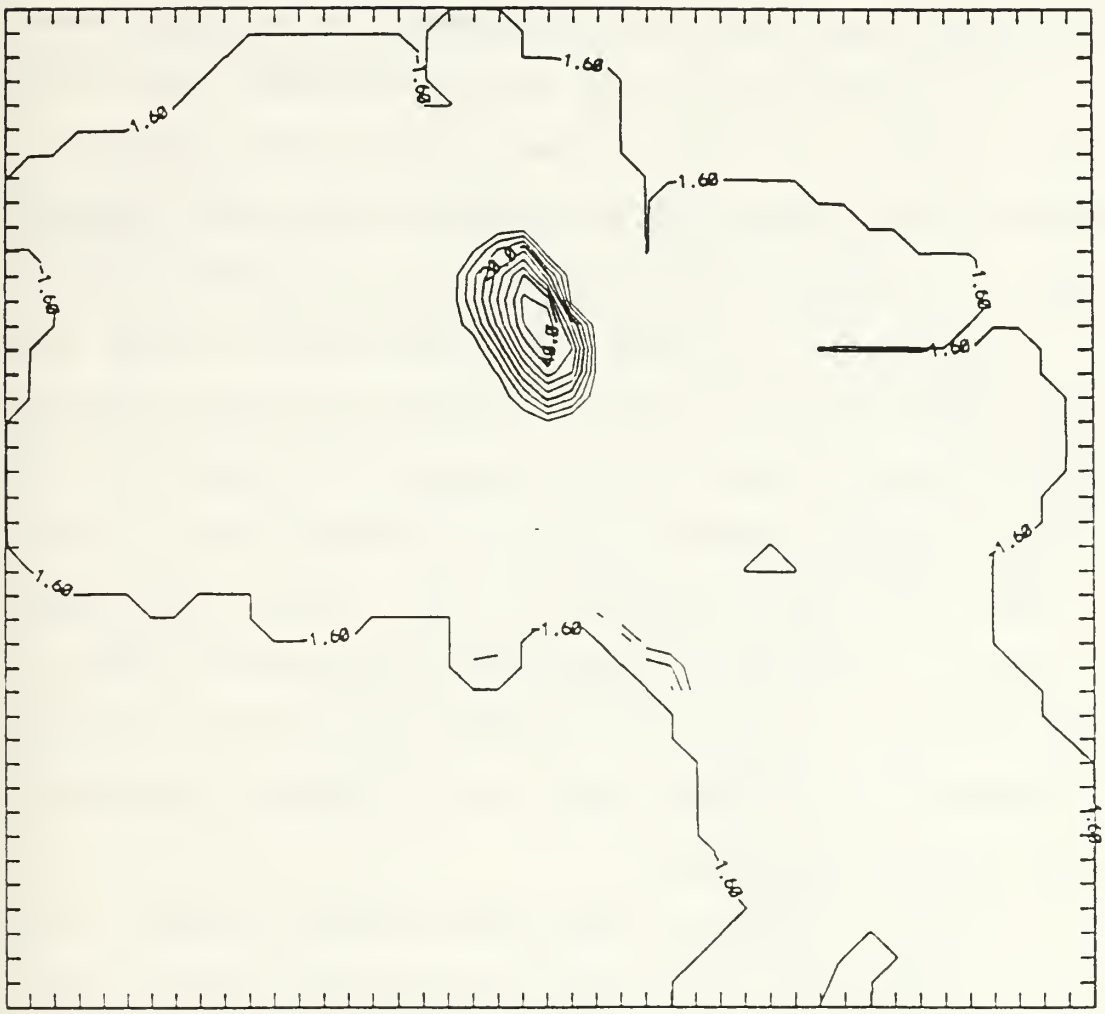

Figure 7.4 Simulated ice thickness contours (cm) for August, 1977. Constant ocean heat flux = 25 W/m^2 (run D2).

a totally unrealistic simulated winter ice cover. Although the prescribed heat flux in the Barents and Norwegian Seas during winter was positive, it was still considerably less than in the base model case (run D1). This resulted in considerably less melting and extended ice coverage there.

Run D3 used an ocean heat flux set to zero. This produced even heavier ice during winter in the North Atlantic and Greenland Sea (Figure 7.5) because the ocean heat flux in that region was reduced even further from the values used in run D1. The ice also remained longer and stayed thicker around the western ice boundary where excessive meltback occurred in run D1 in summer (Figure 7.6). However the meltback was still somewhat severe compared to the observed data. For the purposes of these observations the western ice boundary included the Beaufort, Chukchi and East Siberian Seas. The central pack thickness and distribution remained relatively unchanged from the base model as the normal simulated heat flux there was also zero.

Run D4 had no stress from ocean surface currents. In this case the pack ice thicknesses decreased slightly but the relative distribution of the ice thickness changed very little. In comparison to the base run, the ice cover over the Beaufort Gyre was rotated counter-clockwise approximately fifteen degrees (Figures 7.7 - 7.8). The MIZ expanded outward in all regions except the EGC where the ice advection was suppressed. The thickness gradient marking the poleward side

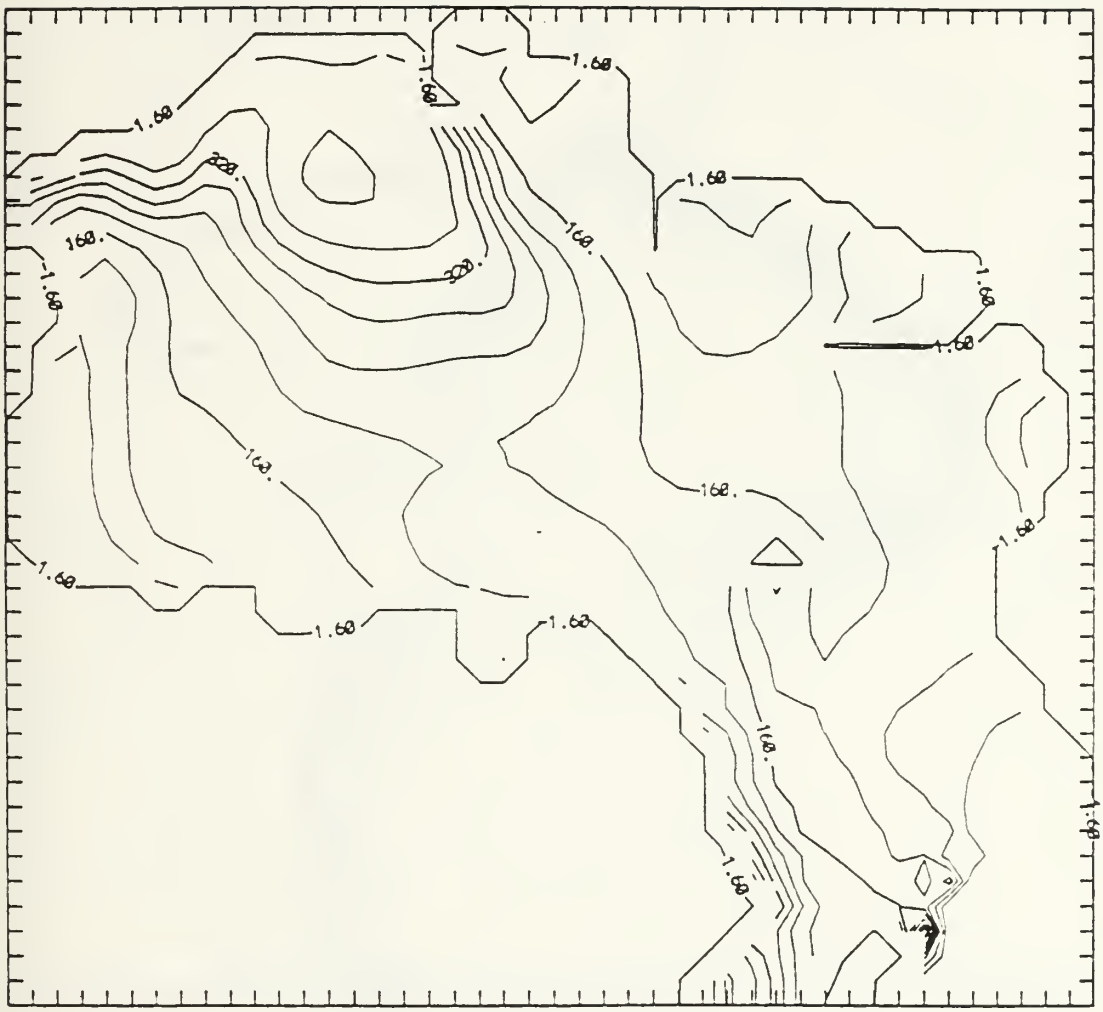

Figure 7.5 Simulated ice thickness contours (cm) for April, 1977. Ocean heat flux = 0.0 W/m^2 (run D3).

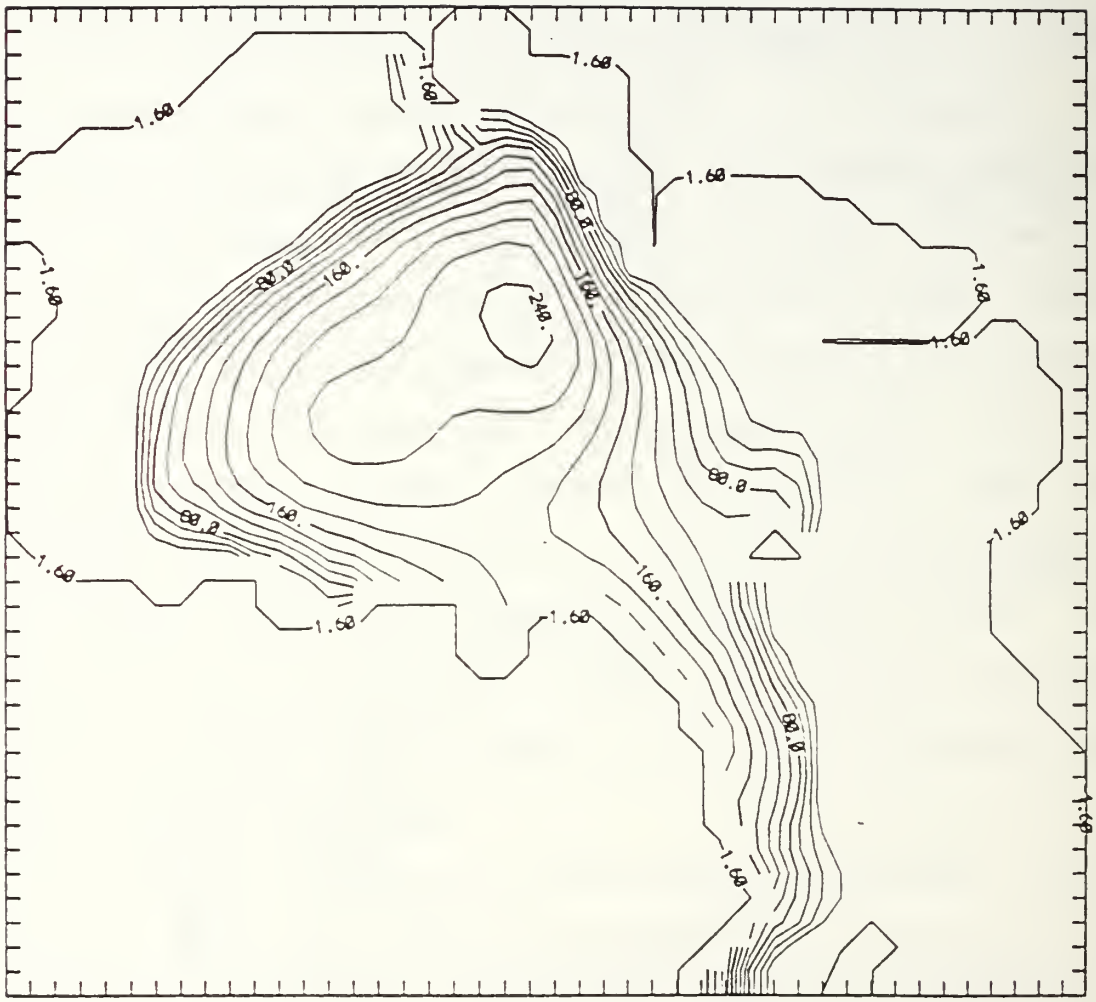

Figure 7.6 Simulated ice thickness contours (cm) for August, 1977. Ocean heat flux = 0.0 W/m^2 (run D3).

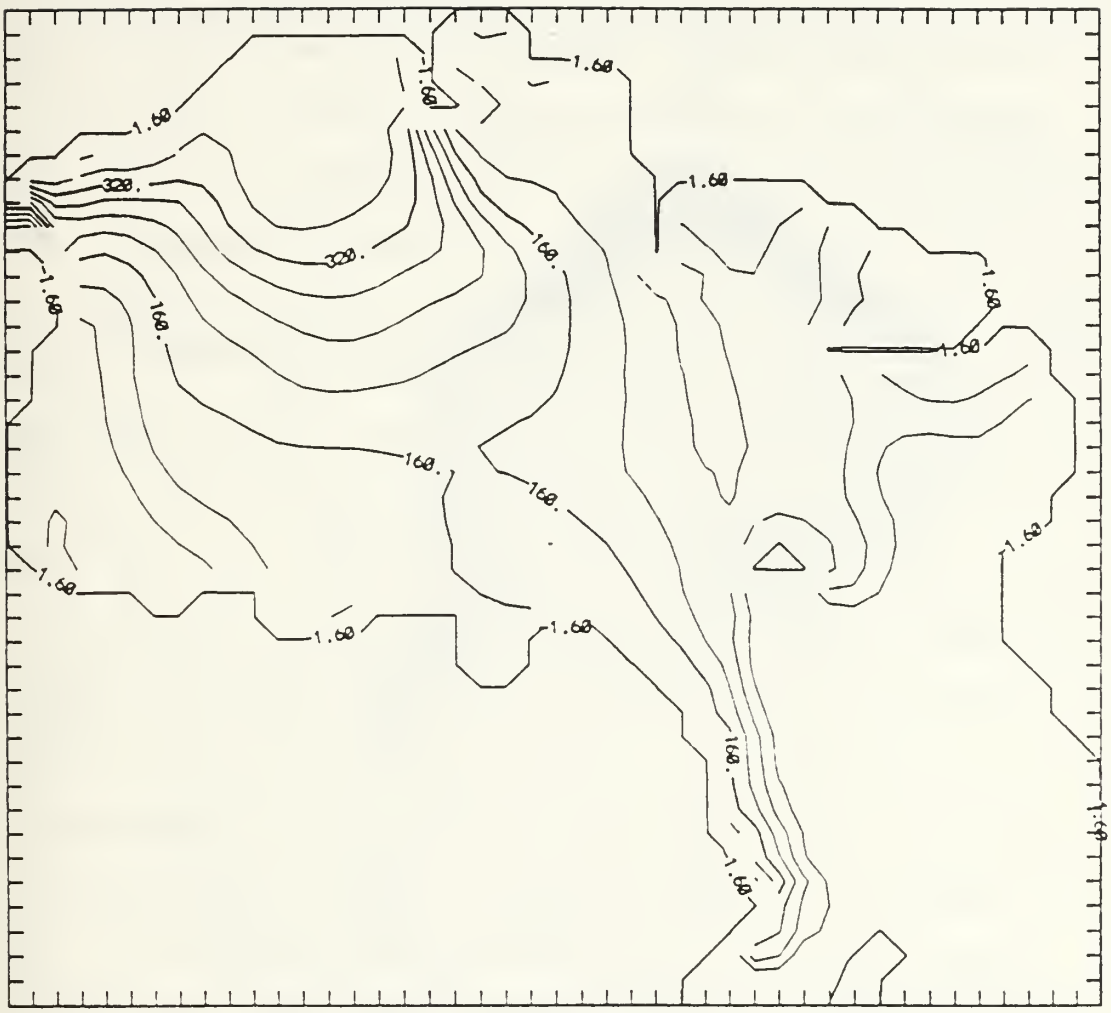
1.60
1.60
1.60

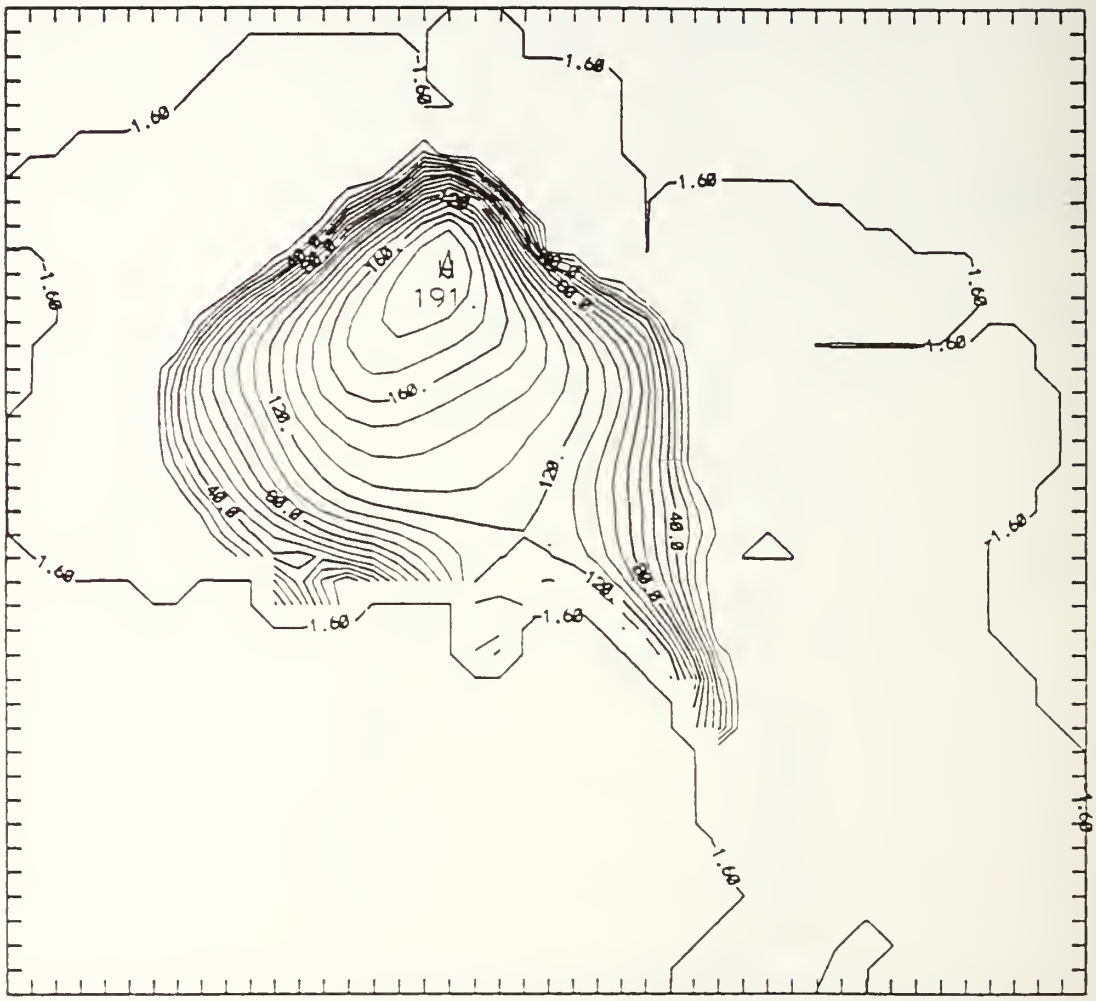

Figure 7.8 Simulated ice thickness contours (cm) for August, 1977. Level two current velocities = 0.0 m/s (run D4).

of the Transpolar Drift Stream (TPD) also became less intense. Three supplementary runs were conducted with the same dynamic conditions as run D4 but using different ice strength values as in the ice strength experiment. As ice strength was increased, which reduced the plasticity of the ice, the main features separating run D4 from run D1 became less noticeable.

In run D5, a similar counter-clockwise rotation to the ice field as in run D4 was observed for the Beaufort Gyre ice cover. The reduced advection in the TPD and EGC was evidenced by the reduced thickness gradients in the current regions (See Figure 7.9). The combined reductions in ice pack thickness from higher ocean heat flux in the central Arctic and no dynamic ocean forcing resulted in a complete ice meltback by August.

The direct dynamic forcing of the wind on the frozen surface was removed in run D6 by setting the ice/air and snow/air drag coefficients to zero. Ice thickness was reduced by approximately 50% within six months and the thickness distribution pattern also changed substantially (Figures 7.10-7.11). The central pack shifted over 1000 km towards the Beaufort Sea, but due to the reduced ice thickness, the thickness gradient there changed very little. Ice remained in the western boundary seas at least one month longer than the standard case and the initial MIZ retreat in that region was not as severe. However the overall reduced thickness resulted in a smaller total ice cover in the Arctic by August.

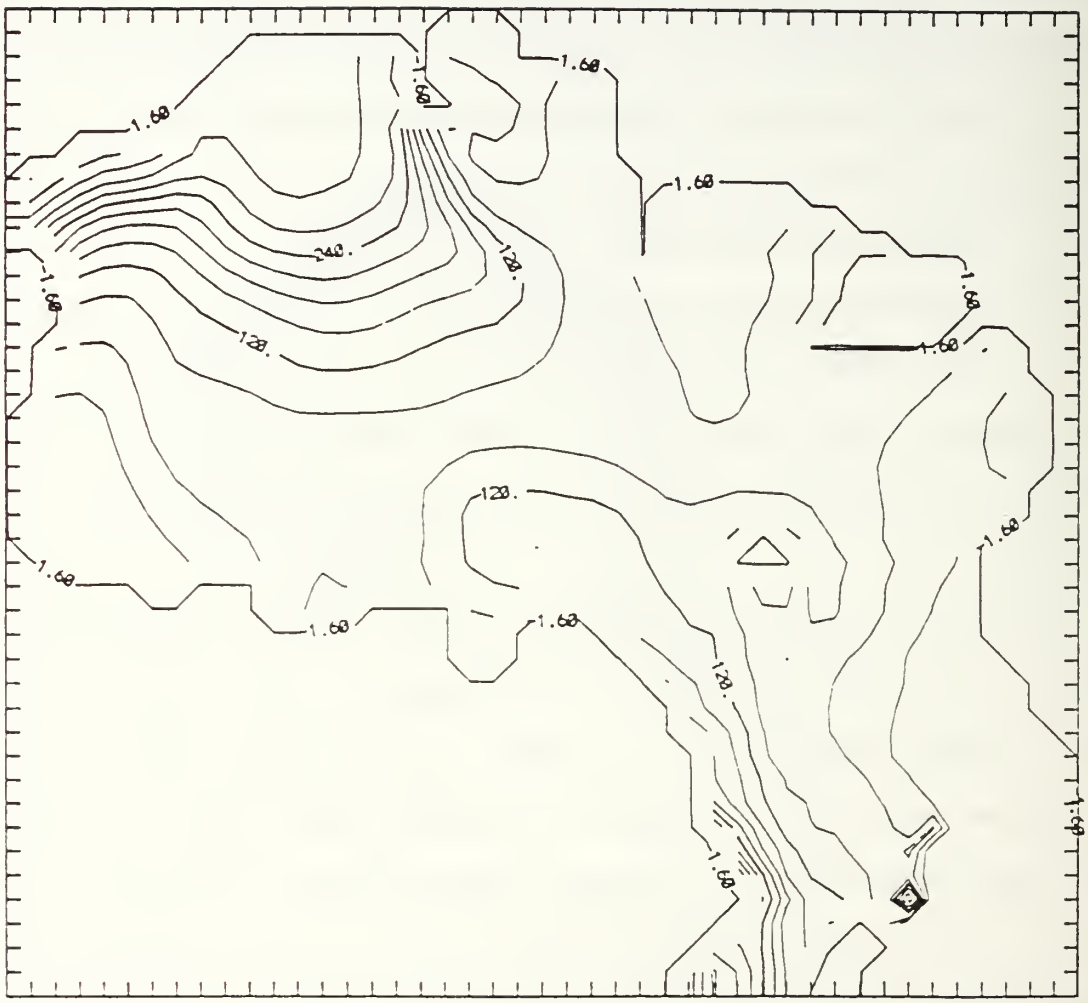

Figure 7.9 Simulated ice thickness contours (cm) for April, 1977. Ocean heat flux and level two velocities = 0.0. (run D5).

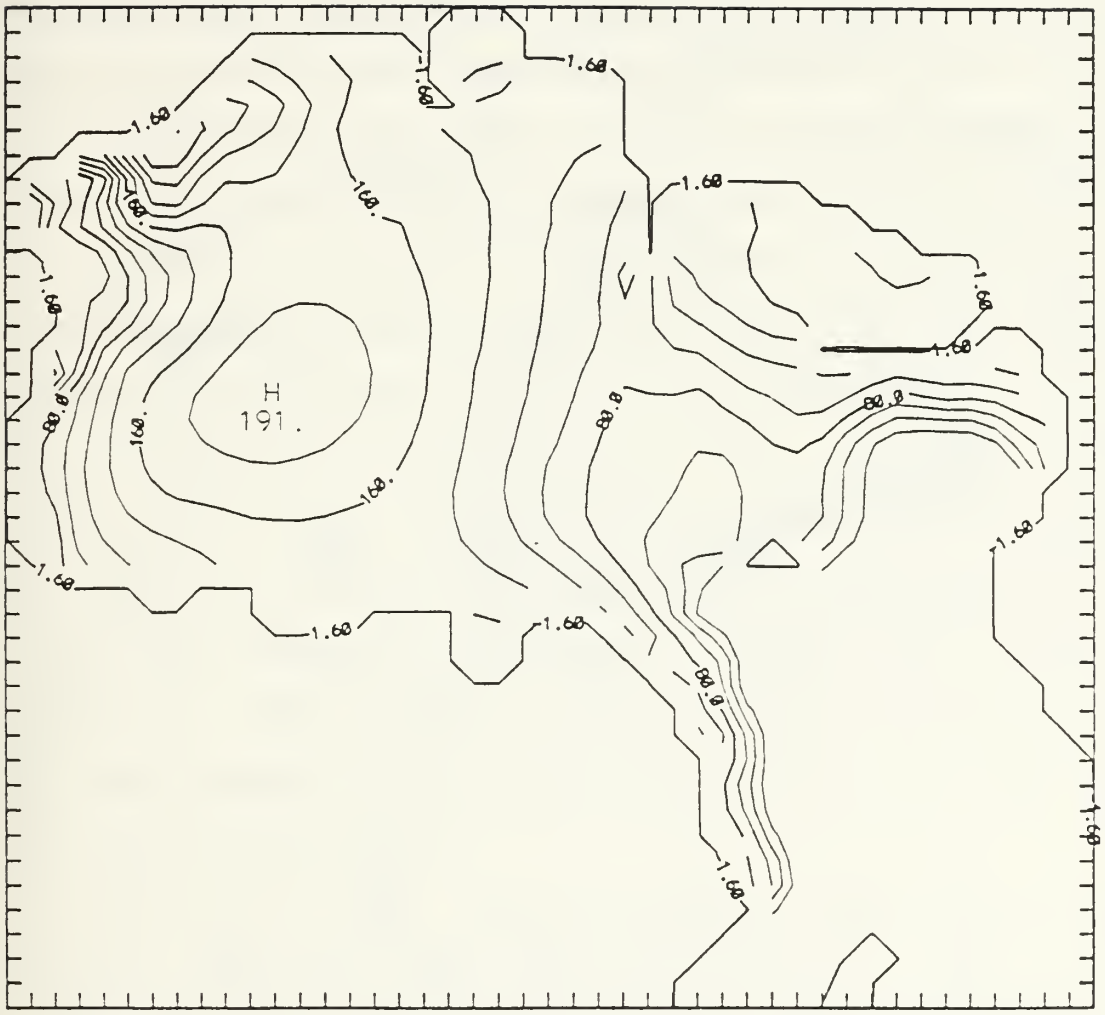

Figure 7.10 Simulated ice thickness contours (cm) for April, 1977. Wind stress = 0.0. (run D6).

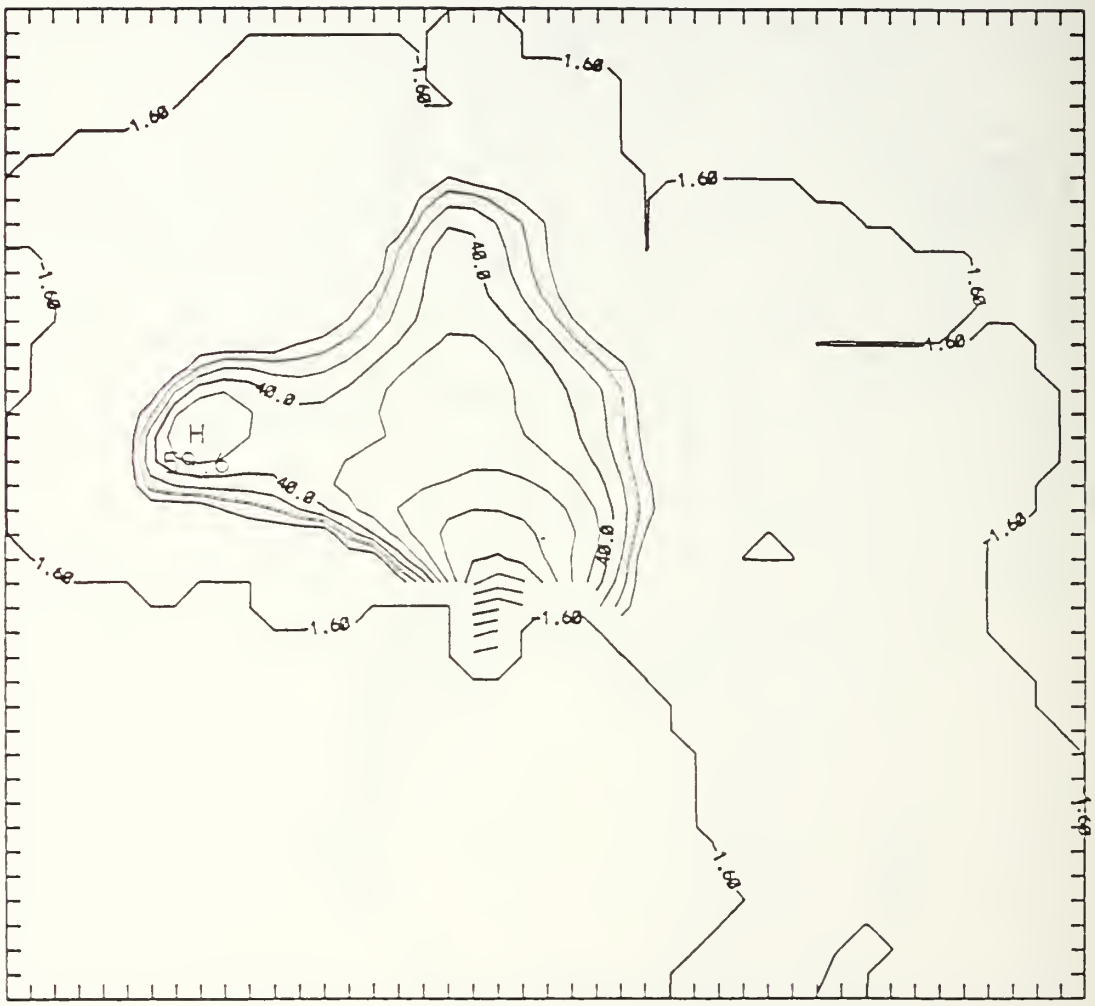

Figure 7.11 Simulated ice thickness contours (cm) for August, 1977. Wind stress = 0.0. (run D6).

The advection of ice in the TPD and EGC was noticeably reduced.

The run D7 simulation removed all direct dynamic forcing from both the air and ocean. No horizontal ice velocity was permitted. The same large shift of the central ice pack towards the Beaufort Sea was observed similar to run D6 but the ice thicknesses were not as severely reduced. The MIZ retreat in the Beaufort Sea started earlier but did not move as far poleward as in run D6. Run D7 showed a noticeable ice retreat poleward of Spitsbergen and in the EGC which would correspond to the removal of the TPD and EGC (Figures 7.12 - 7.13). A comparison of the summer thickness contours for runs D5, D6 and D7 shows that in those simulations where the central pack is reduced to thicknesses on the order of 150 cm or less, the subsequent evolution of the ice cover changes dramatically. There appears to be a critical thickness below which the influence of the various mechanisms controlling the ice changes significantly.

Finally run D8 used the same dynamic limitations as run D7; however the ocean heat flux was also set to zero. The same excessive ice cover over the Barents Sea as was observed in run D3 was repeated and the same general ice thickness and distribution pattern as for run D7 was produced. However in contrast to all the other runs, the ice remained over the western boundary seas for the entire year-long simulation.

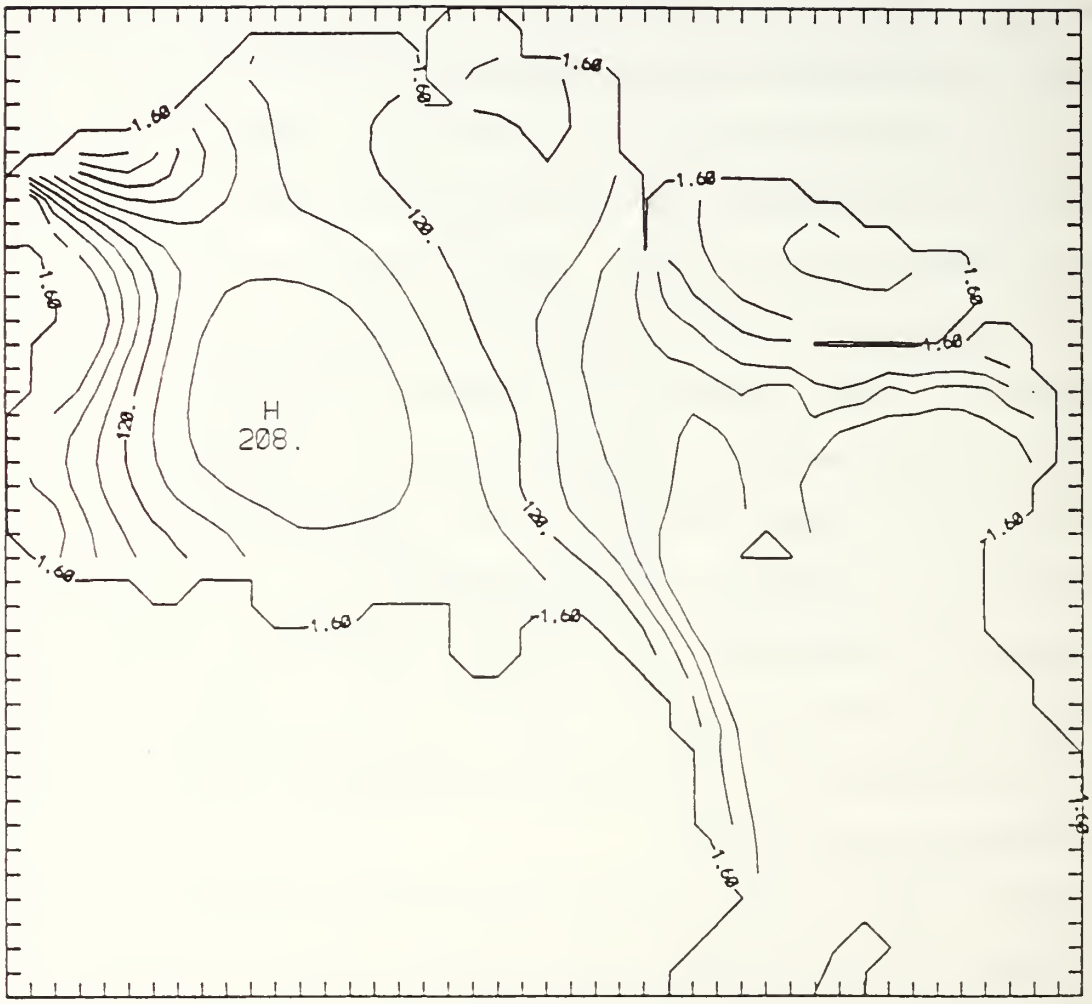

Figure 7.12 Simulated ice thickness contours (cm) for April, 1977. Wind and ocean current stress = 0.0. (run D7).

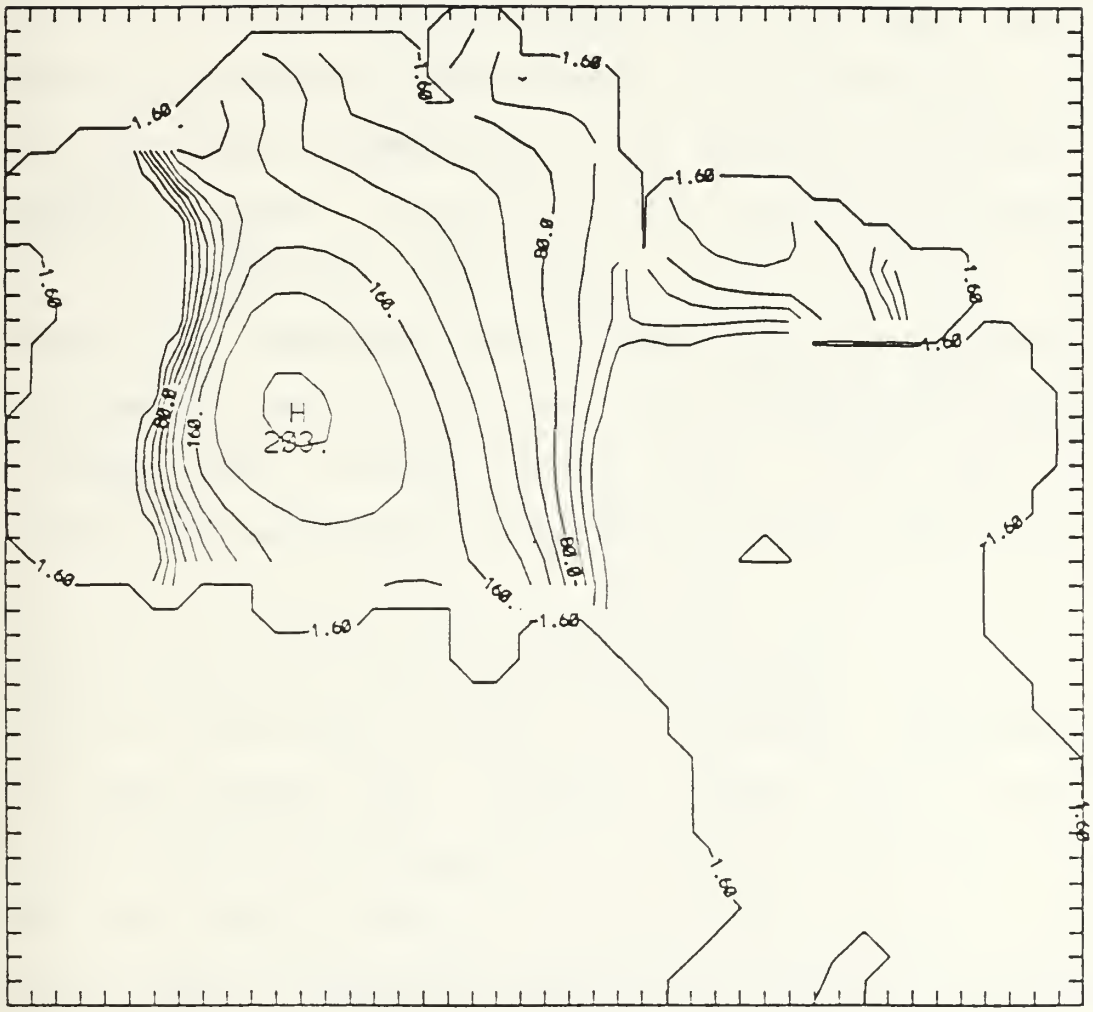
1.60
1.60
1.60

Furthermore, the ice edge did not retreat poleward of Spitsbergen, a condition closer to the observed fields than the previous simulations (Figures 7.14 - 7.15).

C. DISCUSSION

This experiment was conducted primarily to determine whether ocean heat flux or water stress from ocean currents was the more important process determining the limit and thickness distribution of the ice cover. These are the two primary processes which become more realistic once the prognostic ocean is included in the linked model. The results indicated that such a simple determination was not possible. As has been noted in the previous chapters, there appear to be many factors working in combination and often with opposing effects.

The direct dynamic influence of ocean surface currents influences the simulated ice cover by distorting it in the direction of the surface currents. The Canadian Basin ice pack is rotated clockwise by the Beaufort Gyre and ice is advected along the streamlines of the TPD and the EGC. This increases the thickness gradient poleward of the TPD and pushes the summer ice edge in the eastern Arctic towards Spitsbergen and well south along the east coast of Greenland. The region of thickest multi-year ice is shifted towards the Fram Strait. The ocean currents converge the ice to the center of the gyre and into a region off the north coast of

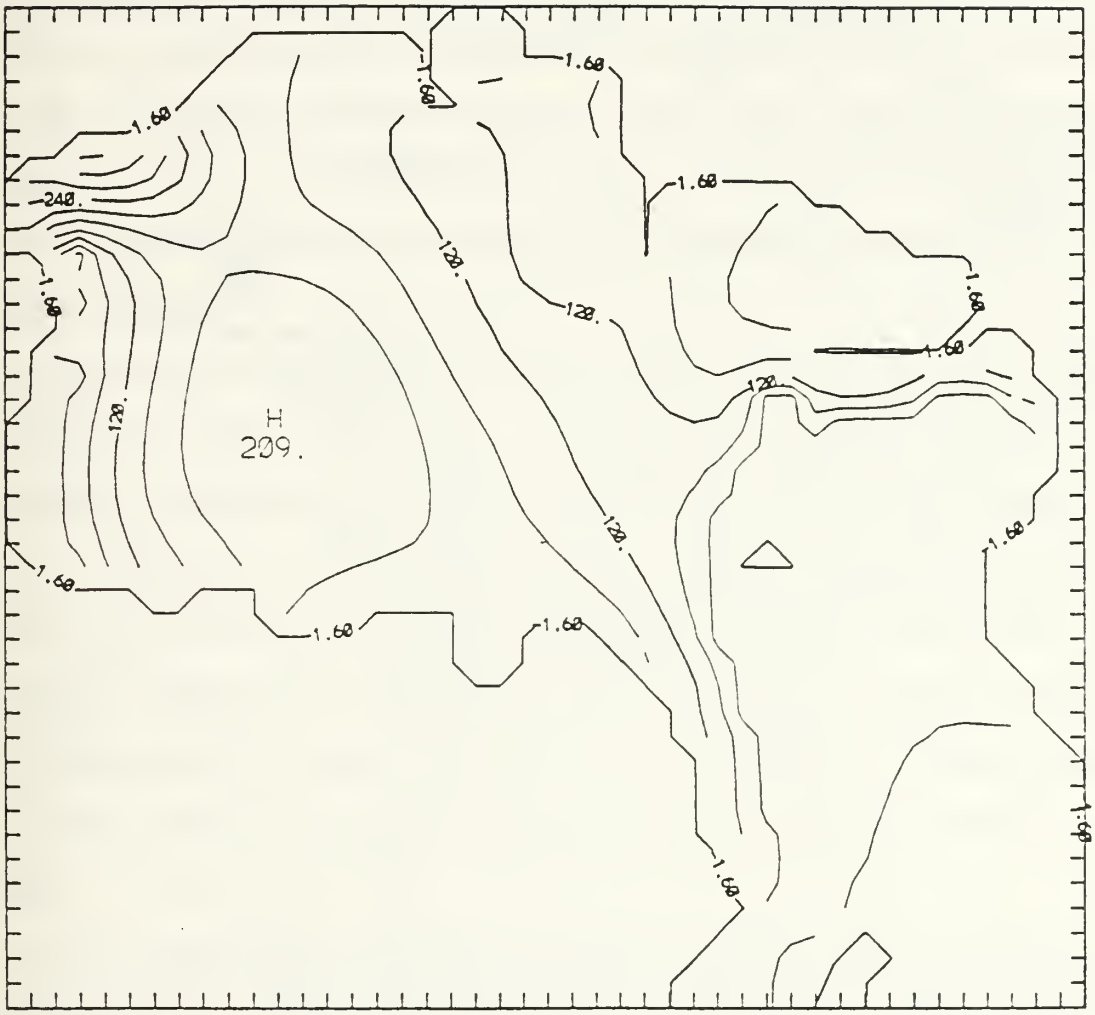

Figure 7.14 Simulated ice thickness contours (cm) for April, 1977. Wind and ocean current stress and ocean heat flux = 0.0. (run D8).

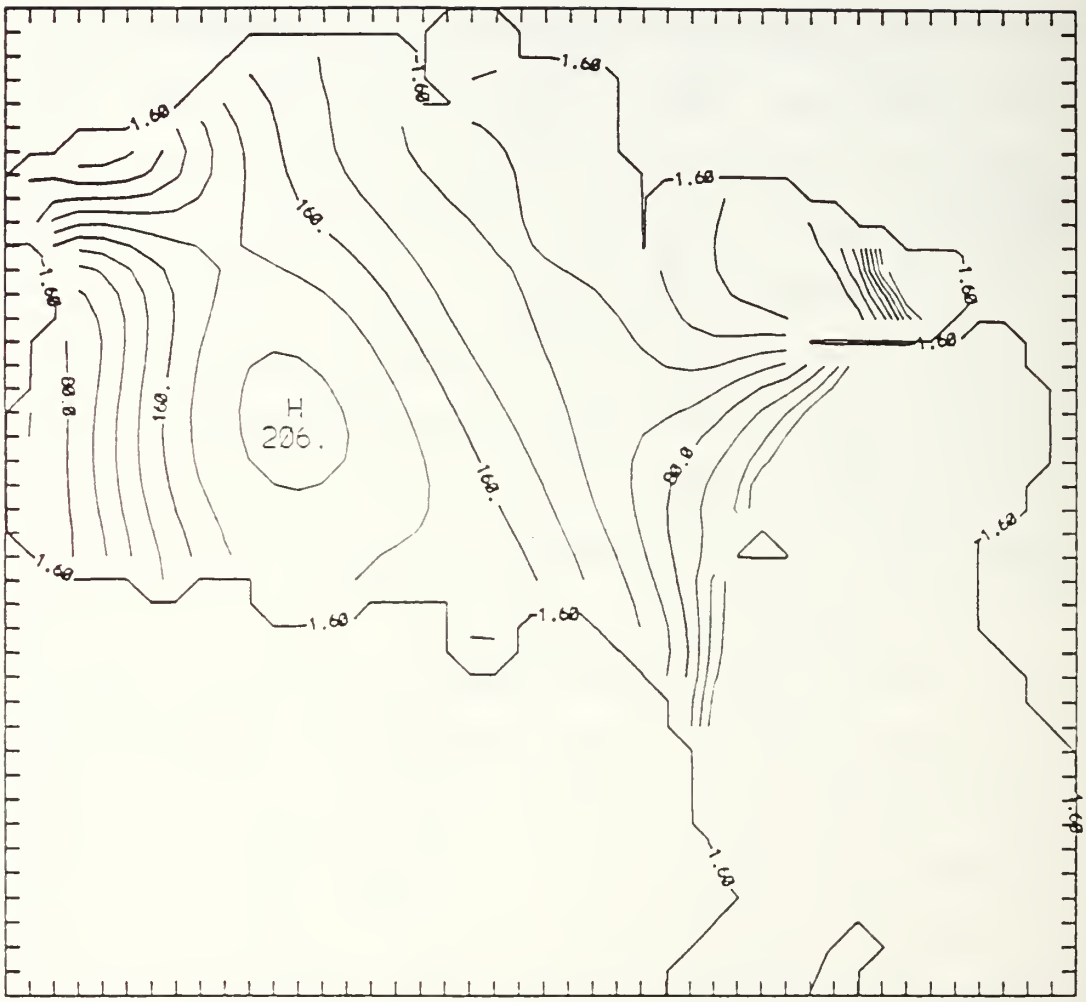
1.60
1.60
1.60

Greenland and the Canadian Archipelago. This accounts for at least a portion of the thicker ice evident in those regions.

The ice is advected parallel to the coastline all around the perimeter of the Canadian Basin. This reduces the ice thickness immediately poleward of the Canadian Archipelago but the ice does not collect in the Beaufort Sea since most of it is quickly melted by the high ocean heat flux there. The ice that is left continues to be pushed along the coastline out of the Beaufort and Chukchi Seas and into the Laptev Sea.

The ice cover in the Norwegian and Barents Seas is nearly unaffected when the water stress from ocean currents is ignored. However changes to the ocean heat flux result in major changes to the simulated ice cover. Of course the heat flux at any position is a function of earlier horizontal and vertical advection. Therefore the currents do serve a purpose in this region. However it is notable that the dynamic impact of these currents at the space and time scales used here is small.

The wind stress appears to have a much stronger effect on the ice cover than the ocean current stress at these spatial and temporal scales. The ice thickness and distribution is drastically altered when wind stress is removed from the simulations. The wind stress appears to provide the majority of the compressive forcing which produces the realistic ice thicknesses in the central pack and convergence regions. For

the 1977 forcing year, the wind provided an offshore component to the ice edge position around the entire western half of the Arctic Basin, particularly in the East Siberian Sea. In the eastern Arctic Basin the wind stress appeared to increase the ice advection along the TPD and the EGC and the ice cover was pushed southward in the Barents Sea. It should be noted that the Walsh monthly mean wind fields used in this study vary interannually in direction and intensity (Walsh, private communication). Therefore considerable differences in the wind forcing and corresponding changes to the ice fields would probably be observed had a different forcing year been used in this experiment. Nevertheless, the relative strength of this forcing mechanism would be expected to remain similar.

The ocean heat flux, wind stress and ocean currents form a feedback which amplifies the influence of each of the individual mechanisms on the melt cycle. For example, the ocean heat flux thins the ice which then allows the dynamic forcing to have more effect. Conversely, the thicker ice regions which develop over areas of reduced or negative ocean heat flux become less sensitive to the dynamic forcing. This feedback is stronger when the ice strength is reduced as described in the ice strength experiment.

D. CONCLUSIONS

The simulations conducted in this experiment support the view that the importance of the various dynamic and

thermodynamic mechanisms controlling the monthly variations of ice coverage vary regionally across the Arctic Basin. The ocean heat flux appeared to be the dominant mechanism controlling the extent of the monthly average ice cover while the wind and current stresses appeared to be the mechanisms determining the ice thickness and distribution. However the dynamic forcing from winds and currents had quite different effects in the different regions of the Arctic Basin. In the western basin which was incorporated in regions 1 and 2, the wind and currents acted in concert with the ocean heat flux to clear the ice from the boundary seas. In contrast, these same forces acted to increase the ice cover in the TPD and EGC (region 3) while in the Barents and Norwegian Sea (region 4), the wind stress tended to oppose the effects of ocean heat flux and current stress had little impact. In general, the forcing from ocean currents was usually weaker than from ocean heat flux or wind stress. The exceptions were in the strong current regions along the coast in the Canadian Basin and along the axis of the TPD and EGC. Inclusion of wind and current stresses always tended to increase the ice area, either directly or indirectly. In regions 3 and 4 the effect was direct by off-ice advection. In regions 1 and 2 the effect was indirect. The dynamics initially caused the ice to converge which thinned the ice on the boundaries thereby allowing more ice growth and subsequent convergence. As the central pack became thicker, it also became stiffer. The

thickness gradients began to extend further from the central core and the MIZ also increased in thickness. The ocean flux was unable to melt the same extent of a thicker MIZ; therefore the ice area expanded.

The ocean does not appear to control the ice coverage significantly through direct dynamic forcing. However it does appear to have a very important thermodynamic role. The three dimensional ocean circulation positions the heat contained in the intermediate depth ocean layers in the appropriate regions. This heat is then available whenever the vertical circulation, driven by conditions at the surface, extends deep enough to tap it. The ocean essentially preconditions the ocean below the mixed layer so that the heat necessary to control the ice edge at any location is available.

The dramatic changes to the ice cover evident in the simulations where wind stress and ocean heat flux were modified emphasized the sensitivity of the model to these parameters. The importance of realistic ocean heat flux was already suggested in previous chapters and is further supported by the results of this experiment. This experiment also emphasized the importance of appropriate wind forcing fields if the monthly average ice cover is to be simulated accurately in the Arctic.

VIII. STATISTICAL CONSIDERATIONS

The time series of "observed" ice concentration data covered the same regions at the same grid scale and over the same time period as the simulated data. This permitted calculation of the correlations between the various model simulations and the observed fields. The differences between the correlations calculated for each new experiment were compared to determine if the changes incorporated into the model improved the accuracy of the simulated ice concentration fields. A large increase in the correlation coefficient indicated that the modifications made to the model improved the accuracy of the output. The sign of the correlation differences were usually consistent indicating that the modifications made had produced a noticeable and consistent change. However statistical analysis of the results was required in order to determine if these changes were statistically significant.

Chervin and Schneider (1976) and Chervin (1980) investigated a similar problem as applied to atmospheric general circulation models (GCMs). They suggested that a knowledge of the "noise climatology" or natural variability inherent in a GCM was a prerequisite for judging the significance of the results from prescribed change model experiments. Change model experiments are similar to what has

been done in this work in which various elements of a base model are changed to investigate changes in the simulated end conditions. Chervin and Schneider (1976) noted that the basic problem was one of

> distinguishing between signal (that part of the difference between the results of a prescribed change experiment and an unperturbed control case which is attributable to the prescribed change) and noise (some measure of inherent model variability) in a prescribed change response.

The model variability, in the case of the atmospheric GCM's referred to above, was a result of the numerical representation of random processes in the atmosphere. Each run of such a model allows for some randomness and as a result the simulated fields will vary from run to run with no change in boundary conditions or numerical code within the model. The numerical model used here does not have a similar output variability. The simulated ice fields produced will not change unless the boundary conditions or numerical code is modified. However in this work, it is not the model output fields which are directly compared but the difference between models of the correlations between simulated and observed ice concentration fields. Therefore it is these correlation differences which must be examined to determine their statistical significance.

A. METHOD

The correlations calculated in this work use 120 sample pairs (every month for ten years). Each value in each paired

sample was the average of several hundred grid values of ice area contained within each of the four designated regions. A common method to establish the variability and subsequently the confidence intervals of the correlation differences, required that subsets of the paired samples be selected and assumed independent. The time series of 120 paired samples were divided into subsets which were deemed independent and correlations calculated for each. Means and standard deviations for these subset correlations were then determined. However if the number of subsets was too small or if the subsets were not independent of each other, their means were likely to be biased. Significant persistence of ice concentration anomalies has been observed in areas of the eastern Arctic to lags of several months and in exceptional cases to over a year (Fleming, 1987). The method presented here strikes a compromise balancing the opposing requirements of independence versus a fairly large number of subsets. A subset size of one year was selected because it was exceptional to find dependence at lags over a year. This determined that the maximum number of subsets was 10.

The standard formulation used to calculate the 95% confidence interval was:

$$XB \pm t_{0.975} \times SD \times (n)^{1/2}$$

where XB was the average correlation over 10 subsets, t was the Student t distribution value at 95% confidence level and

9 degrees of freedom, SD was the estimated standard deviation of the 10 subset correlations and n was the number of years (10). This formula was derived from normal theory which required $n \geq 20$ and observations independent and identically distributed. Obviously our sample size of 10 made this technique suspect, however it was the largest sample possible in view of the dependence consideration.

An alternative technique used to investigate the statistical significance of the difference between the various correlations was called "Jackknife." (For a complete description see, for example, Mosteller and Tukey (1977)). This technique offers a way to establish sensible confidence limits in complex situations in which the observations are not necessarily independent and identically distributed. The correlations were calculated with all the data and then after dividing the data into subsets, correlations were recalculated by leaving out each subset, one at a time. The subset size chosen was again one year. Pseudo values were determined by weighting the correlations appropriately to account for the sampling "overlap" and the Student t tables were then used to establish the confidence limits. The procedure is outlined below.

The correlations calculated for two different models using all 10 years of data are $r_1(0)$ and $r_2(0)$. The correlation difference, $Y(0)$, is then

$$Y(0) = r_1(0) - r_2(0)$$

If $r_1(n)$ and $r_2(n)$ are the correlations leaving out year n, where n=1,2,...,10, then

$$Y(n) = r_1(n) - r_2(n)$$

The nth pseudo value, $Y^*(n)$, is calculated as follows:

$$Y^*(n) = (10 \times Y(0)) - (9 \times Y(n))$$

where 10 and 9 are the weights appropriate to our one year subset size. The variances, s^2, of the ten pseudo values are calculated and the approximate two-sided 95% confidence limit for the difference of the true correlation was given by:

$$Y(0) \pm t_{0.975} \times (s^2/10)^{1/2}$$

where $t_{0.975} = 2.262$. This value was found in the Student t table using 9 degrees of freedom.

B. RESULTS

The common and Jackknife techniques were applied to the correlations calculated in the Interactive Ocean Experiment (Table 5). For the common method, means, standard deviations and confidence intervals were calculated from each group of ten subset correlations. These are shown in Table 8. Confidence intervals were calculated for both sets of correlations (the B series from the model with the interactive ocean and the C series from the model using the ten year

TABLE 8

MEANS, STD DEVIATIONS AND CONFIDENCE INTERVALS OF THE CORRELATIONS OF 10, 1-YEAR SUBSETS. RESULTS FOR EXPERIMENT B (FIRST LINE) AND C (SECOND LINE) IN ALL FOUR REGIONS

ICE AREA TIME SERIES

REGION	MEANS CORR B/CORR C	STD DEV CORR B/CORR C	95% CONF. INT. CORR B/CORR C
1	.9322	.0580	.8907-.9737
	.9200	.0504	.8839-.9561
2	.9323	.0529	.8945-.9701
	.9198	.0627	.8750-.9646
3	.9628	.0164	.9511-.9745*
	.9396	.0271	.9202-.9590*
4	.9500	.0190	.9364-.9636*
	.9061	.0466	.8728-.9394*

ANOMALY TIME SERIES

REGION	MEANS CORR B/CORR C	STD DEV CORR B/CORR C	95% CONF. INT. CORR B/CORR C
1	.3472	.4404	.0322-.6622
	.2779	.3864	.0015-.5543
2	.7198	.1696	.5985-.8411*
	.5670	.3614	.3085-.8255
3	.4021	.2422	.2289-.5753
	.3305	.2583	.1457-.5153
4	.6266	.2428	.4529-.8002
	.4952	.2354	.3268-.6636

B simulation was with fully interactive ocean model
C simulation was with 10-year mean cycle ocean
* difference between the correlations is 95% significant

average ocean condition). The intervals were then compared to determine if they confirmed each other and how important the variance of the correlations was.

The differences between the correlations for regions 3 and 4 of the ice area time series were determined to be significant at the 95% confidence level. The average of the C correlations fell outside the confidence limits of the B correlations and the average of the B correlations fell outside the confidence interval of the C correlations. This provided some measure of confirmation. The correlation differences between B and C for the ice area anomaly time series were primarily insignificant at the 95% confidence level. One exception was the B model's region 2. In that case, the C model average correlation fell outside the B model's correlation confidence interval. However, the opposite was not true due to a much higher correlation variance for the C model.

In the process of applying the Jackknife technique, the correlation differences (B subtract C) for all four regions, for both time series, and for 10 pseudo value subsets were calculated. These are shown in Table 9. Note that they were consistently positive. Table 10 shows the calculated pseudo values, their means, their standard deviations and the calculated 95% confidence intervals for the ice area time series. Table 11 shows the same information for the ice area

TABLE 9

CORRELATION DIFFERENCES BETWEEN B AND C FOR THE TOTAL TIME SERIES AND FOR THE 10 PSEUDO SUBSETS (ONE YEAR REMOVED)

ICE AREA TIME SERIES

PSEUDO SUBSET	REGION 1	REGION 2	REGION 3	REGION 4
TOTAL	.0274	.0464	.0355	.0854
1	.0295	.0328	.0388	.1079
2	.0266	.0453	.0290	.0883
3	.0340	.0494	.0388	.0540
4	.0221	.0461	.0341	.0941
5	.0316	.0579	.0353	.0809
6	.0270	.0469	.0436	.0888
7	.0306	.0533	.0362	.0928
8	.0248	.0482	.0306	.0792
9	.0233	.0306	.0322	.0825
10	.0233	.0494	.0349	.0814

ICE AREA ANOMALY TIME SERIES

PSEUDO SUBSET	REGION 1	REGION 2	REGION 3	REGION 4
TOTAL	.0973	.1780	.2336	.2840
1	.1093	.1038	.2496	.3731
2	.0922	.2539	.1826	.3110
3	.1271	.1647	.2911	.1577
4	.0974	.1978	.2185	.3166
5	.1407	.2125	.2104	.2498
6	.0976	.2034	.2978	.2807
7	.1257	.1956	.2644	.3094
8	.0819	.1714	.1586	.2004
9	.0792	.1068	.2240	.3455
10	.0312	.1797	.2263	.2971

TABLE 10

PSEUDO VALUES FOR THE ICE AREA TIME SERIES
MEANS, STD DEVIATIONS AND 95% CONFIDENCE INTERVALS OF THE PSEUDO VALUES

ICE AREA TIME SERIES

YEAR REMOVED	REGION 1	REGION 2	REGION 3	REGION 4
1	.0085	.1688	.0058	-.1171
2	.0346	.0563	.0940	.0593
3	-.0320	.0194	.0058	.3680
4	.0751	.0491	.0481	.0071
5	-.0104	-.0571	.0373	.1259
6	.0310	.0419	-.0374	.0548
7	-.0014	-.0157	.0292	.0188
8	.0508	.0302	.0796	.1412
9	.0643	.1886	.0652	.1115
10	.0643	.0194	.0409	.1214
STD DEV	.0361	.0756	.0388	.1246
MEANS	.0285	.0501	.0369	.0891
CONFIDENCE INTERVAL	.0016 TO .0532 *	-.0077 TO .1005	.0077 TO .0633 *	-.0037 TO .1745

* indicates that the correlation difference is 95% significant

TABLE 11

PSEUDO VALUES FOR THE ICE AREA ANOMALY TIME SERIES MEANS, STD DEVIATIONS AND 95% CONFIDENCE INTERVALS OF THE PSEUDO VALUES

ICE AREA ANOMALY TIME SERIES

YEAR REMOVED	REGION 1	REGION 2	REGION 3	REGION 4
1	-.0107	.8458	.0896	-.5179
2	.1432	-.5051	.6926	.0410
3	-.1709	.2977	-.2839	1.4207
4	.0964	-.0002	.3695	-.0094
5	-.2933	-.1325	.4424	.5918
6	.0946	-.0506	-.3442	.3137
7	-.1583	.0196	-.0436	.0554
8	.2359	.2374	.9086	1.0364
9	.2602	.8188	.3200	-.2695
10	.6922	.1627	.2993	.1661
STD DEV	.2794	.4145	.3997	.5883
MEANS	.0889	.1694	.2450	.2828
CONFIDENCE INTERVAL	-.1026 TO .2972	-.1185 TO .4745	-.0523 TO .5195	-.1368 TO .7048

anomaly time series. The correlations are considered significantly different using the Jackknife method if the confidence interval does not include zero. This is the case for region 1 and 3 of the ice area time series; however, no similar cases exist for the anomaly time series.

C. DISCUSSION

The consistently positive differences between the correlations from the B and C models would suggest that the B model was a significant improvement over the C model. However neither of the two statistical approaches used here was able to confirm this at the 95% confidence level for more than three of the eight correlation difference cases. The main reason for this was the high degree of correlation variability.

Correlation variability was most noticeable in the ice area anomaly time series because the dominating influence of the annual cycle was removed, thereby reducing the correlation coefficient values and allowing more correlation variability. This was also apparent by comparing the actual time series plots (Figures 4.19 - 4.22 with 4.31 - 4.38). The variability indicates that the model did very well for some years in some regions yet very poorly in others. The simulated ice condition at any time was a direct function of the forcing and initial conditions. The model had no inherent variability. Therefore the changing performance of the model had to be a

result of some other cause. One explanation could be that some mechanism which was not properly represented in the model was controlling the ice and varying dramatically in importance from year to year, and region to region. The model would perform fine when this mechanism had little influence but would be unable to account for those periods or regions when the mechanism was important. Alternatively, the prescribed forcing may be in error. In particular the monthly averaged atmospheric forcing may have too long a temporal resolution to adequately represent strong, short term episodic changes. The ice dynamics experiment indicated that these could be important because wind stress was able to alter the ice field dramatically in short periods of time and the subsequent evolution of the ice field was also modified. Of course some combination of model limitation and forcing error was also possible.

D. CONCLUSIONS

This work was done to determine if the correlation differences between the different model simulations and observed fields of ice concentration could be shown to be statistically significant. In general, it appears that the correlations determined between modelled and observed fields of ice area are apparently not yet stable enough to do so. The improvement in the correlations from model C to model B was consistent in all regions, for all subsets and for both

the ice area and anomalous ice area time series. This would certainly suggest that the improvement was real. However the correlations were so variable, particularly in the ice area anomaly case, that supporting statistics could not be provided.

IX. SUMMARY

This work has involved the development of a linked ice-ocean numerical model capable of simulating the annual cycle and interannual variations of ice cover in the Arctic. The accuracy of the simulated seasonal ice area and ice edge position appears to be an improvement over any other large scale models operating at present, yet the computational requirements have been maintained at very reasonable levels.

A. MAIN CONCLUSIONS

The objectives for this thesis have been met. It has been shown that the inclusion of an interactive, prognostic ocean component in the ice model provides substantial improvement to simulations of both the annual cycle and interannual variations of the ice cover. Closer examination of the effects of the various ice control mechanisms indicated that the main reason for improved ice cover simulation with the prognostic ocean was a more realistic representation of the ocean heat flux. The ocean heat flux varied considerably between regions and between seasons. The surface currents were also highly variable. However, in general, the forcing from ocean currents has a second order effect on the ice cover. Exceptions to this were evident in the strongest current regions (East Greenland Current, Transpolar Drift

Stream and boundaries of the Beaufort Gyre) where the dynamic impact of the currents had a more pronounced effect on the ice.

The linked model was sensitive to changes in the ice rheology. Based on comparison with highly averaged observed thickness data (Bourke and Garret, 1987) the optimum value chosen for the strength parameter in the "bulk viscous" rheology was $P^* = h \times 10^4$. This value reduced the rigidity of the ice pack, allowing greater compression and therefore more realistic ice thickness and distribution. However, the reduction in the ice strength degraded the correlation between simulated and observed total ice cover. The ice retreat in the western Arctic, which was already somewhat severe at the higher ice strength, receded further when P^* was reduced. Since there was no compensating improvement in the winter ice extent, the correlation coefficients decreased.

The increased melting in the western Arctic at the reduced ice strength appeared to be a result of a feedback between ice formation rates and ocean heat flux. The reduced ice strength permitted a stronger response of the ice to dynamic forcing. This forcing was generally off-shore in the western Arctic. The ice was forced to converge in the central pack and along the north shore of the Canadian archipelago, opening up large areas of open water and thin ice over the shelves in the western Arctic seas. This permitted faster cooling of the surface water, greater ice production, more

salt extrusion and greater vertical mixing. The mixing was strong enough to break through the halocline and increase the ocean heat flux to the surface. This resulted in more extensive melting.

The fully linked model with the prognostic ocean was quite insensitive to albedo changes in the ice cover. This result was a clear contrast to previous model studies which demonstrated strong sensitivity to this parameter. The main mechanism included in this model but not in the models which displayed albedo sensitivity was the interannually variable ocean heat flux. This term appears to dominate the thermodynamic balance near the ice edge. The ocean heat flux thereby controls the concentration of the ice in this region and the overall extent of the ice pack. The thermodynamic impact of changing surface albedo is relegated to minor importance.

Results from the dynamic mechanism experiment supported the idea that the ocean heat flux dominated the albedo effect. However these results also indicated that there were conditions, particularly when the ice was thin, when the albedo did become important. Those cases which showed some albedo sensitivity had a combination of a small ocean heat flux and thin ice. Under these conditions, the change in the thermodynamic balance due to a change in the surface albedo could become relatively large and the model's albedo sensitivity was increased. These conditions were possible

over the shallow shelves, in newly frozen leads within the central pack and along some areas of the MIZ. Realistic representation of the frozen-surface albedo was therefore considered worthwhile and the improved albedo scheme of Ross and Walsh (1987) was incorporated into the model.

Examination of the relative importance of the various dynamic and thermodynamic ice cover forcing mechanisms indicated that each part of the fully linked model had a unique but interactively important role in the evolution of the ice cover. The ocean heat flux appeared to be the overall dominant factor controlling the position of the ice edge and the extent of the ice cover. Within the polar pack, it was the dynamic forcing, and in particular, the wind forcing which controlled the ice thickness and thickness distribution.

The dynamic portion of the ice model can be viewed as working in concert with the ocean model to produce the desired ice cover. The ocean model does not provide much of a dynamic effect from surface currents but it does provide an important thermodynamic control. The ocean circulation below the mixed layer acts to position heat below those regions where observations indicate that the ice is usually thin or melted away. The dynamic ice model in turn tends to compress the ice in those areas where it should regionally be thickest and thin the ice in those areas where the heat flux will be used to melt back the ice cover. The linkage between these two

processes is controlled by conditions at the surface and the response of the mixed layer.

Vertical mixing needs to be induced to tap the intermediate layer heat source while stratification must be induced to shut the heat off. However, the large horizontal diffusion coefficient required for numerical stability probably causes excessive lateral mixing of heat within the intermediate layer. The increased heat available in some regions may be sufficient to maintain excessive heat flux into the mixed layer, despite stratification from fresh meltwater.

It must be noted that this assessment of the relative importance of the various mechanisms is limited in application to the space and time scales associated with this model. However Ikeda et al. (1988) have presented similar conclusions based on a model of much smaller scale in the Labrador Sea. Additionally, Walsh et al. (1985) and Hibler and Bryan (1987) also present conclusions consistent with those here regarding the dominance of thermodynamic processes in the determination of ice cover extent.

Correlations between simulated ice area and observed ice area were calculated for each major change in the model configuration. Two statistical approaches were used to determine if the difference between correlations obtained from each different model configuration were large enough to be statistically significant. Limited success was achieved in that the difference between the two model runs from the

interactive ocean experiment, in region 3, were 95% significant for both statistical approaches. However, statistical significance could not be determined at the 95% confidence level for the majority of regions because the variability of the correlations was too high. The large correlation variability indicated that the model was doing very well in some time periods but poorly in others. Two explanations were proposed. First, that some process controlling the ice area, for example the mixed layer, could be inadequately represented by the model. In those conditions where the process was relatively unimportant, the model would do fine. However, if conditions changed wherein the process became important, the model simulations would be degraded. A second possible explanation is that the atmospheric forcing is not being handled correctly. In particular, the monthly averaged wind stress is probably not accounting for the effects of short term, intense weather features. The dynamic mechanism experiment pointed out the large impact that the wind stress has on the ice field; therefore, this underestimation of the wind stress could result in periods of poor model performance.

This work has shown that the relative importance of the various processes controlling the ice cover in the Arctic is regionally dependent. For example, in the western Arctic the dynamic effects assist the ocean heat flux in clearing the western boundary seas of ice. In contrast, the dynamics in

the eastern Arctic tend to oppose the clearing of ice from that region. That is, the dynamic forcing pushes the ice edge southward while the ocean heat flux tries to melt the MIZ northward. Various other combinations of effects are also evident in smaller sub-regions within the Arctic Basin. In order to allow for these variations, an ice model applied to the Arctic must be able to represent each mechanism reasonably well and be sensitive to the regional differences that change the importance of those mechanisms. Inclusion of a fully interactive prognostic ocean model in a linked ice-ocean model is necessary to do this.

B. MODEL LIMITATIONS

The discussion above already pointed out a potential problem if the monthly averaged wind fields did not provide sufficient temporal resolution of the wind to account for strong, episodic wind anomalies. The limitations of the forcing data must also be considered. This must include not only the atmospheric forcing, which is known to have some weaknesses, but also the prescribed inflow at the boundaries.

A thermodynamic role for the ocean has been proposed wherein the ocean acts to precondition the waters below the surface layer in certain regions with heat. However, despite the recent reassessment of the Intermediate Water circulation by Aagaard (1988) which would appear to support the large scale circulation simulated by the model used here,

considerable ambiguity on the smaller scale remains. Furthermore, although the simulations indicate that considerable interannual variability exists for the geostrophic surface currents, the accuracy of this variability has not been determined.

The representation of the mixed layer, which is the critical link between the ice and ocean portions of the model, was very simplified. It was noted above that the processes which occur above and below the mixed layer generally act to position the heat under areas of reduced ice thickness. However it is the action of the mixed layer, largely driven from the surface, which actually connects the ocean with the ice. The simulation of any such connection is currently limited by the vertical resolution of the upper ocean layers and the simple representation of the mixing which occurs there.

The drag coefficients used here are the same for air/ice and air/water and constant for the ice/water. Recent studies in the Arctic have shown that these drag coefficients vary dramatically with the surface type, ice concentration, ridge concentration and several other factors (e.g., Guest and Davidson, 1987). The drag coefficients determine the stress and are therefore important to the evolution of the ice field. Their simplification reduces the dynamic complexity of the forcing.

C. PROPOSED FUTURE WORK

The surface mixed layer is the link between the ice and ocean sub-models, and consequently has an effect on the majority of the ice forcing parameters. The relative importance of many of these parameters has been examined in this work. The most active times of large-scale ice edge advance and retreat occur at the start of the freezing season, and the middle of the melt season, when the pack begins to break apart. It is also the same times when the mixed layer can undergo significant changes due to convective and dynamic mixing. Several authors have noted the importance of incorporating a realistic mixed layer model in model simulations of sea surface temperature (SST). Fleming (1987) and Garcia (1988) have shown the strong correlation between SST and ice concentration in the Arctic. It would therefore be worthwhile to examine the importance of including a mixed layer model into the linked ice-ocean model used here.

The role of atmospheric forcing in the interannual variability of Arctic sea ice was examined in Hibler and Walsh (1982). That paper concluded that simulations of interannual fluctuations in the ice cover were improved with the inclusion of interannually-varying, atmospherically-forced dynamics. A similar conclusion was drawn by Walsh et al., (1985) using a more elaborate model; however neither of these efforts included interannual variations of the ocean. A re-analysis of the role of interannually variable atmospheric forcing

would be valuable using this model, as it includes an interannually varying ocean. Further, mean monthly vice daily atmospheric forcing could be examined.

The drag coefficients currently used are quite simple, as noted above. A sensitivity study examining the importance of the drag coefficients to simulations of the ice cover would be valuable and, if warranted, a more elaborate representation which accounts for the coefficient dependencies should be developed and incorporated into the model. It is anticipated that this would generate more leads in the ice, encouraging increased ice growth and a thicker ice cover. Greater compression might also occur in the MIZ and rough surface compression regions where the drag coefficients are larger.

The work proposed above would progress our knowledge of ice cover simulation and Arctic Ocean circulation on the seasonal time scale. The next logical step would be incorporation of this model into an atmospheric GCM. This would be feasible using the current code because it has a relatively small computation requirement. The computation requirements of such a coupled GCM are expected to be well within the capabilities of the next generation of supercomputers.

Finally, in order to improve the simulation and prediction of Arctic ice on a daily basis (a capability desired by most of the world's Navies), the effects of mesoscale ocean features and short duration atmospheric forcing must be

examined. To this end, the next major improvement of this model should include an increase in the horizontal resolution to at least 1/8 or 1/10 degree, bi-harmonic diffusion, an increase in the number of vertical levels to approximately 40 and daily if not six hourly atmospheric forcing.

D. FINAL GEM

Walsh et al., (1985) stated:

> ...model-derived trends (of Arctic ice cover) may be misleading in the absence of a realistic treatment of ice dynamics.

To this I would add:

> and the direct and interactive effects of three-dimensional ocean circulation.

BIBLIOGRAPHY

Aagaard, K., J.H. Swift, and E.C. Carmack, 1985: Thermohaline circulation in the Arctic Mediterranean seas. J. Geophys. Res., 90, 4833-4846.

Aagaard, K., 1988: Some Thoughts on the Large-Scale Circulation of the Arctic Ocean. Preprint Volume Second Conference on Polar Meteorology and Oceanography, March 29-31, 1988, Madison, Wisconsin, Pub. Am. Met. Soc., Boston, Mass.

Bourke, R.H., and R.P. Garret, 1987: Sea ice thickness distribution in the Arctic Ocean. Cold Regions Science and Technology, 13, 2107-2117.

Bryan, K., 1969: A numerical method for the study of the circulation of the world ocean. J. Comput. Phys., 4, 347-376.

Bryan, K., 1984: Accelerating the convergence to equilibrium of ocean-climate models. J. Phys. Oceanogr., 14, 666-673.

Cattle, H., 1985: A survey of possible repercussions of the Soviet river diversion programme on Arctic sea ice. Polar Record, 22, 485-498.

Chervin, R.M., and S.H. Schneider, 1976: On determining the statistical significance of climate experiments with general circulation models. J. Atmos. Sci., 33, 405-412.

Chervin, R.M., 1980: On the simulation of climate and climate change with general circulation models. J. Atmos. Sci., 37, 1903-1913.

CIA, 1978: Polar Regions Atlas, National Foreign Assessment Center, CIA, 66 pp.

Coachman, L.K., and K. Aagaard, 1974: Physical oceanography of Arctic and Subarctic Seas. In: Marine Geology and Oceanography of the Arctic seas (Y. Herman, Ed.), Springer-Verlag, New York, 1-72.

Coachman, L.K., and Barnes, 1961: The contribution of Bering Sea water to the Arctic Ocean. Arctic, 14(3), 146-161.

Cox, M.D., 1984: A primitive equation three-dimensional model of the ocean. GFDL Ocean Group Tech. Rept. No. 1, GFDL/NOAA, Princeton University, Princeton, 250 pp.

Eckart, 1958: Properties of water, Part III. Amer. J. Sci., 256, 225-240.

Fleming, G.H., 1987: Predictability of ice concentration in the high-latitude North Atlantic from statistical analysis of SST and ice concentration data. M.Sc. Thesis, Naval Postgraduate School, Monterey, CA, 142 pp.

Garcia, K.S., 1988: Predictability of ice concentration anomalies in the high latitudes of the North Atlantic using a statistical approach. M.Sc. Thesis, Naval Postgraduate School, Monterey, CA, 87 pp.

Gill, A.E., 1982: Atmosphere-Ocean Dynamics, Academic Press, New York, 662 pp.

Guest, P.S., and K.L. Davidson, 1987: The effect of observed ice conditions on the drag coefficient in the summer East Greenland Sea marginal ice zone. J. Geophys. Res. ,92, 6943-6954.

Hibler, W.D. III, 1979: A dynamic thermodynamic sea ice model. J. Phys. Oceanogr., 9, 815-846.

Hibler, W.D. III, 1980: Modeling a variable thickness sea ice cover. Mon. Wea. Rev., 108, 1943-1973.

Hibler, W.D. III, and J. Walsh, 1982: On modelling seasonal and interannual fluctuations of the arctic sea ice. J.Phys. Oceanogr., 12, 1514-1523.

Hibler, W.D. III, and K. Bryan, 1984: Ocean circulation: Its effects on seasonal sea-ice simulations. Science, 489-492.

Hibler, W.D. III, and K. Bryan, 1987: A diagnostic ice-ocean model. J.Phys. Oceanogr., 17, 987-1015.

Hibler, W.D. III, 1988: Modelling sea ice thermodynamics and dynamics in climate studies. in Physically Based Modelling and Simulation of Climate and Climatic Change, Part 1, M.E. Schlesinger (Ed.), Kluwer Academic Publ., Dordrecht, 509-563.

Huschke, R.E., Ed., 1959: Glossary of Meteorology, American Meteorology Society, Boston, Mass., 638 pp.

Huyer, A., and F.G. Barber, 1970: A heat budget of the water in Barrow Strait for 1962. Dept. of Energy, Mines and Resources, Marine Sci. Br., Manuscript Report Series No. 12, 43 pp.

Ikeda, M., G. Symonds, and T. Yao, 1988: Simulated fluctuations in annual Labrador sea-ice cover. Atmosphere-Ocean, 26(1), 16-39.

Kraus, E.B., Ed., 1977: Modelling and prediction of the upper layers of the ocean. Proc. NATO Advanced Study Institute, Urbino, Italy, Pergamon Press, 325 pp.

Kraus, W., 1986: The North Atlantic Current. J.Geophys. Res., 91, 5061-5074.

Kukla, G., and D. Robinson, 1980: Annual cycle of surface albedo. Mon. Wea. Rev., 108, 56-68.

Langleben, M.P., 1972: The decay of an annual ice cover. J. Glaciol., Vol.II, No. 63, 337-344.

LeSchack, L.A., W.D. Hibler III, and F.H. Morse, 1971: Automatic processing of arctic pack ice data obtained by means of submarine sonar and other remote sensing techniques, Propogation Limitations in Remote Sensing, AGARD Conf. Proc. 90, 5-1-5-19.

LeSchack, L.A., 1980: Arctic Ocean sea ice statistis derived from the upward-looking sonar data recorded during five nuclear submarine cruises. LeSchack Associates Ltd., Silver Spring, Md.

Manabe, S., and R.J. Stouffer, 1980: Sensitivity of a global climate model to an increase of CO_2 concentration in the atmosphere. J. Geophys. Res., 85, 5529-5554.

Maykut, G.A., 1978: Energy exchange over young sea ice in the central Arctic. J. Geophys. Res., 83, 3646-3658.

Maykut, G.A., and N. Untersteiner, 1969: Numerical Prediction of the Thermodynamic Response of Arctic Sea Ice to environmental Changes, Rand Corp. Memo. RM-6093-PR, Santa Monica, CA, 173 pp.

Maykut, G.A., and N. Untersteiner, 1971: Some results from a time-dependent thermodynamic model of sea ice. J. Geophys. Res., 76, 1550-1575.

Mesinger, F., and A. Arakawa, 1976: Numerical Methods Used in Atmospheric Models, GARP Publications Series No. 17, WMO-ICSU Jt. Organizing Committee, Geneva, 64 pp.

Mostellor, F., and J.W. Tukey, 1977: Data Analysis and Regression, Addison-Wesley Publishing Co., Redding, Mass.

Overland, J.E., 1985: Atmospheric boundary layer structure and drag coefficients over sea ice. J. Geophys. Res., 90, 9029-9049.

Parkinson, C.L., and W.M. Washington, 1979: A large-scale numerical model of sea ice. J. Geophys. Res., 84, 311-337.

Parkinson, C.L., C.C. Josefino, H.J. Zwally, D.J. Cavalieri, P. Gloerson, and W.J. Campbell, 1987: Arctic Sea Ice 1973-1976: Satellite Passive Microwave Observations, NASA SP-489, National Aeronautics and Space Administration, Washington, DC, 296 pp.

Pond, S., and G.L. Pickard, 1983: Introductory Dynamical Oceanography, Pergammon Press, Oxford, U.K., 329 pp.

Robinson, D.A., G. Scharfen, M.C. Serreze, G. Kukla, and R.G. Barry, 1986: Snow melt and surface albedo in the Arctic basin. Geophys. Res. Letters, 13, 945-948.

Ross, B., and J.E. Walsh, 1987: A comparison of simulated and observed fluctuations in summertime Arctic surface albedo. J. Geophys. Res., 92, 13115-13125.

Sater, J.E., A.G. Ronhovde and L.C. van Allen, 1971: Arctic Environment and Resources, Arctic Institute of North America, Washington, DC, 309 pp.

Semtner, A.J., 1974: An oceanic general circulation model with bottom topography. Numerical Simulation of Weather and Climate, Tech. Rept. No. 9, Department of Meteorology, University of California, Los Angeles, 99 pp.

Semtner, A.J., 1976a: A model for the thermodynamic growth of sea ice in numerical investigations of climate. J. Phys. Oceanogr., 6, 379-389.

Semtner, A.J., 1976b: Numerical simulation of the Arctic Ocean circulation. J. Phys. Oceanogr., 6 409-425.

Semtner, A.J., 1984a: On modelling the seasonal cycle of sea ice in studies of climatic change. Clim. Change, 6, 27-37.

Semtner, A.J., 1984b: The climatic response of the Arctic Ocean to Soviet river diversions. Clim. Change, 6, 109-130.

Semtner, A.J., 1984c: Modelling the ocean in climate studies. Ann. Glaciol., 5, 133-140.

Semtner, A.J., 1986a: History and methodology of modelling the world ocean circulation. Proceedings of the NATO Advanced Study Institute on Advanced Physical Oceanographic Numerical Modelling, D. Reidel Publishing Co., Dordrecht.

Semtner, A.J., 1986b: Finite-difference formulation of a world ocean model. Proc. NATO Institute on Advanced Physical Oceanographic Numerical Modelling, D. Reidal Publishing Co., Dordrecht.

Semtner, A.J., 1987: A numerical study of sea ice and ocean circulation in the Arctic. J. Phys. Oceanogr., 17, 1077-1099.

Semtner, A.J., and R.M. Chervin, 1988: A simulation of the global ocean circulation with resolved eddies. J. Geophys. Res., 93, 15502-15522.

Shine, K.P., and A. Henderson-Sellers, 1985: The sensitivity of a thermodynamic sea ice model to changes in surface albedo parameterization. J. Geophys. Res., 90, 2243-2250.

Takano, K., 1974: A general circulation model for the world ocean. Numerical Simulation of Weather and Climate, Tech. Rept. No. 8, Department of Meteorology, University of California, Los Angeles, 47 pp.

Tritton, D.J., 1977: Physical Fluid Dynamics, Van Nostrand Reinhold Co., New York, 362 pp.

Van Ypersele, J.P., 1986: A numerical study of the response of the southern ocean and its sea ice to a CO_2-induced atmospheric warming. Ph.D. Thesis, Universite Catholique de Louvain-la-Neuve and National Center for Atmospheric Research NCAR/CT-99, 135 pp.

Walsh, J.E., and C.M. Johnson, 1979: An analysis of arctic sea ice fluctuations, 1953-1977. J. Phys. Oceanogr., 9, 580-591.

Walsh, J.E., W.D. Hibler III, and B. Ross, 1984: A model simulation of 20 years of northern hemisphere sea ice fluctuations. Ann. Glaciol., 5, 170-176.

Walsh, J.E., W.D. Hibler III and B. Ross, 1985: Numerical simulation of Northern Hemisphere sea ice variability, 1951-1980. J. Geophys. Res., 90, 4847-4865.

Washington, W.M., A.J. Semtner, C. Parkinson and L. Morrison, 1976: On the development of a seasonal change sea ice model. J. Phys. Oceanogr., 6, 679-685.

Washington, W.M., A.J. Semtner, G.A. Meehl, D.J. Knight and T.A. Mayer, 1980: General circulation experiment with a coupled atmosphere, ocean and sea ice model. J. Phys. Oceanogr., 10, 1887-1908.

Washington, W.M., and C.L. Parkinson, 1986: An Introduction to Three-Dimensional Climate Modelling, University Science Books and Oxford University Press, Mill Valley and Oxford, 157-158.

Weatherly, G.L., 1972: A study of the bottom boundary layer of the Florida Current. J. Phys. Oceanogr., 2, 54-72.

Weeks, W.F., Kovacs, A. and Hibler, W.D. III, 1971. Presssure ridge characteristics in the Arctic coastal environment. In: S.S. Wetteland and P. Braun (Eds.), Proceedings from the First International Conference on Port and Ocean Engineering under Arctic Conditions, Vol. 1, Trondheim, Norway, 152-183.

Weigel, A.M., 1987: Mesoscale variability in the West Spitsbergen Current and adjacent waters in Fram Strait. Tech. Rep. NPS 68-87-002, Dept of Oceanography, Naval Postgraduate School, Monterey, California.

INITIAL DISTRIBUTION LIST

		NO. COPIES
1.	Defense Technical Information Center Cameron Station Alexandria, VA 22314	2
2.	Library, Code 0142 Naval Postgraduate School Monterey, CA 93943-5000	2
3.	Chairman (Code 68Co) Department of Oceanography Naval Postgraduate School Monterey, CA 93943-5000	1
4.	Chairman (Code 63Rd) Department of Meteorology Naval Postgraduate School Monterey, CA 93943-5000	1
5.	Superintendent Naval Postgraduate School ATTN: Dr. A. J. Semtner (Code 68Se)	3
	Dr. R. H. Bourke (Code 68Bf)	1
	Dr. D. C. Smith IV (Code 68Si)	1
	Dr. M. L. Batteen (Code 68Bv)	1
	Dr. R. L. Haney (Code 63Hy)	1
	Dr. L. D. Johnson (Code 55Jo	1
	Dr. J. Morison (Code 68Mo) Monterey, CA 93943-5000	1
6.	Director Naval Oceanography Division Naval Observatory 34th and Massachusetts Avenue NW Washington, DC 20390	1
7.	Commander Naval Oceanography Command NSTL Station Bay St. Louis, MS 39522	1
8.	Commanding Officer Naval Oceanographic Office NSTL Station Bay St. Louis, MS 39522	1

9. Commanding Officer — 1
Fleet Numerical Oceanography Center
Monterey, CA 93940

10. Commanding Officer — 2
Naval Ocean Research and Development
Activity
NSTL Station
Bay St. Louis, MS 39522

11. Commanding Officer — 1
Naval Environmental Prediction
Research Facility
Monterey, CA 93940

12. Chairman, Oceanography Department — 1
U. S. Naval Academy
Annapolis, MD 21402

13. Chief of Naval Research — 1
800 N. Quincy Street
Arlington, VA 22217

14. Office of Naval Research (Code 420) — 1
Naval Ocean Research and Development
Activity
800 N. Quincy Street
Arlington, VA 22217

15. Naval Ocean Research and Development — 1
Activity
Program Manager Arctic Sciences (1125 AR)
ATTN: Dr. T. Curtin
800 N. Quincy Street
Arlington, VA 22217

16. Scientific Liaison Office — 1
Office of Naval Research
Scripps Institution of Oceanography
La Jolla, CA 92037

17. Library — 1
Department of Oceanography
University of Washington
Seattle, WA 98105

18. Library — 1
CICESE
P. O. Box 4803
San Ysidro, CA 92073

19. Library 1
School of Oceanography
Oregon State University
Corvallis, OR 97331

20. Commander 1
Oceanographic Systems Pacific
Box 1390
Pearl Harbor, HI 96860

21. Chief, Ocean Services Division 1
National Oceanic and Atmospheric
Administration
8060 Thirteenth Street
Silver Springs, MD 20910

22. Direccion General De Oceanografia 1
Departmento De Hidrograficia
Ave COYOACAN 131
Mexico 12, D. F.

23. Director 1
Instituto Hidrografico
Rua Das Trinas, 49
Lisboa, Portugal

24. Director De Hidrografia y Navegacion 1
de la Marina
Calle Saenz Pena - 5th Cuadro - La Punta
Cal lao-5 Peru

25. Department of Oceanography 1
University of British Columbia
Vancouver, B. C., Canada
V6T 1W5

26. Library 1
Bedford Institute of Oceanography
P. O. Box 1006
Dartmouth, N. S., Canada
B2Y 4A2

27. Department of Oceanography 1
Dalhousie University
Halifax, N. S., Canada
B3H 4J1

28. Royal Roads Military College
ATTN: Dr. D. Krauel 1
Dr. G. Fleming 2
Dr. J. Mothersill 1
F.M.O. Victoria
Victoria, B. C., Canada
V0S 1B0

29. Institute of Ocean Sciences, Pat Bay 1
P. O. Box 6000
9860 West Saanich Road
Sidney, B. C., Canada
V8L 4B2

30. Library 1
Defence Research Establishment Pacific
F.M.O. Victoria, B. C., Canada
V0S 1B0

31. Library 1
Defence Research Establishment Atlantic
F.M.O. Halifax, N. S., Canada
B3K 2X0

32. Weapons Division 1
Canadian Forces Fleet School Halifax
F.M.O. Halifax, N. S., Canada
B3K 2X0

33. DPED 1
National Defence Headquarters
Ottawa, Ont., Canada
K1A 0K2

34. Canadian Forces Maritime Warfare School 1
ATTN: SSO Environment
F.M.O. Halifax, N. S., Canada
B3K 2X0

35. Department of Meteorology 1
McGill University
ATTN: Dr. L. Mysak
805 Sherbrooke St. W
Montreal, P. Q., Canada
H3A 2K6

36. Dr. Steve Ackley 1
USA CRREL-RS
72 Lyme Road
Hanover, NH 03755

37. National Center for Atmospheric Research
SCD Director, Dr. Bill Buzbee 1
CGD Director, Dr. W. Washington 1
P.O. Box 1470
Boulder, CO 80307

38. Polar Science Center/APL
ATTN: Dr. N. Untersteiner 1
Dr. D. Rothrock 1
Dr. R. Colony 1
1013 NE 40th Street
Seattle, WA 98105

39. Dr. W. Hibler, III 1
Dartmouth College
Thayer School of Engineering
Hanover, NH 03755

40. Dr. Ruth Preller 1
NORDA, Code 322
NSTL Station
Bay St. Louis, MS 39522

41. Commanding Officer 1
Naval Polar Oceanography Center
4301 Suitland Road
Washington, DC 20395-5180

42. NASA Goddard Space Flight Center 1
Ice-Ocean Branch
ATTN: Dr. C. Parkinson
Greenbelt, MD 20791

43. Dr. George J. Boer 1
Canadian Climate Centre
4905 Dufferin Street
Downsview, Ontario
M3H 2K6

44. Dr. Motoyoshi Ikeda 1
Fisheries & Oceans, Canada
Bedford Institute of Oceanography
P.O. Box 1006
Dartmouth, N.S.
B2Y 4A2

45. Dr. Peter Lemke 1
Max-Planck-Institute für Meteorologie
Bundesstr. 5
D-2000 Hamburg 13
West Germany

46. Dr. Barrie Maxwell 1
Head, Arctic Section
Canadian Climate Centre/AES
4905 Dufferin Street
Downsview, Ontario
M3H 5T4

47. Dr. John E. Walsh 1
Department of Atmos. Sciences
University of Illinois at Urbana-Champaign
105 South Gregory Avenue
Urbana, IL 61801

QC 16 S85

T Thesis
F F4983 Fleming
c c.1 Development of a large-scale coupled sea-ice model for inter-annual simulations of ice cover in the Arctic.

30 JUL 93 36703
36703

Thesis
F4983 Fleming
c.1 Development of a large-scale coupled sea-ice model for inter-annual simulations of ice cover in the Arctic.

thesF4983
Development of a large-scale coupled sea
3 2768 000 88751 7
DUDLEY KNOX LIBRARY